

UNIVERSITY OF MIAMI

INVESTIGATION OF CO-FLOW JET FLOW CONTROL AND ITS APPLICATIONS

By

Alexis M. Lefebvre

A DISSERTATION

Submitted to the Faculty  
of the University of Miami  
in partial fulfillment of the requirements for  
the degree of Doctor of Philosophy

Coral Gables, Florida

May 2015

©2015  
Alexis M. Lefebvre  
All Rights Reserved

UNIVERSITY OF MIAMI

A dissertation submitted in partial fulfillment of  
the requirements for the degree of  
Doctor of Philosophy

INVESTIGATION OF CO-FLOW JET FLOW CONTROL AND ITS APPLICATIONS

Alexis M. Lefebvre

Approved:

\_\_\_\_\_  
Gecheng Zha, Ph.D.  
Professor of  
Mechanical & Aerospace Engineering

\_\_\_\_\_  
Na Li, Ph.D.  
Assistant Professor of  
Mechanical & Aerospace Engineering

\_\_\_\_\_  
Amir Rahmani, Ph.D.  
Systems Engineer  
NASA Jet Propulsion Laboratory

\_\_\_\_\_  
Bertrand Dano, Ph.D.  
Research Faculty at FIU

\_\_\_\_\_  
Weiyong Gu, Ph.D.  
Professor and Chairman of  
Mechanical & Aerospace Engineering

\_\_\_\_\_  
M. Brian Blake, Ph.D.  
Dean of the Graduate School

LEFEBVRE, ALEXIS M.

(Ph.D., Mechanical & Aerospace Engineering)

Investigation of Co-Flow Jet Flow Control and its Applications

(May 2015)

Abstract of a dissertation at the University of Miami.

Dissertation supervised by Professor Gecheng Zha.

No. of pages in text. (232)

This thesis investigates the performance of co-flow jet (CFJ) flow control and its applications using experimental testing and computational fluid dynamics (CFD) simulations. First, the study examines the CFJ energy expenditure, lift enhancement, drag reduction, stall margin increase, dynamic stall removal, and performance variation with Mach number. These investigations are conducted for a variety of stationary airfoils, pitching airfoils, and 3D CFJ wings. Then, the CFJ airfoil is applied to design an ultra-high wing loading general aviation electric airplane (EA).

For a stationary airfoil and wing, CFJ increases the lift coefficient ( $C_L$ ), reduces the drag and may produce thrust at a low angle of attack (AoA). The maximum lift coefficient is substantially increased for a 2D CFJ airfoil and reaches a value of 4.8 at  $C_\mu = 0.30$ . The power consumption of the CFJ pump, measured by the power coefficient ( $P_c$ ), is influenced by a variety of parameters, including the momentum coefficient ( $C_\mu$ ), the AoA, the injection slot location, and the internal cavity configuration. A low  $C_\mu$  of 0.04 produces a rather small  $P_c$  in the range of 0.01 - 0.02 while a higher  $C_\mu$  rapidly increases the  $P_c$ . Due to

the stronger leading edge suction effect, increasing the AoA decreases the  $P_c$ . That is until the flow is near separation, within about  $2^\circ$ -  $3^\circ$  of the stall AoA. An injection slot location within 2% - 5% chord from the leading edge very effectively reduces the power coefficient since the leading edge suction effect is typically the strongest within this range. An internal cavity design with no separation is crucial to minimize the CFJ power consumption. When the Mach number is increased from 0.03 to 0.3, the suction pressure behind the airfoil leading edge is lowered due to the compressibility effect. This increases the CFJ airfoil maximum lift coefficient and decreases the power coefficient because of the lower required jet injection pressure. The drag coefficient remains fairly stable within this range of Mach numbers. At Mach 0.4, as the AoA increases, the flow on the suction surface becomes transonic. Consequently, a strong  $\lambda$  shock wave interrupts the jet and triggers a boundary-layer separation. The shock wave boundary-layer interaction and wave drag increase the total drag and the power coefficient significantly due to a large increase in entropy. Overall, the CFJ effectiveness is enhanced with an increasing Mach number as long as the flow remains subsonic, typically with free stream Mach number less than 0.4.

For a pitching airfoil, CFJ is able to remove the dynamic stall with a substantial lift increase and drag decrease. Two pitching airfoil oscillations with dynamic stall are studied in this thesis, namely the mild dynamic stall and the deep dynamic stall. At Mach 0.3, the CFJ with a relatively low  $C_{\mu}$  of 0.08 removes the mild dynamic stall. Thereby, the time-averaged lift is increased by 32% and the time-averaged drag is decreased by 80%. The resulting time-averaged aerodynamic  $(L/D)_{ave}$ , which does not take the pumping power into account, reaches 118.3. When  $C_{\mu}$  is increased, the time-averaged drag becomes negative, which demonstrates the feasibility of a CFJ to propel helicopter blades using its pump

as the only source of power. The deep-stall is mitigated at  $C_\mu = 0.12$  and completely removed at  $C_\mu = 0.20$  with a great  $(L/D)_{ave}$  increase. At Mach 0.4, the CFJ mitigates the mild dynamic stall. However, the energy consumption is higher than at Mach 0.3 due to the appearance of shock waves in the flow.

A 3D CFJ wing based on NACA 6415 airfoil with an aspect ratio of 20 produces a maximum  $L/D$  of 38.5 at a remarkably high cruise  $C_L$  of 1.20 with an AoA of  $5.0^\circ$  and a low  $C_\mu$  of 0.04. The takeoff and landing performance is also excellent with a maximum  $C_L$  of 4.7 achieved at  $C_\mu$  of 0.28 and AoA of  $40.0^\circ$ . When the wing thickness is increased from 15% to 21%, not only the lift is increased by about 5% but the structural strength is also improved. Overall the CFJ wing efficiency is found to be similar to that of conventional wings, but the lift coefficient at cruise condition is much higher, typically by 2-3 times. Hence CFJ is particularly suitable to design a compact wing with high wing loading.

In the final study of this thesis, a CFJ Electric Aircraft (CFJ-EA) is designed for the general aviation. The aircraft has a high wing loading so that it can carry more battery and reach a longer range with a relatively small wing size. The CFJ-EA mission is to carry 4 passengers at a cruise Mach number of 0.15 with a range of 315nm. The CFJ-EA cruises at a very high  $C_L$  of 1.3, which produces a wing loading of  $182.3\text{kg}/\text{m}^2$ , about 3 times higher than that of a conventional general aviation airplane. To determine the aircraft range and endurance, we introduce the corrected aerodynamic efficiency  $(L/D)_c$  defined as  $(L/D)_c = L/(D + P/V_\infty)$ , where the L and D are the aerodynamic lift and drag, P is the CFJ pumping power and  $V_\infty$  is the free stream velocity. The  $(L/D)_c$  of the CFJ-EA is excellent with a cruise value of 23.5 at a low  $C_\mu$  of 0.04. Takeoff and landing distances are also good due to a very high maximum  $C_L$  of 4.8, achieved with a high  $C_\mu$  of 0.28. During

takeoff and landing, the wing pivots around its 1/4 chord axis so that it can achieve an AoA of 25.0° with the fuselage rotated by only 5.0°. Based on a measure of merit defined as  $MPS = \text{Miles} * \text{Passengers} / S$ , where S is the wing planform area, the MPS of the present EA design is about half that of a conventional reciprocating engine general aviation airplane, and is 1.5 to 2.5 times greater than the MPS of the state of the art EA. This suggests that, compared to the conventional EA, a same size CFJ-EA has a far greater range, or a smaller CFJ-EA achieves the same range. Therefore, the CFJ-EA concept may open the door to a new class of general aviation EA designs. The same CFJ airfoil flow control technology is also suitable for airplanes and rotorcraft using conventional propulsion systems including high altitude planform, general aviation, commercial aviation or military transport to improve the range, reduce the wing size and/or reduce the takeoff and landing distances.

*Dedicated to everyone that shares the passion for Aeronautics  
and works for its Excellence*

# Contents

List of Figures . . . . .	vii
List of Tables . . . . .	xv
List of Symbols . . . . .	xvi
<b>Chapter 1 Introduction</b>	<b>1</b>
1.1 Airfoil Design . . . . .	1
1.1.1 Chronological Evolution . . . . .	1
1.1.2 Modern Airfoil Design . . . . .	3
1.2 High Lift Flow Control . . . . .	5
1.2.1 Vortex Generator . . . . .	7
1.2.2 Slat and Flap . . . . .	8
1.2.3 Suction and Blowing . . . . .	11
1.2.4 Plasma Actuator . . . . .	18
1.2.5 Circulation Control Airfoil . . . . .	20
1.2.6 CFJ Flow Control Method . . . . .	22
1.3 CFJ Airfoil for Rotorcraft . . . . .	28
1.3.1 Background . . . . .	28
1.3.2 Dynamic Stall Mitigation . . . . .	29
1.3.3 CFJ Airfoil, an Effective Solution to Remove Dynamic Stall . . . . .	31
1.4 CFJ Airfoil for Electric Aircraft . . . . .	31
1.4.1 Environmental Background . . . . .	33
1.4.2 Electric Energy Storage . . . . .	34
1.4.3 Propulsive Efficiency . . . . .	35
1.4.4 A Necessary Revolution of Aircraft Technology . . . . .	37
1.4.5 CFJ General Aviation Electric Aircraft: A Revolutionary Concept . . . . .	39
1.5 Outline and Strategy of the Thesis . . . . .	40
<b>Chapter 2 The Fluid Flow Governing Equations</b>	<b>42</b>
2.1 The Navier-Stokes Equations . . . . .	42
2.2 Spalart-Allmaras Turbulence Model . . . . .	47
<b>Chapter 3 Numerical Methodology</b>	<b>52</b>
3.1 Implicit Discretization . . . . .	52
3.2 Implicit Time Integration . . . . .	54
3.3 Gauss-Seidel Line Relaxation . . . . .	55
3.4 User Prescribed $C_\mu$ Boundary Condition for CFJ . . . . .	56
3.5 Validation Study . . . . .	57
<b>Chapter 4 CFJ Airfoil Parameters</b>	<b>59</b>
4.1 Lift, Drag and Moment Calculation . . . . .	59

4.2	Jet Momentum Coefficient . . . . .	61
4.3	Power Coefficient . . . . .	61
4.4	Corrected Aerodynamic Efficiency . . . . .	62
<b>Chapter 5</b>	<b>Mission Analysis</b>	<b>64</b>
5.1	Background . . . . .	64
5.2	Range Estimate for Electric Aircraft . . . . .	65
<b>Chapter 6</b>	<b>Experimental Investigation of CFJ Airfoils</b>	<b>68</b>
6.1	Experimental Setup . . . . .	68
6.2	Flow Visualization . . . . .	71
6.3	Particle Image Velocimetry . . . . .	73
<b>Chapter 7</b>	<b>Numerical Investigation of Stationary CFJ Airfoils</b>	<b>80</b>
7.1	Mach number effect on Performance Enhancement and Energy Expenditure	81
7.1.1	Mesh . . . . .	82
7.1.2	CFD Validation at $M=0.03$ . . . . .	82
7.1.3	Performance at High Mach Number 0.3 and 0.4 . . . . .	84
7.2	CFJ Airfoil Trade Study Part I : Energy Consumption and Aerodynamic Efficiency . . . . .	90
7.2.1	Mesh . . . . .	90
7.2.2	Baseline Airfoil . . . . .	92
7.2.3	CFJ Airfoil Trade Study . . . . .	94
7.2.4	Final CFJ Airfoil from Trade Study . . . . .	104
7.3	CFJ Airfoil Trade Study Part II : Moment and Drag . . . . .	108
7.3.1	Mesh . . . . .	108
7.3.2	Low Moment CFJ Airfoils . . . . .	109
7.3.3	CFJ Airfoil with Thrust Generation . . . . .	111
<b>Chapter 8</b>	<b>Numerical Investigation of Pitching CFJ Airfoils</b>	<b>118</b>
8.1	CFJ Pitching Airfoils at $M_\infty = 0.3$ . . . . .	119
8.1.1	Mesh . . . . .	119
8.1.2	Geometry and Oscillation Description . . . . .	120
8.1.3	Baseline and CFJ Airfoils Undergoing No-stall Oscillation . . . . .	121
8.1.4	Baseline Airfoil Undergoing Mild-Stall Oscillation . . . . .	122
8.1.5	CFJ Airfoil Undergoing Mild-Stall Oscillation . . . . .	125
8.1.6	Baseline Airfoil Undergoing Deep-Stall Oscillation . . . . .	131
8.1.7	CFJ Airfoil Undergoing Deep-Stall Oscillation . . . . .	131
8.1.8	Discussion . . . . .	141
8.2	CFJ Pitching Airfoils at $M_\infty = 0.4$ . . . . .	141
8.2.1	Mesh . . . . .	141
8.2.2	Geometry and Oscillation Description . . . . .	143
8.2.3	Design 1 Airfoil . . . . .	144
8.2.4	Design 2 (CFJ-NACA1209) and Design 3(CFJ-NACA2209a) Airfoils	147
8.2.5	Design 4(CFJ-NACA2209b) Airfoil . . . . .	148
<b>Chapter 9</b>	<b>Numerical Investigation of CFJ Wings</b>	<b>160</b>
9.1	Mesh . . . . .	160
9.2	Wing Configurations . . . . .	162
9.3	Design 1 CFJ Wing . . . . .	164
9.4	CFJ Spanwise Location . . . . .	171

9.5	CFJ Injection Location & Redesigned Cavities . . . . .	171
9.6	Airfoil Thickness . . . . .	175
9.7	Wing Aspect Ratio . . . . .	175
9.8	Recapitulation of the CFJ Wings Performance at Cruise . . . . .	177
9.9	CFJ Wing Maximum Lift Coefficient in Takeoff or Landing Condition . . .	178
<b>Chapter 10</b>	<b>Conceptual Design of a CFJ Electric Aircraft</b>	<b>184</b>
10.1	The CFJ Flying Wing Design . . . . .	185
10.1.1	Mesh . . . . .	185
10.1.2	Aircraft Configuration . . . . .	185
10.1.3	Qualitative Analysis . . . . .	189
10.1.4	Quantitative Analysis . . . . .	193
10.1.5	Mission Analysis . . . . .	195
10.2	The High Aspect Ratio Wing Design . . . . .	198
10.2.1	Mesh . . . . .	198
10.2.2	Aircraft Configuration . . . . .	199
10.2.3	Cruise Condition with Low $C_{\mu}$ . . . . .	202
10.2.4	Takeoff/Landing Condition with High $C_{\mu}$ . . . . .	211
10.2.5	Mission Analysis . . . . .	215
<b>Chapter 11</b>	<b>Conclusions</b>	<b>220</b>
	References . . . . .	224

# List of Figures

1.1	Evolution of airfoil sections from 1908 to 1944. The last two shapes (N.A.C.A. 661 -212 and N.A.C.A. 74 7A315) are low-drag sections designed to have laminar flow over 60 to 70 percent of chord on both the upper and the lower surface. . . . .	4
1.2	Airfoil flow patterns at transonic speeds discussed at NACA University Conference, 1948 . . . . .	5
1.3	Boundary layer development over an airfoil. . . . .	6
1.4	Vortex generator effect on the flow over an airfoil with increasing AoA. . . . .	8
1.5	Boeing 777 at takeoff with flaps and slats fully deployed. Notice the vortex generators located on the outboard flap. Credit: Boeing. . . . .	9
1.6	Airfoil with triple-slotted flap, slat, and spoiler. . . . .	10
1.7	Flow around a circular cylinder with one-sided suction of the boundary layer. . . . .	12
1.8	Generic airfoils with tangential blowing and suction. . . . .	14
1.9	A plasma actuator creates a dielectric barrier discharge in the vicinity of the wall. . . . .	19
1.10	Implementation of CFJ on a generic airfoil. . . . .	23
1.11	Massive flow separation of baseline NACA 6415 airfoil at AoA=25°. . . . .	23
1.12	Attached flow of CFJ NACA 6415 airfoil at AoA=25° measured by PIV in experiment. . . . .	24
1.13	Coherent vortex structures in the region of CFJ airfoil injection, AoA=5°, $C_{\mu} = 0.02$ . . . . .	24
1.14	Comparison of lift coefficient of CFJ airfoils with different obstruction factors at constant mass flow $\dot{m} = 0.03kg/s$ . . . . .	27
1.15	Comparison of the drag polars of discrete CFJ airfoils with different obstruction factors at constant mass flow $\dot{m} = 0.06kg/s$ . . . . .	27
1.16	Blade velocity variation with the position on the rotor disk. Because of the rotation motion, the inner portion of the blade is slower than the outer portion. . . . .	28
1.17	The e-Genius broke 7 world records in July 2014. . . . .	33
1.18	The Taurus G4 airplane, winner of the Green Flight Challenge in 2011, Image by Wernher Krutein / Photovault.com . . . . .	33
1.19	Volume and mass specific energy characteristics of different energy storage systems. . . . .	36
1.20	Typical on-board conversion chains with typical component efficiencies and total chain efficiency. . . . .	37
1.21	Current battery technology and expected development. . . . .	38

3.1	Discretization domain indicating the cell center(i,j)	53
3.2	Typical boundary condition setup for a CFJ airfoil simulation.	57
6.1	The CFJ airfoil in the wind tunnel with zoomed-in injection region. The tabs are in position DCFJ2/3.	70
6.2	Overall Performance enhancement for various obstruction factors at the constant mass flow rate $\dot{m}$ of 0.090 kg/s.	72
6.3	DCFJ airfoil flow visualization in the position DCFJ2/3A and AoA=15°. The frame is positioned in the mid plane of a tab. The flow is observed for $\dot{m} = 0.000kg/s$ (top) and $\dot{m} = 0.090kg/s$ at two different time (middle and bottom).	73
6.4	Flow visualization at various spanwise locations for DCFJ2/3B at AoA=0° and $\dot{m} = 0.030$ for the centerline of a discrete jet (top), the edge of a tab (middle) and the centerline of a tab (bottom).	74
6.5	Average velocity plotted along a discrete jet (left) and over a tab (right) for a DCFJ 2/3A, at AoA=15° (top) and a DCFJ 3/4A, at AoA=25° (bottom). The mass flow is fixed at $\dot{m} = 0.090kg/s$ for all cases.	75
6.6	Average velocity field over a tab (top) and tab/jet edge (middle) and over a jet (bottom). The airfoil is in a DCFJ 2/3B configuration with AoA=0° and $\dot{m} = 0.030$ .	77
6.7	Comparison of streamlines between jet and tab flow (top) DCFJ 3/4A with AoA=25° and $\dot{m} = 0.090$ , (bottom) DCFJ 2/3B with AoA=0° and $\dot{m} = 0.030$ .	78
6.8	Velocity iso-surface at 15m/s (top) and 18.5m/s (bot) for the DCFJ 2/3B at AoA = 0° and $\dot{m} = 0.030$ , comparison between simulation (top) and experiment (bottom).	79
6.9	Vorticity iso-surface $\omega Z$ for DCFJ 2/3B with AoA=0° and $\dot{m} = 0.030$ . Iso-surface value: $\omega Z = \pm 0.15s^{-1}$ (blue= counter-clockwise rotation, red= clockwise rotation).	79
7.1	CFJ 6415 2D O-mesh topology with detailed view of the injection and suction cavities.	83
7.2	Lift, drag and power coefficient comparison between experimental data and CFD calculations at M=0.03 and $C_{\mu} = 0.08$ .	84
7.3	Lift, drag, power comparison and corrected aerodynamic efficiency variations from M=0.03 to M=0.4 and $C_{\mu} = 0.08$ .	86
7.4	Drag polar (left) and drag polar corrected to account for the pumping power (right) at various Mach number and $C_{\mu} = 0.08$ .	87
7.5	Pressure coefficient comparison between the CFJ and the baseline airfoil plotted at AoA 0°, 10° and 20°. The free stream Mach number varies from 0.03 to 0.3 and $C_{\mu}$ is 0.08.	88
7.6	Computed total pressure inside the injection and suction cavities at M=0.3 and $C_{\mu} = 0.08$ .	89
7.7	CFJ 6415 airfoil Mach contours plotted at AoA 0°, 10° and 20°. The free stream Mach number is 0.03 and $C_{\mu}$ is 0.08.	90
7.8	CFJ 6415 airfoil Mach contours plotted at AoA 0°, 10° and 20°. The free stream Mach number is 0.3 and $C_{\mu}$ is 0.08.	91

7.9	CFJ 6415 airfoil Mach contours plotted at AoA 0°, 10° and 20°. The free stream Mach number is 0.04 and $C_{\mu}$ is 0.08. . . . .	92
7.10	Mach number line contours within the injection region plotted at AoA 0°, 10° and 20°. The free stream Mach number is 0.03 and $C_{\mu}$ is 0.08. . . . .	93
7.11	Mach number line contours within the injection region plotted at AoA 0°, 10° and 20°. The free stream Mach number is 0.3 and $C_{\mu}$ is 0.08. . . . .	94
7.12	Mach number line contours within the injection region plotted at AoA 0°, 10° and 20°. The free stream Mach number is 0.4 and $C_{\mu}$ is 0.08. . . . .	95
7.13	NACA 23121 CFJ airfoil O-mesh topology. . . . .	96
7.14	NACA 23121 baseline airfoil O-mesh topology. . . . .	96
7.15	NACA 23121 baseline airfoil C-mesh topology. . . . .	97
7.16	NACA 23121 baseline Mach contours at different AoA. . . . .	97
7.17	Numerically obtained forces and moment compared with experimental data for the NACA 23121 geometry. . . . .	98
7.18	Geometries with variable jet exit location. . . . .	98
7.19	Variation of forces, moment and power consumption with the jet exit location at $AoA = 10^{\circ}$ and $C_{\mu} = 0.16$ . . . . .	99
7.20	Overlay of the suction geometries. . . . .	100
7.21	Variation of forces, moment and power consumption with suction size at $AoA = 10^{\circ}$ and $C_{\mu} = 0.16$ . The horizontal axis represents the ratio of the current suction size to the original suction size which is 1.5%chord. . . . .	101
7.22	Geometries overlapped for the different suction location. . . . .	101
7.23	Variation of forces, moment and power consumption with suction location at $AoA = 10^{\circ}$ and $C_{\mu} = 0.16$ . . . . .	102
7.24	Thickness study overlapped geometries. In addition an airfoil with a 4% jet exit location is generated for the 12% thickness airfoil. . . . .	103
7.25	Variation of forces, moment and power consumption with airfoil thickness at $AoA = 10^{\circ}$ and $C_{\mu} = 0.16$ . The black squares data stand for the 6% jet exit location while the crosses data stands for the 4% jet exit location. . . . .	103
7.26	Variation of forces, moment and power consumption with Reynolds number at $AoA = 10^{\circ}$ and $C_{\mu} = 0.16$ . . . . .	104
7.27	Corrected aerodynamic efficiency gain during CFJ trade study. . . . .	105
7.28	Final airfoil geometry accordingly to the trade study on the injection and suction size and location. . . . .	106
7.29	Mach contours variation with AoA at $C_{\mu} = 0.16$ . Images include zoomed-in pictures of suction and injection areas. . . . .	106
7.30	Variation of forces, moment and power consumption with AoA for various $C_{\mu}$ . . . . .	108
7.31	NACA 23121 CFJ airfoil O-mesh topology. . . . .	109
7.32	Geometry of the NACA 23121, NACA 34121 and NACA 6321 CFJ airfoils and their variations. . . . .	111
7.33	Variation of forces, moment and power consumption for the NACA 23121 CFJ airfoils variations at $AoA = 10^{\circ}$ and $C_{\mu} = 0.16$ . . . . .	112
7.34	Variation of forces, moment and power consumption for the NACA 34121 CFJ airfoils variations at $AoA = 10^{\circ}$ and $C_{\mu} = 0.16$ . . . . .	113

7.35	Variation of forces, moment and power consumption for the NACA 6321 CFJ airfoils variations at $AoA = 10^\circ$ and $C_\mu = 0.16$ . . . . .	114
7.36	Geometry of the NACA 23112 CFJ airfoil with original jet size and the 2/3 jet size. . . . .	114
7.37	Variation of forces, moment and power consumption for the NACA 23112 CFJ airfoils with $AoA$ and $C_\mu$ . . . . .	115
7.38	Variation of forces, moment and power consumption for the NACA 23112 CFJ airfoils with $AoA$ and $C_\mu$ . The jet size is reduced to 2/3 of the original jet size. . . . .	117
7.39	$(\frac{L}{D})_c$ versus $C_D$ for the NACA 23112 CFJ airfoil with original and reduced injection sizes plotted for various $C_\mu$ . The thrust generation area is zoomed-in on the right plot. . . . .	117
8.1	SC1095 CFJ pitching airfoil mesh topology. . . . .	119
8.2	Baseline pitching airfoil $C_l$ , $C_d$ and $C_m$ compared with experimental data for the no-stall case. . . . .	122
8.3	CFJ pitching airfoil $C_l$ , $C_d$ and $C_m$ compared with baseline calculation for the no-stall case. . . . .	123
8.4	Instantaneous Mach contour of the baseline pitching airfoil with streamlines at different $AoA$ for the mild-stall case. . . . .	124
8.5	Baseline pitching airfoil $C_l$ , $C_d$ and $C_m$ compared with experimental data for the mild-stall case. . . . .	125
8.6	Instantaneous Mach contour of the CFJ pitching airfoil at $C_\mu = 0.08$ with streamlines at different $AoA$ for the mild-stall case. . . . .	126
8.7	CFJ pitching airfoil $C_l$ , $C_d$ and $C_m$ compared with Baseline calculation for the mild-stall case. . . . .	127
8.8	Evolution of injection mass flow, suction mass flow and $C_\mu$ (top) and injection and suction pressure (bot) with the oscillation cycle for the mild-stall case. . . . .	128
8.9	Numerically obtained pressure coefficient comparison between CFJ pitching airfoil and baseline pitching airfoil for the mild-stall case. . . . .	130
8.10	Instantaneous Mach contour of the baseline pitching airfoil with streamlines at different $AoA$ for the deep-stall case. . . . .	132
8.11	Baseline pitching airfoil $C_l$ , $C_d$ and $C_m$ compared with experimental data for the deep-stall case. . . . .	133
8.12	Instantaneous Mach contour of the CFJ pitching airfoil geometry 1 at $C_\mu = 0.12$ with streamlines at different $AoA$ for the deep-stall case. . . . .	134
8.13	Instantaneous Mach contour of the CFJ pitching airfoil geometry 2 at $C_\mu = 0.20$ with streamlines at different $AoA$ for the deep-stall case. . . . .	135
8.14	Instantaneous Mach contour of the CFJ pitching airfoil geometry 3 at $C_\mu = 0.24$ with streamlines at different $AoA$ for the deep-stall case. . . . .	136
8.15	Dynamic-stall analysis using the instantaneous Mach contour and pressure coefficient of the CFJ pitching airfoil geometry 1 at $C_\mu = 0.12$ . . . . .	137
8.16	CFJ pitching airfoil $C_l$ , $C_d$ and $C_m$ compared with Baseline calculation for the deep-stall case. . . . .	138

8.17	Numerically obtained pressure coefficient comparison between 3 CFJ pitching airfoil geometries and baseline pitching airfoil for the deep-stall case. . . . .	140
8.18	Design 3 (CFJ-NACA2209a) airfoil mesh topology. Similar mesh is applied to the other airfoils. . . . .	142
8.19	Airfoils and cavities geometry comparison. . . . .	144
8.20	Instantaneous Mach contour of the baseline design1 pitching airfoil with streamlines at different AoA during oscillation 1. . . . .	146
8.21	Instantaneous Mach contour of the CFJ Design 1 pitching airfoil at $C_{\mu} = 0.08$ with streamlines at different AoA during oscillation 1. . . . .	147
8.22	Design1 baseline pitching airfoil $C_l$ , $C_d$ and $C_m$ compared with Design1 CFJ data during oscillation 1. . . . .	148
8.23	Time-averaged performance of the Design 1 baseline and CFJ airfoils. . . . .	149
8.24	Instantaneous Mach contour of the baseline NACA2209 pitching airfoil with streamlines at different AoA during oscillation 1. . . . .	150
8.25	NACA2209 baseline pitching airfoil $C_l$ , $C_d$ and $C_m$ compared with Design 2 data during oscillation 1. . . . .	151
8.26	NACA2209 baseline pitching airfoil $C_l$ , $C_d$ and $C_m$ compared with Design 3 data during oscillation 3. . . . .	152
8.27	Time-averaged performance of the NACA2209 baseline and Design 3 airfoil. . . . .	153
8.28	Instantaneous Mach contour of the Design 4 pitching airfoil at $C_{\mu} = 0.06$ with streamlines at different AoA during oscillation 1. . . . .	154
8.29	Instantaneous Mach contour of the Design 4 pitching airfoil at $C_{\mu} = 0.08$ with streamlines at different AoA during oscillation 2. . . . .	155
8.30	Instantaneous Mach contour of the Design 4 pitching airfoil at $C_{\mu} = 0.08$ with streamlines at different AoA during oscillation 3. . . . .	155
8.31	Time-averaged performance of the NACA2209 baseline and Design 4 airfoil. . . . .	156
8.32	Time-averaged total pressure ratio and power coefficient of the Design 4 airfoil during motion 1. . . . .	156
8.33	NACA2209 baseline pitching airfoil $C_l$ , $C_d$ and $C_m$ compared with Design 4 data during oscillation 1. . . . .	157
8.34	NACA2209 baseline pitching airfoil $C_l$ , $C_d$ and $C_m$ compared with Design 4 data during oscillation 2. . . . .	158
8.35	NACA2209 baseline pitching airfoil $C_l$ , $C_d$ and $C_m$ compared with Design 4 data during oscillation 3. . . . .	159
9.1	NACA 6415 baseline wing mesh topology. The surface mesh is displayed on the left plot and the outer mesh on the right plot. . . . .	161
9.2	NACA 6415 CFJ wing mesh topology. The surface mesh is displayed on the left plot and the injection and suction cavity mesh on the right plot. . . . .	162
9.3	CFJ airfoils geometry. . . . .	163
9.4	Surface pressure contours with streamlines for the Design 1 CFJ wing at $C_{\mu} = 0.08$ . The AoA is $15^{\circ}$ on the left and $25^{\circ}$ on the right. . . . .	165
9.5	Mach contours with streamlines at 0%, 50% and 99% spanwise location for the Design 1 CFJ wing at $C_{\mu} = 0.08$ . The AoA is $15^{\circ}$ for the left plots and $25^{\circ}$ for the right plots. . . . .	166

9.6	Close up view of the experimental injection and suction cavities for the Design 1 CFJ wing. Mach contours at 50% spanwise location, $C_{\mu} = 0.08$ and $AoA = 15^{\circ}$ . . . . .	166
9.7	Pressure coefficient (left) and isentropic Mach number (right) at various spanwise location for the baseline NACA 6415 wing without CFJ at $AoA = 15^{\circ}$ . . . . .	167
9.8	Pressure coefficient (left) and isentropic Mach number (right) at various spanwise location for the Design 1 CFJ wing at $AoA = 15^{\circ}$ and $C_{\mu} = 0.08$ . . . . .	167
9.9	Forces, moment and energy expenditure versus AoA for the Design 1 CFJ wing. Simulations performed at $M=0.15$ and $0.04 \leq C_{\mu} \leq 0.08$ . . . . .	168
9.10	Mass-averaged total pressure ratio between the injection and suction cavities for the Design 1 CFJ wing. . . . .	169
9.11	Mass-averaged total pressure ratio between the injection cavity and the free stream for the Design 1 CFJ wing . . . . .	170
9.12	Static pressure contours at 50% spanwise location for the Design 1 CFJ wing. The CFJ wing is in cruise condition at $AoA = 5.0^{\circ}$ and $C_{\mu} = 0.04$ . The free stream static pressure is 1.00. . . . .	170
9.13	Surface pressure contours with streamlines for the Design 2 CFJ wing at $C_{\mu} = 0.08$ . The top plot is at $AoA=15^{\circ}$ and the bottom plot at $AoA=25^{\circ}$ . . . . .	172
9.14	Forces, moment and energy expenditure versus AoA for the Design 2 CFJ wing. Simulations performed at $M=0.15$ and $0.04 \leq C_{\mu} \leq 0.08$ . . . . .	173
9.15	Mach contours with streamlines at 50% spanwise location for the Design 3 CFJ wing at $C_{\mu} = 0.08$ and $AoA = 15^{\circ}$ . A close up view of the redesigned injection and suction cavities is provided. . . . .	173
9.16	Forces, moment and energy expenditure versus AoA for the Design 3 CFJ wing. Simulations performed at $M=0.15$ , $0.04 \leq C_{\mu} \leq 0.08$ . . . . .	174
9.17	Forces, moment and energy expenditure versus AoA for the Design 4 CFJ wing. Simulations performed at $M=0.15$ , $0.04 \leq C_{\mu} \leq 0.08$ . . . . .	176
9.18	Forces, moment and energy expenditure versus AoA for the Design 5 CFJ wing. Simulations performed at $M=0.15$ , $0.04 \leq C_{\mu} \leq 0.08$ . . . . .	177
9.19	Corrected aerodynamic efficiency versus $C_L$ for the Design 1-5 CFJ wings. Simulations performed at $M=0.15$ and $0.04 \leq C_{\mu} \leq 0.08$ to simulate typical cruise conditions. . . . .	179
9.20	Surface isentropic Mach number contours with streamlines for the Design 4 CFJ wing at $AoA = 25^{\circ}$ and $C_{\mu} = 0.20$ . Simulations performed at $M=0.1$ , to simulate the takeoff and landing conditions. . . . .	180
9.21	Forces, moment and energy expenditure versus AoA for the Design 4 CFJ wing. Simulations performed at $M=0.1$ and $0.16 \leq C_{\mu} \leq 0.28$ to simulate the takeoff and landing conditions. . . . .	181
9.22	Corrected aerodynamic efficiency versus AoA for the Design 4 CFJ wing. Simulations performed at $M=0.1$ and $0.16 \leq C_{\mu} \leq 0.28$ to simulate the takeoff and landing conditions. . . . .	182
9.23	Mass-averaged total pressure ratio between the injection and suction cavities for the Design 4 CFJ wing for a typical takeoff or landing. . . . .	182

9.24	Static pressure contours at 50% spanwise location for the Design 4 CFJ wing. The CFJ wing is in takeoff/landing condition at $AoA = 25.0^\circ$ and $C_\mu = 0.20$ . The free stream static pressure is 1.00. . . . .	183
10.1	Geometry and mesh overview for the baseline Eplane. . . . .	186
10.2	Geometry and mesh overview for the CFJ-EA Design 1, Design 2 and Design 3. . . . .	187
10.3	Slightly off-center profile comparison between the baseline and CFJ-EA. . . . .	187
10.4	Surface pressure contours with streamlines for the baseline EA at $AoA = 5^\circ$ . The red, respectively blue, streamlines originate from the pressure side, respectively the suction side, of the aircraft. . . . .	190
10.5	Surface pressure contours with streamlines for the CFJ-EA Design 1 at $C_\mu = 0.08$ and $AoA = 5^\circ$ . . . . .	191
10.6	Surface pressure contours with streamlines for the CFJ-EA Design 2 at $C_\mu = 0.08$ and $AoA = 10^\circ$ . . . . .	191
10.7	Surface pressure contours with streamlines for the CFJ-EA Design 3 at $C_\mu = 0.08$ and $AoA = 10^\circ$ . . . . .	192
10.8	Surface pressure contours with streamlines at 0% span and 50% span for the CFJ-EA Design 3 at $C_\mu = 0.08$ and $AoA = 10^\circ$ . . . . .	192
10.9	Mach contours with streamlines at various span for the CFJ EA Design 3 at $C_\mu = 0.08$ and $AoA = 10^\circ$ . . . . .	193
10.10	Surface pressure contours with streamlines for the CFJ-EA Design 3 at $C_\mu = 0.08$ and $AoA = 25^\circ$ . . . . .	194
10.11	Lift, drag and moment coefficients versus AoA for the CFJ-EA Design 3 and the baseline EA. . . . .	195
10.12	Aerodynamic efficiency, power coefficient, and corrected efficiency versus AoA for the CFJ-EA Design 3 and the baseline EA. . . . .	196
10.13	Corrected efficiency versus lift coefficient for the CFJ-EA Design 3 and the baseline EA. . . . .	196
10.14	Mesh overview for the CFJ-EA. Only one mesh point out of two is displayed for clarity. . . . .	200
10.15	CFJ-EA isometric view (unit: meters). . . . .	201
10.16	Surface pressure contours, cruise conditions, $C_\mu = 0.04$ and $AoA = 5^\circ$ . . . . .	203
10.17	$C_p$ at different spanwise locations, cruise conditions, $C_\mu = 0.04$ and $AoA = 5^\circ$ . The 7% spanwise location corresponds to the wing root. . . . .	204
10.18	Isentropic Mach number at different spanwise locations, cruise conditions, $C_\mu = 0.04$ and $AoA = 5^\circ$ . The 7% spanwise location corresponds to the wing root. . . . .	204
10.19	Eplane Mach contours at various spanwise locations, cruise conditions, $C_\mu = 0.04$ and $AoA = 5^\circ$ . . . . .	205
10.20	Eplane surface pressure contours, maneuvering, $C_\mu = 0.04$ and $AoA = 15^\circ$ . . . . .	207
10.21	Iso-surfaces at Mach 0.05 (blue) and Mach 0.20 (green) for the CFJ EA at $C_\mu = 0.04$ and $AoA = 15^\circ$ . . . . .	208
10.22	Surface pressure contours, maneuvering, $C_\mu = 0.08$ and $AoA = 15^\circ$ . . . . .	208
10.23	Forces and moment versus AoA, simulations performed at $M=0.15$ , $0.04 \leq C_\mu \leq 0.08$ . . . . .	209

10.24	Energy expenditure and aerodynamic efficiency versus AoA, simulations performed at $M=0.15$ , $0.04 \leq C_{\mu} \leq 0.08$ . The pumping efficiency is 85%. .	210
10.25	Corrected aerodynamic efficiency versus $C_L$ , simulations performed at $M=0.15$ , $0.04 \leq C_{\mu} \leq 0.08$ . The pumping efficiency is 85%. . . . .	210
10.26	Mass-averaged total pressure ratio between the injection and suction cavities, simulations performed at $M=0.15$ , $0.04 \leq C_{\mu} \leq 0.08$ . . . . .	211
10.27	Static pressure contours at 50% spanwise location. The aircraft is in cruise condition. The free stream static pressure is 1.00. . . . .	212
10.28	Eplane isentropic Mach contours, takeoff/landing condition, maneuvering, simulations performed at $AoA = 15^{\circ}$ , $M=0.10$ and $C_{\mu} = 0.24$ . . . . .	213
10.29	Energy expenditure and aerodynamic efficiency versus AoA, simulations performed at $M=0.10$ , $0.16 \leq C_{\mu} \leq 0.28$ . . . . .	214
10.30	Energy expenditure and aerodynamic efficiency versus AoA, simulations performed at $M=0.10$ , $0.16 \leq C_{\mu} \leq 0.28$ . The pumping efficiency is 85%. .	215
10.31	Mass-averaged total pressure ratio between the injection and suction cavities, simulations performed at $M=0.10$ , $0.16 \leq C_{\mu} \leq 0.28$ . . . . .	215

# List of Tables

6.1	The various discrete CFJ configurations studied. . . . .	71
7.1	Reynolds number variation with free stream velocity and Mach number . . .	81
7.2	Block dimensions for the CFJ 6415 airfoil . . . . .	82
8.1	Block dimensions for CFJ SC1095 airfoil . . . . .	120
8.2	Pitching airfoil geometry description, length are given in % of chord. . . . .	121
8.3	Pitching airfoil oscillation description. . . . .	121
8.4	Summary of the aerodynamic performance for all the cases studied. The $(L/D)_{ave}$ consider only the aerodynamic forces applied on the airfoil and not the pumping power. . . . .	141
8.5	Pitching airfoil geometry description, length are given in % of chord. . . . .	145
8.6	Pitching airfoil oscillation description. . . . .	145
9.1	CFJ wings geometry. . . . .	163
10.1	EA geometry parameters. . . . .	188
10.2	Mission analysis for the baseline EA, CFJ-EA Design 3 and the hybrid EA. A comparison is made with the kerosene burning Cessna 172 and the electric aircraft Antares 20. Some of the data are only estimates. . . . .	198
10.3	Mission analysis comparison between the CFJ-EA, Cessna 172 reciprocating engine airplane and three state of the art electric airplanes. Some of the data are only estimates. . . . .	218
10.4	Performance change with the battery specific energy and the structure factor. Identical data are represented with " for clarity. . . . .	219

# List of Symbols

$a, c$	speed of sound, $\sqrt{\gamma p / \rho}$
$A, B, C$	Jacobian matrix of inviscid flux $\mathbf{E}, \mathbf{F}, \mathbf{G}$ in $\xi, \eta, \zeta$ direction
$C$	speed of sound in generalized coordinates, $c\sqrt{l_\xi^2 + l_\eta^2 + l_\zeta^2}$
$\mathbf{C}$	absolute velocity vector
$C_L, C_D, C_M$	lift, drag and moment coefficients
$C_p$	specific heat capacity at constant pressure
$C_p$	pressure coefficient
$d$	distance from the closest wall
$dQ$	heat added to system
$dW$	total work done on the system
$dE$	change in total energy of system
$D$	drag, source term of Navier-Stokes equations in generalized coordinates
$E^*$	battery specific energy density
$\mathbf{E}, \mathbf{F}, \mathbf{G}$	inviscid flux vectors in $\xi, \eta, \zeta$ direction
$e$	total energy per unit mass
$\eta$	propeller efficiency
$\mathbf{F}$	sum of fluid force acting on the structure or on a finite control volume
$H$	total enthalpy
$I$	identity matrix
$J$	Jacobian of the coordinate transformation, $\frac{\partial(\xi, \eta, \zeta)}{\partial(x, y, z)}$
$L$	reference length, lift
$(L/D)_c$	corrected efficiency $L/(D + P/V_\infty)$

$\mathbf{l}, \mathbf{m}, \mathbf{n}$	normal vector on $\xi, \eta, \zeta$ inter surface with the magnitude equal to the interface area
$l_t$	grid moving velocity
$L, M, N$	Jacobian matrix of viscous flux $\mathbf{R}, \mathbf{S}, \mathbf{T}$ in $\xi, \eta, \zeta$ coordinates
$\dot{m}$	mass flow across the pump
$m$	pseudo time marching step
$n$	physical time marching step
$p$	static pressure
$p_t$	total pressure
$P$	pumping power consumption
$P_c$	pumping power coefficient
$\mathbf{Q}$	conservative variable vector
$\mathbf{R}, \mathbf{S}, \mathbf{T}$	viscous flux vectors in $\xi, \eta, \zeta$ direction
$R$	aircraft range
$Re$	Reynolds number, $\frac{\rho_\infty V_\infty L_\infty}{\mu_\infty}$
$s$	structure factor
$S$	planform area
$S_v$	S-A turbulence model source term
$T$	static temperature
$\mathbf{T}$	surface stress vector, $\boldsymbol{\sigma} \cdot \mathbf{n}$
$T_o$	total temperature
$t$	time, cruise duration
$u, v, w$	velocity components in $x, y, z$ direction
$u^+$	dimensionless velocity, $u/u_\tau$

$u_\tau$	friction velocity, $\sqrt{\tau_w/\rho}$
$\mathbf{V}$	velocity vector
$V$	fluid velocity or cell volume, cruise velocity
$W$	aircraft weight
$W_b$	battery weight
$W_p$	payload weight
$W_s$	structure weight
$P_b$	power drawn from the battery
$x, y, z$	Cartesian coordinates
$y^+$	dimensionless wall normal distance, $\frac{u_\tau y}{\nu}$

**- Greek Symbols -**

$\alpha$	swirl angle defined as $\tan^{-1}(C_\theta/C_m)$ , angle of attack
$\beta$	pitch angle defined as $\tan^{-1}(C_r/C_x)$
$\Delta t$	physical time step
$\delta_{ik}$	Kronecker delta function
$\varepsilon$	convergence criterion taken by FSI solver
$\gamma$	specific heat ratio
$\mu$	viscosity
$\mu_t$	turbulent dynamic viscosity
$\nu$	kinematic viscosity
$\tilde{\nu}$	working variable of the S-A model related to turbulent eddy viscosity
$\rho$	fluid density
$\tau_{ik}$	shear stress in Cartesian coordinates

$\tau_w$  fluid shear stress at the wall surface

$\xi, \eta, \zeta$  generalized coordinates

**- Subscripts -**

$i, j, k$  indices

$j, s$  subscript, stands for injection and suction

$t, o$  subscript, stands for total

$\infty$  free stream conditions

**- Abbreviations -**

*AoA* Angle of Attack

*AFC* Active Flow Control

*CC* Circulation Control

*CFD* Computational Fluid Dynamics

*CFJ* Co-Flow Jet

*CFL* Courant-Friedrichs-Lewy number

*CUSP* Convective Upwind and Split Pressure

*DCFJ* Discrete Co-Flow Jet

*EA* Electric Aircraft

*FASIP* Flow-Acoustics-Structure Interaction Package

*FSI* Fluid-Structural Interaction

*FVS* Flux Vector Splitting

*FW* Flying Wing

*HAR* High Aspect Ratio

*LE* Leading Edge

<i>LES</i>	Large Eddy Simulation
<i>LHS</i>	Left Hand Side
<i>M</i>	Mach number
<i>OF</i>	Obstruction factor
<i>MPS</i>	Miles*Passengers/Surface
<i>RANS</i>	Reynolds Averaged Navier-Stokes equations
<i>RHS</i>	Right Hand Side
<i>S – A</i>	Spalart-Allmaras (S-A) one equation turbulence model
<i>TE</i>	Trailing edge
<i>URANS</i>	Unsteady Reynolds Averaged Navier-Stokes equations
<i>WENO</i>	Weighted Essentially Non-Oscillatory scheme
<i>ZNMF</i>	Zero-net mass flux

# Chapter 1

## Introduction

Airfoils are the most fundamental element of wings and fluid machinery such as airplanes, wind turbines, compressors, etc. It is thus important to have an overview of airfoil design development first. Then we will introduce the current state-of-the-art of high lift flow control methods and lastly we will present the CFJ flow control method.

### 1.1 Airfoil Design

#### 1.1.1 Chronological Evolution

Airfoil development studies picked up in the late 1800's. The scientists mimicked the curvature and shape of bird wings in order to increase the amount of lift generated by the primitive airfoil. Indeed, getting the required amount of lift to be able to sustain flight was, at the time, the biggest concern for the design of the first flying machine [1]. In the early 19th century, the Wrights brothers started systematic wind tunnel experiments to study the effect of airfoil geometry. This research led to the historical first flight of

1903. However, the performance gap between the wind tunnel experiments, conducted at low speed and on small wings, and the real aircraft performance remained an issue at the time. This is because the Reynolds number effect, which was introduced by Stokes in 1851 [2] and further studied by Reynolds in 1883 [3], plays an important role in the flow behavior. Indeed the very low Reynolds number of the experiments fooled the researchers into thinking that thin and highly cambered airfoils would perform well whereas in reality it is actually quite the opposite. This erroneous common belief changed in 1911, when Prandtl submitted the design of a revolutionary wind tunnel design still in use today, the Göttingen-type [4]. The new design allowed Prandtl and its fellow researchers to perform larger scale wind tunnel testing with full scale model starting in 1917. Thick airfoils were found to stall at a higher angle of attack (AoA) compared to their thin counterparts, thereby increasing the maximum lift. In addition, the drag of the thick airfoils was found to be smaller than anticipated by the common belief of the time. Some of the findings of the wind tunnel testing are presented in Prandtl's lifting line theory published in 1918 [5].

With this new understanding of the Reynolds number, thicker and less cambered airfoils were developed over the following decades. Some airfoils like the Clark Y and Gottingen 398 illustrated in Fig. 1.1 were quite successful and served as a basis for a family of airfoils developed by the National Advisory Committee for Aeronautics (NACA) from the 1920's onward. The first NACA designs, the NACA 4 digits airfoils (Fig. 1.1), are among the most common airfoils today. The NACA 4 digits aerodynamic performance is overall excellent, however their somewhat high pitching moment led to the development of the NACA 5 digit airfoils (Fig. 1.1) commonly used in tailless aircraft designs. In the NACA 5 digits airfoil, the camber is concentrated at the leading edge in a compromise that favors low airfoil mo-

ment at the expense of the lift. In the 1940's, the NACA developed very low drag airfoils, namely the laminar airfoils (Fig. 1.1). Laminar airfoils are usually thin with a small leading edge radii. The thickness distribution is changed dramatically with a maximum thickness achieved around 50% chord. These designs achieve lower friction drag by keeping the flow laminar through a greater percentage of the airfoil chord. Furthermore, the airfoil camber repartition reduces the moment [6]. Despite showing tremendous potential in many studies, the concept is hard to apply because it mostly works for low Reynolds number for which the laminar-turbulent boundary layer transition is delayed to a more downstream location.

In the early 1970's, NASA finalized the design of supercritical airfoils. As the aircraft approaches the speed of sound, the supercritical airfoil maintains a lower Mach number than a conventional airfoil over its suction surface, thereby delaying the shock formation to the rear of the airfoil and reducing the shock strength. The lift is increased and the wave drag is decreased when compared to a conventional airfoil under the same conditions. The flow around a transonic airfoil is seen in Fig. 1.2.

### **1.1.2 Modern Airfoil Design**

Today's airfoils are usually designed for their intended application. Different flow conditions (i.e. Reynolds number ( $Re$ ), Mach number ...) can lead to rather different airfoils. At very low  $Re$ , airfoil sections can be rather peculiar. At slightly higher  $Re$ , thin and highly cambered airfoils like the Wright airfoil of 1908 (Fig. 1.1) are effective. At Medium  $Re$ , thicker airfoils with less camber, like the NACA 4 digit or 5 digit reach their peak effectiveness. Finally, at high  $Re$ , and in the transonic region, supercritical airfoils are the most

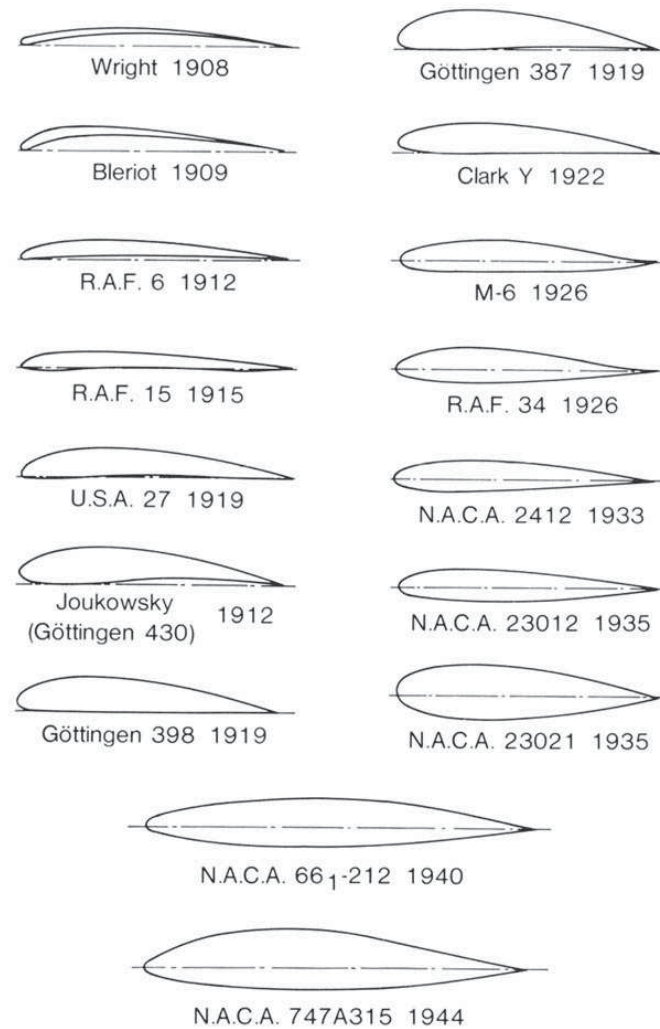


Figure 1.1: Evolution of airfoil sections from 1908 to 1944. The last two shapes (N.A.C.A. 661 -212 and N.A.C.A. 74 7A315) are low-drag sections designed to have laminar flow over 60 to 70 percent of chord on both the upper and the lower surface. Figure extracted from [7].

effective. In addition to the flow condition, design goals (fuel accommodation, stealth, solar panel ...) can also influence the airfoil shape.

The design work becomes ever more complex when considering the 3D effects. Because the flow conditions vary in the spanwise direction, the design of a modern wing requires the creation of a multitude of airfoils, each of which is generated to accommodate the local flow conditions and to reduce the lift-induced drag of the final wing.

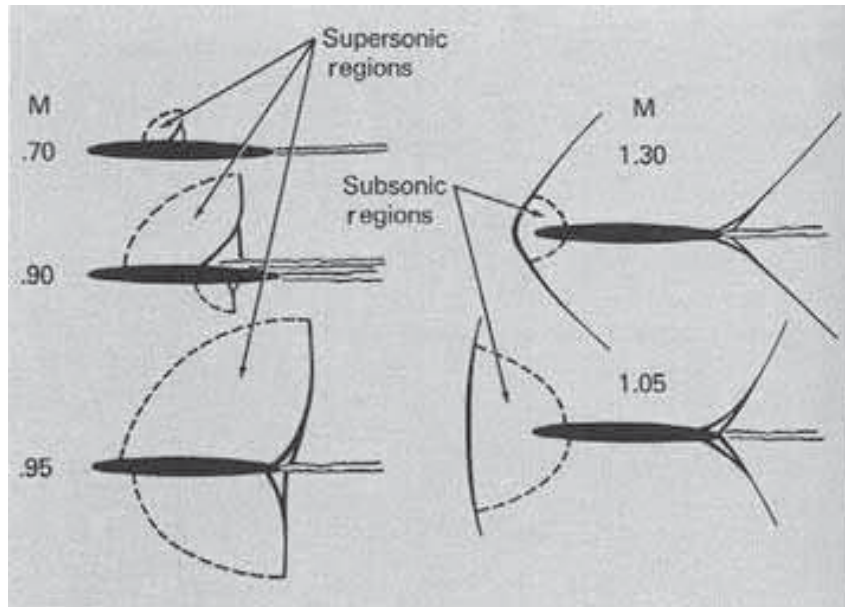


Figure 1.2: Airfoil flow patterns at transonic speeds discussed at NACA University Conference, 1948 [8].

## 1.2 High Lift Flow Control

In previous section, we saw how airfoils have evolved from their primitive state to a more refined and efficient shapes, specially designed for the flow conditions and performance goals of the aircraft they are mounted on. Those airfoils are then stacked to generate a wing shape suitable for the intended application. But the shape of the airfoil and wing is not the only constraint in the design of a successful aircraft. Another fundamental compromise, the wing dimensioning, must be done in order to generate the proper takeoff/landing and cruise performance. On one hand, a large wing provides a high lift during the takeoff and landing phases of the flight, thereby shortening their distances. On the other hand, a small wing is more effective at cruise but is unlikely to provide the required performance during takeoff and landing. In order to circumvent the small wing shortcomings during takeoff/landing, it can be fitted with high lift devices and/or utilize flow control.

High lift devices and flow control methods aimed at significantly increasing the maximum lift of the wing without increasing its size. The flow control methods described in this thesis are based on the boundary layer principles first described by Prandtl in 1904 [9]. When an adverse pressure gradient act on the flow, the boundary layer size increases, and the boundary layer velocity directly above the wall decreases (the velocity at the wall remain zero because of the no-slip condition). If the adverse pressure gradient increases, the boundary layer velocity direction changes and the boundary layer separates (see Fig. 1.3). This local phenomenon is accompanied with the creation of large vortices, an increase of the drag and a decrease of the lift, which is known as the stall. Alternately, a thin boundary layer with reasonably large momentum can sustain a large adverse pressure gradient before it detaches. This understanding led to the current era of airfoil design where boundary layer control method plays an important role.

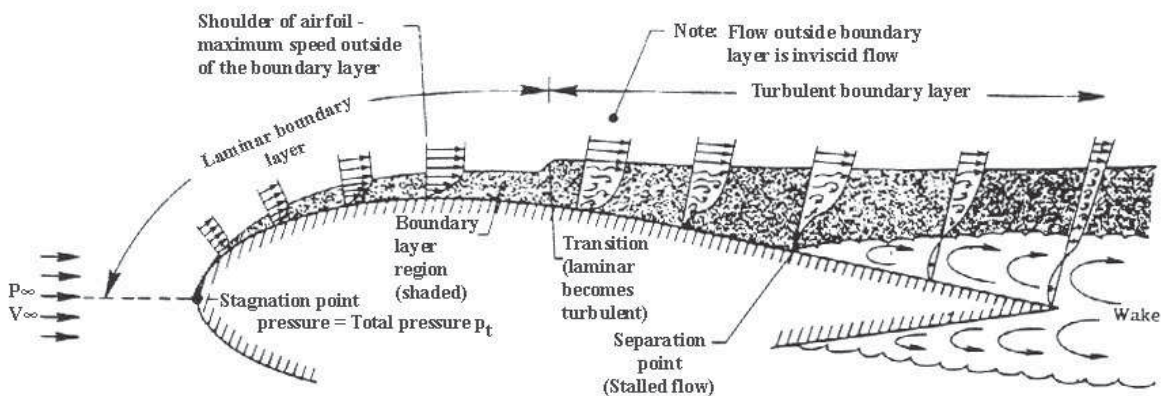


Figure 1.3: Boundary layer development over an airfoil. Figure extracted from [10].

The vortex generators, flaps and slats are called passive flow control because no external source of energy is supplied. In the passive flow control method, the energy is transferred from the main flow to the boundary layer. Conversely, the active flow control method requires an external source of energy. For active flow control, the energy is transferred

from this external source of energy (pump, aircraft compressor, plasma discharge ...) to the fluid. Schlichting [11] presents a comprehensive overview of boundary layer and flow control methods. Smith extended Schlichting work to include high lift aerodynamics, a study that encompass both airfoil design, wing design, boundary layer control and flow control methods [12]. A more recent overview from the DLR is available at [13]. Due to their intrinsic complexity, active flow control methods are not as common as their passive equivalent. Nonetheless the recent research presented below show their enormous potential.

### **1.2.1 Vortex Generator**

Vortex generators (VGs) are among the most common flow control methods because of their ease of implementation and effectiveness. VGs improve performance and control authority at low airspeed and high AoA by generating vortex structures that transfer energy from the main flow into the boundary layer (see Fig. 1.4). McFadden et al. (1955) utilized VGs on the wing and rudder to delay stall [14]. They found that the use of vortex generator increases the maximum  $C_L$  by up to 0.15. In addition, the lift over drag ratio was little changed by the addition of VGs. More recently (1994), Storms et al. [15] studied the effect of VGs on a NACA 4412 airfoil. The maximum lift was increased by 0.34 over the baseline airfoil, with a significant drag increase. VGs are also commonplace on engine nacelle to prevent the large flow separation that would happen at high AoA as studied by Cole et al. in 1958 [16]. More recently Barrett et al. studied experimentally an intelligent vortex generator that deploys close to the stall AoA and conforms to the wing otherwise [17]. The NACA 4415 wing section stall AoA was delayed by up to  $3^\circ$  and the maximum  $C_L$  increased by up to 14%.

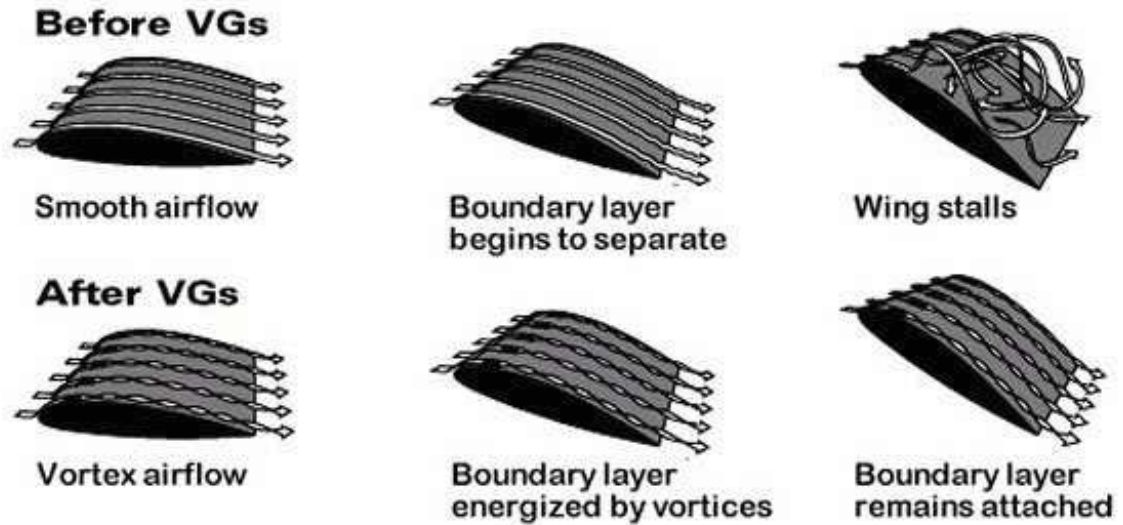


Figure 1.4: Vortex generator effect on the flow over an airfoil with increasing AoA. Figure extracted from [18].

### 1.2.2 Slat and Flap

Slats and flaps are, along with the vortex generator, the most common lift enhancing systems used in aviation and are used to shorten takeoff and landing distances. The deployment of flaps and slats increases the camber and in most cases, the planform area of the wing (see Figs. 1.5 and 1.6). Thereby the lift increases at the expense of a higher drag and moment. Slats and flaps also add complexity and weight to the wing structure. Fig. 1.5 shows the highly advanced Boeing 777 wing with flaps and slats fully deployed. The LE of the wing accommodates a single slotted slat. The inboard flap is a double slotted flap while the outboard flap is single slotted. Vortex generators are also used on the outboard flap to prevent flow separation.

Slats and flaps were first studied in the 1910's by the Royal Aircraft Factory and the National Physical Laboratory in the United Kingdom and in Germany. The first flap to be implemented on an actual aircraft is the plain flap. In this configuration, the trailing edge



Figure 1.5: Boeing 777 at takeoff with flaps and slats fully deployed. Notice the vortex generators located on the outboard flap. Credit: Boeing.

of the airfoil rotates around a hinge mounted to the airfoil element and the flap element. The motion is similar to that of an aileron. Despite its modest aerodynamic efficiency, the plain flap is still common today because of its simplicity. In order to increase the effectiveness and efficiency of the plain flap, the slotted flap is constructed with a gap between the wing and the flap. This modification allows for some pressure side flow to energize the weakening boundary layer on the suction side, thereby a higher flap deflection can be reached and the maximum lift is increased. Multiple slots can be used to further enhance the performance (see Fig. 1.6), at the cost of an increase in wing structural complexity and weight. Plain flaps and slotted flaps were a major subject of study for the NACA in the early 40's due to the ever increasing demand for payload and performance. Notably Harris et al. studied a variety of NACA airfoils equipped with a 15% chord plain flap, a single slotted flap [19] and a 30% chord double slotted flap [20]. The single slotted and double slotted flaps showed a large increase in maximum lift up to  $C_L = 3.6$ , at the expense of a drag and

a moment penalty. In typical take-off conditions, the double slotted flap airfoil reached  $C_L = 3.0$  with  $C_D = 0.18$  and  $C_M = -0.7$ .

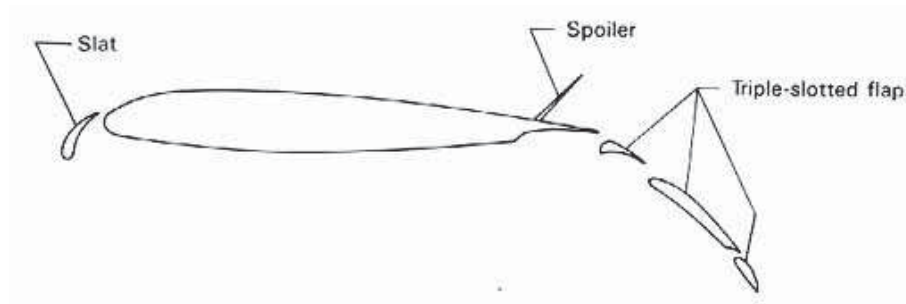


Figure 1.6: Airfoil with triple-slotted flap, slat, and spoiler. Figure extracted from [21].

In the same manner as the airfoil trailing edge can accommodate a flap, the airfoil leading edge can accommodate a slat (see Fig. 1.6). The slat is a fix or retractable surface that forces the air on the suction surface of the main wing element, thereby increasing the stall AoA and the maximum lift. Axelson et al. (1954) studied the effect of the slat position on a generic NACA 64A010 airfoil, for a variety of Mach numbers and AoA [22]. At low AoA, the airfoil with extended undrooped slat generates about the same lift and drag than the baseline. If the extended slat is drooped, the lift is decreased by up to 0.2 and the drag is increased by up to 0.03. When the AoA is increased and approached or excess the stall AoA of the baseline airfoil, the slatted airfoil generates significantly more lift and the drag is decreased. The slatted configuration achieved a maximum lift coefficient of  $C_{Lmax} = 1.4$ , which is about 0.5 higher than the baseline airfoil. A low subsonic Mach number increased the slatted configuration effectiveness when compared to high subsonic. Similar results are found by Liebeck et al. (1973) in [23].

Modern wing designs often combine various slats and flaps elements (see Fig. 1.5). Morgan Jr. (1981) studied experimentally such a wing in [24]. The supercritical test wing

is similar in configuration and shape to the typical modern commercial aircraft wing design. The combination of slats and flaps shifted the  $C_L$  vs AoA curve upward by as much as 1.5. The drag was also significantly increased. For instance, L/D is reduced from 16.52 for the cruise configuration with slaps and flaps retracted to 11.72 for the high lift configuration with slats and flaps deployed. This maximum L/D occurred at a  $C_L$  of 0.68 for the cruise configuration and 0.90 for the high lift configuration. Alternately, different slats and flaps configurations achieved a peak L/D of 10.20 respectively 7.55 at a  $C_L$  of 1.55, respectively 2.0. Compared to the cruise configuration, the maximum  $C_L$  is about doubled and reached 2.9. The stall AoA was about  $15^\circ$  for both the cruise and high lift configurations. Lastly, the  $C_M$  value is increased with the use of slats and flaps and reached -0.8, thereby the trimmed performance of the high lift configuration wing would be significantly lower. More results about slats and flaps used in combination with active flow control are shown in the section below.

### 1.2.3 Suction and Blowing

Shortly after writing the first description of the boundary layer concept in 1904 [9], Prandtl successfully delayed the flow separation on a circular cylinder by sucking in the low energy fluid in the boundary layer (see Fig. 1.7). Downstream of the slit, the newly created boundary layer is thin and able to sustain a large adverse pressure gradient before it separates. A generic airfoil with boundary layer suction is sketched Fig. 1.8 a). The large cavity represents the vacuum chamber which is responsible for sucking in the boundary layer.

The effect of boundary layer suction on a wing performance was studied as early as 1935 by Schrenk in [25]. Two geometries were studied, a 40% thickness ratio wing with

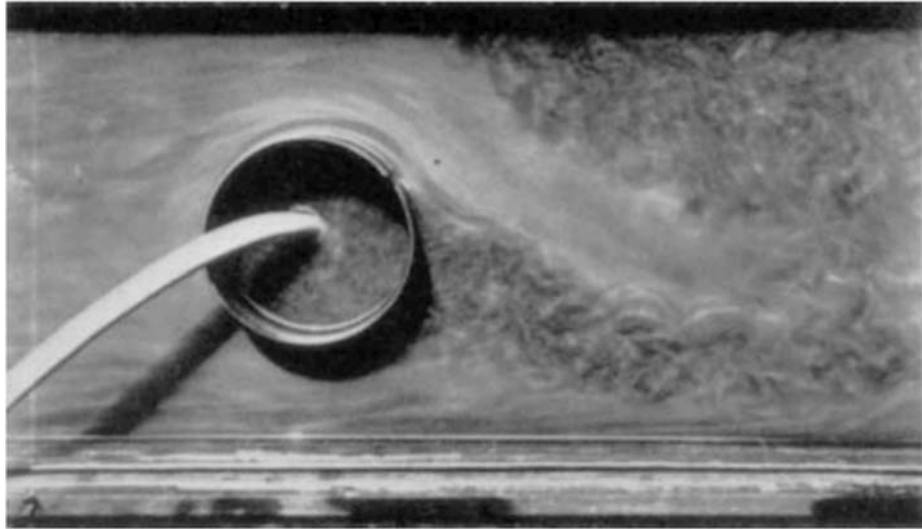


Figure 1.7: Flow around a circular cylinder with one-sided suction of the boundary layer. Figure extracted from [11].

various suction slot positions and widths and a 20% thickness ratio wing with a suction slot located close to the trailing edge flap. A mass flow coefficient is introduced to sort out the data as  $C_Q = \frac{Q}{V_\infty A}$  where  $Q$  is the mass flow of air removed by suction,  $V_\infty$  is the free stream velocity and  $A$  is the wing planform area. The thick wing performance is very poor without suction. However, a small suction mass flow coefficient  $C_Q$  of 0.0022 is sufficient to keep the flow attached up to  $AOA = 20^\circ$ , thereby increasing  $C_L$  and lowering  $C_D$  to 3.05 and 0.0233 respectively. Under a stronger  $C_Q$  of 0.0594, the maximum  $C_L$  reached 3.67 at about  $30^\circ$ . Little change on the flow is observed with the suction width for a same suction mass flow. However, a smaller suction width requires a lower suction pressure and hence can lead to a somewhat higher power consumption. The most rearward suction location requires a higher  $C_Q$  to achieve the same control authority than a more upward location. The suction pressure however is lower due to the higher pressure of the rear flow. The airfoil with flap performs poorly without suction due to separation on the flap. However, a relatively small  $C_Q$  value of 0.0041 is sufficient to maintain the flow attached until the AoA of  $20^\circ$  with

a flap deflection of  $45^\circ$ . Under those conditions,  $C_L$  and  $C_D$  values are 3.40 and 0.0278 respectively. The maximum  $C_L$  of 3.82 is achieved with a stronger  $C_Q$  of 0.0059 and a flap deflection of  $60^\circ$ . However this condition was difficult to maintain due to flow fluctuations between the adhering and separating condition. More recently, Poppleton (1955) performed wind tunnel testing on a swept-back wing of aspect ratio 4.6 [26]. They studied the effect of boundary layer suction, either distributed or through a slot. The slotted configuration reached a maximum lift of  $C_L = 1.48$ , a  $\Delta C_L$  increase of 0.65 over the airfoil without suction. The power coefficient  $P_c$  for this case was relatively high  $\approx 0.17$ . Alternately, a lower actuation power of  $P_c \approx 0.09$  was also able to provide an important maximum lift increase with a  $\Delta C_L$  of 0.55 when compared with the non excited airfoil. The distributed suction yield a similar lift increase, but at a slightly higher energy cost.

Despite its effectiveness, boundary layer suction can be difficult to implement because of the required low pressure source. In the case of blowing - the use of jets of air on the airfoil surface - the high pressure source is already available in the compressor stage of the aircraft engine. The ease of implementation is one of the reasons why blowing is still among the most studied active flow control method today. The sketch Fig. 1.8 b) shows a generic airfoil with blowing. The large cavity represents the pressurized flow which is injected on the suction surface of the airfoil. The energized boundary layer can sustain a greater adverse pressure gradient before it separates.

Schwier (1947) tested continuous blowing on a NACA23012-64 airfoil with various flap configurations [28]. The study used a coefficient of blown-out air to sort the data. The maximum coefficient of blown-out air used during the study is 0.02. The use of jets on the configuration without flap led to a maximum  $C_L$  of 1.8, an increase of 0.65 over the

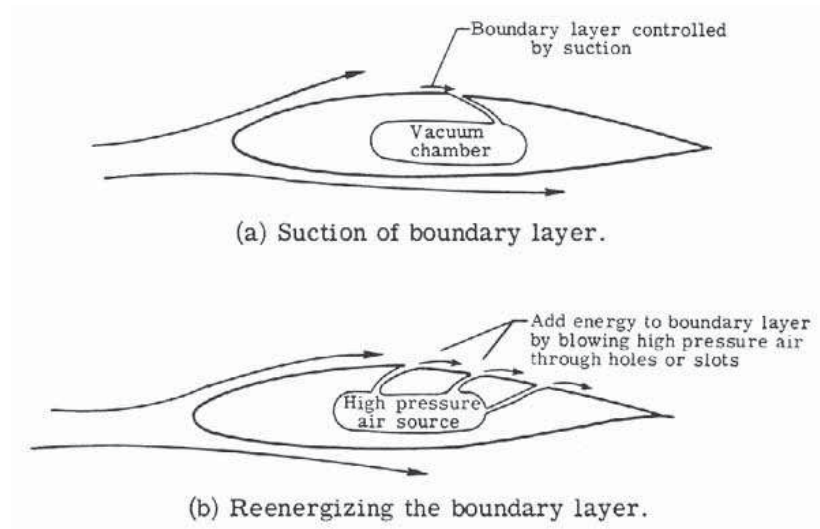


Figure 1.8: Generic airfoils with tangential blowing and suction. Figure extracted from [27].

same airfoil without jets. The use of jets in combination with the flap was more effective and reached a maximum  $C_L$  of 3.3 for a flap deflection of  $45^\circ$ . The addition of a slat to the previous combination further increased the maximum  $C_L$  to an outstanding 3.7. In a pitching airfoil experimental investigation, Muller-Vahl et al. (2015) recorded the effect of continuous blowing on a NACA 0018 airfoil from the leading edge and at mid-chord slots [29]. Muller focused on the dynamic stall of the airfoil as it oscillates between  $-2.5^\circ$  and  $32.5^\circ$ . The dynamic stall mitigation obtained by leading edge blowing yield an average lift increase  $\Delta C_L$  of about 0.5 for a  $C_\mu$  of 5%. The mid-chord blowing was able to remove the trailing edge separation but not the leading edge separation, hence the more modest  $\Delta C_L$  of about 0.25 for a similar  $C_\mu$ . The average drag is dramatically reduced for the leading edge blowing at  $C_\mu = 5\%$  but less so for the mid-chord blowing. Compared with the baseline case without blowing, the leading edge blowing decreases the moment value when the flow is re-attached thanks to the blowing and yield a similar moment otherwise.

Alternately, the mid-chord blowing promote a shift of the  $C_M - \alpha$  toward higher moment values for all flow conditions.

Recently, new unsteady flow control methods are developed with significant reduction of the power consumption when compared with the aforementioned steady flow control methods. This new techniques are to enhance the unsteady mixing of the jet with the main flow, thereby lowering the mass flow requirement for a same effect. Tremendous power consumption gains are possible mainly thanks to the mass flow reduction. Among the unsteady flow control methods, three are of particular interest: the swept jet, the pulsed jet and the synthetic jet. A swept jet blows air continuously, however the injection direction changes with respect to time, allowing the jet to reach an increased surface area as well as enhancing the mixing with the main flow. The pulsed jet blows air intermittently at a defined frequency. If the air is pulsed parallel to the local flow, the actuator directly enhance the boundary layer momentum. Alternately, if the pulse direction is perpendicular to the main flow, the actuator works as a fluidic vortex generator and the performance is similar to a typical vortex generator. Finally, the synthetic jet control method is made up of the surrounding flow which is injected and withdrawn periodically from the main flow by the mean of a moving diaphragm, in a similar manner to a sound speaker and hence producing acoustic waves.

Petz et al. (2007) studied experimentally the pulsed jet on a NACA 4412 airfoil equipped with a flap [30]. The pulsed jets were located on the flap LE in an attempt to prevent the flow separation that occurs for high deflection angles. The pulsed jets delayed the stall AoA by up to  $10^\circ$ , thereby producing an increased maximum  $C_L$  of  $\approx 3.1$ , about 0.3 above the unexcited case. Furthermore, the drag is reduced due to the removal of the separated

flow on the highly deflected flap. As a result, the lift over drag ratio (L/D) increased by up to 20-25%. However, there is little improvement of the overall performance at low AoA and/or at low flap deflection angle, when the flow is already attached. A broader numerical and experimental investigation on pulsed jet was performed by Ciobaca et al. (2010-2013) on the DLR F15 airfoil [13,31,32]. The actuators were located both at the airfoil and flap leading edges. The study shows that leading edge blowing mostly increases the stall AoA, whereas trailing edge blowing over the flap mostly shifts the  $C_L - \alpha$  curve upward. The latter is due to the reattachment of the flow on the highly deflected flap. Both the leading edge and trailing edge pulsed jet increase the maximum  $C_L$  by about 0.15, and their simultaneous effect increases the maximum  $C_L$  by about 0.30. The  $C_{\mu}$  was 1.28% for the leading edge blowing and 0.75% for the trailing edge flap blowing. Further testing at higher Reynolds number up to  $10^7$  showed a decrease of the control authority with the Reynolds number.

Phillips et al. (2010) studied experimentally the effect of a sweeping jet integrated on the flap element of a NACA 0021 airfoil [33]. The flow separation on the flap was controlled using a relatively low  $C_{\mu}$  in the range 1.15-3.13%. In the absence of excitation, the flow is separated for the entire range of AoA for a modest flap deflection of  $20^\circ$ . Sweeping jets with  $C_{\mu} = 1.15\%$  sufficed to attach the flow over the flap for a small range of AoA, thereby increasing the lift by almost a factor of 2 and decreasing the drag at least by a factor of 3. Augmenting the  $C_{\mu}$  further does not improve the lift significantly after the flow over the flap had already attached, but a reduction in drag is evident due to the additional thrust input of the jet. For example, at  $C_{\mu} = 2.11\%$  and  $AoA = 0^\circ$ , the sweeping jet increases the  $C_L$  from 0.73 to 1.6 and reduces the drag to only about 0.006. Therefore, the L/D increases from approximately 15 to 60 after accounting for the  $C_{\mu}$  input as thrust. A higher  $C_{\mu}$  of

3.13 yield a maximum  $C_L$  of 2.7. Lastly, Phillips et al. were able to remove the dynamic stall effect during a rapid flap deflection with improved performance recorded for a flap deflection of up to  $30^\circ$ . A different application is proposed by Graff et al. (2013). Their experimental investigations recorded the effect of a sweeping jet flow control on a generic vertical tail [34]. The actuators were located close to the rudder hinge line. The side force was increased by as much as 50% with a  $C_\mu$  in the range 1-2%. The slight drag increase ( $\approx 10\%$ ) is attributed to the stronger lift-induced drag. A lower  $C_\mu$  of approximately 0.1% augmented the side force by 20% with a reduced power consumption. The typical power coefficient  $C_P$  of the study is in the range 5% - 20%. In order to achieve an efficient control authority, the optimum jet velocity is found to be approximately three times that of the free stream velocity.

Chang was among the pioneers in the study of synthetic jet. Chang's experiments of 1961 [35] suggests that a drag reduction of up to 20% at  $Re=80,000$  is possible by using the acoustic wave produced by the actuator to control the flow separation. The energy consumption is low, and the drag equivalent power reduction is 19 times lower than the acoustic power injected into the flow. The drag reduction had a continuous dependence upon Strouhal number. In 1975, Collins et al. [36] further studied acoustic waves to attach the separated flow on an airfoil at high AoA. Their experiments showed a  $C_L$  increase of up to 53% and a drag reduction of up to 49%. Collins et al. achieved an outstanding efficiency and recorded a drag power reduction as much as 3380 times lower than the acoustic power injected into the flow. By 1987, the actuator size became small enough to be fitted inside the airfoil. Huang et al. studied such actuators in [37]. The airfoil was symmetric with an injection location near the LE. The optimum excitation frequency is found to be twice

that of the shedding frequency of the separated shear-layer. The stall AoA was delayed by up to  $7^\circ$  and the maximum  $C_L$  increased from about 1.5 for the unexcited airfoil to almost 2.0. A similar study by Hsiao et al. (1990) [38] recorded a stall AoA delayed by as much as  $5^\circ$ . At an AoA of  $20^\circ$ , the use of acoustic excitation increased  $C_L$  from about 0.75 to 1.05 and reduced the drag from about 0.38 to 0.13. The maximum  $C_L$  achieved is 1.05, a modest increase of about 0.05 compared with the unexcited airfoil. More recently Ishibashi et al. (2015) studied numerically the effect of synthetic jets on a NACA 0012 airfoil at  $AoA = 12^\circ$  [39]. The jet is located at 10% chord and the jet exit angle is varied. The jet exit angle more aligned with the main flow is identified as the most effective. Similarly to previous studies, the flow excitation is able to attach the flow past the stall AoA of the unexcited airfoil. For example, at an AoA just past the stall AoA of the unexcited airfoil,  $C_L$  increases from 0.605 to 0.921 and  $C_D$  decreases from 0.147 to 0.050.

#### 1.2.4 Plasma Actuator

Plasma flow control method is a recent technique in which a dielectric barrier discharge ionize the surrounding flow. The ionized flow is submitted to an electric field to be accelerated by the resulting electro-hydro-dynamic forces. Plasma actuators can act in two modes; they can directly add momentum to the boundary layer when used in continuous mode, or alternately, they can manipulating the flow instabilities in a manner that is prone to flow re-attachment when used as an unsteady actuator. The latest method doesn't introduce a significant momentum into the boundary layer and is usually found to be more effective at higher Reynolds numbers. A generic plasma actuator is seen in Fig. 1.9.

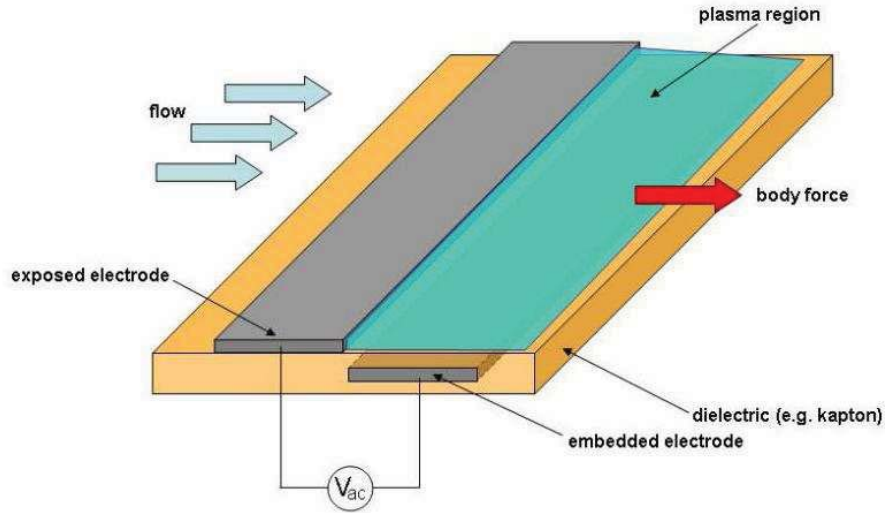


Figure 1.9: A plasma actuator creates a dielectric barrier discharge in the vicinity of the wall. Figure extracted from [40].

Post et al. (2004) studied experimentally the separation control of a generic airfoil using plasma actuators to generate a steady wall jet in the direction of the flow [41]. The plasma actuators delayed the stall AoA by up to  $8^\circ$  and the resulting maximum  $C_L$  is increased from about 0.55 to 0.75. The drag is lower for AoAs past or close to the stall AoA of the unexcited airfoil. There is however no improvement of the airfoil lift and drag in the region where the flow is already attached. The relatively low Reynolds number of 158,000 is not representative of real flight conditions, nonetheless, the performance increase is not negligible and the estimated power is low, about 20W for the 25.4 cm airfoil at 10 m/s. A similar effect is obtainable with vortex generators, however the advantage of plasma actuators is that they do not generate parasite drag when not used. Two years later, Post and al. (2006) inquired the actuator effect on the dynamic stall of a NACA 0015 pitching airfoil [42]. The airfoil motion (in degree) was prescribed by  $\alpha = 15 + 10\sin(\omega t)$  with a reduced frequency  $k = \omega c / 2U_\infty$  of 0.08. Steady and unsteady plasma actuation data were recorded. During the experimental study, the average lift was increased by up to 12.6%

compared with no flow control and the dynamic stall was mitigated with a slightly lower drop of  $C_L$  and  $C_M$  at the onset of the pitch down motion. The power used by the actuator was in the range 2 - 20 W per foot span for a 5 inch chord airfoil. Another application is proposed by Corke et al. (2006) in which plasma flow control is used to control the amount of lift generated on a plasma flow control optimized HSNLF(1)-0213 wing [43]. Unlike other airfoils, the HSNLF(1)-0213 features a small TE recirculation even at low AoA. The small recirculation is easily controlled by the plasma actuator to modify the lift. The numerical and computational investigation shows a constant  $C_L$  increase of about 0.1 until the stall AoA. The  $C_D$  was also reduced at low AoA due to the removal of the flow separation. A recent experimental investigation by Little et al. (2010) recorded the effect of unsteady plasma actuation on the LE and flap separation of the NASA EET airfoil [44, 45]. The excitation prevents the leading edge separation for up to  $6^\circ$  past the unexcited airfoil stall AoA at a Reynolds number of  $1.10^6$  with a power of about 10-12W. Albeit the precise  $C_L$  increase cannot be calculated due to the lack of resolution in the  $C_P$  distribution, it can be roughly estimated to about 15-20% for a best case scenario. Little et al. were however unable to fully reattached the separated flow on the flap due to the lack of actuator control authority. Nonetheless, they recorded a lift coefficient increase of up to 0.09 with a power coefficient of about 7%.

### **1.2.5 Circulation Control Airfoil**

The circulation control (CC) airfoil [46–48] relies on the Coanda effect, which creates a favorable pressure gradient on a curved surface to prevent flow separation. Such a favorable pressure gradient exists at the airfoil leading edge (LE) due to the LE suction and in the

vicinity of a blunt trailing edge (TE) due to the low base pressure. Hence, a blunt TE is usually required to render the CC effective. However, a thick TE increases drag at cruise condition. To overcome the dependence on a blunt TE for CC airfoil, a movable flap at the airfoil TE has been suggested by Englar [49]. Unfortunately, such moving parts impose a weight penalty. At large angles of attack (AoA), the flow cannot overcome the large adverse pressure gradient. As a result, a favorable pressure gradient near the TE cannot be achieved and, hence, the Coanda effect is difficult to realize. If only TE blowing is used, a CC airfoil stalls at a smaller AoA than a non-CC airfoil. To maintain sufficient stall margin, LE blowing also needs to be added [50]. A considerable penalty of the blowing is the dumped blowing jet mass flow, which may be induced from the propulsion system bleed or other pumping system and reduces the overall aircraft efficiency. Furthermore, for a CC airfoil, the drag measured in a wind tunnel is not the actual drag that occurs in flight because the penalty to draw the mass flow from the free stream as the supply for the jet injection is not included in the drag measurement. The actual drag, also called "equivalent" drag, needs to include this penalty [51, 52]. To mitigate the penalty, a pulsed jet CC airfoil is shown to significantly reduce the jet mass flow rate [52]. Zhang et al. use a plasma-induced jet to remove the dependency of CC airfoil on the air source supply [53]. The resulting  $C_{LMAX}$  is increased by from 1.15 on the original airfoil to about 1.55 with the plasma jet activated. However the Reynolds number of  $6.84 \times 10^5$  used for the simulation is low and in actual take-off and landing condition with Reynolds number in the millions, the plasma-induced jet would lack the proper authority to keep the flow attached. More recently, Traub et al. studied the performance of a self-contained CC wing with the pump located inside a S8036 airfoil [54]. The maximum lift coefficient is increased by 39% from 0.848 to 1.176 for a  $C_\mu$

of about 1.8%. For the sake of comparison, the CC airfoil is mounted with a plain flap. The blowing increases the CC airfoil maximum lift by 16% above the highest lift obtained with the flap without blowing. The drag is reduced by the blowing but remains relatively high, about the same value than the airfoil with a flap deflection of  $20^\circ$ . Part of the high drag can be explained by the higher lift, thereby higher induced drag of the CC airfoil. Albeit no number is published, the added power consumption of the pump and the relatively high drag of the CC wing means that the CC wing energy efficiency is fairly low.

### 1.2.6 CFJ Flow Control Method

For most of the aforementioned active flow control methods, the increase of lift and decrease of drag are contained to AoA or flap deflections where the flow on the unexcited airfoil or flap is separated. In this case, the lift increase and drag decrease come from the reattachment of the flow. There is usually zero to little gain observed with the flow control method at low AoA where the unexcited flow is already attached. Similarly, utilizing a stronger excitation generally does not yield further improvement after the flow already reattached, except for some drag reductions mostly observed for continuous blowing and that are attributed to the large momentum injected in the flow. Another limitation common to most unsteady flow control method is the lack of large maximum  $C_L$  increase when used on an airfoil alone. To further increase the maximum  $C_L$ , those flow control are paired with a flap or slat which increases the weight and complexity of the wing. Especially, synthetic jets and plasma flow control methods have limited control authority and are their effectiveness is confined to low Reynolds number flows. To overcome these disadvantages, Zha and his team [51, 55–65] developed a novel concept of active flow control airfoil using co-flow

jet, which radically augments the lift, reduces drag, and increases the stall AoA at low energy expenditure.

The CFJ airfoil concept is illustrated in Fig. 1.10. The airfoil suction surface is modified with an injection slot near the LE and a suction slot near the TE. A small mass flow is withdrawn into the airfoil suction slot, pressurized by a pumping system inside the airfoil, and re-injected through the injection slot tangentially to the main flow. The whole process does not add any mass flow to the system and hence is a zero-net mass flux (ZNMF) flow control and the energy loss are minimized.

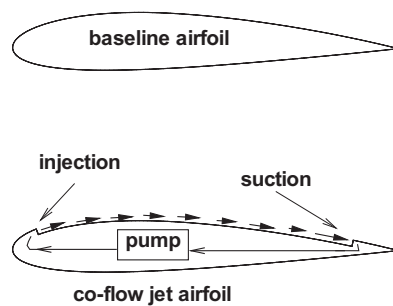


Figure 1.10: Implementation of CFJ on a generic airfoil.

Figure 1.11: Massive flow separation of baseline NACA 6415 airfoil at  $AoA=25^\circ$ .

The CFJ airfoil is a unique low energy expenditure ZNMF flow control, which has the injection slot near the suction peak of the airfoil where the lowest main flow pressure is located, and the suction slot at the near TE where the highest main flow pressure is located. The CFJ airfoil total pumping power is hence lower than that of the flow control methods with injection only, such as a CC airfoil. Furthermore, a flow control method using injection only will have to do more work to overcome the ram and captured area drag, which do not exist for CFJ airfoils due to the ZNMF [51]. The injection and suction

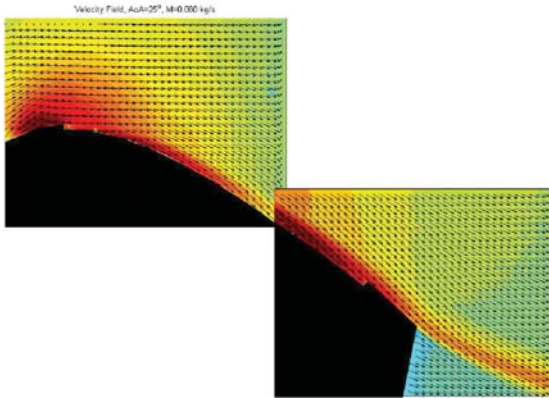


Figure 1.12: Attached flow of CFJ NACA 6415 airfoil at  $AoA=25^\circ$  measured by PIV in experiment.

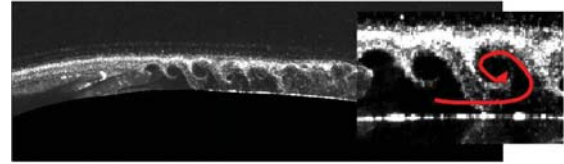


Figure 1.13: Coherent vortex structures in the region of CFJ airfoil injection,  $AoA=5^\circ$ ,  $C_\mu = 0.02$ .

of CFJ airfoils are efficiently integrated and they both enhance boundary-layer momentum and airfoil circulation.

The fundamental mechanism of CFJ airfoils is that the turbulent mixing between the jet and main flow energize the wall boundary-layer. The large vortex structures and adverse pressure gradient are beneficial to enhance mixing. The mixing allows the flow to overcome a large adverse pressure gradient and remain attached at a very high angle of attack. Hence, the stall margin is significantly increased. At the same time, the energized boundary layer drastically increases the circulation, augments lift, and reduces the total drag or generates thrust (net negative drag). The portion of CFJ energy used to overcome the increased local friction drag due to higher jet speed is small since the mixing occurs immediately when the jet penetrates into the boundary layer under an adverse pressure gradient. Unlike a jet in cross flow (JICF) which enhances mixing between the jet and main flow but retards the main flow due to the cross flow blockage created by the jet, the co-flow jet mixing only enhances the streamwise flow momentum since the jet is tangential to the main flow. The momentum retardation due to JICF will result in a significant entropy and drag increase.

The thrust generation or drag reduction by a CFJ airfoil can be explained by two mechanisms [51, 55–57]: First, due to the very high circulation, the LE suction is so strong that the low pressure at the LE results in a thrust when the AoA is below a certain value. The slightly increased local surface friction due to higher jet velocity is offset by this LE super-suction, or pressure drag reduction, which is the same mechanism that bird wings generate thrust at down stroke flapping at high AoA. Second, the energized main flow fills the wake and reduce velocity deficit. From control volume analysis, it is known that a shallower wake velocity deficit means a smaller drag. When the wake velocity deficit is reversed, the airfoil will generate thrust, which occurs for the CFJ airfoil as demonstrated in both experiment and numerical simulation [51, 55–60, 63, 64]. CFJ airfoils appear to be the only flow control method that generates both significant lift and thrust at the same time. This is due to the tangential jet injection momentum even though the jet suction will offset the benefit. Fig. 1.11 shows a massive flow separation of the baseline NACA 6415 airfoil at AoA of  $25^\circ$  in our wind tunnel testing [59]. Fig. 1.12 shows the PIV-measured velocity field with CFJ at the same AoA. This demonstrates that the flow is attached with a higher speed within the wake than in the free stream, a reversed velocity deficit. In this case, thrust is generated. The flow is attached at a momentum coefficient  $C_\mu$  of 0.06 for this case. Fig. 1.13 shows the coherent vortex structure in the vicinity of the injection slot from our experimental flow visualization.

Fig. 1.14 compares the measured lift coefficient of several CFJ airfoils with the baseline airfoil at a constant jet mass flow rate [59, 60]. The CFJ airfoils in Fig. 1.14 have different slot blockages to generate discrete holes and hence different jet velocity while keeping the same mass flow rate. For example, the open slot (black solid circles) has zero blockage.

The symbol OF stands for the obstruction factor (blockage), which is the percentage of the slot area blocked. OF of  $3/4$  means that 75% of the injection slot area is blocked and it results in many small discrete holes for the CFJ injection. Fig. 1.14 shows that the open slot CFJ airfoil increases the maximum lift coefficient by about 50%, whereas the discrete CFJ airfoil with OF of  $2/3$  increases the lift by about 100%. When the mass flow is increased, the measured maximum lift coefficient is further augmented as shown in Fig. 1.15.

A unique feature of CFJ airfoils is their ability to generate a large thrust while increasing the lift due to the streamwise momentum increase of the flow. Fig. 1.15 shows all the airfoils generate thrust (negative drag) in the wind tunnel testing with the maximum amount produced by a CFJ airfoil using discrete jets with obstruction factor of  $3/4$ . The minimum drag is reduced by 4000% to an enormous thrust coefficient of about 0.8. By comparing with the open slot CFJ airfoil, the discrete CFJ (DCFJ) airfoil needs half of the mass flow rate to achieve the same lift augment and drag reduction [60]. However, the power consumed by the DCFJ is significantly higher than the open slot CFJ airfoil since the smaller holes create more blockage loss for the jets. Nonetheless, the extraordinary high lift and high thrust generated by the DCFJ deserve the extra energy cost [60].

The CFJ airfoil enhances the airfoil performance with low energy expenditure. Dano et al. [60] investigated experimentally the energy expenditure at Mach number of 0.03. Their study indicates that the CFJ airfoil gains drastic performance enhancement at high AoA for a low energy expenditure. Additional numerical studies performed by Lefebvre et al. in [63, 64] confirmed the trends. When the Mach number is increased from 0.03 to 0.3, the performance enhancement is increased and the power coefficient is decreased. The

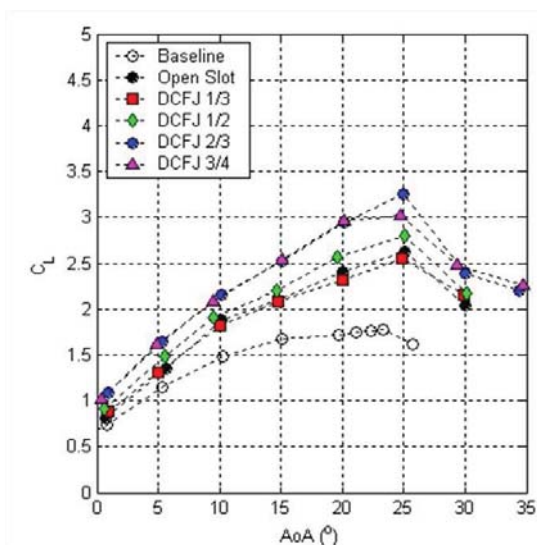


Figure 1.14: Comparison of lift coefficient of CFJ airfoils with different obstruction factors at constant mass flow  $\dot{m} = 0.03\text{kg/s}$ .

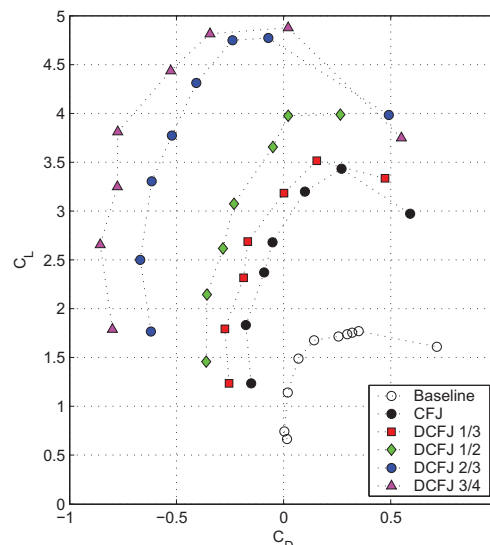


Figure 1.15: Comparison of the drag polars of discrete CFJ airfoils with different obstruction factors at constant mass flow  $\dot{m} = 0.06\text{kg/s}$ .

energy consumption remains contained until  $M=0.4$  [61], at which the energy consumption increases significantly due to the appearance of shock wave structure in the flow.

Based on the trade study in [63, 64], a high performance wing utilizing CFJ is designed by Lefebvre et al. Unlike a conventional wing, the CFJ wing's peak aerodynamic efficiency appears at a significantly higher  $C_L$  which allows the aircraft to efficiently carry an increased payload. Finally two revolutionary electric aircrafts are designed by Lefebvre et al. [65]. The two aircrafts represent two radically different approaches to tackle the electric flight challenge. The first design is more conservative and uses a high aspect ratio wing with a fuselage while the second design make use of a pure flying wing concept. Both designs are implemented with CFJ which removes the flap and slats configuration during take-off, climb and landing.

## 1.3 CFJ Airfoil for Rotorcraft

### 1.3.1 Background

The forward moving helicopter blades speed varies depending on the blade position relatively to the helicopter motion (see Fig. 1.16). As a result, each blade undergoes a sinusoidal movement to achieve the balance of lift between advancing and retreating side of the rotor disk. The AoA is small for the advancing blade while the retreating blade must increase its AoA to keep the balance of lift. This unsteady motion allows higher AoA than the static stall AoA. However, if the AoA is too high, the retreating blade stalls, generally on its inner section due to the higher local AoA, leading to a phenomenon called dynamic stall.

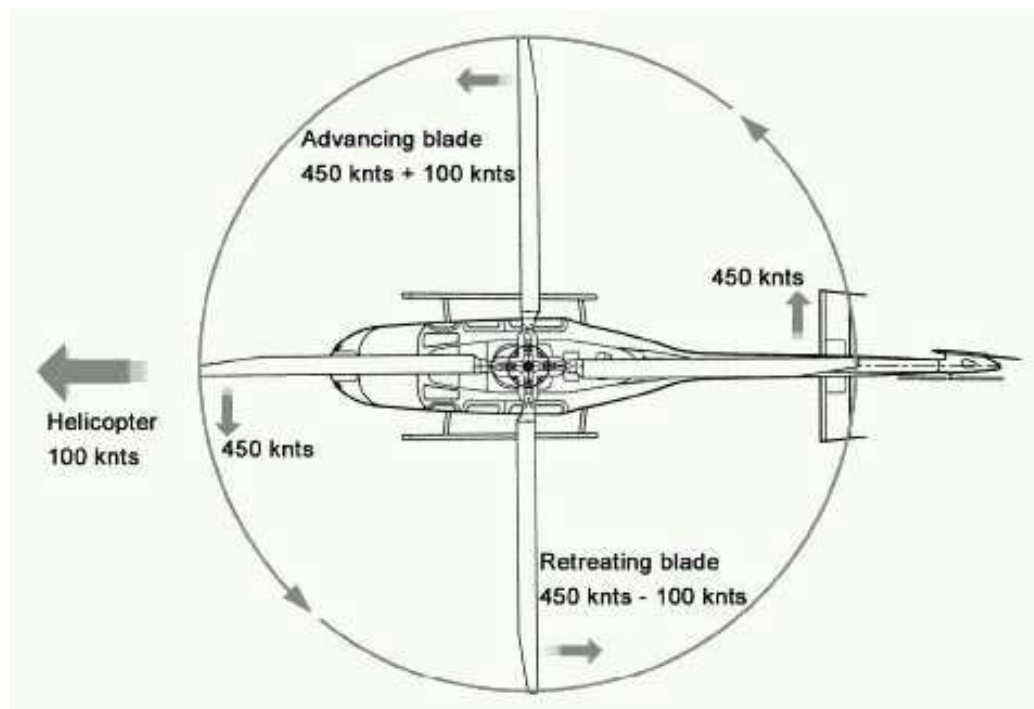


Figure 1.16: Blade velocity variation with the position on the rotor disk. Because of the rotation motion, the inner portion of the blade is slower than the outer portion. Figure extracted from [66].

The physics of the dynamic stall is well documented by Bousman [67]. His study includes a level flight case at high altitude, a diving turn at high load factor, and the UTTAS pull-up maneuver. The dynamic stall is characterized by the shedding of a vortex at a near leading edge position. McCroskey et al. [68] observed that dynamic stall come from the breakdown of a turbulent boundary layer as opposed to the burst of a laminar separation bubble. As the dynamic vortex is created, the blade experiences a peak in term of lift, drag and moment. However, as the vortex structures move downward, the performance collapse resulting in a hysteresis loop behavior for forces and moment. The sudden nose-down moment peak generates sever blade torsion that may lead to fatigue, mechanical failure [69], and may severely impair the maneuverability of the aircraft [67].

### **1.3.2 Dynamic Stall Mitigation**

In order to extend the flight envelop of rotorcraft, research has been done to mitigate the dynamic stall. Early studies show that modifying the airfoil profile alone [70, 71] could improve slightly the performance during a light stall but have limited effect on the deep-stall. This suggests that more radical solution have to be found to remove the dynamic stall. One of the methods is to introduce slat in the blade design. McAlister et al. [72] studied experimentally the VR-7 slatted airfoil for a range of AoA. The slat configuration is able to minimize the lift collapse due to dynamic stall and to effectively smooth the moment coefficient. Reynolds number shows little influence on the slat effect. However the slatted configuration has only a moderate increase in average L/D over the cycle and maximum drag reaches a value well above 0.3 at large AoA.

In a more recent study, Mishra [73] showed the effect of 2 slats configurations on the dynamic stall of the UH60A Black Hawk rotor blade. The results confirmed the static slat effectiveness at reducing the forces hysteresis during the dynamic stall and smoothing the moment coefficient. The dynamic slats did not generate better results than the static slat configuration.

Yee et al. [74] studied the aerodynamic characteristics of the Gurney flap using 2D simulation for various Mach number and flap height. They found that a 2% chord height Gurney flap increases the effective camber and nose-down moment of the airfoil. The performance is slightly improved in the light stall but no substantial improvement is found for the deep-stall case.

Thakkar et al. [75] explored a new single-crystal piezoceramic for its potential to torsionally actuate the elastic rotor blade utilizing the induced shear mechanism of piezoceramics. Their numerical study shows a possible reduction of the AoA by up to  $8.7^\circ$ , thereby suggesting the possibility to dynamically twist the blade to suppress the dynamic stall. However performance improvements are yet to be quantified.

Another promising study have been done by Sun et al. [76] in their numerical study of tangential jet effect on dynamic stall using RANS equations using Baldwin-Lomax turbulence model. Their study focused on a pitching motion of a NACA0012 oscillating with  $10^\circ$  amplitude about a  $15^\circ$  mean angle at a reduced frequency in the range 0.15-0.25. They were able to mitigate the stall at  $C_\mu = 0.7$  using steady jets. They also found that using unsteady jets with strength periodically varying with the wing cycle is more effective at reducing the dynamic stall. Finally the jet position of about 0.6% chord location was found more effective than a further downstream position.

### **1.3.3 CFJ Airfoil, an Effective Solution to Remove Dynamic Stall**

The CFJ airfoil can remove the dynamic stall, increasing significantly the aerodynamic performance and reducing the moment variation of the pitching airfoil. In a study at free stream Mach number 0.3 [62], the dynamic stall is removed and the average lift is greatly increased. In addition the CFJ airfoil thrust fully overcome the drag at a  $C_{\mu}$  of 0.20, suggesting that a CFJ helicopter blade using its pump as the only source of power may be feasible. Lastly, the removal of the dynamic stall reduces the variation of moment during the pitching cycle, thereby decreasing the mechanical constraint on the blade. At free stream Mach number of 0.4 [77], the transonic flow and shock boundary layer interaction reduces the effectiveness and increase the power consumption of the CFJ pitching airfoil. Applying CFJ to the inner part of the rotor blade, where the dynamic stall effect is the strongest, could potentially improve the loading distribution with more load in the inner radius and less load on the outer radius of a rotor blade. It can then significantly reduce the tip Mach number and improve the efficiency and reduce the noise. A CFJ rotor blade can achieve dynamic stall free operations, which substantially reduced the blade vibration and noise due to the wake noise reduction. It has a great potential to revolutionize the future rotor-craft with higher speed, high maneuverability, low noise, and longer life span.

## **1.4 CFJ Airfoil for Electric Aircraft**

The main challenge of general aviation (GA) electric airplanes (EA) resides in the limited amount of energy that can be carried on board of the aircraft. The specific energy density of Li-ion battery is typically 60 times lower than that of kerosene. Hence for the same weight,

the energy stored on an electric plane will only be a fraction of its kerosene counterpart. This drastically limits the GA EA range and payload. Due to this limitations, today's GA EA are usually 1 or 2 passenger aircraft with a range typically shorter than 100nm. To mitigate the range limitation, a GA EA often adopts a glider design with high aspect ratio and low wing loading to achieve maximum aerodynamic efficiency.

The e-Genius shown in Fig. 1.17 is a typical configuration example of the current GA EA, which has a large aspect ratio of 19.6 and a payload of 2 passengers. The design is very successful and set 7 world record as of July 2014. The Taurus G4 shown in Fig. 1.18, won the 2011 Green Flight Challenge. By combining two fuselages, the Taurus G4 achieves an aspect ratio of 22.5 and is the first 4 passengers EA. Both the e-genius and the Taurus G4 have a range over 200nm due to a very high cruise L/D ratio of about 28. However, both designs have a relatively low cruise wing loading, which limits the amount of battery they can carry and their range. To increase the range of EAs without increasing their size, the cruise wing loading must be increased. A conventional aircraft cannot achieve a high cruise wing loading while keeping a reasonable cruise aerodynamic efficiency. In addition, a high cruise wing loading leads to a smaller stall margin and longer takeoff and landing (TOL) distances. To overcome the limitation of low cruise wing loading, a revolutionary new concept aircraft design must be pursued.

A detailed overview of current and future electric aircraft technologies are presented in [78]. We thank Martin Hepperle for authorizing us to extract some of the plots presented in the following paragraph.



Figure 1.17: The e-Genius broke 7 world records in July 2014.



Figure 1.18: The Taurus G4 airplane, winner of the Green Flight Challenge in 2011, Image by Wernher Krutein / Photovault.com

### 1.4.1 Environmental Background

According to ElBaradei, Director General of the International Atomic Energy Agency (IAEA) [79], an unprecedented energy crisis is well under way. The recent oil price drop is an exception and the price in the near future is likely to soar again. At the same time, global demand for energy is rising fast as the population increases and developing countries such as China and India undergo dramatic economic growth. According to the International En-

ergy Agency (IEA), the world's energy needs could be 50% higher in 2030 than they are today. Yet the fossil fuels, on which the world strongly depends, are finite and pose environmental concerns. The emission of Carbon Dioxide (CO<sub>2</sub>) has serious consequences on the worldwide climate change and rising ocean level, while the emission of Nitrogen Oxides (NO<sub>x</sub>) causes a number of serious health issues. In particular, one form of NO<sub>x</sub>, the nitrogen dioxide, is unhealthy to breathe, especially for children, the elderly, asthmatics and people with chronic obstructive pulmonary disease. This is why it is urgent to reduce our dependency on the fossil fuels by creating viable alternatives.

One aspect of this thesis is to tackle tomorrow's energy challenges by generating a revolutionary CFJ electric airplane concept. The range limitation of the conventional electric aircraft is much improved with the new concept, which is capable of range up to 315nm with a reasonable airplane size, rendering the electric flight a viable alternative for general aviation.

#### **1.4.2 Electric Energy Storage**

Fossil fuels have an outstanding energy density both in a gravimetric sense with 11.8 kWh/kg and in a volumetric sense with 8.9 kWh/L. In addition kerosene is chemically stable, non-explosive, non-toxic and can be easily transported from the place of production. These features make fossil fuel utterly convenient and difficult to replace.

Alternately, fuel cell and battery technology have evolved considerably in the past 10 years pushed by the development of personal computers and mobile devices such as cell phones for the batteries and the emerging market of electric vehicle. However, the current state-of-the-art Lithium-Polymer battery volumetric density is still about 18 times smaller

than the fuel and about 60 lower for the gravimetric density (see Fig. 1.19). The fuel cell weight is also a disadvantage. While the fuel, typically  $H_2$ , has a rather high gravimetric and volumetric density, the added weight of the infrastructure (fuel cell, air pumps, water supply, heavy fuel storage ... ) render the final product rather bulky, even when compared with the battery. Only for longer flight distances, where the fuel mass becomes more dominant relatively to the infrastructure weight, may the fuel cell become a viable alternative to battery systems. Within the scope of this thesis, the use of battery is preferred due to the relatively small range of the designed general aviation aircraft.

In addition to the low energy density of battery and fuel cell systems, there are obvious risks associated with the liquid hydrogen or the highly chemically active components of the Li-ion batteries. Recently, two Boeing 787 batteries caught fire within two days leading to the grounding of the entire fleet by the FAA.

### **1.4.3 Propulsive Efficiency**

The conversion of energy from on-board batteries to propulsion involves multiple steps, each of which generates energy losses. The overall efficiency of a system is thus the product of the efficiency of each step. In order to compare different propulsion systems, Hepperle assumed a typical efficiency for each step and the results are shown Fig. 1.20.

The battery efficiency is the highest with a total chain efficiency of 73%. This is mainly due to the high efficiency of each step, at the exception of the propeller with a typical efficiency of about 80%. The fuel cell takes the second place with a 44% chain efficiency, a significant drop compared with the battery efficiency mainly due to the losses during the fuel conversion into electricity. Turboprop and turbofan using kerosene come in 3rd and 4th

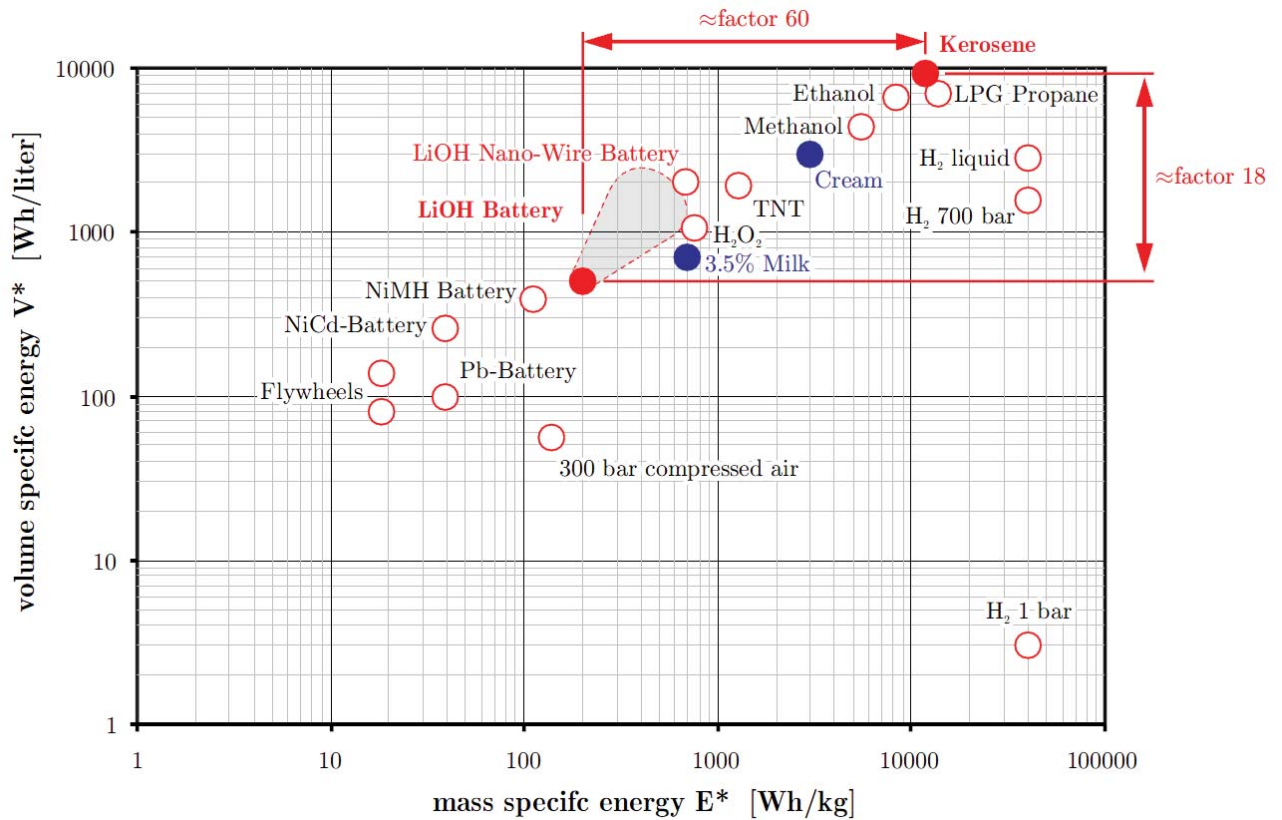


Figure 1.19: Volume and mass specific energy characteristics of different energy storage systems [78].

place respectively mainly due to the low thermodynamic efficiency of the Brayton cycle. While the excellent battery chain efficiency is beneficial, in real life application, the weight of the aircraft plays an important role in the total energy consumption of the aircraft. As aforementioned, the weight penalty due to the batteries or fuel cell is drastic. In addition, the aircraft using battery has a constant weight during the flight, thereby its energy usage is constant during the cruise. Whereas, a conventional kerosene aircraft sees its weight reducing over time as the fuel is consumed, reducing the cruise power consumption over time. This phenomenon is exacerbated for long range aircraft due to the large amount of weight loss during the cruise.

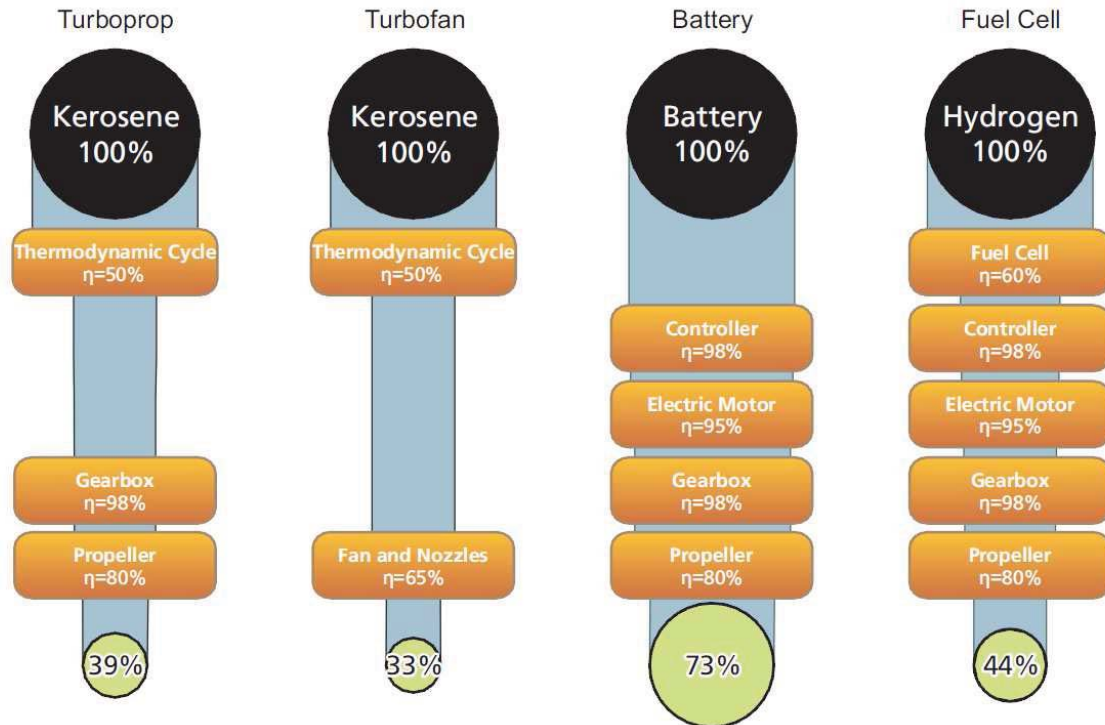


Figure 1.20: Typical on-board conversion chains with typical component efficiencies and total chain efficiency [78].

#### 1.4.4 A Necessary Revolution of Aircraft Technology

As aforementioned the increased weight and reduced available energy of the electric aircraft significantly reduces the range when compared with the kerosene airplane. In order to circumvent this shortcomings, both the battery energy density and the airplane efficiency has to increase substantially.

Today's state of the art battery uses Lithium-Ion technology and has a mass specific energy storage in the range of 200 Wh/kg. Even with the expected mass specific energy of 250 Wh/kg by 2025, this is still very limiting. Fortunately, new technologies are underway, such as the sulfur-based batteries, which promise a substantial increase of energy density (see Fig. 1.21).

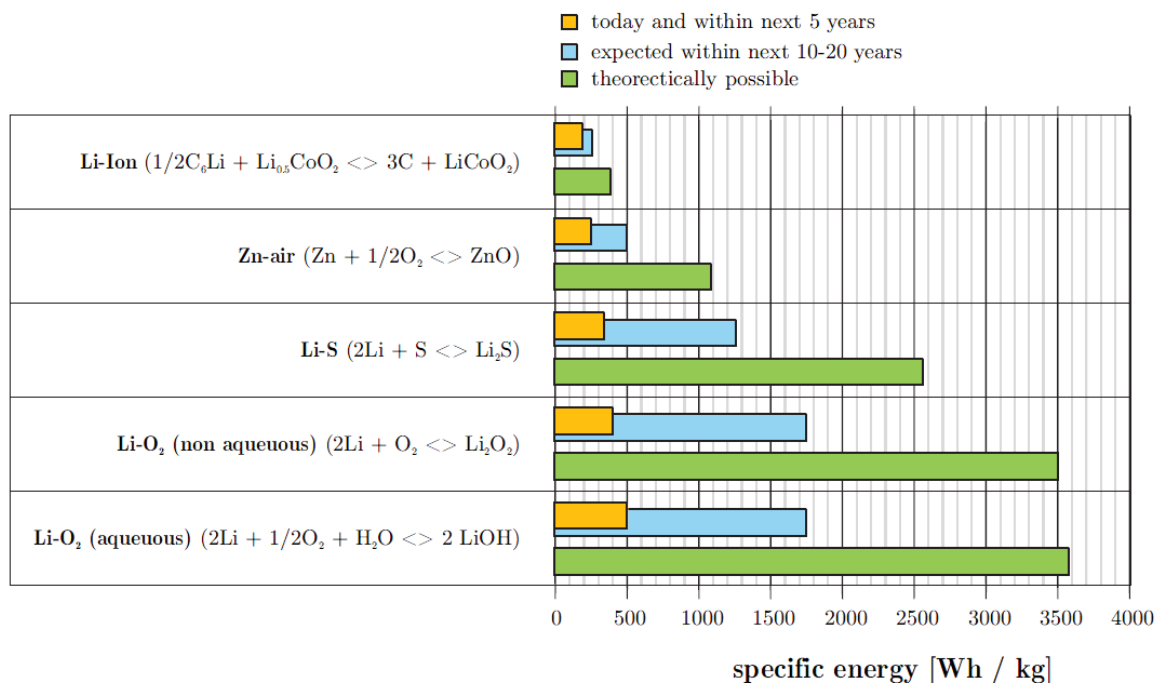


Figure 1.21: Current battery technology and expected development [78].

The aircraft energy consumption, can be improved by increasing the aerodynamic efficiency measured by  $L/D$  and decreasing the aircraft weight. Higher  $L/D$  is usually achieved through the use of higher aspect ratio wings, careful aerodynamic design, and lower cruise speed. The weight reduction can be achieved through the use of light weight composite materials and advanced structure design. Not surprisingly, the majority of today's electric aircraft designs are modified from sail planes because of their light weigh structure and high  $L/D$  (e.g. Antares 23E, ElectroLight2, Taurus Electro G2, Silent 2 Electro, LAK 17...). In some cases the large wing area can accommodate solar panels that recharge the batteries during flight (Solar Impulse, Sunseeker, Path Finder, Helios ...). However the low cruise speed and small amount of batteries storage render those aircraft dependent on weather condition and winds. Unless the plane uses updrafts to stay in the air, the range is limited

to typically less than 100nm. For all of the reasons cited above, today's electric aircraft is not mature yet for the general aviation market.

#### **1.4.5 CFJ General Aviation Electric Aircraft: A Revolutionary Concept**

The advanced CFJ flow control airfoil recently developed by Zha and his team [51, 55–62] offers a promising new concept that can significantly increase the cruise wing loading with a high aerodynamic efficiency, low energy expenditure and high stall AoA. The maximum aerodynamic L/D of CFJ is usually very high since the CFJ significantly reduces the drag or even generates thrust. The aerodynamic lift and drag will be used for the aircraft design to size the payload and engine thrust required. For an active flow control airfoil however, the measure of aerodynamic efficiency cannot use the conventional definition of L/D, but needs to consider the energy consumption for the flow control. The proper aerodynamic efficiency for CFJ airfoil is hence defined as :

$$\left(\frac{L}{D}\right)_c = \frac{L}{D + P/V_\infty} \quad (1.1)$$

where P is the power consumed by the active flow control system,  $V_\infty$  is the free stream speed.

At the maximum  $(L/D)_c$ , a CFJ airfoil usually has a higher  $C_L$  than that of a conventional airfoil. Hence the CFJ wing is able to cruise at a much higher wing loading. As a result, the battery payload and the range would be greatly increased by using a CFJ airplane. In addition, a CFJ wing can achieve a very high maximum  $C_L$  of about 4.8, which removes the takeoff distance penalty usually occurring for high wing loading aircraft.

The CFJ wing is used for the whole flight mission without additional high lift flap or slat systems. At takeoff and landing phase when the high maximum lift coefficient is needed, the maximum CFJ pumping power is utilized. At cruise, a small pumping power is used to achieve high cruise lift and high aerodynamic efficiency. The wing weight could be reduced due to the absence of moving parts.

If we introduce a measure of merit for aircraft as  $MPS = Miles * Passengers / S$ , where  $S$  is the wing planform area, the MPS of the present EA design is about half that of a conventional reciprocating engine general aviation airplane, and 1.5 to 2.5 times greater than the MPS of the state of the art EA. This suggests that the CFJ-EA has a far greater range than a same size EA using a conventional wing design. Or for the same range, the CFJ-EA has a much smaller size than a conventional design. The CFJ-EA concept may open the door to a new class of general aviation EA designs. The same CFJ flow control technology can also be used for other general aviation airplanes with conventional propulsion systems and high altitude airplanes to reduce the wing size.

## 1.5 Outline and Strategy of the Thesis

The performance of co-flow jet (CFJ) flow control method and its applications are investigated using experimental testing and computational fluid dynamics (CFD) simulations. This leads to a detailed study of the energy expenditure, lift enhancement, drag reduction, stall margin increase, dynamic stall removal, and performance variation with Mach number. These investigations are conducted for a variety of stationary airfoils, pitching airfoils and high aspect ratio wings. Finally CFJ is applied to design two high efficiency general aviation electric airplanes.

The order of the manuscript chapters is as follow; The fluid dynamics governing equations are presented in Chapter 2, followed by the CFD numerical methodology in Chapter 3. The parameters used in CFJ performance analysis are given in Chapter 4, and the airplane mission analysis equations are derived in Chapter 5. A brief description of the experimental work is given Chapter 6. The numerical investigations results are presented in Chapters 7, 8, 9 and 10. First, the stationary CFJ airfoil performance and energy expenditure with the variation of Mach number and airfoil shape are presented. Secondly, pitching CFJ airfoils performance are investigated. Thirdly, 3D CFJ wings are investigates. Lastly, a revolutionary concept electric airplane is designed which fully utilizes the superior performance of CFJ airfoils.

# Chapter 2

## The Fluid Flow Governing Equations

### 2.1 The Navier-Stokes Equations

The governing equations are the spatially filtered compressible Navier-Stokes equations. The spatial filtering removes the small scale high frequency components of the fluid motion, while keeping the unsteadiness associated with the large scale turbulent motion. Following the derivation of Knight et al. [80], the filtered compressible Navier-Stokes equations in Cartesian coordinates can be expressed as:

$$\frac{\partial \mathbf{Q}}{\partial t} + \frac{\partial \mathbf{E}}{\partial x} + \frac{\partial \mathbf{F}}{\partial y} + \frac{\partial \mathbf{G}}{\partial z} = \frac{1}{Re} \left( \frac{\partial \mathbf{E}_v}{\partial x} + \frac{\partial \mathbf{F}_v}{\partial y} + \frac{\partial \mathbf{G}_v}{\partial z} \right) \quad (2.1)$$

where  $t$  is time,  $Re$  is the Reynolds number. The variable vector  $\mathbf{Q}$ , inviscid flux vectors  $\mathbf{E}$ ,  $\mathbf{F}$ ,  $\mathbf{G}$ , and the viscous fluxes  $\mathbf{E}_v$ ,  $\mathbf{F}_v$ ,  $\mathbf{G}_v$  are given as the following.

$$\mathbf{Q} = \begin{pmatrix} \bar{\rho} \\ \bar{\rho}\tilde{u} \\ \bar{\rho}\tilde{v} \\ \bar{\rho}\tilde{w} \\ \bar{\rho}\tilde{e} \end{pmatrix}, \mathbf{E} = \begin{pmatrix} \bar{\rho}\tilde{u} \\ \bar{\rho}\tilde{u}^2 + \bar{p} \\ \bar{\rho}\tilde{u}\tilde{v} \\ \bar{\rho}\tilde{u}\tilde{w} \\ (\bar{\rho}\tilde{e} + \bar{p})\tilde{u} \end{pmatrix}, \mathbf{F} = \begin{pmatrix} \bar{\rho}\tilde{v} \\ \bar{\rho}\tilde{v}\tilde{u} \\ \bar{\rho}\tilde{v}^2 + \bar{p} \\ \bar{\rho}\tilde{v}\tilde{w} \\ (\bar{\rho}\tilde{e} + \bar{p})\tilde{v} \end{pmatrix}, \mathbf{G} = \begin{pmatrix} \bar{\rho}\tilde{w} \\ \bar{\rho}\tilde{w}\tilde{u} \\ \bar{\rho}\tilde{w}\tilde{v} \\ \bar{\rho}\tilde{w}^2 + \bar{p} \\ (\bar{\rho}\tilde{e} + \bar{p})\tilde{w} \end{pmatrix}$$

$$\mathbf{E}_v = \begin{pmatrix} 0 \\ \bar{\tau}_{xx} + \sigma_{xx} \\ \bar{\tau}_{xy} + \sigma_{xy} \\ \bar{\tau}_{xz} + \sigma_{xz} \\ Q_x \end{pmatrix}, \mathbf{F}_v = \begin{pmatrix} 0 \\ \bar{\tau}_{yx} + \sigma_{yx} \\ \bar{\tau}_{yy} + \sigma_{yy} \\ \bar{\tau}_{yz} + \sigma_{yz} \\ Q_y \end{pmatrix}, \mathbf{G}_v = \begin{pmatrix} 0 \\ \bar{\tau}_{zx} + \sigma_{zx} \\ \bar{\tau}_{zy} + \sigma_{zy} \\ \bar{\tau}_{zz} + \sigma_{zz} \\ Q_z \end{pmatrix}$$

The overbar denotes a regular filtered variable, and the tilde is used to denote the Favre filtered variable. In above equations,  $\rho$  is the density,  $u, v, w$  are the Cartesian velocity components in  $x, y, z$  directions,  $p$  is the static pressure, and  $e$  is the total energy per unit mass.

The  $\bar{\tau}$  is the molecular viscous stress tensor and is estimated as:

$$\bar{\tau}_{ij} = -\frac{2}{3}\tilde{\mu}\frac{\partial\tilde{u}_k}{\partial x_k}\delta_{ij} + \tilde{\mu}\left(\frac{\partial\tilde{u}_i}{\partial x_j} + \frac{\partial\tilde{u}_j}{\partial x_i}\right), \quad i, j = 1, 2, 3 \quad (2.2)$$

The above equation is in tensor form, where the subscript 1, 2, 3 represent the coordinates,  $x, y, z$ , and the Einstein summation convention is used.

The molecular viscosity  $\tilde{\mu} = \tilde{\mu}(\tilde{T})$  is determined by Sutherland law.

The  $\sigma$  is the subgrid scale stress tensor due to the filtering process and is expressed as:

$$\sigma_{ij} = -\bar{\rho}(\widetilde{u_i u_j} - \tilde{u}_i \tilde{u}_j) \quad (2.3)$$

The energy flux  $Q$  is expressed as:

$$Q_i = \tilde{u}_j(\bar{\tau}_{ij} + \sigma_{ij}) - \bar{q}_i + \Phi_i \quad (2.4)$$

where  $\Phi$  is the subscale heat flux:

$$\Phi_i = -C_p \bar{\rho}(\widetilde{u_i T} - \tilde{u}_i \tilde{T}) \quad (2.5)$$

The  $\bar{q}_i$  is the molecular heat flux:

$$\bar{q}_i = -\frac{C_p \tilde{\mu}}{Pr} \frac{\partial \tilde{T}}{\partial x_i} \quad (2.6)$$

$$\bar{\rho} \tilde{e} = \frac{\bar{p}}{(\gamma-1)} + \frac{1}{2} \bar{\rho}(\tilde{u}^2 + \tilde{v}^2 + \tilde{w}^2) + \rho k \quad (2.7)$$

where  $\gamma$  is the ratio of specific heats,  $\rho k$  is the subscale kinetic energy per unit volume.

$$\rho k = \frac{1}{2} \bar{\rho}(\widetilde{u_i u_i} - \tilde{u}_i \tilde{u}_i) = -\frac{1}{2} \sigma_{ii} \quad (2.8)$$

In the present calculation, the  $\rho k$  in Eq.(2.7) is omitted based on the assumption that the effect is small.

In generalized coordinates, Eq.(2.1) can be expressed as the following:

$$\frac{\partial \mathbf{Q}'}{\partial t} + \frac{\partial \mathbf{E}'}{\partial \xi} + \frac{\partial \mathbf{F}'}{\partial \eta} + \frac{\partial \mathbf{G}'}{\partial \zeta} = \frac{1}{\text{Re}} \left( \frac{\partial \mathbf{E}'_{\mathbf{v}}}{\partial \xi} + \frac{\partial \mathbf{F}'_{\mathbf{v}}}{\partial \eta} + \frac{\partial \mathbf{G}'_{\mathbf{v}}}{\partial \zeta} \right) \quad (2.9)$$

where

$$\mathbf{Q}' = \frac{\mathbf{Q}}{J} \quad (2.10)$$

$$\mathbf{E}' = \frac{1}{J} (\xi_t \mathbf{Q} + \xi_x \mathbf{E} + \xi_y \mathbf{F} + \xi_z \mathbf{G}) \quad (2.11)$$

$$\mathbf{F}' = \frac{1}{J} (\eta_t \mathbf{Q} + \eta_x \mathbf{E} + \eta_y \mathbf{F} + \eta_z \mathbf{G}) \quad (2.12)$$

$$\mathbf{G}' = \frac{1}{J} (\zeta_t \mathbf{Q} + \zeta_x \mathbf{E} + \zeta_y \mathbf{F} + \zeta_z \mathbf{G}) \quad (2.13)$$

$$\mathbf{E}'_{\mathbf{v}} = \frac{1}{J} (\xi_x \mathbf{E}_{\mathbf{v}} + \xi_y \mathbf{F}_{\mathbf{v}} + \xi_z \mathbf{G}_{\mathbf{v}}) \quad (2.14)$$

$$\mathbf{F}'_{\mathbf{v}} = \frac{1}{J} (\eta_x \mathbf{E}_{\mathbf{v}} + \eta_y \mathbf{F}_{\mathbf{v}} + \eta_z \mathbf{G}_{\mathbf{v}}) \quad (2.15)$$

$$\mathbf{G}'_{\mathbf{v}} = \frac{1}{J} (\zeta_x \mathbf{E}_{\mathbf{v}} + \zeta_y \mathbf{F}_{\mathbf{v}} + \zeta_z \mathbf{G}_{\mathbf{v}}) \quad (2.16)$$

where  $J$  is the transformation Jacobian. The inviscid fluxes in generalized coordinate system are expressed as:

$$\mathbf{E}' = \begin{bmatrix} \bar{\rho}U \\ \bar{\rho}\tilde{u}U + l_x\bar{p} \\ \bar{\rho}\tilde{v}U + l_y\bar{p} \\ \bar{\rho}\tilde{w}U + l_z\bar{p} \\ (\bar{\rho}\tilde{e} + \bar{p})U - l_t\bar{p} \end{bmatrix}, \mathbf{F}' = \begin{bmatrix} \bar{\rho}V \\ \bar{\rho}\tilde{u}V + m_x\bar{p} \\ \bar{\rho}\tilde{v}V + m_y\bar{p} \\ \bar{\rho}\tilde{w}V + m_z\bar{p} \\ (\bar{\rho}\tilde{e} + \bar{p})V - m_t\bar{p} \end{bmatrix}, \mathbf{G}' = \begin{bmatrix} \bar{\rho}W \\ \bar{\rho}\tilde{u}W + n_x\bar{p} \\ \bar{\rho}\tilde{v}W + n_y\bar{p} \\ \bar{\rho}\tilde{w}W + n_z\bar{p} \\ (\bar{\rho}\tilde{e} + \bar{p})W - n_t\bar{p} \end{bmatrix}$$

where  $U$ ,  $V$  and  $W$  are the contravariant velocities in  $\xi$ ,  $\eta$  and  $\zeta$  directions.

$$\begin{aligned} U &= l_t + \mathbf{l} \bullet \mathbf{V} = l_t + l_x\tilde{u} + l_y\tilde{v} + l_z\tilde{w} \\ V &= m_t + \mathbf{m} \bullet \mathbf{V} = m_t + m_x\tilde{u} + m_y\tilde{v} + m_z\tilde{w} \\ W &= n_t + \mathbf{n} \bullet \mathbf{V} = n_t + n_x\tilde{u} + n_y\tilde{v} + n_z\tilde{w} \end{aligned} \quad (2.17)$$

$\mathbf{l}$ ,  $\mathbf{m}$ ,  $\mathbf{n}$  are the normal vectors on  $\xi$ ,  $\eta$ ,  $\zeta$  surfaces with their magnitudes equal to the elemental surface area and pointing to the directions of increasing  $\xi$ ,  $\eta$ ,  $\zeta$ .

$$\mathbf{l} = \frac{\nabla\xi}{J}, \mathbf{m} = \frac{\nabla\eta}{J}, \mathbf{n} = \frac{\nabla\zeta}{J} \quad (2.18)$$

$$l_t = \frac{\xi_t}{J}, m_t = \frac{\eta_t}{J}, n_t = \frac{\zeta_t}{J} \quad (2.19)$$

For simplicity, all the overbar and tilde in above equations will be dropped in the rest of this thesis. Please note that the Navier-Stokes equations, Eq.(2.9), are normalized based on a set of reference parameters. The detailed normalization procedure can be found in [81].

## 2.2 Spalart-Allmaras Turbulence Model

The transport equation of the Spalart-Allmaras one equation turbulence model is derived by using empiricism, dimensional analysis, Galilean invariance and selected dependence on the molecular viscosity [82]. The working variable  $\tilde{v}$  is related to the eddy viscosity  $\nu_t$ . The transport equation is expressed as

$$\begin{aligned} \frac{D\tilde{v}}{Dt} = & c_{b1}\tilde{S}\tilde{v}(1-f_{t2}) - [c_{w1}f_w - \frac{c_{b1}}{\kappa^2}f_{t2}][\frac{\tilde{v}}{d}]^2 \\ & + \frac{1}{\sigma}[\nabla \cdot ((\mathbf{v} + \tilde{\mathbf{v}})\nabla\tilde{v}) + c_{b2}(\nabla\tilde{v})^2] + f_{t1}(\Delta q)^2 \end{aligned} \quad (2.20)$$

In generalized coordinate system, the dimensionless conservative form of Eq.(2.20) is given as the following:

$$\begin{aligned} \frac{\partial \frac{1}{J}\rho\tilde{v}}{\partial t} + \frac{\partial \rho\tilde{v}U}{\partial \xi} + \frac{\partial \rho\tilde{v}V}{\partial \eta} + \frac{\partial \rho\tilde{v}W}{\partial \zeta} = \frac{1}{Re} \left( \frac{\partial \frac{\rho}{\sigma}(\mathbf{v} + \tilde{\mathbf{v}})(\mathbf{l} \bullet \nabla\tilde{v})}{\partial \xi} \right. \\ \left. + \frac{\partial \frac{\rho}{\sigma}(\mathbf{v} + \tilde{\mathbf{v}})(\mathbf{m} \bullet \nabla\tilde{v})}{\partial \eta} + \frac{\partial \frac{\rho}{\sigma}(\mathbf{v} + \tilde{\mathbf{v}})(\mathbf{n} \bullet \nabla\tilde{v})}{\partial \zeta} + \frac{1}{J}S_v \right) \end{aligned} \quad (2.21)$$

where

$$\begin{aligned} S_v = & \rho c_{b1}(1-f_{t2})\tilde{S}\tilde{v} + \frac{1}{Re} \left[ -\rho \left( c_{w1}f_w - \frac{c_{b1}}{\kappa^2}f_{t2} \right) \left( \frac{\tilde{v}}{d} \right)^2 \right. \\ & \left. + \frac{\rho}{\sigma}c_{b2}(\nabla\tilde{v})^2 - \frac{1}{\sigma}(\mathbf{v} + \tilde{\mathbf{v}})\nabla\tilde{v} \bullet \nabla\rho \right] + Re \left[ \rho f_{t1}(\Delta q)^2 \right] \end{aligned} \quad (2.22)$$

The eddy viscosity  $\nu_t$  is obtained from:

$$\nu_t = \tilde{v}f_{v1} \quad f_{v1} = \frac{\chi^3}{\chi^3 + c_{v1}^3} \quad \chi = \frac{\tilde{v}}{\nu} \quad (2.23)$$

where  $\nu$  is the kinematic viscosity. The production term is:

$$\tilde{S} = S + \frac{\tilde{v}}{k^2 d^2} f_{v2}, \quad f_{v2} = 1 - \frac{\chi}{1 + \chi f_{v1}} \quad (2.24)$$

where  $S$  is the magnitude of the vorticity. The function  $f_w$  is given by

$$f_w = g \left( \frac{1 + c_{w3}^6}{g^6 + c_{w3}^6} \right)^{1/6}, \quad g = r + c_{w2}(r^6 - r), \quad r = \frac{\tilde{v}}{\tilde{S} k^2 d^2} \quad (2.25)$$

The function  $f_{i2}$  is given by

$$f_{i2} = c_{i3} \exp(-c_{i4} \chi^2) \quad (2.26)$$

and the trip function  $f_{i1}$  is

$$f_{i1} = c_{i1} g_t \exp \left[ -c_{i2} \frac{\omega_t^2}{\Delta U^2} (d^2 + g_t^2 d_t^2) \right], \quad g_t = \min \left( 0.1, \frac{\Delta q}{\omega_t \Delta x_t} \right) \quad (2.27)$$

where,  $\omega_t$  is the wall vorticity at the wall boundary layer trip location,  $d$  is the distance to the closest wall.  $d_t$  is the distance of the field point to the trip location,  $\Delta q$  is the difference of the velocities between the field point and the trip location,  $\Delta x_t$  is the grid spacing along the wall at the trip location.

The values of the coefficients are:  $c_{b1} = 0.1355$ ,  $c_{b2} = 0.622$ ,  $\sigma = \frac{2}{3}$ ,  $c_{w1} = \frac{c_{b1}}{k^2} + (1 + c_{b2})/\sigma$ ,  $c_{w2} = 0.3$ ,  $c_{w3} = 2$ ,  $k = 0.41$ ,  $c_{v1} = 7.1$ ,  $c_{i1} = 1.0$ ,  $c_{i2} = 2.0$ ,  $c_{i3} = 1.1$ ,  $c_{i4} = 2.0$ .

In S-A one equation turbulence model, the trip point need to be specified before computation. This is not straightforward to do because the exact position of the trip point is not known in most of the cases. Thus, a full turbulent boundary layer is used by setting  $c_{i1} = 0$  and  $c_{i3} = 0$ . No trip point needs to be specified.

It is observed that the S-A one equation turbulence model is sensitive to initial field. If the initial field of  $\tilde{v}$  is set to a small value, e.g.  $\tilde{v} < 1$ , the solution may converge with  $\tilde{v} = 0$ , which is the trivial solution of  $\tilde{v}$  when  $c_{t1} = c_{t3} = 0$ . This will result in a laminar flow solution. If the initial value is too large ( $\tilde{v} > 3$ ), the computation may diverge. In addition, setting up the initial value of  $\tilde{v}$  also depends on the schemes to be used. In our computation, it is found that it is generally safe to set the initial value of  $\tilde{v}$  to 2.

The boundary conditions of  $\tilde{v}$  are given as the following

$$\text{at walls :} \quad \tilde{v} = 0$$

$$\text{far field inflow :} \quad \tilde{v} = 0.02$$

$$\text{far field outflow :} \quad \tilde{v} \text{ is extrapolated}$$

Coupled Eqs.(2.9) with the S-A model Eq.(2.21), the conservative form of the governing equations are given as the following:

$$\frac{\partial Q}{\partial t} + \frac{\partial \mathbf{E}}{\partial \xi} + \frac{\partial \mathbf{F}}{\partial \eta} + \frac{\partial \mathbf{G}}{\partial \zeta} = \frac{1}{Re} \left( \frac{\partial \mathbf{R}}{\partial \xi} + \frac{\partial \mathbf{S}}{\partial \eta} + \frac{\partial \mathbf{T}}{\partial \zeta} + D \right) \quad (2.28)$$

where,

$$Q = \frac{1}{J} \begin{bmatrix} \rho \\ \rho u \\ \rho v \\ \rho w \\ \rho e \\ \rho \tilde{v} \end{bmatrix} \quad (2.29)$$

$$\mathbf{E} = \begin{bmatrix} \rho U \\ \rho uU + l_x p \\ \rho vU + l_y p \\ \rho wU + l_z p \\ (\rho e + p)U - l_t p \\ \rho \tilde{v}U \end{bmatrix}, \quad \mathbf{F} = \begin{bmatrix} \rho V \\ \rho uV + m_x p \\ \rho vV + m_y p \\ \rho wV + m_z p \\ (\rho e + p)V - m_t p \\ \rho \tilde{v}V \end{bmatrix}, \quad \mathbf{G} = \begin{bmatrix} \rho W \\ \rho uW + n_x p \\ \rho vW + n_y p \\ \rho wW + n_z p \\ (\rho e + p)W - n_t p \\ \rho \tilde{v}W \end{bmatrix} \quad (2.30)$$

$$\mathbf{R} = \begin{bmatrix} 0 \\ l_k \tau_{xk} \\ l_k \tau_{yk} \\ l_k \tau_{zk} \\ l_k \beta_k \\ \frac{\rho}{\sigma} (\mathbf{v} + \tilde{\mathbf{v}}) (\mathbf{l} \bullet \nabla \tilde{\mathbf{v}}) \end{bmatrix}, \quad \mathbf{S} = \begin{bmatrix} 0 \\ m_k \tau_{xk} \\ m_k \tau_{yk} \\ m_k \tau_{zk} \\ m_k \beta_k \\ \frac{\rho}{\sigma} (\mathbf{v} + \tilde{\mathbf{v}}) (\mathbf{m} \bullet \nabla \tilde{\mathbf{v}}) \end{bmatrix}, \quad \mathbf{T} = \begin{bmatrix} 0 \\ n_k \tau_{xk} \\ n_k \tau_{yk} \\ n_k \tau_{zk} \\ n_k \beta_k \\ \frac{\rho}{\sigma} (\mathbf{v} + \tilde{\mathbf{v}}) (\mathbf{n} \bullet \nabla \tilde{\mathbf{v}}) \end{bmatrix} \quad (2.31)$$

$$D = \frac{1}{J} \begin{bmatrix} 0 \\ 0 \\ 0 \\ 0 \\ 0 \\ S_v \end{bmatrix} \quad (2.32)$$

where,  $U, V, W$  are defined as in Eq.(2.17).

$$\beta_k = u_i \tau_{ki} - q_k \quad (2.33)$$

The shear-stress  $\tau_{ik}$  and total heat flux  $q_k$  in Cartesian Coordinate can be expressed as

$$\tau_{ik} = (\mu + \mu_t) \left[ \left( \frac{\partial u_i}{\partial x_k} + \frac{\partial u_k}{\partial x_i} \right) - \frac{2}{3} \delta_{ik} \frac{\partial u_j}{\partial x_j} \right] \quad (2.34)$$

$$q_k = -C_p \left( \frac{\mu}{Pr} + \frac{\mu_t}{Pr_t} \right) \frac{\partial T}{\partial x_k} \quad (2.35)$$

# Chapter 3

## Numerical Methodology

In this chapter, an implicit finite difference discretization for the flow governing equations is described. The inviscid fluxes are discretized using a low diffusion E-CUSP scheme [83]. The fifth-order WENO scheme [84, 85] is used to reconstruct the conservative variables at volume interfaces. A set of fully conservative fourth-order accurate finite central differencing schemes for the viscous terms is employed in this research [86, 87]. The structure governing equations are discretized and solved implicitly in the same manner to be consistent with the flow governing equations.

### 3.1 Implicit Discretization

Let  $J = \frac{1}{\Delta V}$ , then 3D Navier-Stokes equations (2.28) is rewritten in a conservative flux vector form as

$$\frac{\partial \Delta V \mathbf{Q}}{\partial t} + \frac{\partial (\mathbf{E} - \mathbf{R}')}{\partial \xi} + \frac{\partial (\mathbf{F} - \mathbf{S}')}{\partial \eta} + \frac{\partial (\mathbf{G} - \mathbf{T}')}{\partial \zeta} = \Delta V \mathbf{D} \quad (3.1)$$

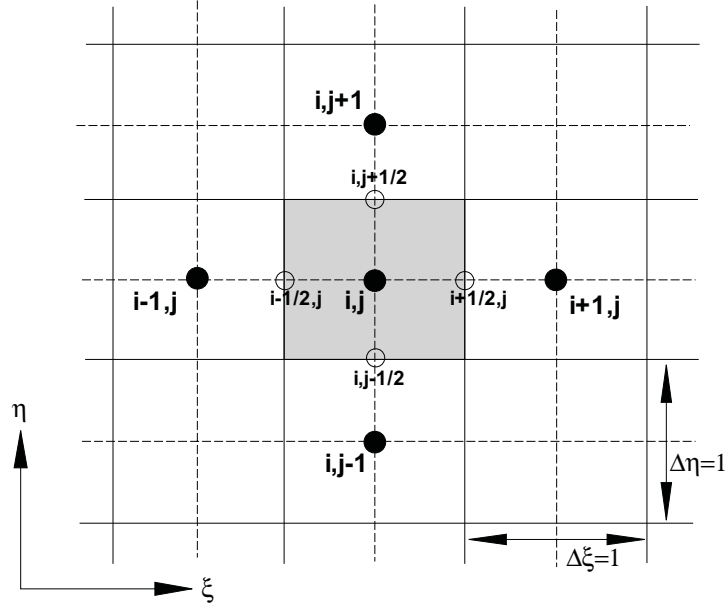


Figure 3.1: Discretization domain indicating the cell center( $i,j$ )

where  $\Delta V$  denotes the volume of the cell and  $\mathbf{R}' = \mathbf{R}/Re$ ,  $\mathbf{S}' = \mathbf{S}/Re$ ,  $\mathbf{T}' = \mathbf{T}/Re$ . For steady state solutions, the governing equation will be elliptic type at subsonic and hyperbolic at supersonic. This will make it difficult to discretize the Navier-Stokes equations using a consistent scheme. The temporal term is thus included for steady state solutions to keep the governing equations to have the same hyperbolic type across Mach number 1. For steady state solution, the accuracy of the temporal term is irrelevant since it must be zero when it is converged. Hence, the temporal term is discretized using first order Euler method for its simplicity. The discretized temporal term becomes

$$\frac{\Delta V(\mathbf{Q}^{n+1} - \mathbf{Q}^n)}{\Delta t} + \left[ \frac{\partial(\mathbf{E} - \mathbf{R}')}{\partial \xi} \right]^{n+1} + \left[ \frac{\partial(\mathbf{F} - \mathbf{S}')}{\partial \eta} \right]^{n+1} + \left[ \frac{\partial(\mathbf{G} - \mathbf{T}')}{\partial \zeta} \right]^{n+1} = \Delta V \mathbf{D}^{n+1} \quad (3.2)$$

where  $n$  and  $n + 1$  are two sequential time levels, which have a time interval of  $\Delta t$ .

### 3.2 Implicit Time Integration

When a unsteady solution is considered, higher order approximation for the time derivative is desirable. For unsteady flow, Jameson formulated so called the 2nd order dual time stepping scheme [88]. By introducing a pseudo time term, the unsteady problem at each physical time step is treated as a steady state problem for pseudo time. Without losing time accuracy, the dual time stepping scheme can greatly improve the computation efficiency by enhancing diagonal dominance [89].

The time accurate governing equations are solved using dual time stepping method suggested by Jameson [88]. To achieve high convergence rate, the implicit pseudo time marching scheme is used with the unfactored Gauss-Seidel line relaxation [90]. The physical temporal term is discretized implicitly using a three point, backward differencing as the following

$$\frac{\partial Q}{\partial t} = \frac{3Q^{n+1} - 4Q^n + Q^{n-1}}{2\Delta t} \quad (3.3)$$

where  $n - 1$ ,  $n$  and  $n + 1$  are three sequential time levels, which have a time interval of  $\Delta t$ . The first-order Euler scheme is used to discretize the pseudo temporal term to enhance diagonal dominance. The semi-discretized equations of the governing equations are finally given as the following

$$\begin{aligned}
& \left[ \left( \frac{1}{\Delta\tau} + \frac{1.5}{\Delta t} \right) I - \left( \frac{\partial R}{\partial Q} \right)^{n+1,m} \right] \delta Q^{n+1,m+1} \\
& = R^{n+1,m} - \frac{3Q^{n+1,m} - 4Q^n + Q^{n-1}}{2\Delta t}
\end{aligned} \tag{3.4}$$

where the  $\Delta\tau$  is the pseudo time step,  $R$  is the net flux evaluated on a grid point using the fifth-order WENO scheme.

### 3.3 Gauss-Seidel Line Relaxation

To enhance diagonal dominance, a first order scheme is used for the implicit pseudo temporal terms. Following the procedure in Hu's Ph.D. thesis [81], the implicit discretized form of Eq.(3.4) is written as the following

$$\begin{aligned}
& \bar{B}\Delta Q_{i,j,k}^{n+1} + A^+\Delta Q_{i+1,j,k}^{n+1} + A^-\Delta Q_{i-1,j,k}^{n+1} + B^+\Delta Q_{i,j+1,k}^{n+1} \\
& + B^-\Delta Q_{i,j-1,k}^{n+1} + C^+\Delta Q_{i,j,k+1}^{n+1} + C^-\Delta Q_{i,j,k-1}^{n+1} = \mathbf{RHS}^n
\end{aligned} \tag{3.5}$$

$\mathbf{RHS}^n$  is the summation of all the terms on the right hand side (RHS) of the equation.

$$\begin{aligned}
\mathbf{RHS}^n = \Delta t \left\{ \left[ \left( \mathbf{R}_{i+\frac{1}{2}}^n - \mathbf{R}_{i-\frac{1}{2}}^n \right) + \left( \mathbf{S}_{j+\frac{1}{2}}^n - \mathbf{S}_{j-\frac{1}{2}}^n \right) + \left( \mathbf{T}_{k+\frac{1}{2}}^n - \mathbf{T}_{k-\frac{1}{2}}^n \right) \right] \right. \\
\left. - \left[ \left( \mathbf{E}_{i+\frac{1}{2}}^n - \mathbf{E}_{i-\frac{1}{2}}^n \right) + \left( \mathbf{F}_{j+\frac{1}{2}}^n - \mathbf{F}_{j-\frac{1}{2}}^n \right) + \left( \mathbf{G}_{k+\frac{1}{2}}^n - \mathbf{G}_{k-\frac{1}{2}}^n \right) \right] \right\} + D^n \cdot \Delta t \tag{3.6}
\end{aligned}$$

Gauss-Seidel line relaxation is applied in each direction ( $i, j, k$ ) and is swept one time step forward and backward in each direction. For example, the equation for Gauss-Seidel relaxation following lines along direction  $i$  with the index from small to large is written as:

$$B^- \Delta Q_{i,j-1,k}^{n+1} + \bar{B} \Delta Q_{i,j,k}^{n+1} + B^+ \Delta Q_{i,j+1,k}^{n+1} = \mathbf{RHS}' \quad (3.7)$$

where

$$\mathbf{RHS}' = \mathbf{RHS}^n - A^+ \Delta Q_{i+1,j,k}^n - A^- \Delta Q_{i-1,j,k}^{n+1} - C^+ \Delta Q_{i,j,k+1}^n - C^- \Delta Q_{i,j,k-1}^{n+1} \quad (3.8)$$

### 3.4 User Prescribed $C_\mu$ Boundary Condition for CFJ

The user prescribed  $C_\mu$  for CFJ boundary condition assumes subsonic inflow and subsonic outflow in the injection and suction cavities respectively as shown Fig. 3.2. These boundary conditions are described in [91]. To achieve zero-net mass-flux with the CFJ flow control, the mass flow that exits the injection slot must equal the mass flow entering the suction slot. Additionally, the jet strength must be controlled in order to reach the prescribed  $C_\mu$ . This is achieved by iterating the jet total pressure at the inflow boundary ( $P_{t2}$ ) until the  $C_\mu$  value is within 1% of the prescribed value. The inflow boundary total temperature and flow angle are assumed constant during this process. At the suction cavity, the injection and suction mass flows are matched by iterating the static pressure at the subsonic outflow boundary ( $P_{s2}$ ). The process is iterated throughout the simulation until the specified momentum coefficient is reached and the injection and suction mass flow match.

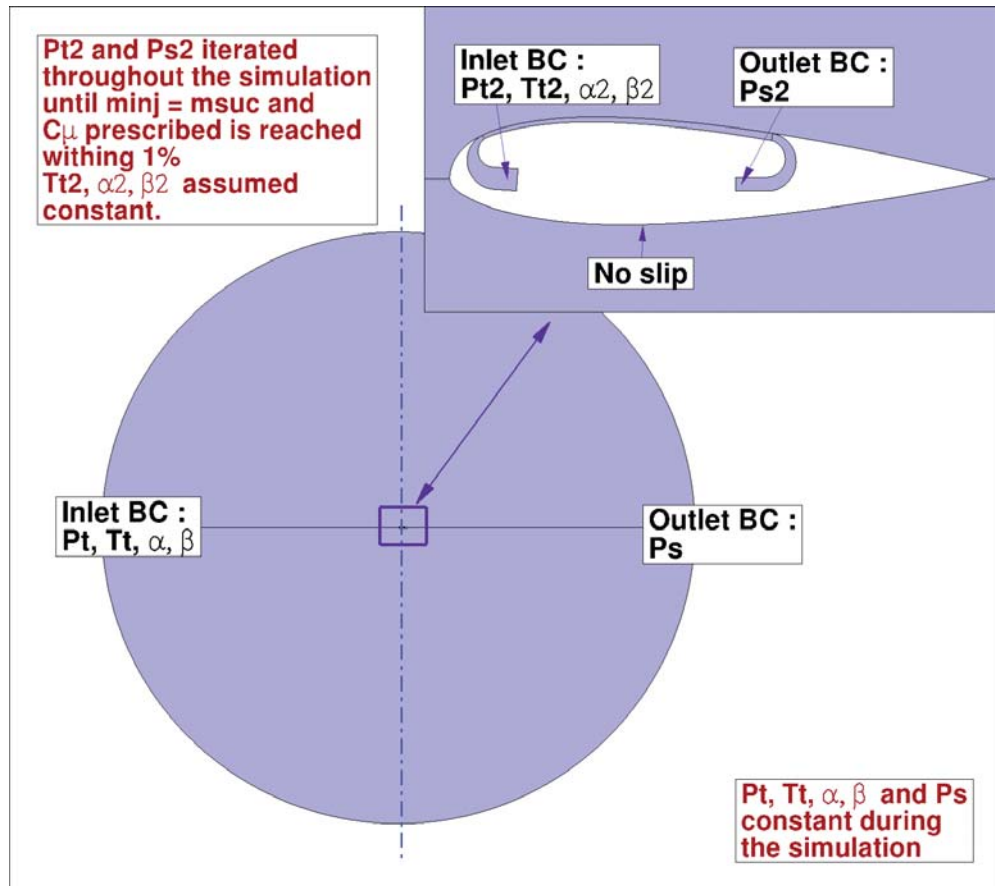


Figure 3.2: Typical boundary condition setup for a CFJ airfoil simulation.

### 3.5 Validation Study

Extensive validations are conducted to demonstrate high accuracy and robustness of the high fidelity simulation RANS methodology [91, 92]. The validated cases include but are not limited to : 1) The flow field over a subsonic and a supersonic flat plates are simulated [92]. The subsonic flow is turbulent and the supersonic flow is laminar. The simulated laminar and turbulent boundary layer profiles agree excellently with the Blasius solution and Law of the Wall, respectively. 2) The 2D Nozzle supersonic flow simulation and the flow field is compared with the experiments. The simulation accurately predicts the shock waves and the shock wave and their reflections [90]. 3) The simulated RAE2822 supercrit-

ical airfoil pressure coefficient is in good agreement with the experimental data [90]. 4) The ONERA M6 wing simulation is performed. Excellent agreement is found between the simulated pressure coefficient and the experiment at different wing span [92, 93]. 5) The NACA6415 CFJ airfoil is simulated for a variety of  $C_{\mu}$ . Experiments are conducted for the same  $C_{\mu}$  in the University of Miami wind tunnel facilities. The predicted lift, drag and moment coefficients agree well with the experiments. The predicted power coefficient is in excellent agreement with the experiment [61]. 6) The pitching airfoil SC1095 simulation is performed during a deep stall case. Very good agreement is found between the computed lift, drag and moment coefficients and the experimental data [62]. 7) The DLR wing-body configuration is simulated and excellent agreement is found between the simulated lift, drag and the experiment.

# Chapter 4

## CFJ Airfoil Parameters

This section introduces the definitions of several parameters used to describe CFJ airfoil performance.

### 4.1 Lift, Drag and Moment Calculation

The momentum and pressure at the injection and suction slots produce a reactionary force, which is automatically measured by the force balance in wind tunnel testing. However, for CFD simulation, the full reactionary force needs to be included. Using a control volume analysis, the reactionary forces can be calculated using the flow parameters at the injection and suction slot opening surfaces. Zha et al. [51] give the following formulations to calculate the lift and drag due to the jet reactionary force for a CFD simulation. By considering the effects of injection and suction jets on the CFJ airfoil, the expressions for these

reactionary forces are given as :

$$F_{x_{cfj}} = (\dot{m}_j V_{j1} + p_{j1} A_{j1}) * \cos(\theta_1 - \alpha) - (\dot{m}_j V_{j2} + p_{j2} A_{j2}) * \cos(\theta_2 + \alpha) \quad (4.1)$$

$$F_{y_{cfj}} = (\dot{m}_{j1} V_{j1} + p_{j1} A_{j1}) * \sin(\theta_1 - \alpha) + (\dot{m}_{j2} V_{j2} + p_{j2} A_{j2}) * \sin(\theta_2 + \alpha) \quad (4.2)$$

where the subscripts 1 and 2 stand for the injection and suction respectively, and  $\theta_1$  and  $\theta_2$  are the angles between the injection and suction slot surfaces and a line normal to the airfoil chord.  $\alpha$  is the angle of attack.

The total lift and drag on the CFJ airfoil can then be expressed as:

$$D = R'_x - F_{x_{cfj}} \quad (4.3)$$

$$L = R'_y - F_{y_{cfj}} \quad (4.4)$$

where  $R'_x$  and  $R'_y$  are the surface integral of pressure and shear stress in  $x$  (drag) and  $y$  (lift) direction excluding the internal injection and suction ducts.

Let us introduce the CFJ reactionary forces components in the  $x$  and  $y$  direction for the injection (*inj* subscript) and suction (*suc* subscript) as :

$$F_{x_{inj}} = (\dot{m}_j V_{j1} + p_{j1} A_{j1}) * \cos(\theta_1 - \alpha) \quad (4.5)$$

$$F_{x_{suc}} = (\dot{m}_j V_{j2} + p_{j2} A_{j2}) * \cos(\theta_2 + \alpha) \quad (4.6)$$

$$F_{y_{inj}} = (\dot{m}_{j1} V_{j1} + p_{j1} A_{j1}) * \sin(\theta_1 - \alpha) \quad (4.7)$$

$$F_{y_{suc}} = (\dot{m}_{j2} V_{j2} + p_{j2} A_{j2}) * \sin(\theta_2 + \alpha) \quad (4.8)$$

The total pitching moment of the CFJ airfoil can be expressed as:

$$M_z = M'_z + F_{x_{inj}} \cdot L_{y_{inj}} + F_{y_{inj}} \cdot L_{x_{inj}} - F_{x_{suc}} \cdot L_{y_{suc}} - F_{y_{suc}} \cdot L_{x_{suc}} \quad (4.9)$$

where  $M'_z$  is the pitching moment generated by the airfoil surface pressure and shear stress excluding the internal injection and suction ducts.  $L_{x_{inj}}$  and  $L_{y_{inj}}$ , respectively  $L_{x_{suc}}$  and  $L_{y_{suc}}$ , are the moment arm in  $x$  and  $y$  direction for the injection, respectively suction. By convention, we define a pitch up moment as a positive moment and a pitch down moment as a negative moment.

For the CFD simulation, the total lift, drag and moment are calculated using Eqs. (4.3), (4.4) and (4.9) respectively.

## 4.2 Jet Momentum Coefficient

The jet momentum coefficient  $C_\mu$  is a parameter used to quantify the jet intensity. It is defined as :

$$C_\mu = \frac{\dot{m}V_j}{\frac{1}{2}\rho_\infty V_\infty^2 S} \quad (4.10)$$

where  $\dot{m}$  is the injection mass flow,  $V_j$  the injection velocity,  $\rho_\infty$  and  $V_\infty$  denote the free stream density and velocity, and  $S$  is the planform area.

## 4.3 Power Coefficient

The CFJ can be implemented by mounting a pumping system inside the wing that withdraws air from the suction slot and blows it into the injection slot. The power consumption

can be determined by the jet mass flow and total enthalpy change as the following :

$$P = \dot{m}(H_{t1} - H_{t2}) \quad (4.11)$$

where  $H_{t1}$  and  $H_{t2}$  are the total enthalpy in the injection cavity and suction cavity respectively,  $P$  is the Power required by the pump and  $\dot{m}$  the jet mass flow rate. Introducing the pump efficiency  $\eta$  and total pressure ratio of the pump  $\Gamma = \frac{P_{t1}}{P_{t2}}$ , the power consumption can be expressed as :

$$P = \frac{\dot{m}C_p T_{t2}}{\eta} (\Gamma^{\frac{\gamma-1}{\gamma}} - 1) \quad (4.12)$$

where  $\gamma$  is the specific heat ratio equal to 1.4 for air. The power consumption can be expressed as a power coefficient below:

$$P_c = \frac{P}{\frac{1}{2}\rho_\infty V_\infty^3 S} \quad (4.13)$$

## 4.4 Corrected Aerodynamic Efficiency

The conventional airfoil aerodynamic efficiency is defined as :

$$\frac{L}{D} \quad (4.14)$$

For the CFJ airfoil, the ratio above still represents the pure aerodynamic relationship between lift and drag. However since CFJ active flow control consumes energy, the ratio above is modified to take into account the energy consumption of the pump. The formula-

tion of the corrected aerodynamic efficiency for CFJ airfoils is :

$$\left(\frac{L}{D}\right)_c = \frac{L}{D + \frac{P}{V_\infty}} \quad (4.15)$$

where  $V_\infty$  is the free stream velocity,  $P$  is the pumping power, and  $L$  and  $D$  are the lift and drag generated by the CFJ airfoil. The formulation above converts the power consumed by the CFJ into a force  $\frac{P}{V_\infty}$  which is added to the aerodynamic drag  $D$ . If the pumping power is set to 0, this formulation returns to the aerodynamic efficiency of a conventional airfoil.

# Chapter 5

## Mission Analysis

### 5.1 Background

Corke's Design of Aircraft [94] provides a conceptual aircraft design methodology. The mission analysis of the conceptual aircraft is implemented using FORTRAN by Espinal et al. [95] and modified for the purpose of this thesis. Using the initial constraints, a preliminary estimate of the aircraft weight at different flight stages is made for a user specified range. It is also possible to have a range estimate for a given aircraft weight, which can be inferred from CFD calculation. Once the weight or range is calculated, the required thrust and the take-off and landing distances are calculated using Corke's mission analysis model. CFD input is essential because it is the only one that can provide the L/D ratio required for the range calculation.

## 5.2 Range Estimate for Electric Aircraft

Unlike conventional reciprocating engine aircraft whose weight is reduced as the fuel is burned, the electric aircraft mass remains constant during the flight and thus the range must be calculated accordingly [78].

Using relations similar to the reciprocating engine aircraft, the energy consumption of the EA is estimated to 2.5% for the start-up and take-off, 7% acceleration to cruise velocity and altitude and 2.5% for the landing phase. In addition, an extra 8% of the battery power should be kept stored in the battery as a safety measure. Thus the specific energy density available for the cruise out to destination flight phase is

$$E_c = 0.8 \cdot E^* \quad (5.1)$$

where  $E^*$  is the specific energy density of the fully charged battery.

The range of an aircraft is then defined by

$$R = V \cdot t \quad (5.2)$$

where  $R$  is the range,  $V$  the cruise velocity and  $t$  the cruise duration.

The cruise duration is equal to the time to drain the battery, which under ideal conditions is

$$t = \frac{W_b \cdot E_c}{P_b} \quad (5.3)$$

where  $W_b$  is the battery weight and  $P_b$  the power drawn from the battery.

Substituting  $t$  to the range equation yields

$$R = \frac{W_b \cdot E_c}{P_b} \cdot V \quad (5.4)$$

The power drawn from the battery relates to the propulsive power required by the aircraft and the total efficiency of the propulsion system as follow

$$P_b = \frac{P_p}{\eta} \quad (5.5)$$

Where  $\eta$  is the propulsive efficiency.

The propulsion power required by the aircraft relates to its weight, lift over drag ratio (L/D) and flight velocity as follow

$$P_p = D \cdot V = \frac{W \cdot g}{L/D} V \quad (5.6)$$

where  $W$  is the weight of the aircraft.

combining Eqs. 5.5 and 5.6, the battery power becomes

$$P_b = \frac{W \cdot g}{L/D \cdot \eta} V \quad (5.7)$$

substituting  $P_b$  into Eq. (5.5) yields

$$\begin{aligned} R &= E_c \cdot \eta \cdot \frac{1}{g} \cdot \left(\frac{L}{D}\right)_c \cdot \frac{W_b}{W} \\ &= E_c \cdot \eta \cdot \frac{1}{g} \cdot \left(\frac{L}{D}\right)_c \cdot \left(1 - \frac{W_p}{W} - \frac{W_s}{W}\right) \\ &= E_c \cdot \eta \cdot \frac{1}{g} \cdot \left(\frac{L}{D}\right)_c \cdot \left(1 - \frac{W_p}{W} - s\right) \end{aligned} \quad (5.8)$$

where  $W_p$  is the payload weight,  $W_s$  is the structure weight and  $s$  is the structure factor, which is the ratio of the empty structure weight to the gross weight. In this design, a conservative structure factor of 0.45 is used. However, the airplane compact size may reduce the structure factor further. Eq. (5.8) indicates that for a constant  $L/D$ , payload and structure factor, increasing the gross weight will result in increasing the battery weight, and hence will give the airplane a longer range. This is the theoretical basis for a high wing loading compact EA.

# Chapter 6

## Experimental Investigation of CFJ

### Airfoils

This chapter describes some of the experimental work in which the author participated [59, 60, 96]. Dr. Dano's contribution in obtaining the experimental data have been invaluable. Experiments are conducted on open slot and discrete CFJ (DCFJ), where the injection slot is composed of multiple discrete jets. Flow visualization and Particle Image Velocimetry (PIV) are used to analyze the flow features. The forces and moment are measured through the balance. The purpose of the study is to better understand the flow mixing mechanism leading to the enhanced performance of CFJ.

#### 6.1 Experimental Setup

The NACA 6415 airfoil was used as the baseline airfoil. For the CFJ airfoil, a high energy jet is injected near the LE in the direction tangent to the main flow and the same amount of mass flow is drawn into the airfoil near the TE. Pressurized air is injected in a spanwise

long cavity near the LE then exits through the spanwise long rectangular slot. A Duocel high density aluminum foam was placed between the inlet and the exit slot to equilibrate the pressure and ensure a uniform exit velocity. Similarly, a spanwise long cavity placed near the TE is used to let the air settle down before being sucked through three suction ports. The airfoil chord is 12", the injection and suction slot height are 0.75% and 1.50% chord, respectively. All airflow and aerodynamic variables were acquired at the University of Miami 24" × 24" × 48" wind tunnel facilities. The injection and suction flow conditions are independently controlled. All wind tunnel free stream, CFJ airflow and aerodynamic variables were recorded using a state-of-the-art Labview<sup>TM</sup> data acquisition system. The LE trip had little influence over the airfoil performance. Various laser flow visualization techniques were used to monitor the circulation over the upper surface. A LaVision digital PIV system with a Litron Nano Nd:YAG 200 mJ/pulse was used to monitor and acquire the velocity field surrounding the airfoil. The velocity field was acquired for multiple spanwise locations. A seeder apparatus was used at the inlet of the wind tunnel to seed uniformly the field of view for PIV acquisition. A seeder box was used to distribute uniformly the seed in a volume of flow for PIV acquisition. An adaptive 64x64 to 32x32 pixels cross-correlation analysis method was used, resulting in a 150x200 vectors (including the airfoil which was masked). 200 instantaneous velocity fields were acquired for each test condition.

The range of AoA varied between 0° to 35°. Nominal free stream velocity is 10 m/s for all tests and the chord Reynolds number is about 195,000. The obstruction factors (OF) is defined by the ratio of the total jet exit area to the current jet exit area. The OF is changed by adding or removing various length tabs at the injection slot. When the OF is increased, the jet exit area is reduced, which in turns increases the jet exit velocity. Therefore, one can

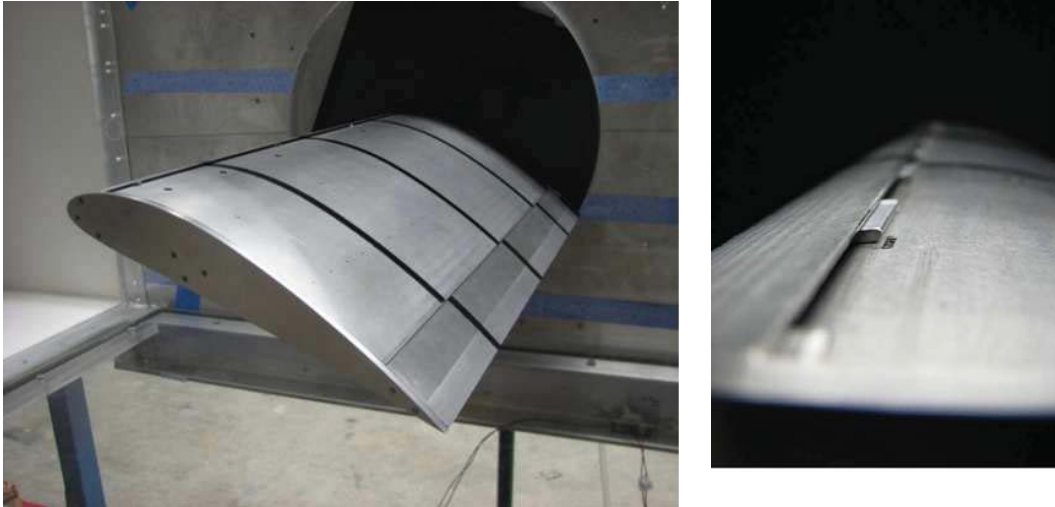


Figure 6.1: The CFJ airfoil in the wind tunnel with zoomed-in injection region. The tabs are in position DCFJ2/3.

see from Eq. (4.10) that, for a same mass flow rate, the  $C_{\mu}$  will change among the tests and consequently the data are plot for the same mass flow rate for comparison. For a given OF, a large number of combinations can be obtained depending on the number of tabs and jet width as shown 6.1. Table 6.1 shows the list of cases studied. Comparison is made between the larger (hereafter labeled A) and smaller number of discrete jets (hereafter labeled B). A close-up photo of discrete tabs in place is shown in Fig. 6.1. The baseline test for comparison is the open slot CFJ (OCFJ) i.e. OF=0. The mass flow rates used are 0.00 kg/s, 0.030 kg/s, 0.060 kg/s and 0.090 kg/s. The corresponding OCFJ jet momentum coefficients are  $C_{\mu} = 0.08, 0.017$  and  $0.26$ . Fig. 6.2 shows a summary of performance enhancement for the open slot CFJ and the DCFJ with obstruction factors of  $1/2, 2/3$  and  $3/4$  at the constant mass flow  $\dot{m}$  of 0.090 kg/s. The DCFJ significantly increase the lift and decrease the drag than the baseline airfoil. However, as indicated in [96], the energy expenditure of DCFJ is also significantly higher.

<b>Config. name</b>	<b>Obstruction Factor</b>	<b>Nb of tabs</b>	<b>Tab width (mm)</b>	<b>Jet width (mm)</b>	<b>Schematic representation</b>
OCFJ	0	0	0	304.8	
DCFJ 2/3	2/3	<b>A</b>	19	10.4 (1.76%)	
		<b>B</b>	9	21.9 (3.7%)	
DCFJ 3/4	3/4	<b>A</b>	14	10.5 (1.79%)	
		<b>B</b>	5	29.5 (5.0%)	

Table 6.1: The various discrete CFJ configurations studied.

## 6.2 Flow Visualization

Flow visualizations in the vicinity of the injection slot(s) were obtained to understand the flow structures and mixing mechanisms. Fig. 6.3 shows, in the top frame, the air flow for DCFJ2/3A at  $AoA=15^\circ$  with the CFJ turned off. One can see that at about mid chord, the flow is separated. A series of large clockwise vortical rollups are observed developing from the separation point. Full stall is observed for  $AoA=20^\circ$  with CFJ off. The middle and bottom frame show the flow visualization in the mid plane of a jet and mid plane of a tab, respectively. For both cases, the conditions were  $AoA=15^\circ$  and  $\dot{m} = 0.090\text{kg/s}$ . It should be noted that the discrete jets were only lightly seeded to create a contrast with the heavily seeded upstream flow. For the jet, series of counter-clockwise vortices are observed as the jet shear layer develops. The flow over the tab doesn't appear to create as much large structures as the jet disturbance. Some unsteady patches of unseeded air can be observed further downstream. This demonstrates that the jet is expanding in the spanwise direction, effectively increasing the mixing downstream of the tabs. Similar results are found for all

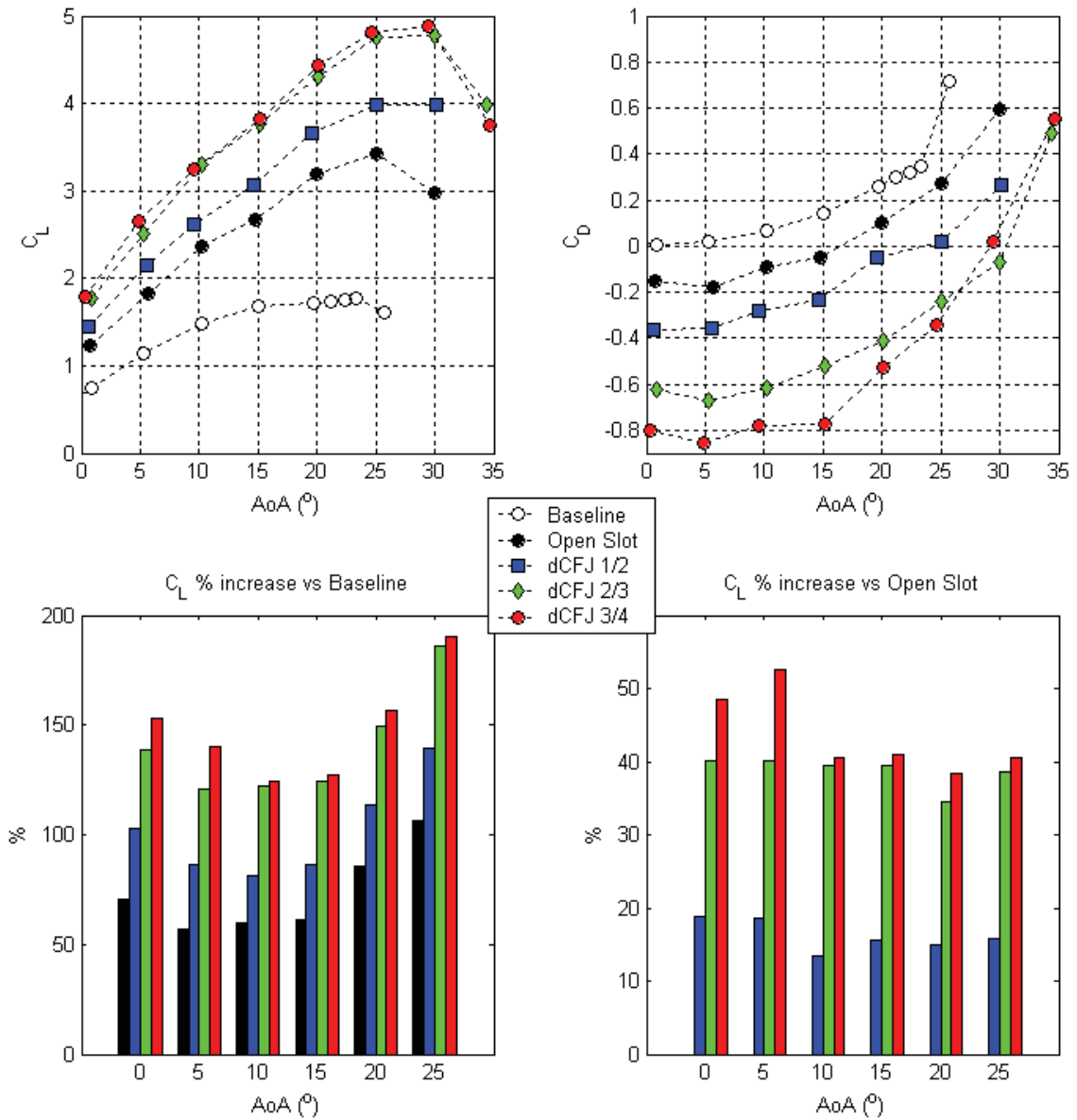


Figure 6.2: Overall Performance enhancement for various obstruction factors at the constant mass flow rate  $\dot{m}$  of 0.090 kg/s.

configurations and in particular DCFJ2/3B whose results are shown in Fig. 6.4. Similar jet incursions in the tab flow plane are observed for the DCFJ2/3A case, but shifted slightly upstream. This illustrates that, for increased distance between jets, the jet expansion tends to be bigger.

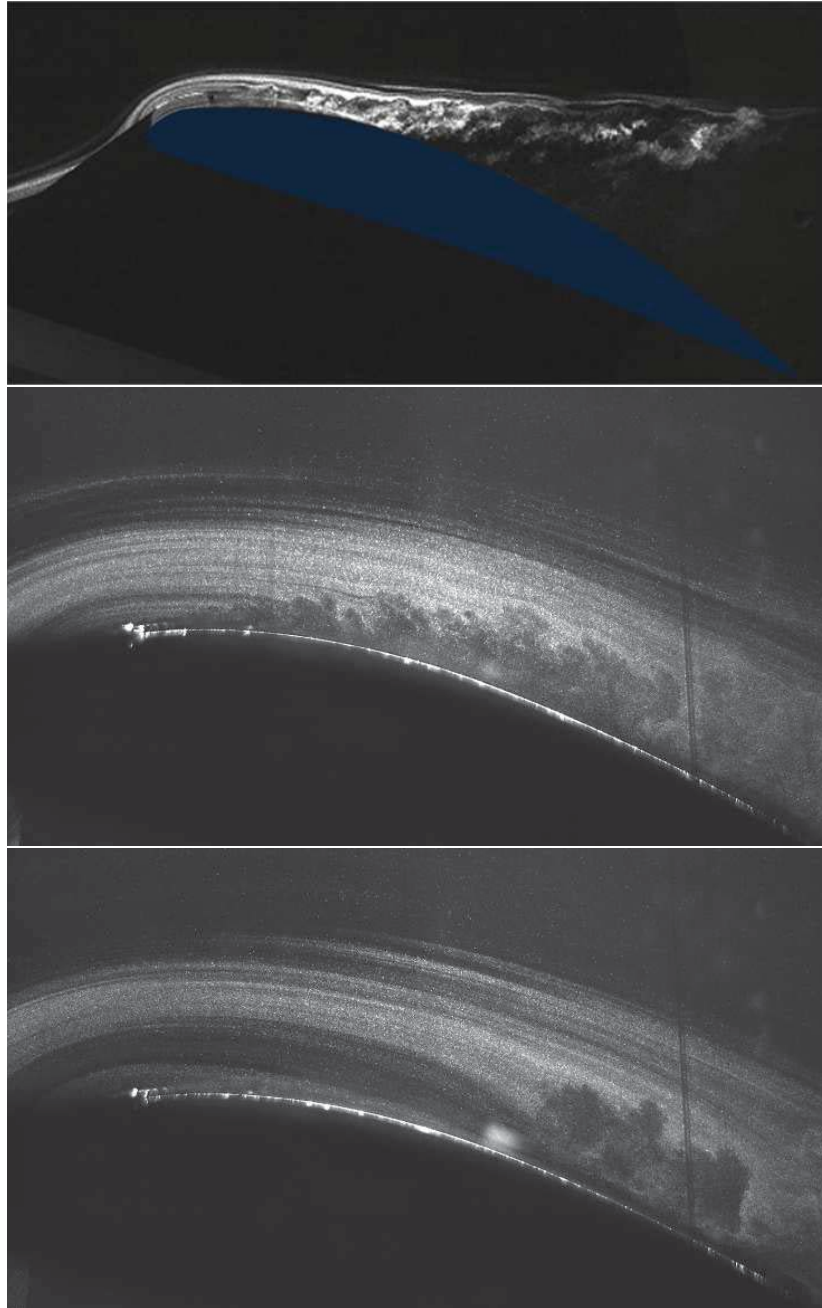


Figure 6.3: DCFJ airfoil flow visualization in the position DCFJ2/3A and  $\text{AoA}=15^\circ$ . The frame is positioned in the mid plane of a tab. The flow is observed for  $\dot{m} = 0.000\text{kg/s}$  (top) and  $\dot{m} = 0.090\text{kg/s}$  at two different time (middle and bottom).

### 6.3 Particle Image Velocimetry

The PIV analysis was done in two phases: first, the 2D velocity field at the centerline of a discrete jet and at the centerline of a tab was acquired for various AoA and various mass

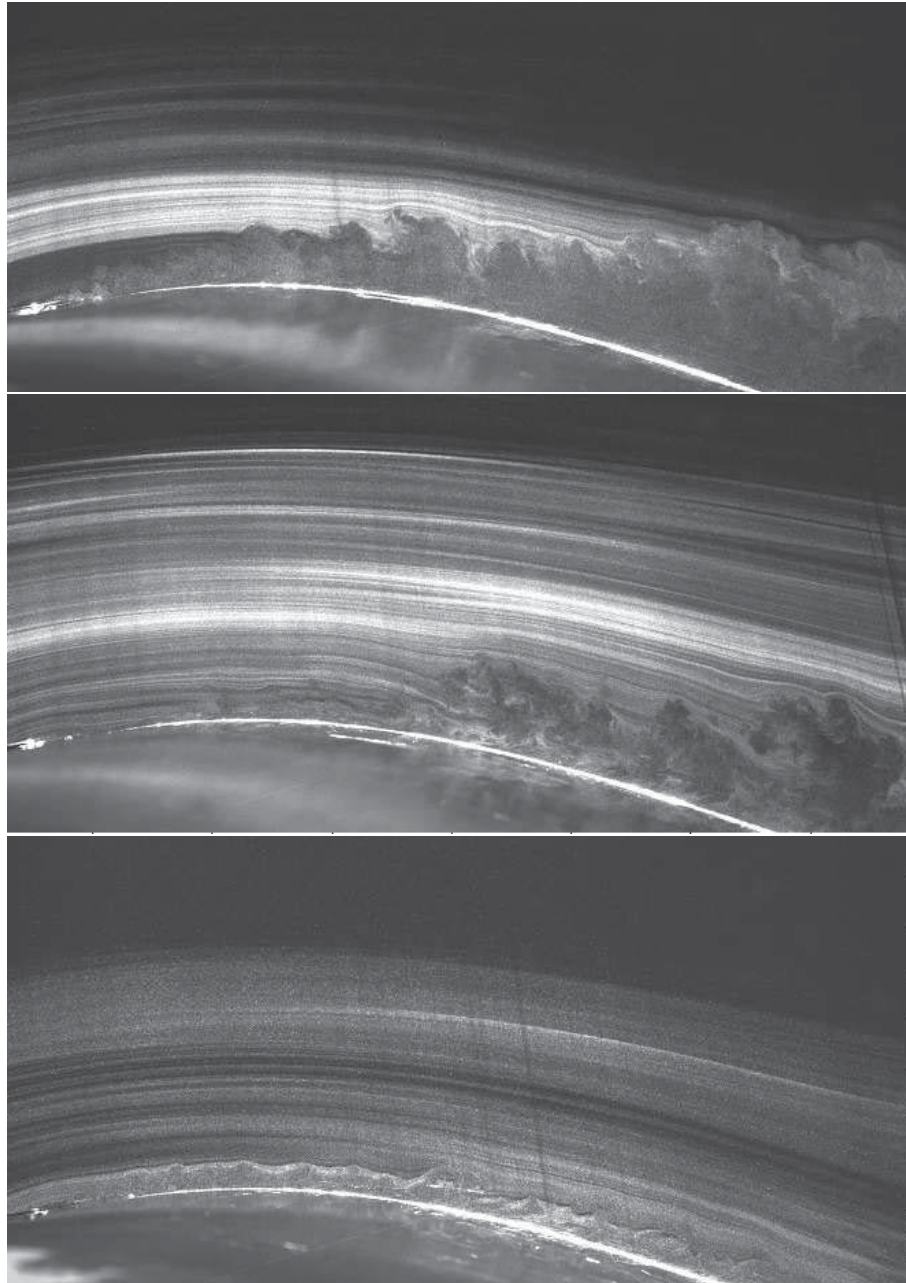


Figure 6.4: Flow visualization at various spanwise locations for DCFJ2/3B at  $AoA=0^\circ$  and  $m = 0.030$  for the centerline of a discrete jet (top), the edge of a tab (middle) and the centerline of a tab (bottom).

flow rates. Phases 2 consisted in acquiring a stereo-PIV of an entire volume of flow from the centerline of a tab to the next tab centerline and visualize the average 3D flow field, with special attention to the spanwise flow pattern.

Sample results from phase 1 are shown in Fig. 6.5 for a free stream velocity of 10m/s. The top frames show the average velocity fields for DCFJ 2/3A at  $\text{AoA}=15^\circ$  and the bottom frames show the DCFJ 3/4A at  $\text{AoA}=25^\circ$ . The mass flow is  $\dot{m} = 0.090\text{kg/s}$  for both frames. The overall velocity in the vicinity of the airfoil LE is much greater than the free stream velocity. Increasing the obstruction increases the velocity magnitude further. No disparity in velocity magnitude is detected in the LE area, showing that adjacent discrete jets are efficiently accelerating the air uniformly over the entire LE. In the tab centerline view, we can see that the velocity decreases slightly past the tab, but increases downstream as the jet spreads spanwise.

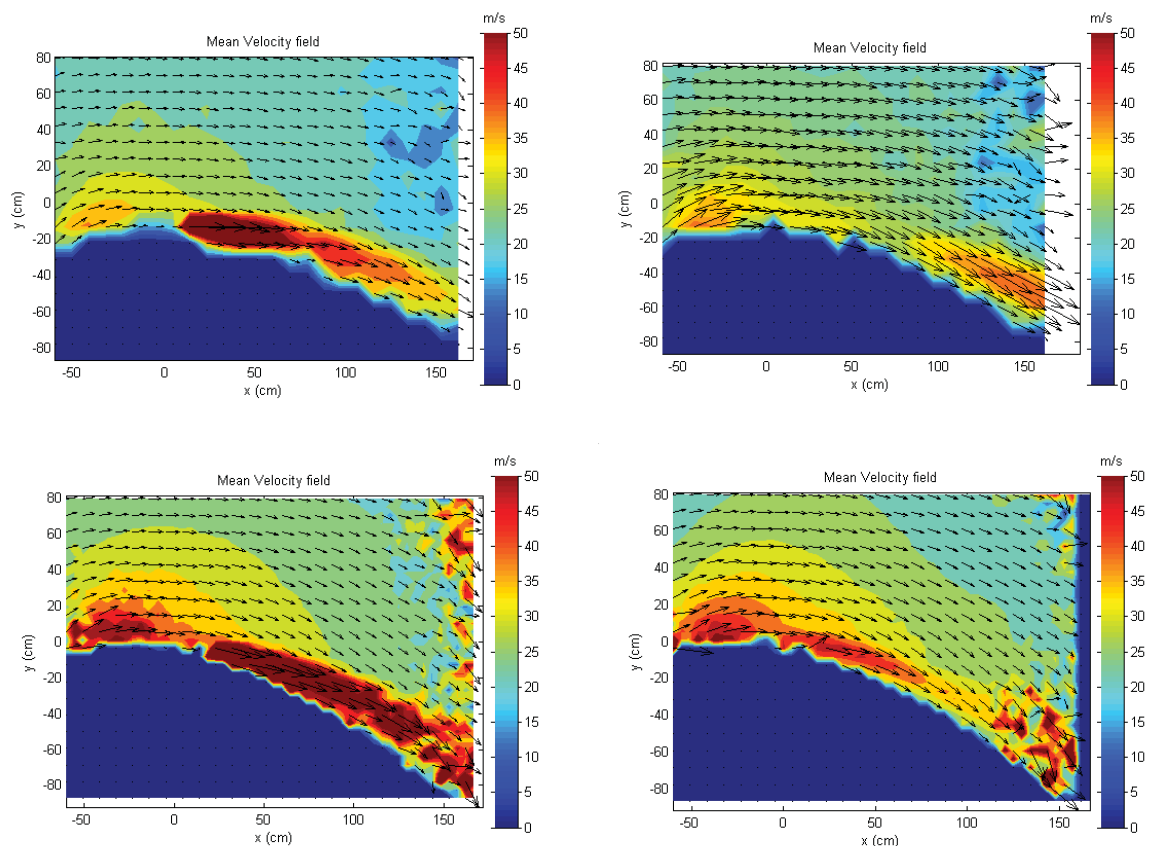


Figure 6.5: Average velocity plotted along a discrete jet (left) and over a tab (right) for a DCFJ 2/3A, at  $\text{AoA}=15^\circ$  (top) and a DCFJ 3/4A, at  $\text{AoA}=25^\circ$  (bottom). The mass flow is fixed at  $\dot{m} = 0.090\text{kg/s}$  for all cases.

Fig. 6.6 shows the 2D velocity field corresponding to the flow visualization shown in Fig. 6.4 over the centerline of a tab, at the edge of the tab-jet and over the centerline of a jet. The flow in the plane of the tab-jet separation shows a large jet incursion and acceleration further downstream. The jet plane clearly shows the jet developing and expanding away from the airfoil surface. This suggests that the jet flow could be sensitive to separation further downstream but, Dano et al. [59] showed that, as long as the jet reaches the vicinity of the suction area, the DCFJ flow is practically impervious to separation. Investigations of the streamline alignment with the airfoil profile, as shown in Fig. 6.7, show that the jet flow is slightly separated from the surface while the tab flow is pulled down toward the surface. These results suggest that the flow in the tab plane is resisting flow separation and highlight the high streamwise vorticity of the flow.

An entire volume of flow from the centerline of a tab to the next tab centerline is acquired using stereo-PIV and processed with Matlab<sup>TM</sup>. The velocity iso-surfaces for DCFJ 2/3B with AoA=0° and  $\dot{m} = 0.030$  are shown in Fig. 6.8 for the LES simulation and the experiment. The  $V=15.5$  m/s iso-surface appears fairly uniform over the LE, confirming the findings in Fig. 6.6. Conversely, the jet flow does not appear to be symmetric, with a larger bulge on the right hand side of the jet. The  $V=18.0$  m/s iso-surface is not observed in the vicinity of the LE, effectively visualizing the 3D jet volume flowing along the airfoil. As in Fig. 6.8, the asymmetry is easily noticeable. The LES simulation plots show very similar flow structures, including the asymmetry of the jet.

The  $\omega_Z$  vorticity component is plotted Fig. 6.9. Positive  $\omega_Z$  (in blue) is found above the jet centerline and appears limited to the jet envelope. Negative  $\omega_Z$  (in red) is found

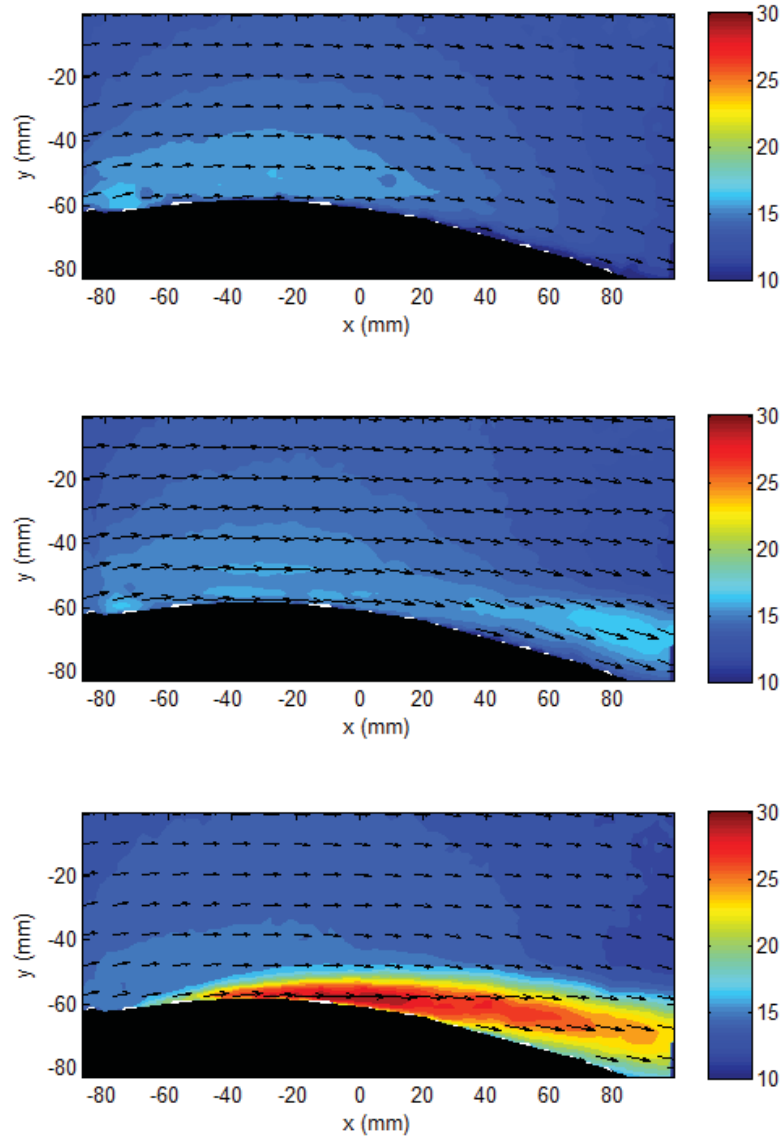


Figure 6.6: Average velocity field over a tab (top) and tab/jet edge (middle) and over a jet (bottom). The airfoil is in a DCFJ 2/3B configuration with  $\text{AoA}=0^\circ$  and  $\dot{m} = 0.030$ .

underlying the jet core, but also along the surface downstream of the tabs and rapidly fades as the spanwise distance from the jet core increases.

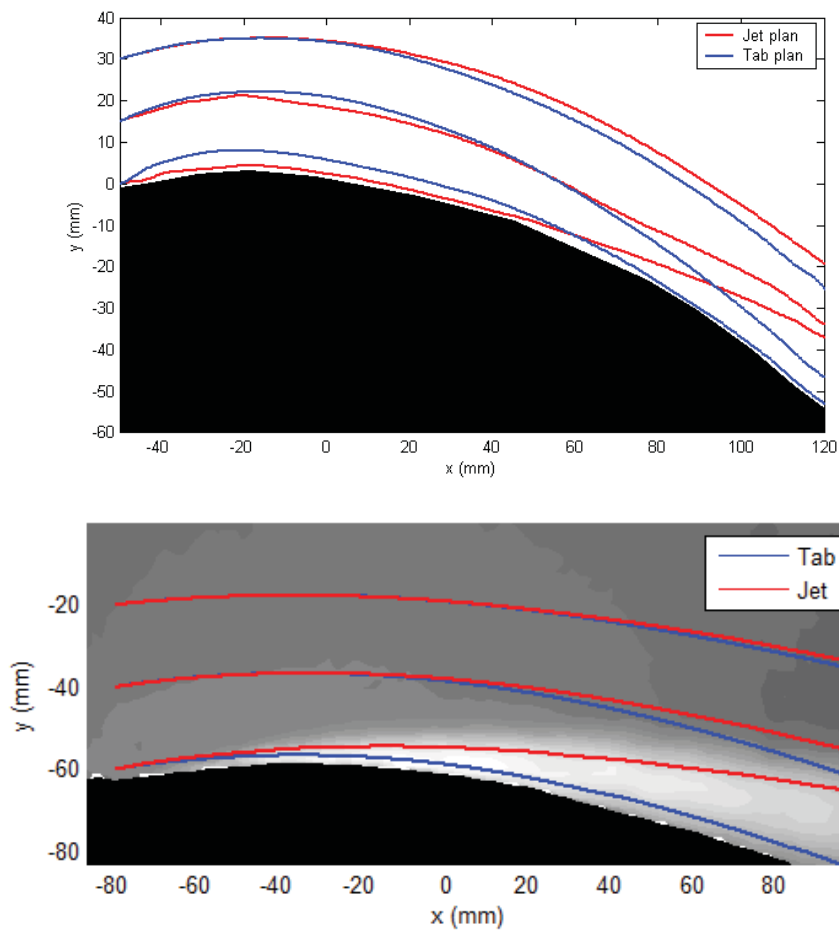


Figure 6.7: Comparison of streamlines between jet and tab flow (top) DCFJ 3/4A with  $\text{AoA}=25^\circ$  and  $\dot{m} = 0.090$ , (bottom) DCFJ 2/3B with  $\text{AoA}=0^\circ$  and  $\dot{m} = 0.030$ .

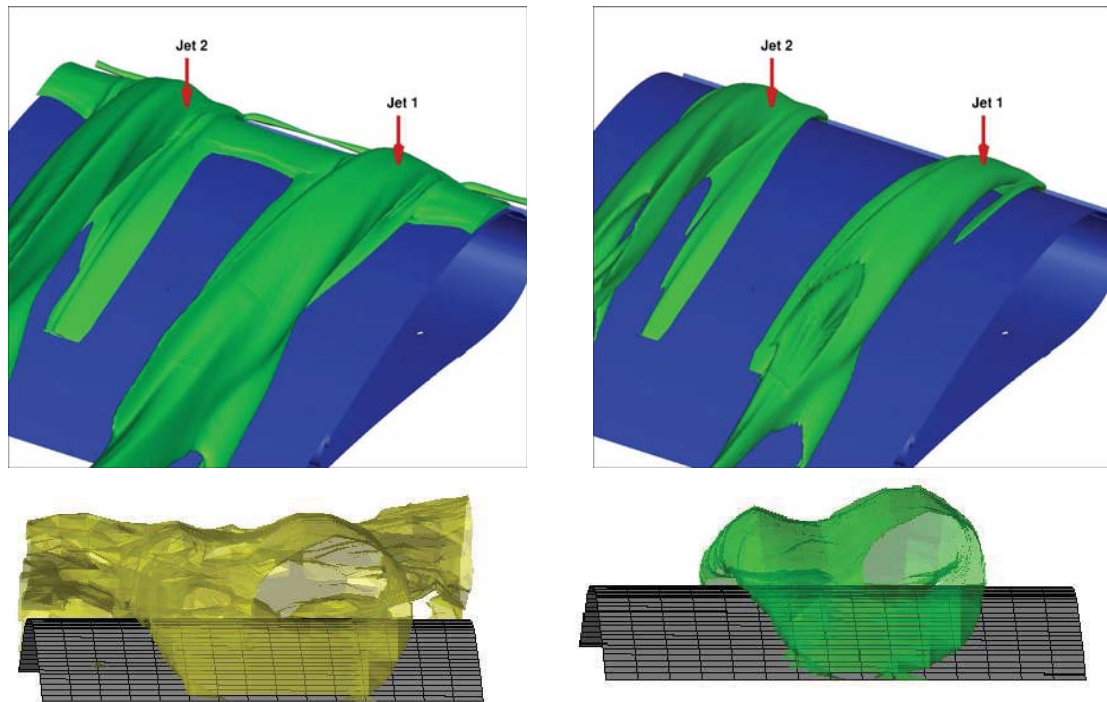


Figure 6.8: Velocity iso-surface at 15m/s (top) and 18.5m/s (bot) for the DCFJ 2/3B at  $AoA = 0^\circ$  and  $\dot{m} = 0.030$ , comparison between simulation (top) and experiment (bottom).

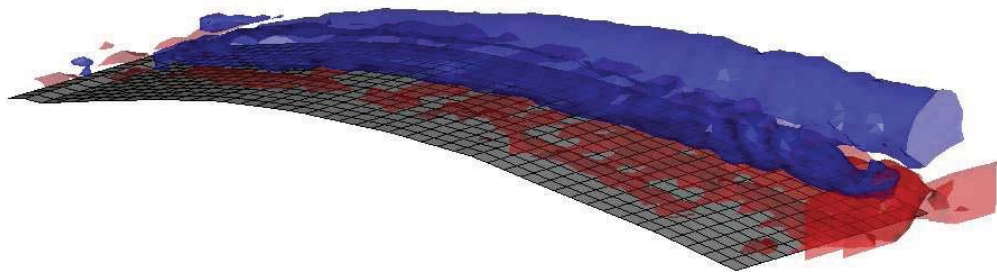


Figure 6.9: Vorticity iso-surface  $\omega_Z$  for DCFJ 2/3B with  $AoA=0^\circ$  and  $\dot{m} = 0.030$ . Iso-surface value:  $\omega_Z = \pm 0.15s^{-1}$  (blue= counter-clockwise rotation, red= clockwise rotation).

## Chapter 7

# Numerical Investigation of Stationary CFJ Airfoils

This chapter investigates the CFJ energy expenditure and performance enhancement for a variety of stationary CFJ airfoils at subsonic and transonic speed [61, 63, 64].

The first section presents the CFJ airfoil energy expenditure and performance enhancement with the Mach number ranging from low to high subsonic  $0.03 \leq M \leq 0.4$  [61]. The purpose is to expand the CFJ airfoil application to a wider Mach number range, where the compressibility effect plays an important role. In particular, there is no study for CFJ airfoils with free stream Mach number up to 0.4. Such Mach number may generate a transonic flow field with shock-boundary layer interaction, which could in turn reduce the effectiveness of a flow control. Therefore, studying the CFJ airfoil aerodynamic performance within this Mach number range is crucial to determine if it is suitable for a system where a transonic flow may be induced.

The second section presents the results of a parametric study performed for a series of CFJ airfoils based on the NACA 23121 geometry [63]. The injection location, suction location, suction size, angle of attack, momentum coefficient, airfoil thickness and Reynolds number are modified and the resulting effects on the lift, drag, moment and energy consumption are recorded. The Mach number is 0.15 and the Reynolds number is  $6.4 \times 10^6$ . The purpose is to enhance the aerodynamic performance and lower the power consump-

tion. The best CFJ configuration is then compared with the best flap configuration on the same airfoil and in the same flow conditions.

The final section presents the results of a parametric study that focuses on the nose-down moment and drag reduction of CFJ airfoils [64]. The NACA 23121, NACA 34121 and NACA 6321 CFJ airfoils are modified to reduce the nose-down moment. Then the NACA23112 identified in the previous section trade study as the best candidate to achieve negative drag and high efficiency is investigated for various  $C_\mu$  and injection sizes. The simulation parameters and flow conditions are the same as in the previous section. The ultimate goal is to generate airfoils with suitable characteristics to use in the design of a low drag flying wing design. Flying wings are by definition tailless designs and hence require the use of airfoils with very slightly positive moment for stability and control. This uncommon moment characteristic was achieved by using a moderate reflex camberline with the CFJ suction slot moved upstream to further increase the moment value, accordingly to the findings of previous section.

## 7.1 Mach number effect on Performance Enhancement and Energy Expenditure

The CFJ 6415 airfoil, which is experimentally studied by Dano et al. in [59, 60, 96] at  $M = 0.03$ , is first simulated to validate the CFD solver. The Mach number is then increased to 0.3 and 0.4. The jet momentum coefficient is  $C_\mu = 0.08$  for all the Mach numbers. The AoA varies from  $0^\circ$  to  $30^\circ$  with an increment of  $5^\circ$ . The Reynolds number based on free stream velocity and chord length are listed in Table 7.1.

<i>Mach</i>	$V_\infty(m/s)$	$Re \cdot 10^5$
0.03	10.297	2.078
0.3	102.968	20.779
0.4	137.290	27.705

Table 7.1: Reynolds number variation with free stream velocity and Mach number

### 7.1.1 Mesh

The 2D mesh is constructed using the O-mesh topology in order to achieve high quality mesh around the airfoil. A total of 451 points are placed around airfoil, 301 points on suction surface, 151 points on the pressure surface and 101 points normal to the airfoil with an additional 31 points across the jet. The total mesh size is 55,500 cells, and is partitioned into 12 blocks for parallel computation. The farfield boundary is located 30 chords away from the airfoil. To resolve the turbulent boundary layer, the first grid point is placed at  $y^+ \approx 1$ . The block definition is found in Table 7.2 and the mesh topology is shown in Fig. 7.1.

Block	$\xi$ -Direction	$\eta$ -Direction	Cell number
1-9	51	101	5000
10	101	31	3000
11	151	31	4500
12	101	31	3000
Total mesh size			55500

Table 7.2: Block dimensions for the CFJ 6415 airfoil

A mesh refinement was performed at  $M=0.3$  by increasing the mesh size by 50% in every direction. The results are in excellent agreement with the baseline mesh.

### 7.1.2 CFD Validation at $M=0.03$

Fig. 7.2 shows the computed lift, drag and power coefficient compared with the experiment for the baseline airfoil and the CFJ airfoil at  $M = 0.03$ . For the lift, a good agreement is obtained up to AoA of  $20^\circ$  when the flow is mostly attached. The CFD under-predicts the stall AoA by about  $5^\circ$  for both the baseline and CFJ airfoil. The computed drag coefficient is significantly under-predicted when the AoA is greater than  $10^\circ$ . This appears to be due to the RANS turbulence model that cannot accurately predict the drag at high AoA when the flow is close to or stalled [97,98].

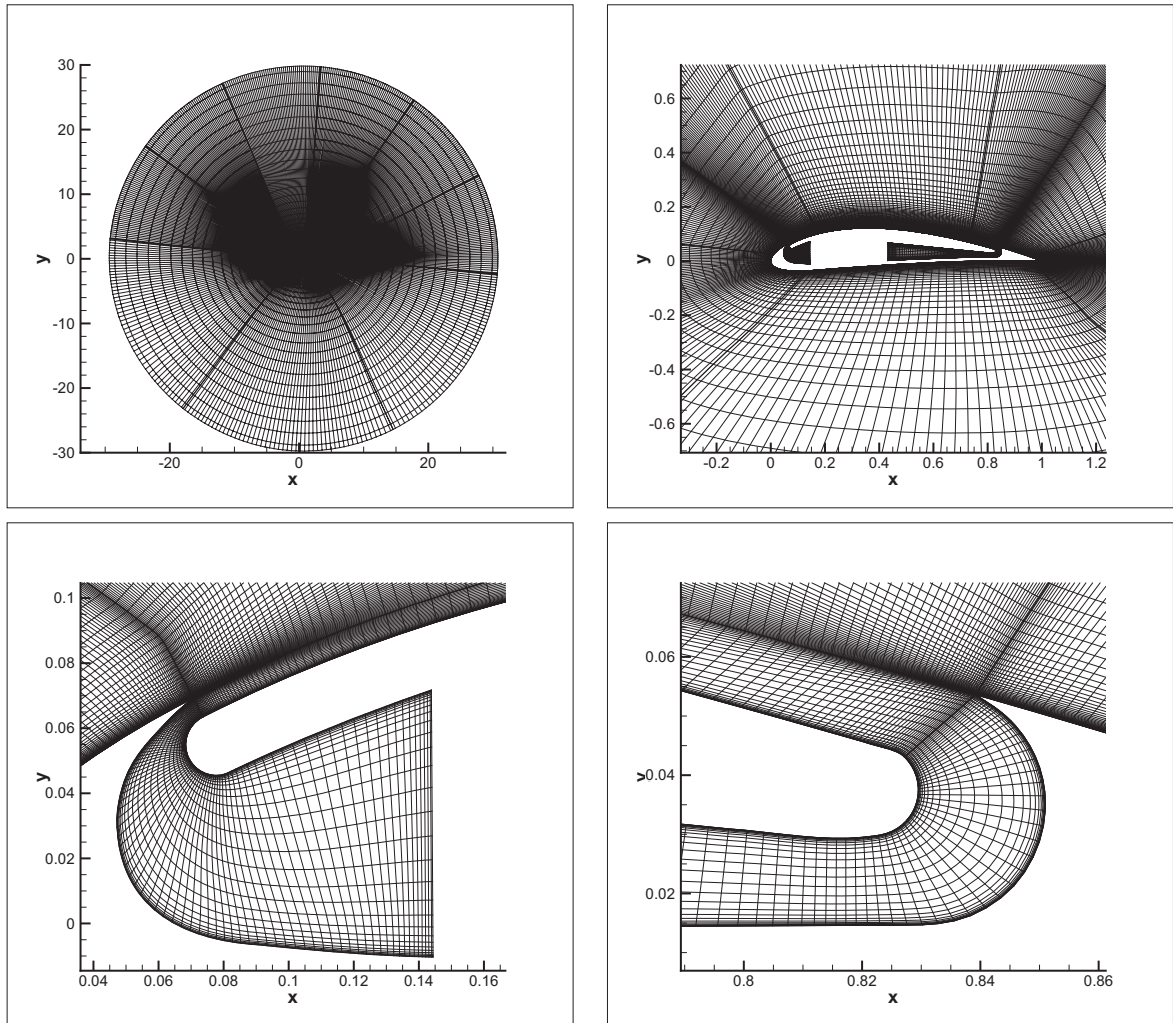


Figure 7.1: CFJ 6415 2D O-mesh topology with detailed view of the injection and suction cavities.

However, the predicted power coefficient agrees very well with the experiment as shown in Fig. 7.2. For the power coefficient plot on the right of Fig. 7.2, the left vertical axis represents the dimensionless power coefficient while the right vertical axis is the required pumping power in watt. The reason why the predicted power consumption agrees well with the experiment may be that the total pressure and total temperature are integrated parameters using mass average, and are predicted more accurately. It is observed that the power coefficient decreases with the increase of AoA up to  $15^\circ$  and rises at higher AoA. The reason is that when the AoA is increased and the flow still remains attached, the airfoil LE suction effect becomes stronger with lower static pressure in the region of the injection jet,

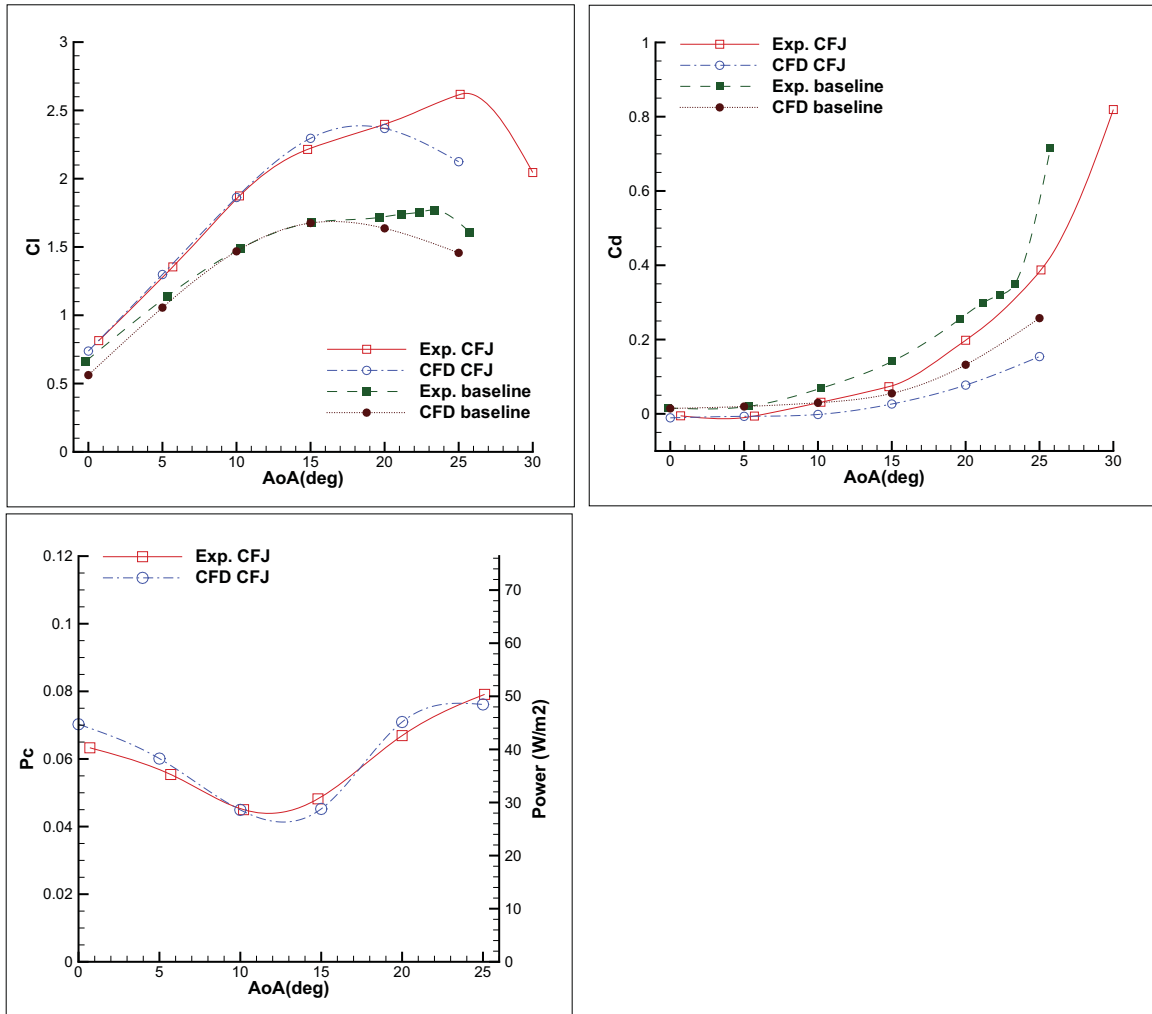


Figure 7.2: Lift, drag and power coefficient comparison between experimental data and CFD calculations at  $M=0.03$  and  $C_{\mu} = 0.08$ .

and hence less power is needed to generate the jet with the same momentum coefficient. However, when the AoA is beyond the separation value, the boundary layer separation creates very large energy loss and the suction power is significantly increased. Overall, the predicted power coefficient excellent agreement with the experiment lays the foundation for further study at higher Mach number.

### 7.1.3 Performance at High Mach Number 0.3 and 0.4

Fig. 7.3 shows the computed lift, drag and power coefficient at Mach number from 0.03 to 0.4. The baseline airfoil lift and drag have little dependency on the free stream Mach num-

ber, and is hence plotted at  $M=0.3$  only. With the Mach number increased from 0.03 to 0.4, the maximum lift coefficient of the CFJ airfoil is increased from 2.2 to 2.8 with  $C_{\mu} = 0.08$ . This is due to the compressibility effect at higher Mach number, which generates a stronger suction effect at the LE. However, at  $M=0.4$ , the airfoil stalls earlier due to the appearance of strong shock wave on the suction surface as to be shown later. The drag coefficient is also significantly increased at Mach 0.4 when the AoA is greater than  $15^{\circ}$  due to the shock wave boundary layer interaction and wave drag. The power coefficient decreases when the Mach number is increased from 0.03 to 0.3. This is due to the compressibility effect that lowers the static pressure of the main flow at the injection region which in turn reduces the pumping energy required to create the jet. At  $M=0.4$ , the power coefficient at  $\text{AoA}=0^{\circ}$  is about the same as at Mach 0.3 and is significantly lower than at Mach 0.03. However, with the AoA increased up to  $15^{\circ}$ , the power coefficient at Mach 0.4 remains fairly flat instead of decreasing as at Mach 0.3. The reason is that the flow reaches supersonic at high AoA and the energy loss is increased as well, in particular when shock waves appear as shown later. When the AoA is greater than  $15^{\circ}$ , the strong shock wave boundary layer interaction generates a large entropy increase which augment the power consumption.

The corrected aerodynamic efficiency versus  $C_L$  is plotted Fig. 7.3. The baseline airfoil is efficient at low  $C_L$  but is surpassed by the CFJ airfoil both in term of maximum lift and efficiency at high  $C_L$ . The baseline airfoil achieves its maximum efficiency at  $C_L = 1.1$ , whereas the CFJ airfoil reaches its between  $C_L = 1.8 - 2.5$ , depending on the Mach number. The CFJ airfoil provides a tremendous increase of maximum  $C_L$  with a high maximum efficiency, comparable to that of the baseline airfoil for the favorable Mach number of 0.3.

Fig. 7.3 also shows the  $1.5 \times 1.5$  refined mesh results for  $C_L$ ,  $C_D$  and  $P_c$  at Mach 0.3. They are virtually identical to the baseline mesh results and indicate that the present CFD simulations are converged based on the mesh size.

The results above are plotted as drag polars in Fig. 7.4. The left polar is the classic lift versus drag plot. The right polar however is corrected to account for the pumping power by adding the power coefficient to the drag coefficient as explained in Eq. (4.15). This plot

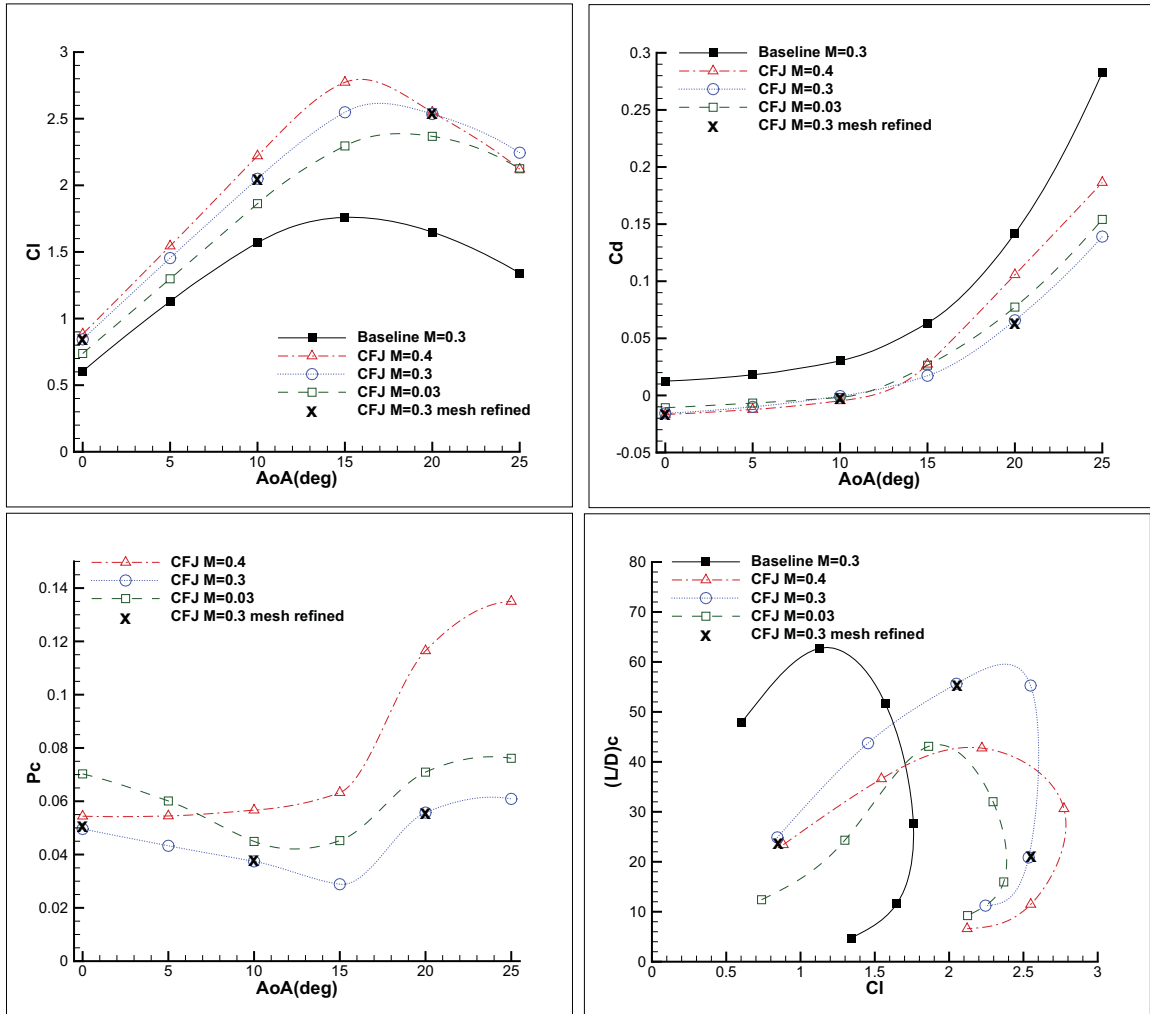


Figure 7.3: Lift, drag, power comparison and corrected aerodynamic efficiency variations from  $M=0.03$  to  $M=0.4$  and  $C_{\mu} = 0.08$ .

shows that the CFJ airfoil performs more efficiently than the baseline airfoil for  $C_L \geq 1.5$ , where the baseline airfoil is about to be stalled.

Fig. 7.5 shows the pressure coefficient on the baseline and CFJ 6415 airfoil surfaces at various AoA for a free stream Mach number of 0.03 and 0.3. The spikes on the CFJ airfoil pressure distribution are due to the injection and suction slots. The CFJ greatly increases the circulation on the suction surface due to increased flow velocity, which augments the lift. The lift augment is greater at higher AoA. The CFJ airfoil has a significantly higher suction peak near the LE than the baseline airfoil, which contributes to the lift increase and the pressure drag decrease. For the CFJ airfoil, the higher free stream Mach number

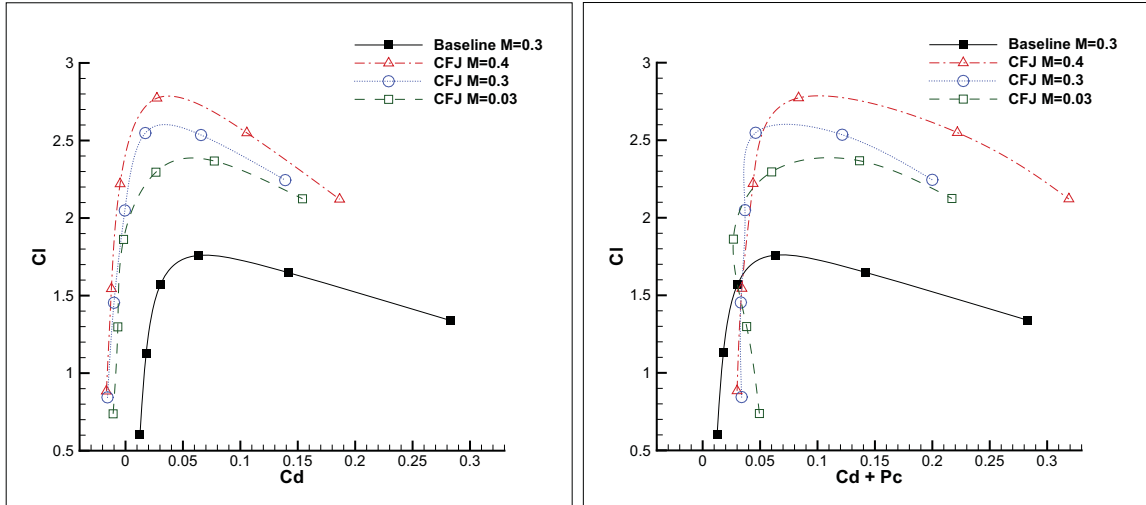


Figure 7.4: Drag polar (left) and drag polar corrected to account for the pumping power (right) at various Mach number and  $C_\mu = 0.08$ .

reduces the suction side pressure more than the baseline airfoil since the CFJ enhances the compressibility effect.

The pumping power defined by Eqs. (4.12)-(4.13) is largely determined by the total pressure ratio between the injection and suction cavities. Fig. 7.6 shows the computed total pressure variation with AoA at injection and suction locations. It indicates that the injection total pressure decreases monotonically with increasing AoA. This is because when the AoA is increased, the static pressure of the main flow at the injection region is decreased. The required injection total pressure is hence decreased accordingly to achieve the same  $C_\mu$ . When the injection total pressure is decreased, the suction total pressure needed is naturally also lower. When the AoA is greater than  $15^\circ$ , the suction total pressure decreases more rapidly due to the flow separation that creates more loss. This total pressure behavior makes the required power decrease at AoA from  $0^\circ$  to  $15^\circ$  and increase for higher AoA.

Fig. 7.7, 7.8 and 7.9 show the Mach number contours with streamlines for the CFJ 6415 airfoil at various AoA for a free stream Mach number of 0.03, 0.3 and 0.4 respectively. The CFJ enhances the suction surface acceleration very effectively. At  $AoA = 20^\circ$ , there is a mild separation near the TE for the Mach 0.03 and 0.3. The separation can be easily removed by increasing  $C_\mu$  slightly such as to 0.12 [63, 64]. In general, the flow field

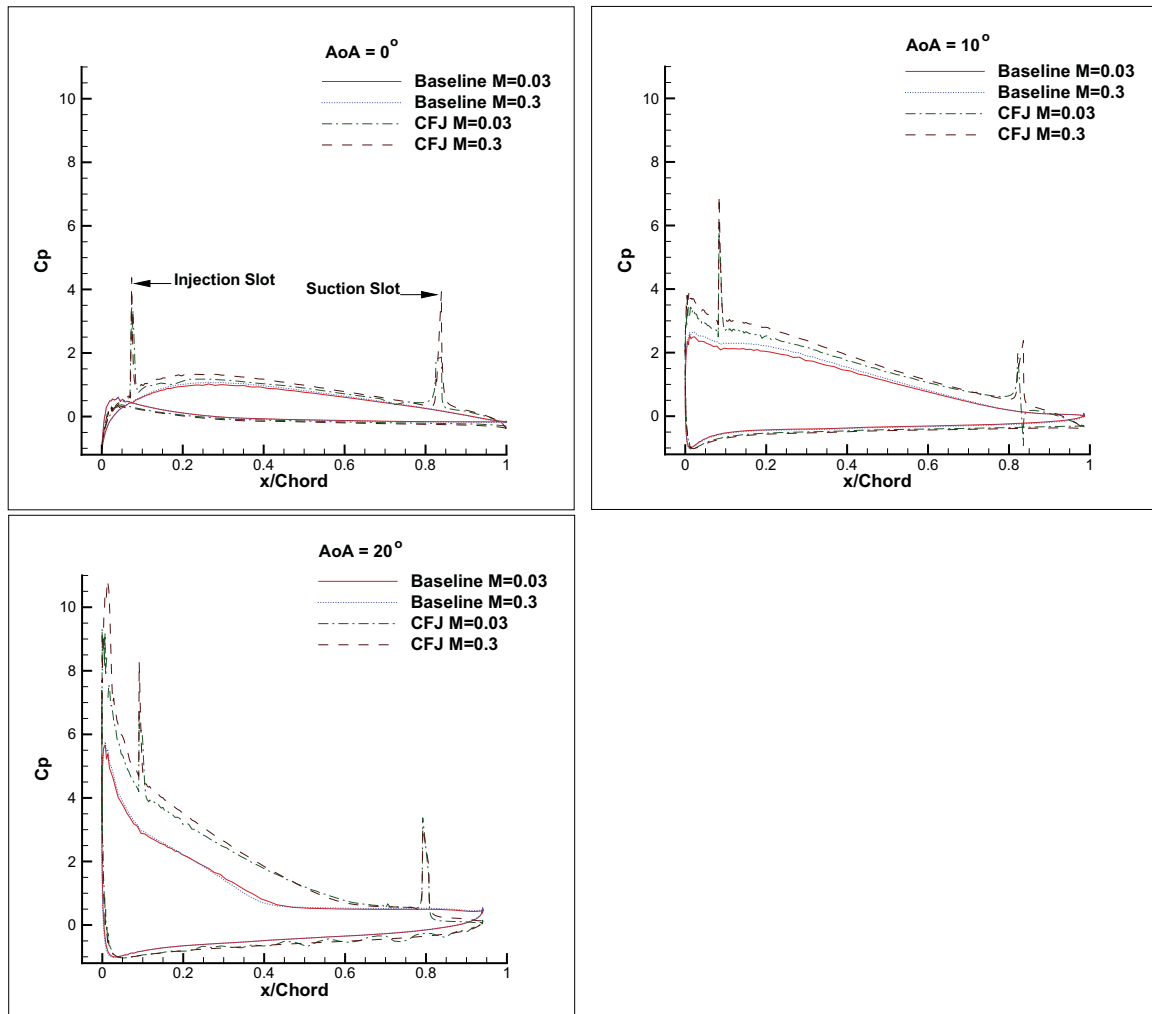


Figure 7.5: Pressure coefficient comparison between the CFJ and the baseline airfoil plotted at  $AoA$   $0^\circ$ ,  $10^\circ$  and  $20^\circ$ . The free stream Mach number varies from 0.03 to 0.3 and  $C_\mu$  is 0.08.

structures of Mach 0.03 and 0.3 are very much the same. However, when the Mach number is increased to 0.4, the flow field structure is changed with to the appearance of a shock wave at the injection jet region. The shock wave - boundary layer interaction triggers a flow separation.

Fig. 7.10, 7.11 and 7.12 show the Mach number contours at the injection jet region for a free stream Mach number of 0.03, 0.3 and 0.4 respectively. At  $M=0.03$ , the flow field with CFJ is subsonic as expected. When the Mach number is increased to 0.3, the jet exit velocity is transonic. At  $AoA = 20^\circ$ , a supersonic region appears in the leading edge region with the maximum Mach number about 1.4. Free stream Mach number of 0.3 is still very

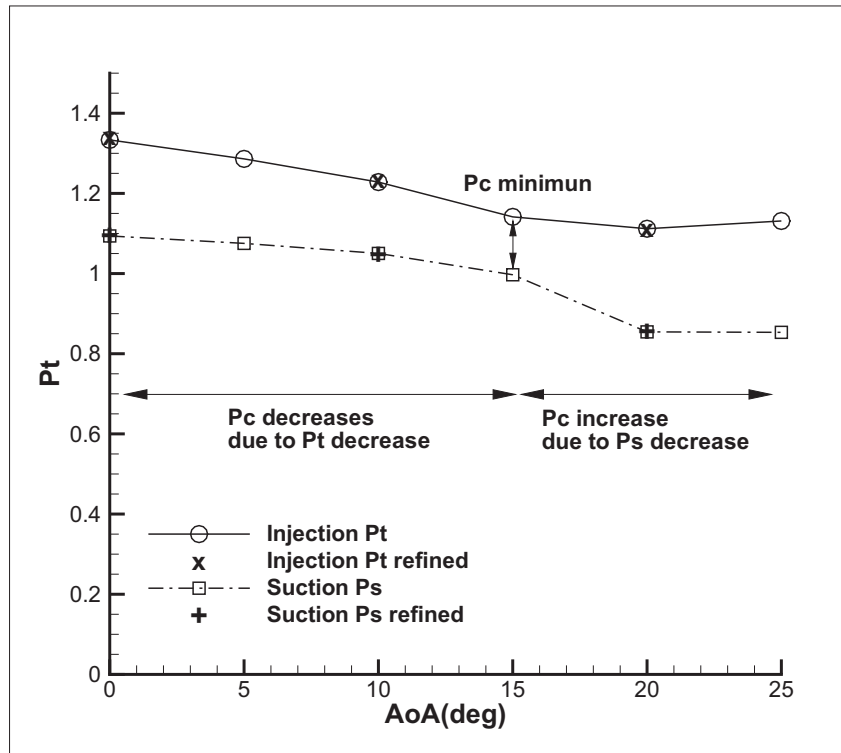


Figure 7.6: Computed total pressure inside the injection and suction cavities at  $M=0.3$  and  $C_{\mu} = 0.08$ .

favorable for lift increase and drag reduction at low power expenditure since the relatively weak shocks are still in the near isentropic region. When the Mach number reaches 0.4, the flow field structure is very different, characterized by supersonic flow and shock waves in the injection region as shown in Fig. 7.12. At  $AoA = 0^\circ$ , the injection jet already reaches Mach 1.5. At  $AoA = 10^\circ$ , the injection jet speed is further increased due to the decreased main flow static pressure at injection region, and a weak shock forms downstream of the injection slot. However the jet remains uninterrupted. At  $AoA = 20^\circ$ , the injection jet Mach number reaches 2.2. A strong  $\lambda$  shock appears in the injection region. The rear leg of the  $\lambda$  shock has greater strength, interrupts the jet, and causes significant flow separation, thus increasing the drag and power coefficient and reducing the stall AoA as shown in Fig. 7.3.

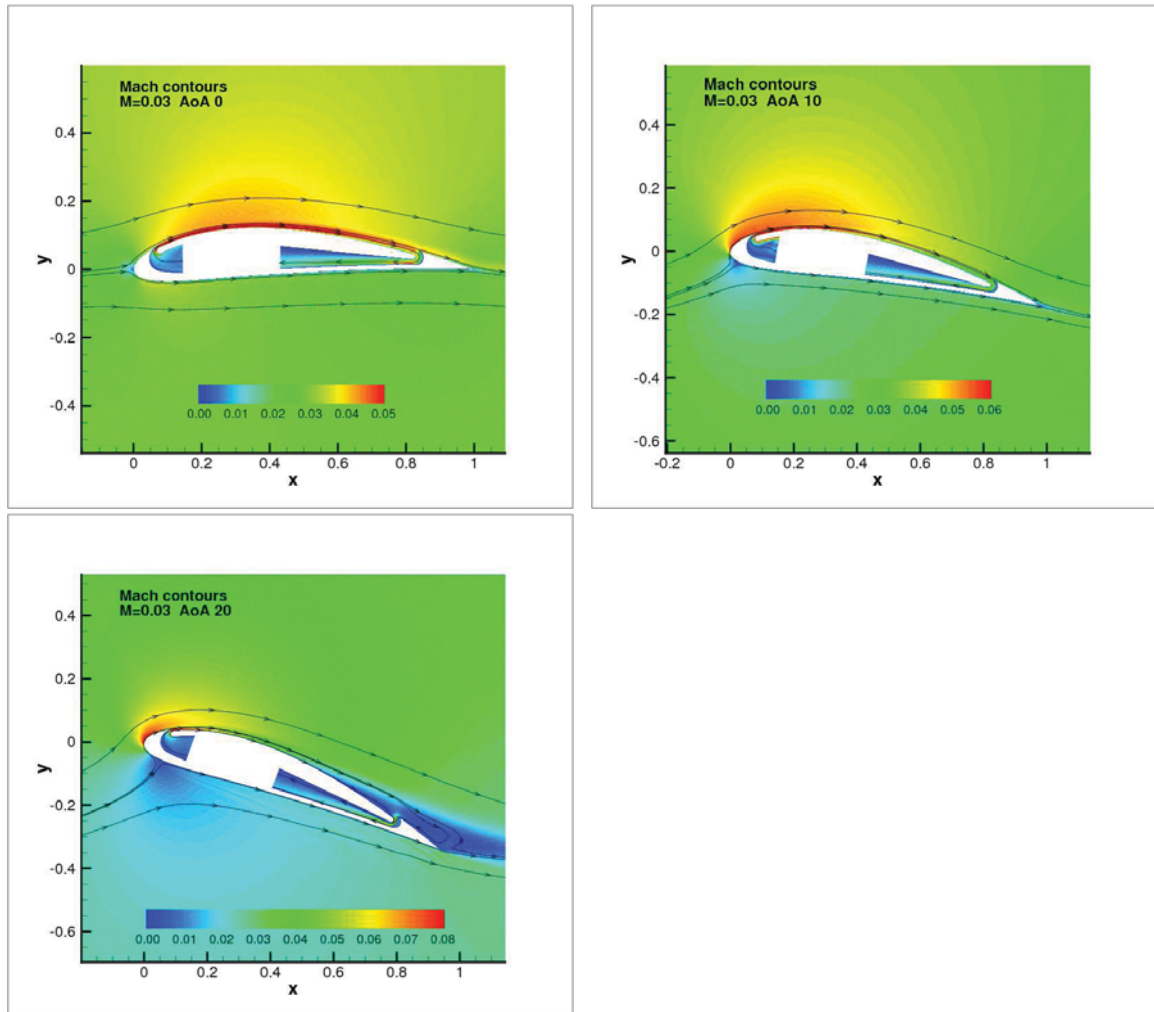


Figure 7.7: CFJ 6415 airfoil Mach contours plotted at AoA  $0^\circ$ ,  $10^\circ$  and  $20^\circ$ . The free stream Mach number is 0.03 and  $C_{\mu}$  is 0.08.

## 7.2 CFJ Airfoil Trade Study Part I : Energy Consumption and Aerodynamic Efficiency

### 7.2.1 Mesh

The NACA 23121 CFJ airfoil grid (Fig. 7.13) is constructed using the O-mesh topology in order to achieve high quality around the airfoil. The mesh uses a total of 330 points around airfoil with 210 points on the suction surface and 120 points on the pressure surface, 180 points in the direction normal to the airfoil with an additional 60 points across the jet. The total mesh size is 75,600 cells and the mesh is split into 14 blocks for the parallel

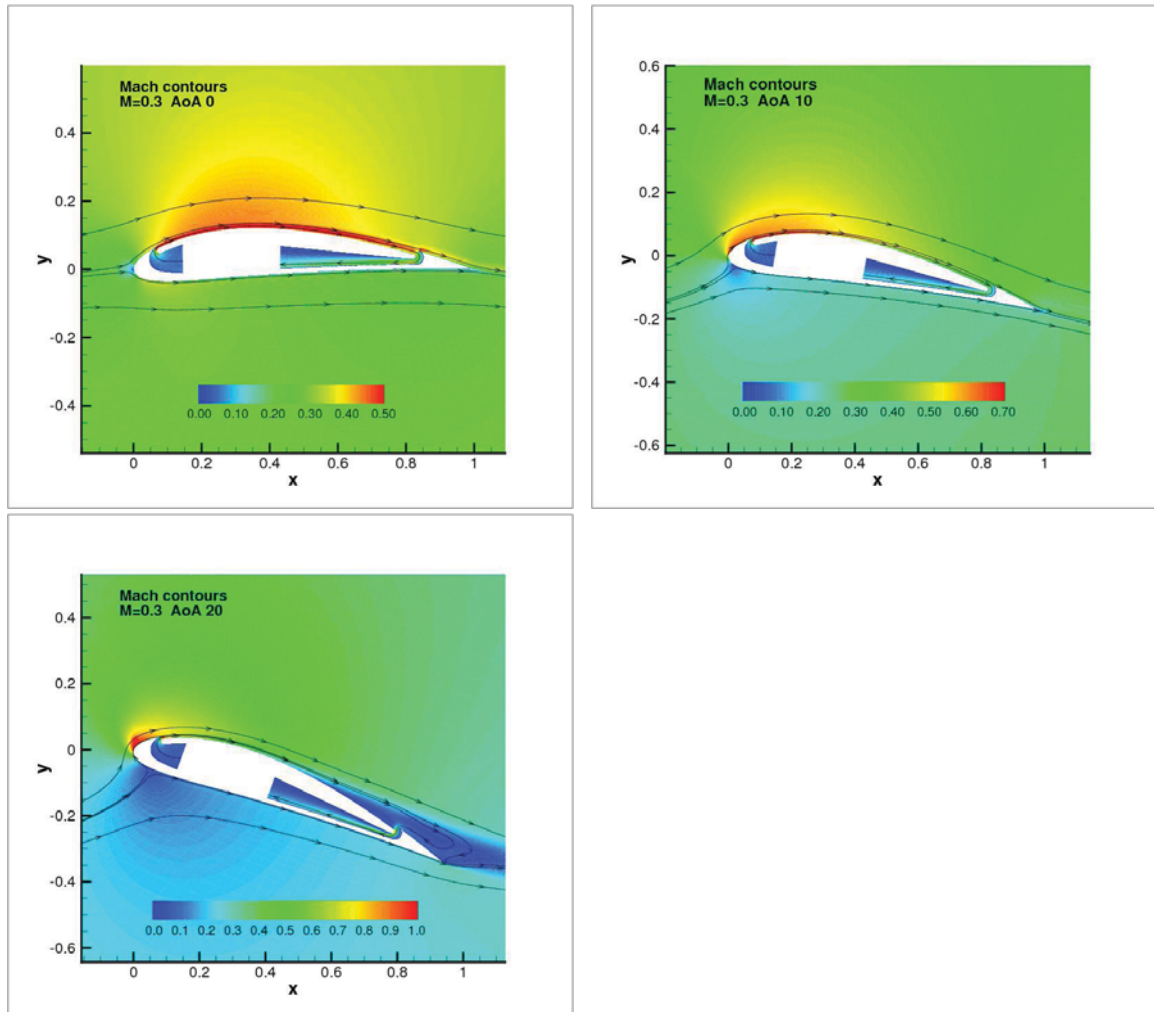


Figure 7.8: CFJ 6415 airfoil Mach contours plotted at AoA  $0^\circ$ ,  $10^\circ$  and  $20^\circ$ . The free stream Mach number is 0.3 and  $C_{\mu}$  is 0.08.

computation. The farfield boundary is located 30 chords away from the airfoil. The first grid point is placed at  $y^+ \approx 1$  to resolve the turbulent boundary layer.

The NACA 23121 baseline airfoil grid (Fig. 7.14) is constructed using the same strategy. The total baseline airfoil mesh size is 48,600 cells with 270 points around the airfoil and 180 points normal to the airfoil. The baseline airfoil mesh is split into 9 blocks for parallel computing.

For both baseline airfoil and CFJ airfoil, a refined O-mesh grid is constructed using 50% more points in every direction and  $y^+ \approx 0.7$ . The refined mesh results are within 1%

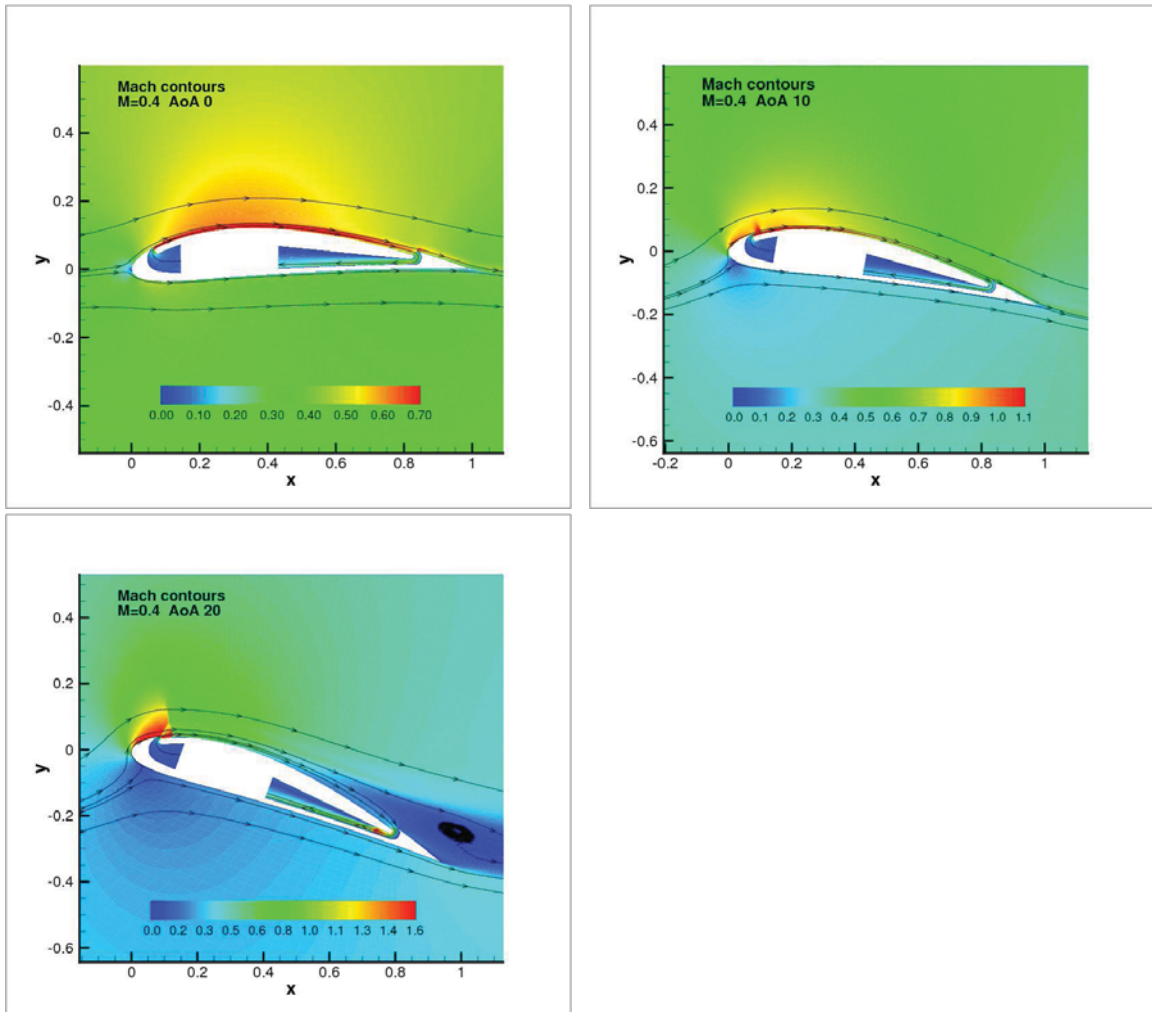


Figure 7.9: CFJ 6415 airfoil Mach contours plotted at AoA  $0^\circ$ ,  $10^\circ$  and  $20^\circ$ . The free stream Mach number is 0.04 and  $C_{\mu}$  is 0.08.

of the the original mesh predictions for the lift and power consumption and within 3% for the drag and the moment.

Additionally, a C-mesh (Fig. 7.15 is constructed for the baseline airfoil using 150 points around the airfoil and 180 points normal to the airfoil. The total mesh size is 99,000 cells and is split into 11 blocks for parallel computing.

## 7.2.2 Baseline Airfoil

The baseline airfoil Mach contours are displayed in Fig. 7.16 for various AoA. The flow acceleration on the suction surface reaches the peak Mach number of 0.35 at  $AoA = 17^\circ$ ,

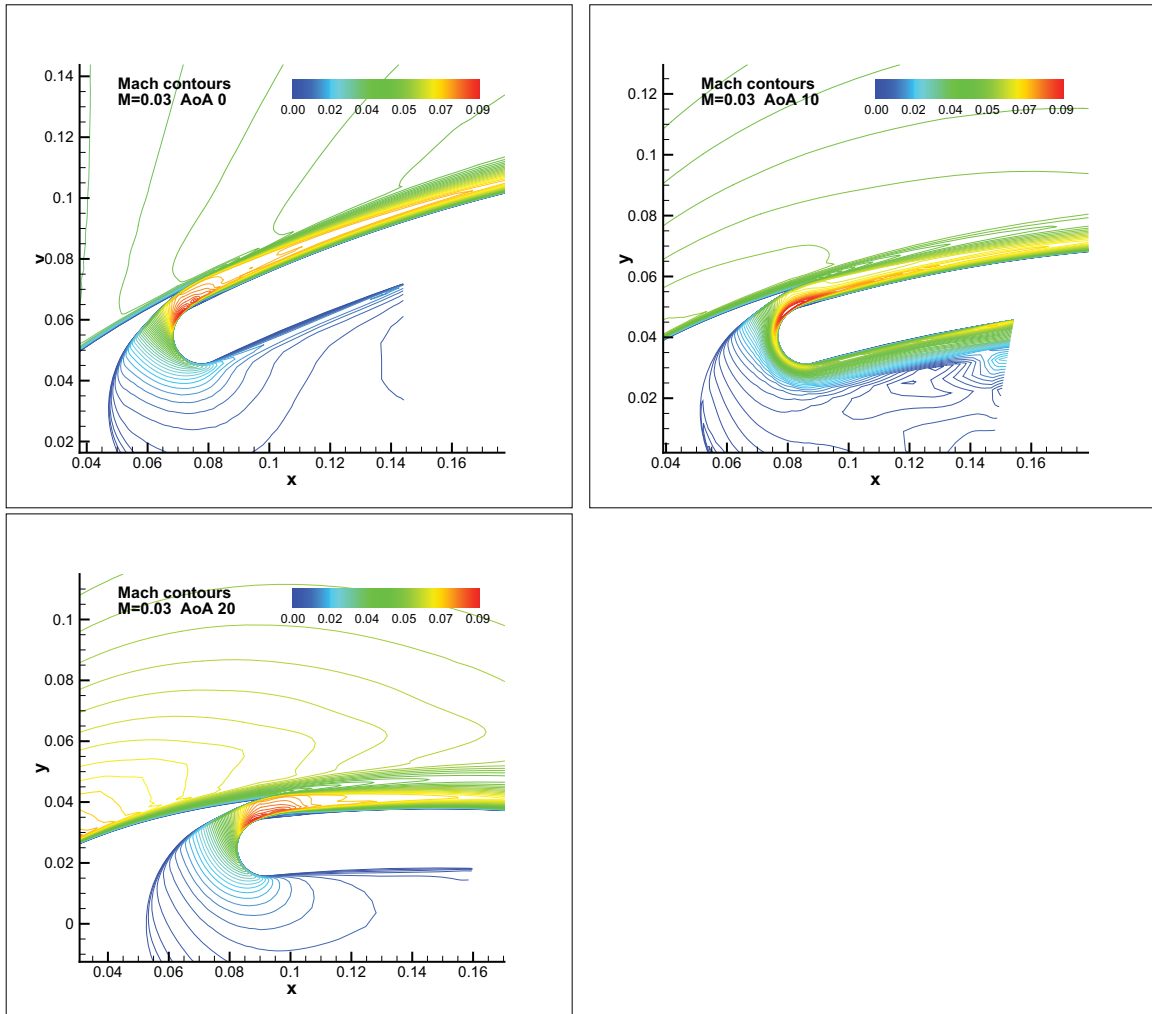


Figure 7.10: Mach number line contours within the injection region plotted at AoA  $0^\circ$ ,  $10^\circ$  and  $20^\circ$ . The free stream Mach number is 0.03 and  $C_\mu$  is 0.08.

which is slightly greater than the stall AoA and a separation region appears at the TE of the airfoil.

The NACA 23121 experimental data are extracted from [99]. The numerically obtained forces and moment compared with experimental data are plotted in Fig. 7.17. The lift prediction is in very good agreement with the experimental data. The experiment has a sharper stall than the CFD. The drag and moment are in good agreement with the experimental results at low AoA. At high AoA, the simulation predicts a significantly higher drag than the experiment. However the experimental value of the drag appears to be very small, especially compared to the similar experiments of T. A. Harris in [19]. The simulation predicts

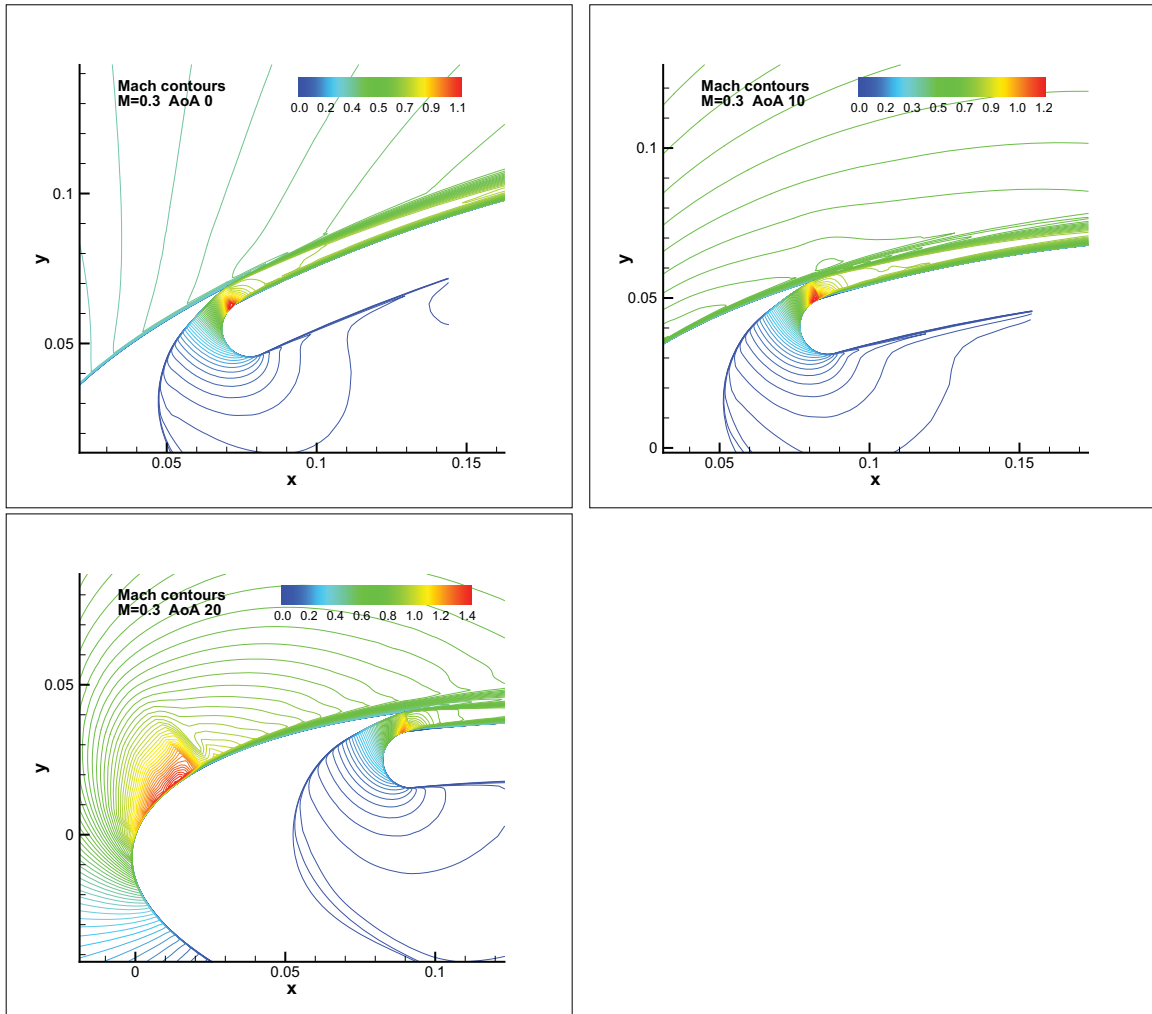


Figure 7.11: Mach number line contours within the injection region plotted at AoA  $0^\circ$ ,  $10^\circ$  and  $20^\circ$ . The free stream Mach number is 0.3 and  $C_{\mu}$  is 0.08.

a large moment increases for  $AoA > 12^\circ$  because of the development of the TE recirculation. The C-mesh with twice larger grid size and different mesh topology generates almost identical results as the O-mesh. It indicates that the simulation is converged based on the mesh size and topology.

### 7.2.3 CFJ Airfoil Trade Study

As aforementioned, injection size, AoA and  $C_{\mu}$  are fixed to 0.75% chord,  $10^\circ$  and 0.16 respectively for this trade study.

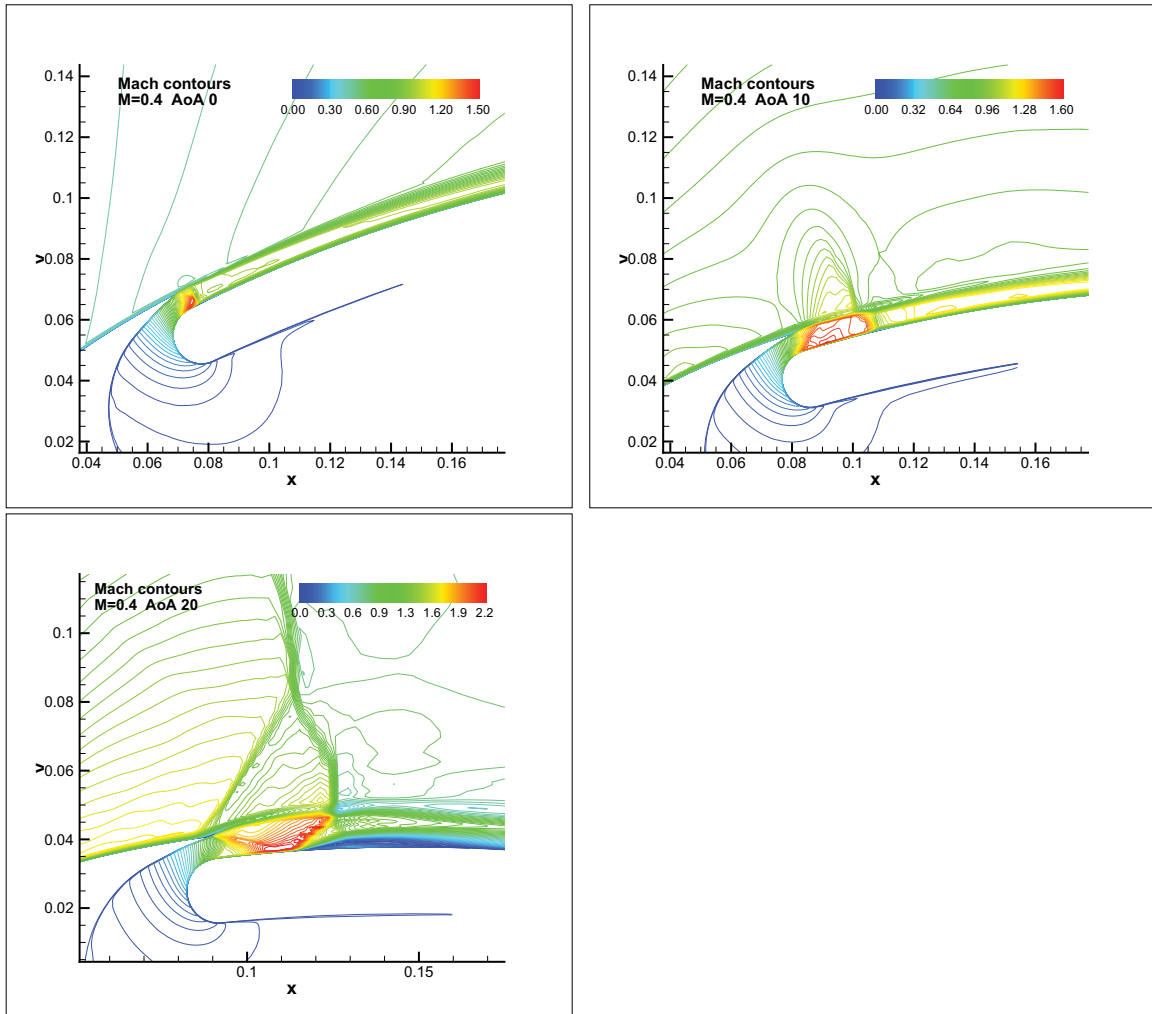


Figure 7.12: Mach number line contours within the injection region plotted at AoA  $0^\circ$ ,  $10^\circ$  and  $20^\circ$ . The free stream Mach number is 0.4 and  $C_{\mu}$  is 0.08.

### 7.2.3.1 Injection Location

The injection location shown in Fig. 7.18 is varied from a 4% chord-wise location to a 7% chord-wise location from leading edge by increments of 1%. The injection is tangential to the local airfoil surface.

Fig. 7.19 shows the variation of the forces, moment and power consumption with the jet exit location. Based on the injection jet force described by Eqs.(4.3) and (4.4), if the injection slope is negative with respect to the horizontal, the jet will have a positive lift contribution. If the slope is positive, it will have a negative lift contribution. The slopes of the jet locations studied are all positive as shown in Fig. 7.18. Hence all the injection

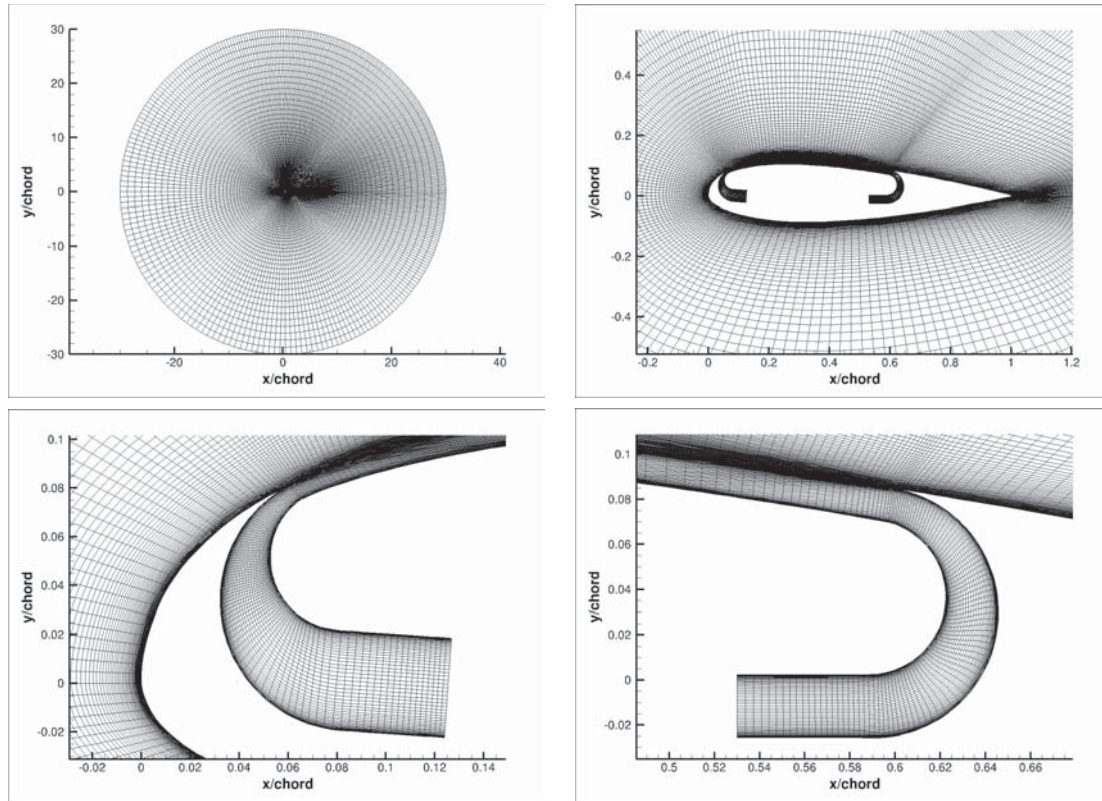


Figure 7.13: NACA 23121 CFJ airfoil O-mesh topology.

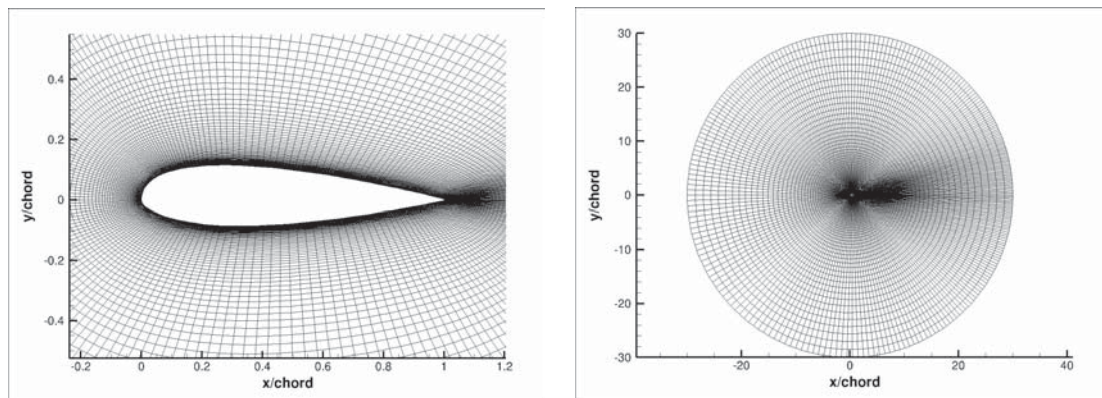


Figure 7.14: NACA 23121 baseline airfoil O-mesh topology.

jets have a negative lift contribution. However, since the circulation is increased, the lift remains about constant as shown in Fig. 7.19. Fig. 7.19 also shows that a more downstream injection location increases the thrust because the injection slope is closer to zero and the injection momentum is more in the stream-wise direction. However the power consumption is slightly increased when the injection slot is moved downstream. This results from the higher local main flow pressure, which requires a higher pump total pressure to

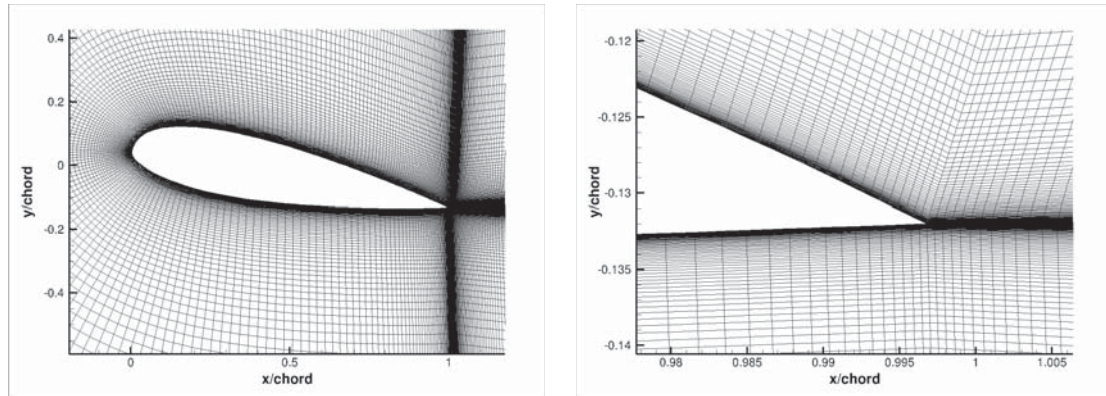


Figure 7.15: NACA 23121 baseline airfoil C-mesh topology.

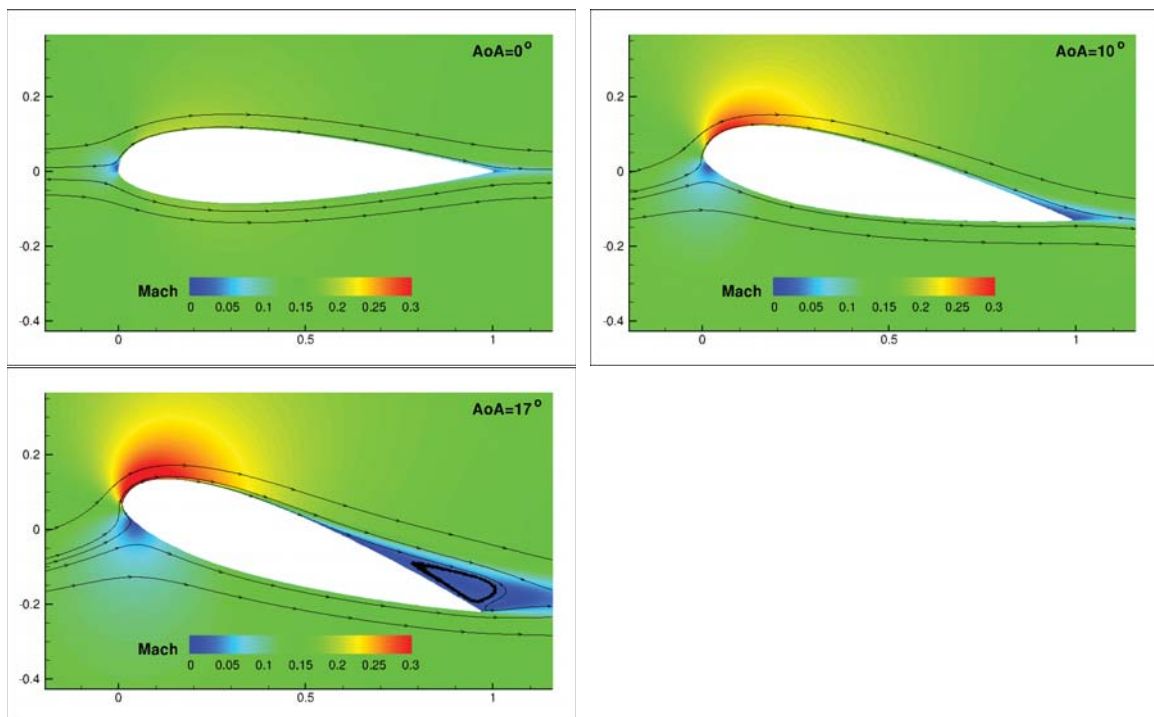


Figure 7.16: NACA 23121 baseline Mach contours at different AoA.

overcome. Overall the  $C_D$  reduction is balanced by the increase of power consumption and the corrected aerodynamic efficiency has little variation.

The moment remains largely unaffected over the range of injection locations tested because both the jet reactionary forces and leverage distances have only small variations. The 6% chord-wise injection location is used for the rest of the trade study because of its slightly higher efficiency.

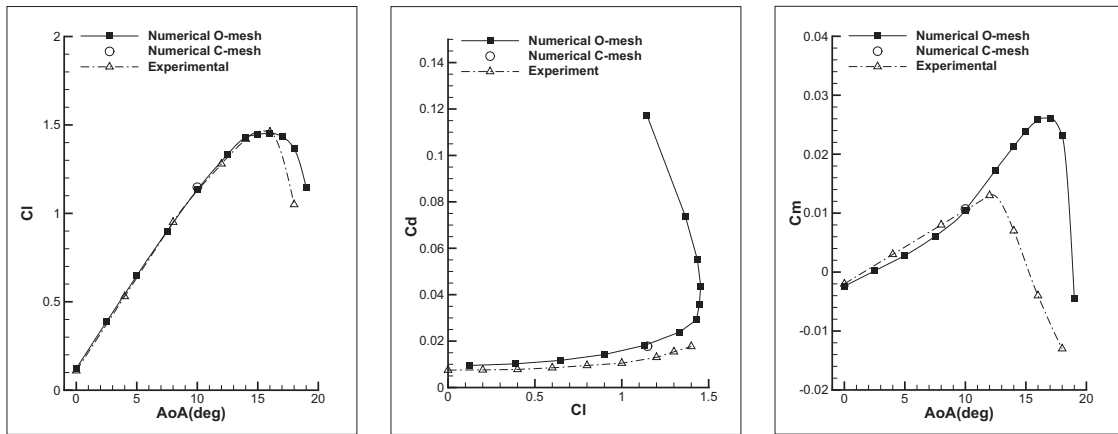


Figure 7.17: Numerically obtained forces and moment compared with experimental data for the NACA 23121 geometry.

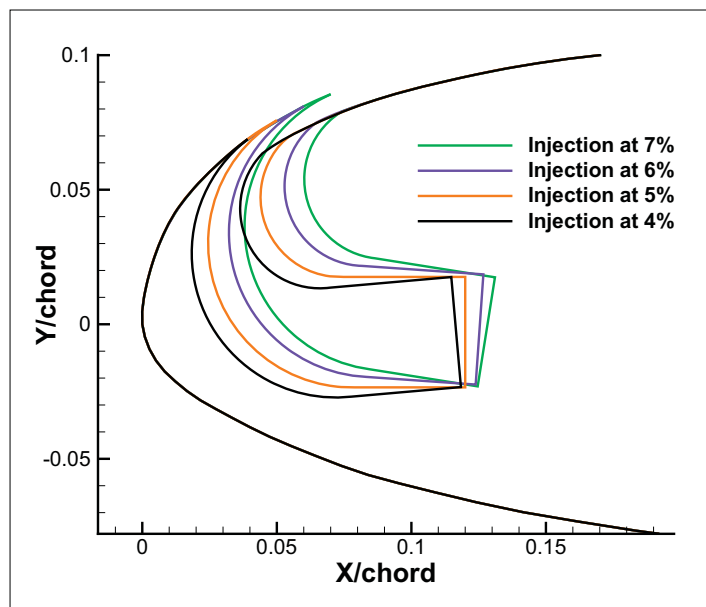


Figure 7.18: Geometries with variable jet exit location.

### 7.2.3.2 Suction Slot Size

The suction slot size shown in Fig. 7.20 is varied from 1.05% chord to 1.5% chord by increments of 0.15%.

As the suction slot size is increased (Fig. 7.21), the suction pressure increases as well to keep the suction mass flow constant. Both the increase of size and pressure increase the overall pressure forces on the suction slot and reduces the overall nose-down moment. Those forces are balanced by the changes in pressure repartition over the airfoil and the

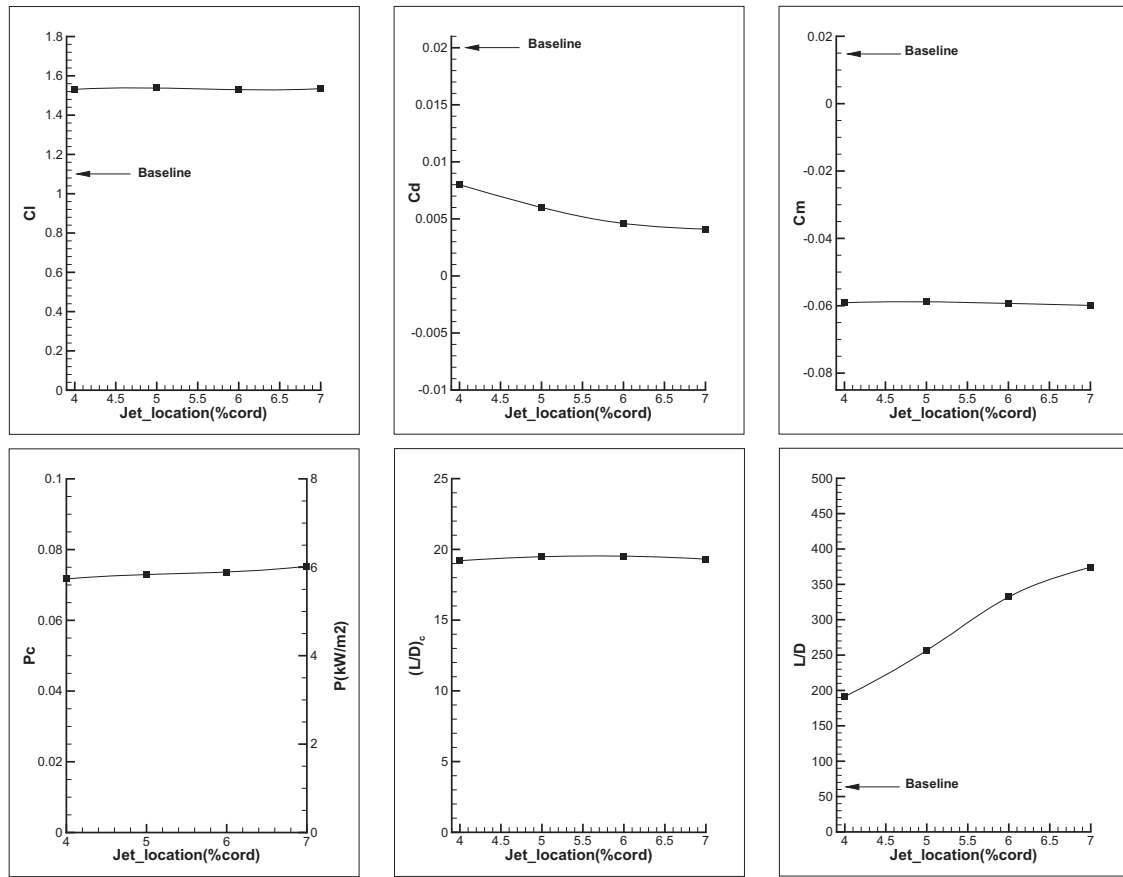


Figure 7.19: Variation of forces, moment and power consumption with the jet exit location at  $AoA = 10^\circ$  and  $C_\mu = 0.16$ .

lift and drag are slightly decrease. The power consumption increases when the suction size decreases because the smaller suction area requires a lower pressure to suck-in the same mass flow. The suction size 1.35% chord, 80% larger than the injection slot size, is used for the rest of the trade study because of its higher efficiency.

### 7.2.3.3 Suction Location

The suction location shown in Fig. 7.22 is varied from 70% chord-wise location to 40% by increment of 10%.

A more downstream suction location increases the lift and decreases the drag as shown in Fig. 7.23 since a longer jet has more space to mix and energize the flow and increases the circulation. A longer jet however comes at the price of a higher energy consumption and

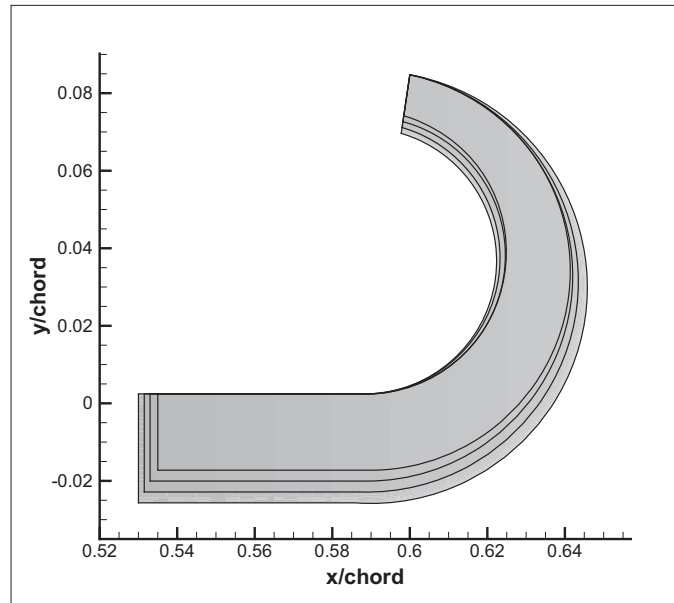


Figure 7.20: Overlay of the suction geometries.

the corrected aerodynamic efficiency is decreased. The suction-induced positive moment is increased when the suction is located more upstream due to the suction slot reactionary force and a longer moment arm. Consequently, the suction location of 40% has the best corrected aerodynamic efficiency and the smallest moment value. We select the 40% suction location configuration for the final CFJ airfoil even though this choice is arguable because of the reduced lift and increased drag when compared to the 70% suction location.

#### 7.2.3.4 Airfoil Thickness

The CFJ airfoil thickness is varied from 12% to 21% as shown in Fig. 7.24. All airfoils are generated with an injection located at 6% chord, except the 12% thickness airfoil which is generated with both 6% and 4% chord injection locations. The corresponding forces, moment and power consumption are displayed in Fig. 7.25.

The lift is increased with the airfoil thickness because the circulation is increased. The drag is decreased for the thinner airfoils because the more horizontal jet generates more thrust. The drag is increased for an injection located at 4% chord since the injection has a smaller streamwise component than for 6% chord location. The nose-down moment is

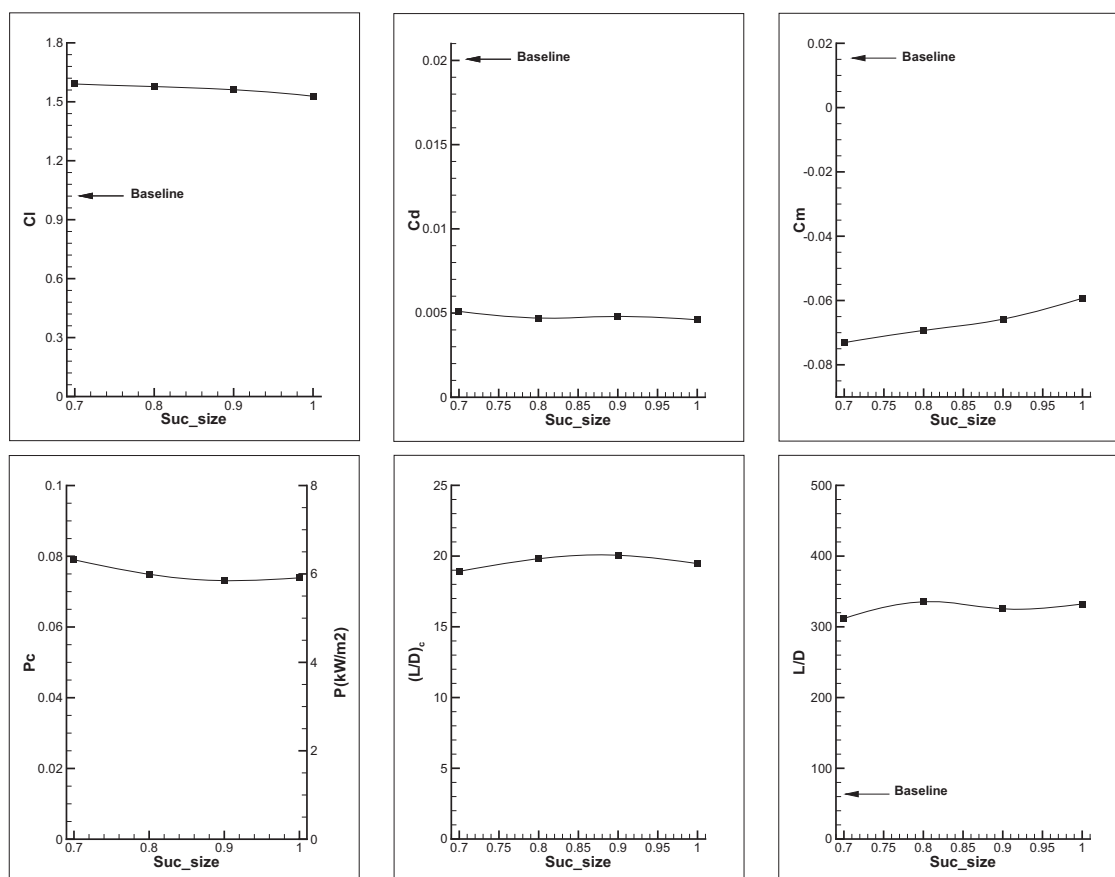


Figure 7.21: Variation of forces, moment and power consumption with suction size at  $AoA = 10^\circ$  and  $C_{\mu} = 0.16$ . The horizontal axis represents the ratio of the current suction size to the original suction size which is 1.5%chord.

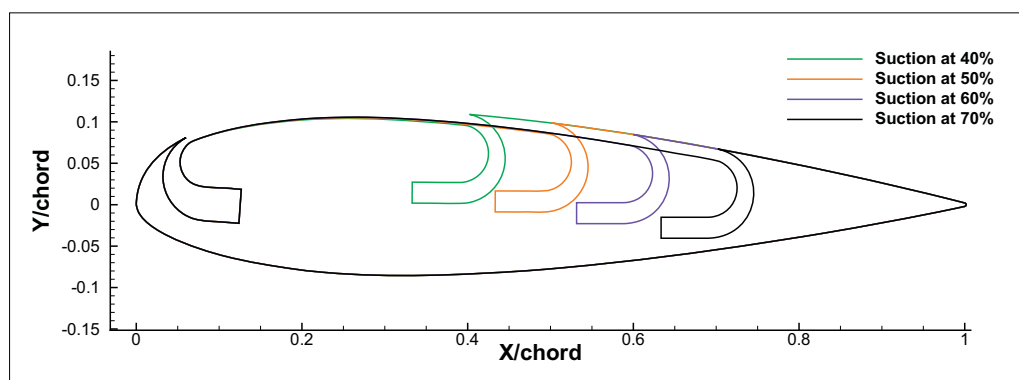


Figure 7.22: Geometries overlapped for the different suction location.

reduced with thinner airfoils because of the reduced moment arm distance from the jet to quarter chord. Surprisingly moving the jet forward to 4% for the 12% thickness airfoil slightly decrease the nose-down moment while previous study showed no dependency of

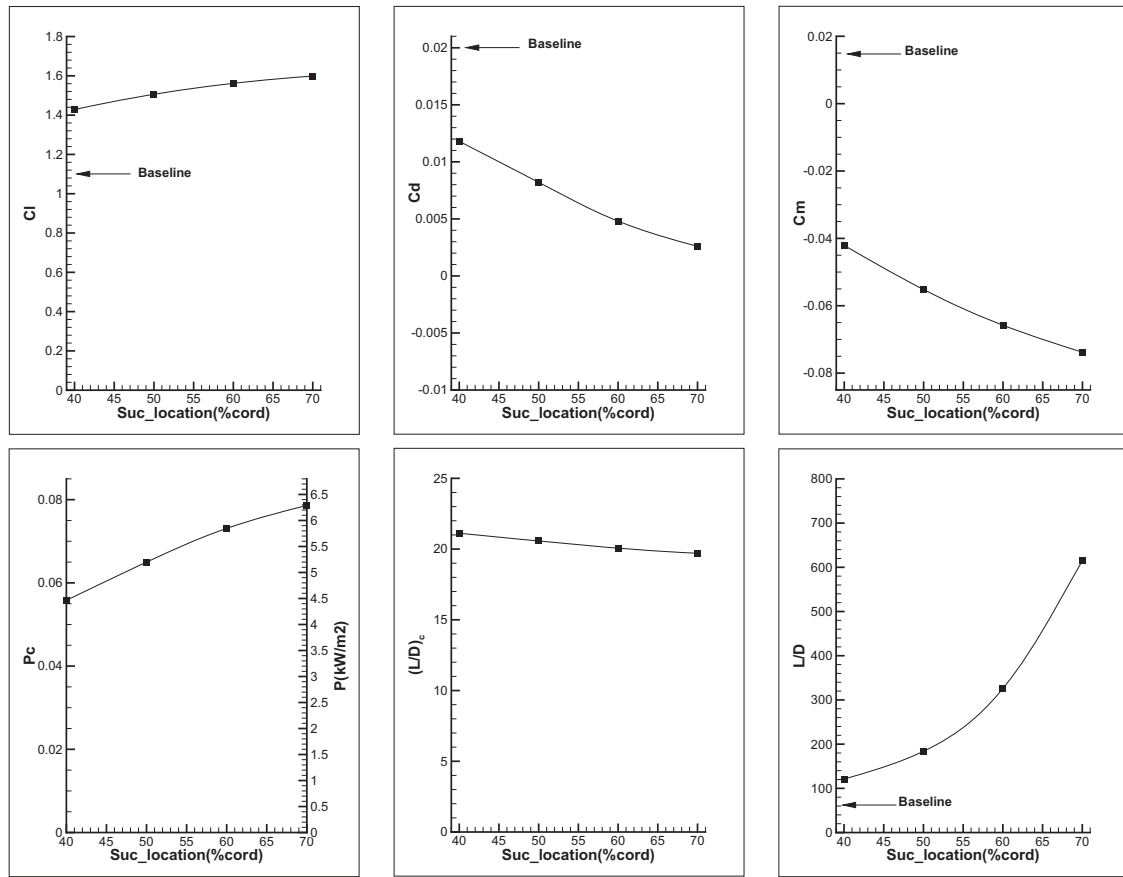


Figure 7.23: Variation of forces, moment and power consumption with suction location at  $AoA = 10^\circ$  and  $C_\mu = 0.16$ .

the moment on the jet exit location. This might be due to the important increase of circulation at the LE generated by the 4% jet location on the thin airfoil. If the jet exit location is kept at 6%, the energy consumption of thinner airfoil is significantly increased, therefore the efficiency is reduced. This is because for thinner airfoils the lowest pressure point is shifted closer to the LE making the injection location of 6% not optimal. This is confirmed by the very good efficiency of the 12% thickness with the injection located at 4% chord that matches the efficiency of the 21% thickness airfoil with jet located at 6%. The thickness ratio of 21% is selected for the final CFJ airfoil geometry.

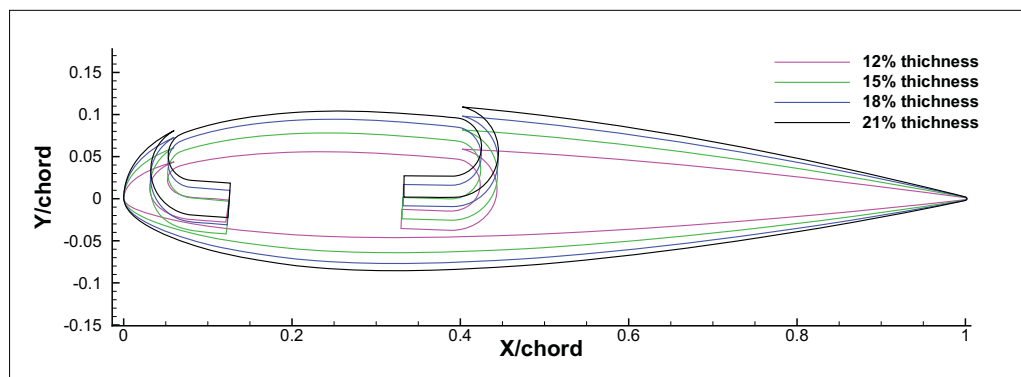


Figure 7.24: Thickness study overlapped geometries. In addition an airfoil with a 4% jet exit location is generated for the 12% thickness airfoil.

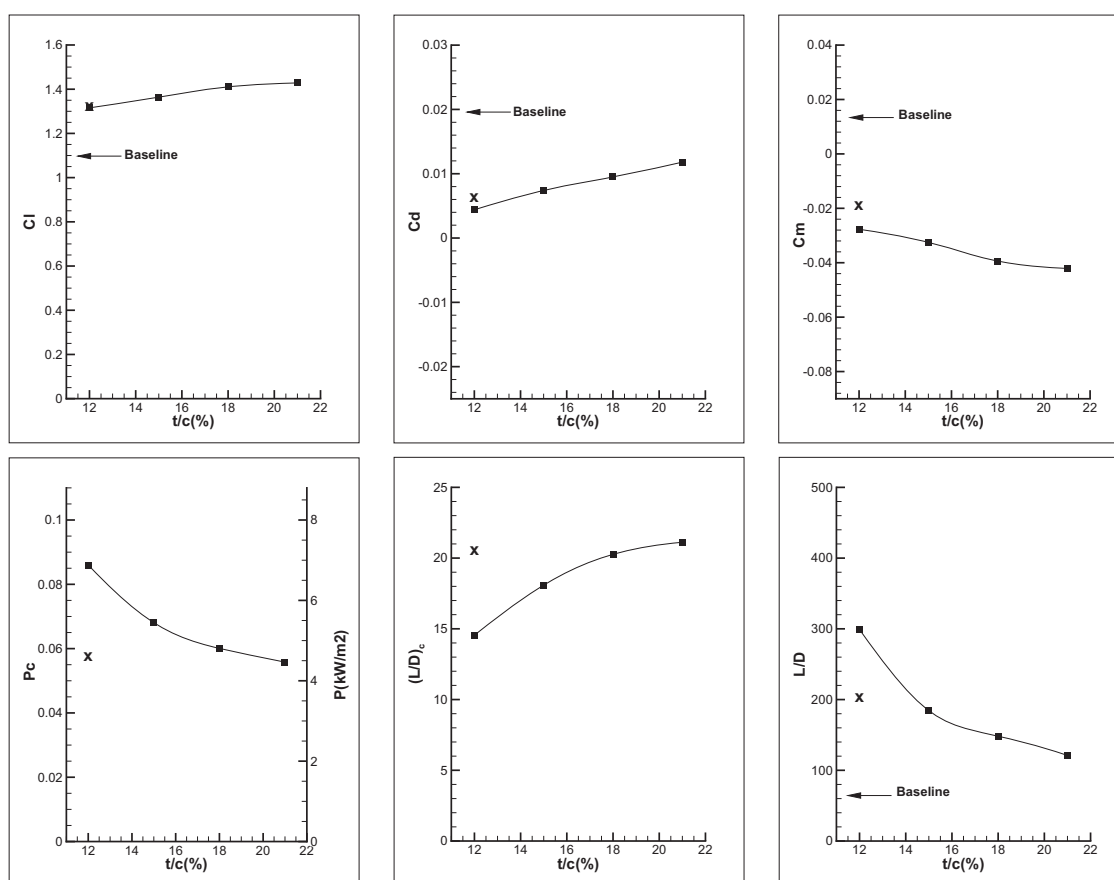


Figure 7.25: Variation of forces, moment and power consumption with airfoil thickness at  $AoA = 10^\circ$  and  $C_\mu = 0.16$ . The black squares data stand for the 6% jet exit location while the crosses data stands for the 4% jet exit location.

### 7.2.3.5 Reynolds Number

The Reynolds number is varied from  $0.8 \times 10^6$  to  $12.8 \times 10^6$  for the geometry displayed in Fig. 7.28 and the results are shown Fig. 7.26. Viscous forces are more important at low

Reynolds number. As a result, the drag and power consumption increase and the efficiency decreases when the Reynolds number is decreased. The lift which is mostly due to pressure forces is little affected by the Reynolds number changes. The airfoil performance becomes insensitive to Reynolds number when it is greater than  $6 \times 10^6$ .

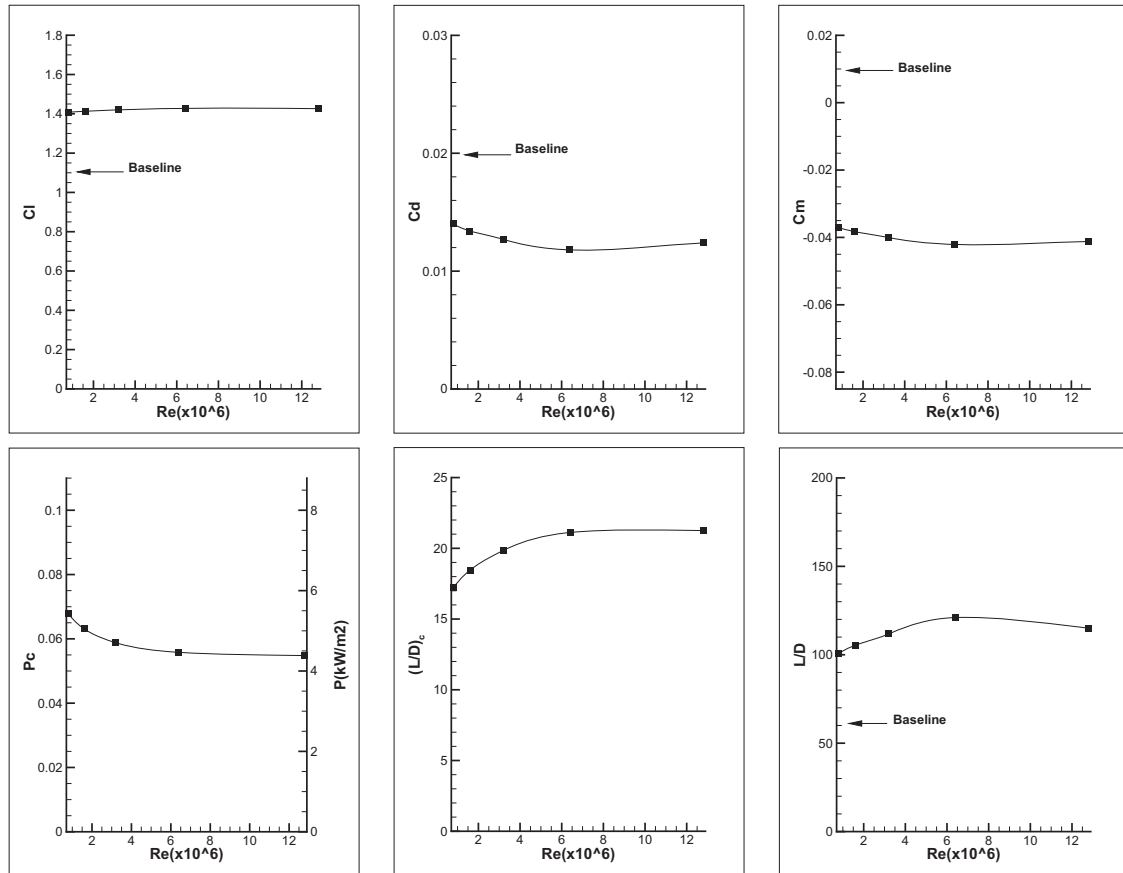


Figure 7.26: Variation of forces, moment and power consumption with Reynolds number at  $AoA = 10^\circ$  and  $C_\mu = 0.16$ .

## 7.2.4 Final CFJ Airfoil from Trade Study

In the trade studies above, the corrected aerodynamic efficiency was increased from 19.4 to 21.2 as seen in Fig. 7.27 and the final CFJ airfoil geometry is displayed on Fig. 7.28. This section study the final CFJ airfoil aerodynamic performance with varying AoA and  $C_\mu$ . The airfoil features a thickness of 21% chord, an injection size of 0.75% chord located at 6% chord and a suction size of 1.35% chord located at 40% chord.

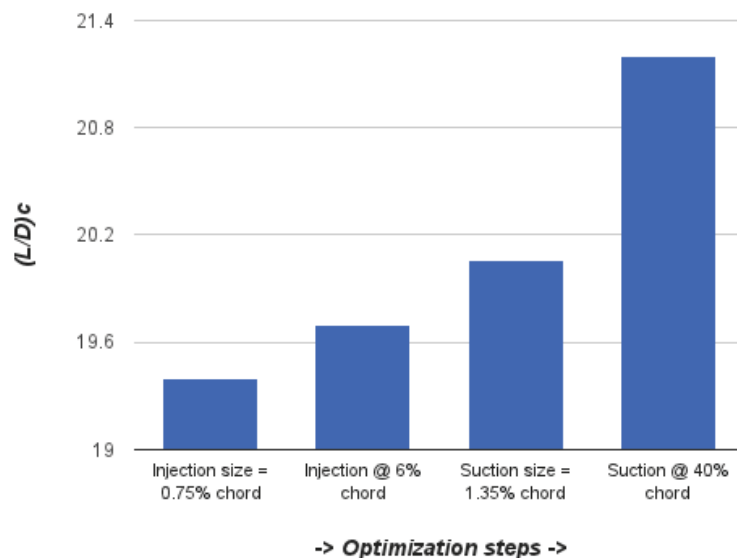


Figure 7.27: Corrected aerodynamic efficiency gain during CFJ trade study.

Fig. 7.29 shows the final airfoil Mach contours variation with the AoA at  $C_{\mu} = 0.16$ . The main flow peak Mach number reaches about 0.55 downstream the LE on suction surface, a large increase compared with the peak Mach number of the baseline airfoil without flow control. The injection mach number increases slightly with the AoA and reached 0.55 at  $AoA = 30.0^{\circ}$ , a 3% increase compared to  $AoA = 0.0^{\circ}$ . Downstream the injection, the jet velocity decreases faster when the AoA increases because of the increased adverse pressure gradient between the injection and the suction slot. For  $AoA < 30.0^{\circ}$ , the jet maintains a fairly high momentum going into the suction slot and makes the pumping energy consumption low. However at  $AoA = 30.0^{\circ}$  the jet loses much of its momentum to the severe adverse pressure gradient and the pumping power are increased. At  $AoA > 30.0^{\circ}$  the airfoil, cannot sustain the large adverse pressure gradient and a recirculation region appears at the TE.

The AoA and  $C_{\mu}$  of the final CFJ airfoil is varied and the corresponding forces, moment and power consumption are displayed in Fig. 7.30. The results are compared with the simulated baseline forces and moment.

At high AoA, unsteady simulations are conducted to capture the boundary-layer separation and turbulent mixing. The lift is greatly enhanced by the use of CFJ with  $C_{Lmax} =$

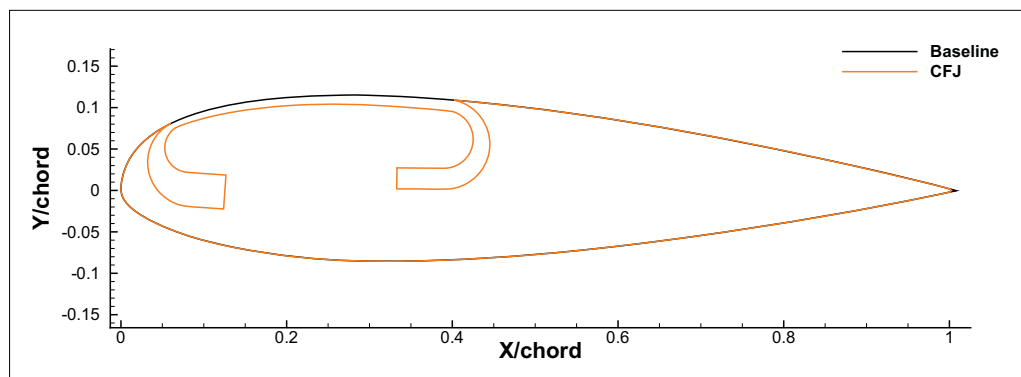


Figure 7.28: Final airfoil geometry accordingly to the trade study on the injection and suction size and location.

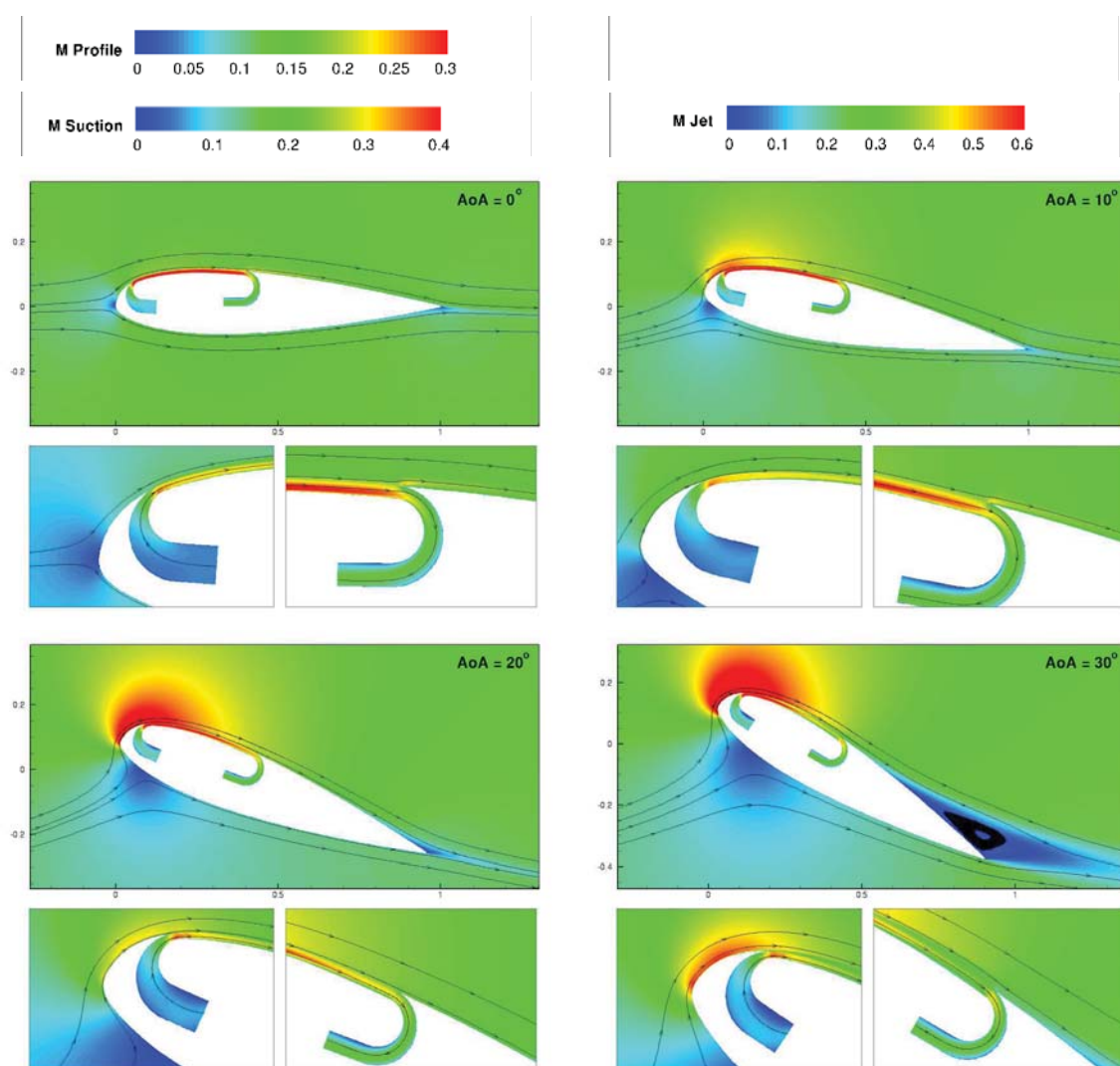


Figure 7.29: Mach contours variation with AoA at  $C_{\mu} = 0.16$ . Images include zoomed-in pictures of suction and injection areas.

2.91 at  $AoA = 32.5^\circ$  and  $C_\mu = 0.16$ ,  $C_{Lmax} = 2.52$  at  $AoA = 25.0^\circ$  and  $C_\mu = 0.12$  and  $C_{Lmax} = 2.01$  at  $AoA = 20.0^\circ$  and  $C_\mu = 0.08$ , a significant improvement compared with the baseline airfoil that reaches a maximum  $C_L$  of 1.50 at  $AoA \approx 16^\circ$ . The CFJ airfoil drag is significantly reduced for all  $C_\mu$  with a minimum value approaching zero at  $AoA = 0^\circ$  and  $C_\mu = 0.16$ . The moment coefficient is fairly flat until  $AoA \approx 15^\circ$  and rapidly increases after. This moment increase is due in part to a flow recirculation developing at the airfoil TE at high AoA. The power coefficient is decreased with the increasing AoA before the recirculation occurs. A similar power coefficient behavior was observed during the wind tunnel testing in [96] and the simulations in [61]. The mechanism is that when the AoA increases, the LE suction is stronger and the pressure of the main flow surrounding the injection slot is lower, hence reducing the pumping power to generate the jet. When the AoA is too high however, the jet total pressure losses are increased due to the large adverse pressure gradient and in turn the pumping power is increased. At  $C_\mu = 0.16$ , the efficiency and power consumption of the CFJ airfoil reaches  $E = 36.8$  and  $Pc = 0.036$  at  $AoA = 22.5^\circ$ . The efficiency and power consumption are considerably improved for the lower  $C_\mu$  and reach  $E = 43.3$  and  $Pc = 0.019$  at  $AoA = 20.0^\circ$  and  $C_\mu = 0.12$ , and  $E = 51.5$  and  $Pc = 0.009$  at  $AoA = 15.0^\circ$  and  $C_\mu = 0.08$ .

The corrected aerodynamic efficiency versus  $C_L$  is plotted Fig. 7.30. The baseline airfoil is efficient at low  $C_L$  but is surpassed by the CFJ airfoil both in term of maximum  $C_L$  and efficiency at high  $C_L$ . The baseline airfoil achieves its maximum efficiency at  $C_L = 0.8$ , whereas the CFJ airfoil reaches his at  $C_L = 2.62$ . The CFJ airfoil provides a tremendous increase of maximum  $C_L$  with a high corrected aerodynamic efficiency and low nose-down moment, largely outperforming the slotted flap airfoil performance shown in [19].

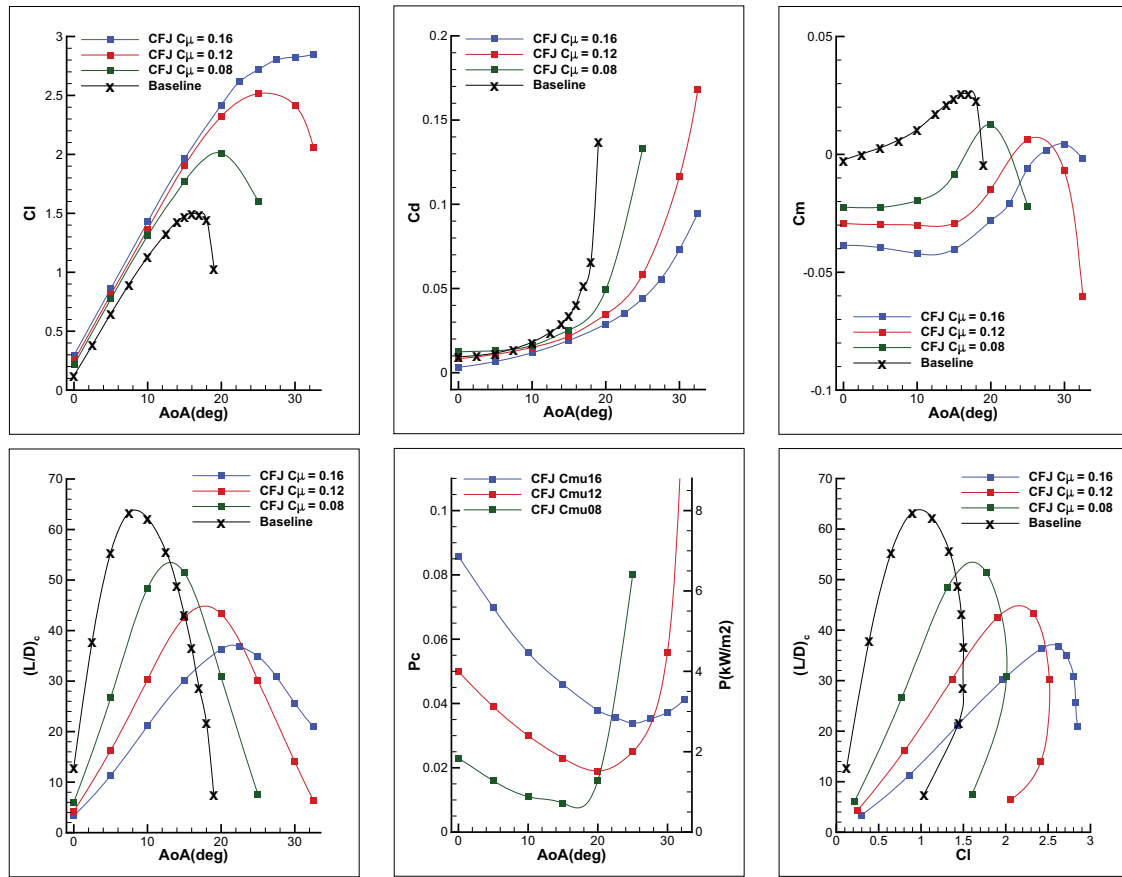


Figure 7.30: Variation of forces, moment and power consumption with AoA for various  $C_\mu$ .

## 7.3 CFJ Airfoil Trade Study Part II : Moment and Drag

### 7.3.1 Mesh

The NACA 23121 CFJ airfoil grid (Fig. 7.31) is constructed using the O-mesh topology in order to achieve high quality around the airfoil. The mesh uses a total of 330 points around airfoil partitioned into 210 points on the suction surface and 120 points on the pressure surface, 180 points are placed in the direction normal to the airfoil with an additional 60 points across the jet. The total mesh size is 75,600 cells and the mesh is split into 14 blocks for the parallel computation. The farfield boundary is located 30 chords away from the airfoil. The first grid point is placed at  $y^+ \approx 1$  to resolve the turbulent boundary layer.

A refined grid is constructed using 50% more points in every direction and  $y^+ \approx 0.7$ . The refined mesh results agree well with the original meshes.

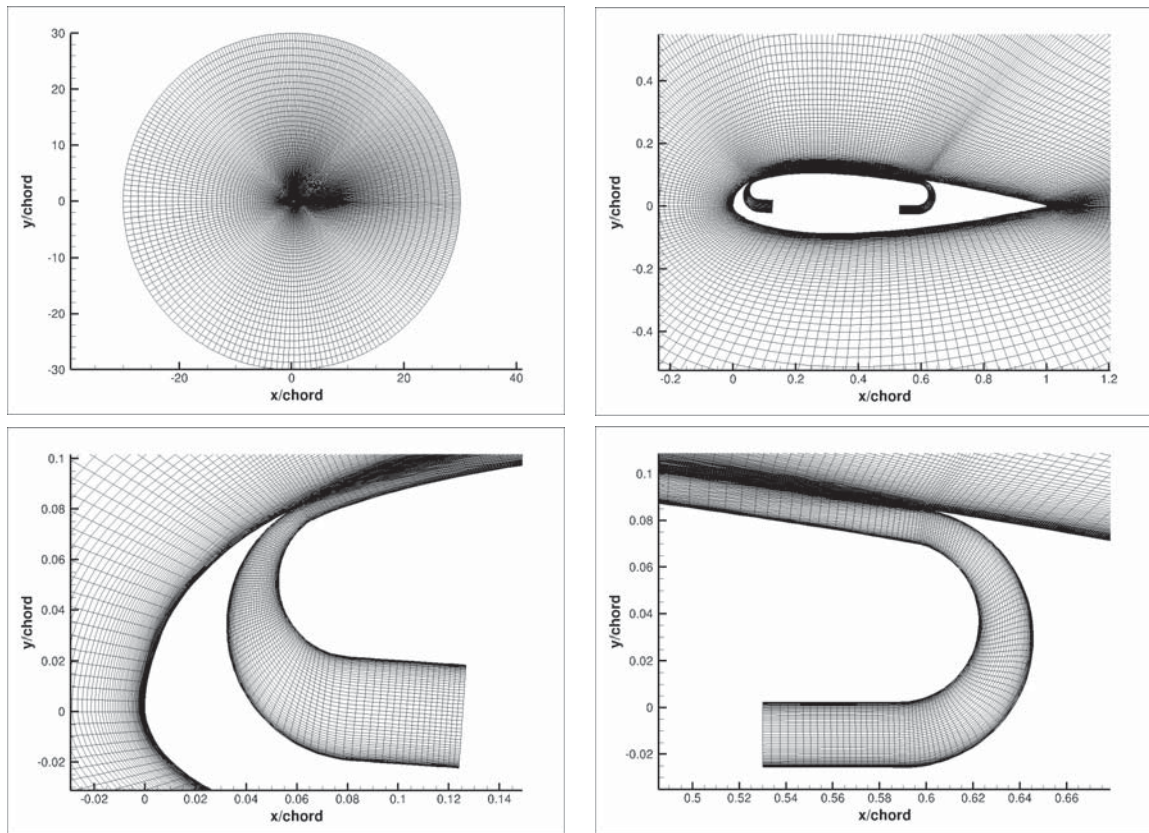


Figure 7.31: NACA 23121 CFJ airfoil O-mesh topology.

### 7.3.2 Low Moment CFJ Airfoils

The suction surface of the NACA 23121, NACA 34121 and NACA 6321 CFJ airfoils is modified to reduce or overcome the nose-down moment and the resulting aerodynamic performance and efficiency is quantified. The airfoils injection and suction slots are located at 6% and 40% chord respectively. Injection and suction slot sizes are 0.75% and 1.35% chord. Because of the large number of geometries created for this section, this study focuses on  $AoA = 10^\circ$  and  $C_\mu = 0.16$ .

The NACA 23121, NACA 34121 and NACA 6321 CFJ airfoil variations are shown in Fig. 7.32. All the injection and suction cavities are the same as in Fig. 7.31 though are

not plotted in Fig. 7.32 for clarity. For all the cases, variation 0 is constructed from the NACA baseline airfoil by lowering the suction surface between the injection and suction slot. The variation 1 airfoil is generated from variation 0 by decreasing the injection angle by  $0.5^\circ$  for the NACA 23121 and NACA 34121 and by  $1.0^\circ$  for the NACA 6321. Doing so also rotates the suction surface downstream of the injection. Reflex camber is then used in the last 20% of the airfoil to link the rotated suction surface to the TE. Variations 2,3 and 4 are constructed similarly by increasing the rotation angle of the suction surface and reflex camber. The injection angle is lowered by  $2.0^\circ$  for the NACA 23121 and NACA 34121, and  $4.0^\circ$  for the NACA 6321. For all the variations the airfoil nose and pressure surface remain unchanged.

The forces, moment and power consumption for the CFJ airfoil variations are displayed from Fig. 7.33 to Fig. 7.35. The NACA 23121 CFJ airfoil lift coefficient is decreased from 1.34 for variation 0 to 1.19 for variation 4 due to the use of increasing reflex camber. Interestingly, the drag is reduced as well because the pressure repartition of reflex airfoils features a higher back pressure that reduces the pressure drag. In addition, the slightly more horizontal injection generates more thrust. The power consumption decreases with the variation number because of the slightly lower injection pressure, however, the decrease of the power consumption and the drag are not enough to compensate for the decrease of lift, and the  $(L/D)_c$  is reduced from 18.1 to 17.2.  $L/D$  is excellent for all variations and ranges between 120.0 and 121.1, a 65% increase over the baseline airfoil value. The NACA 23121 CFJ airfoil variation 1 shows that for a modest concession on the corrected aerodynamic efficiency the moment can be significantly improved. Similar conclusion are found for the NACA 6321 and NACA 34121 CFJ airfoils.

Unlike the NACA 6321 CFJ airfoil, the NACA 23121 and 34121 CFJ airfoil moments vary from negative to positive among the variations. The NACA 23121 variation 1 and NACA 34121 variation 2 airfoils achieved a neutral moment. When comparing those two low moment airfoils, there is a significant advantage in term of corrected aerodynamic

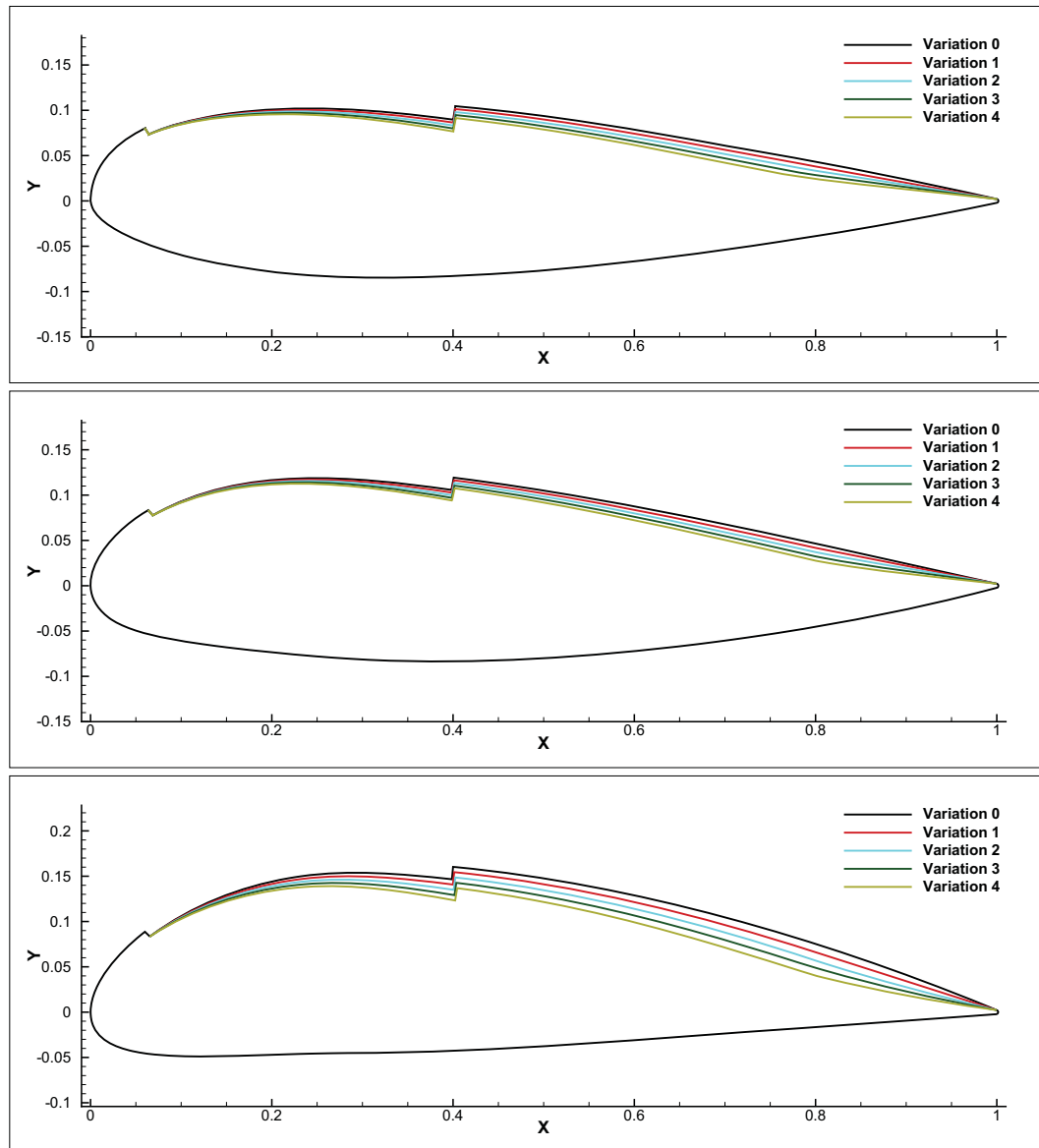


Figure 7.32: Geometry of the NACA 23121, NACA 34121 and NACA 6321 CFJ airfoils and their variations.

efficiency for the NACA 23121 variation ( $(\frac{L}{D})_c$  17.9 vs 16.5) due to the combined effects of a higher lift, a smaller drag and reduced power consumption.

### 7.3.3 CFJ Airfoil with Thrust Generation

The low drag NACA 21112 CFJ thin airfoil studied in [63] is simulated with varying AoA,  $C_{\mu}$  and injection sizes and the resulting aerodynamic performance and efficiency is quantified. The airfoils injection and suction slots are located at 4% and 40% chord respectively.

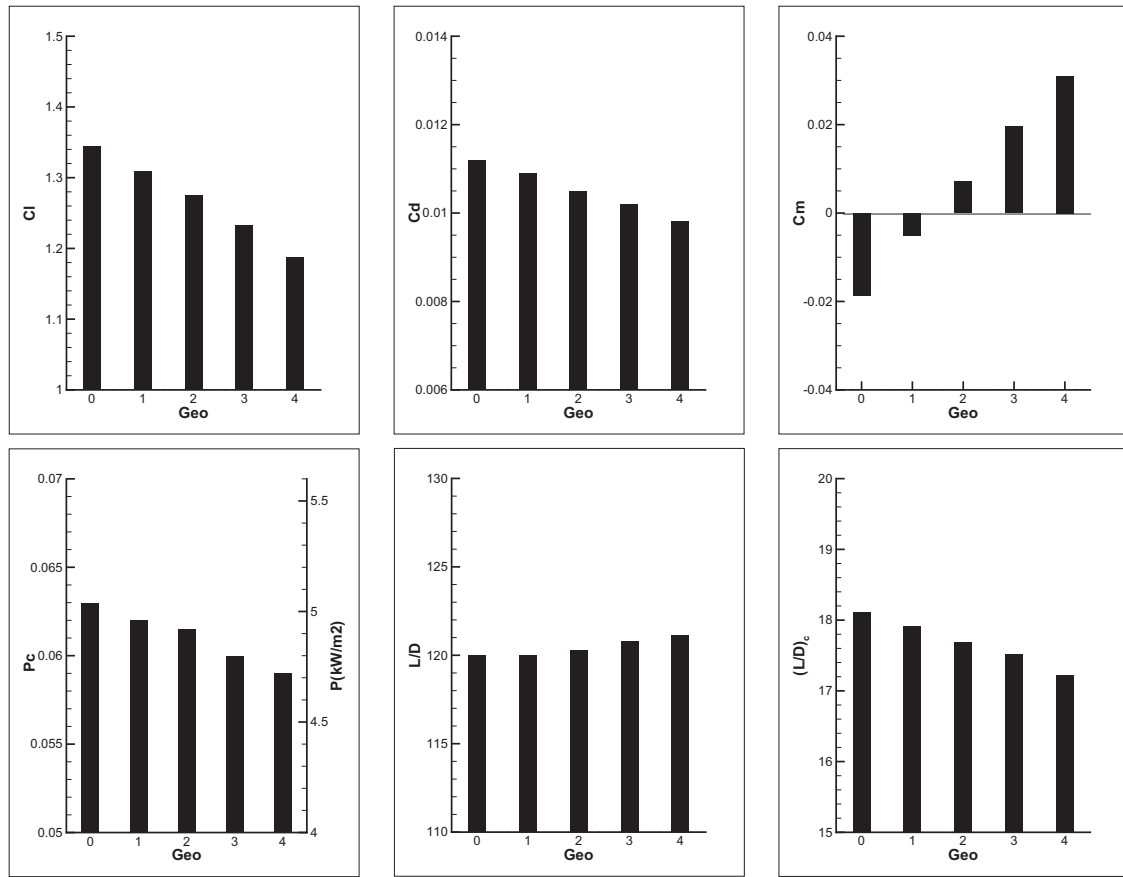


Figure 7.33: Variation of forces, moment and power consumption for the NACA 23121 CFJ airfoils variations at  $AoA = 10^\circ$  and  $C_{\mu} = 0.16$ .

The injection and suction slot sizes are 0.75% and 1.35% chord for the original injection size and 0.50% and 1.00% for the smaller injection size.

The CFJ airfoils studied for thrust generation are shown in Fig. 7.3.3. The NACA 23112 CFJ airfoil is chosen with an injection location moved upstream to 4% chord location because this thin airfoil features a low drag and a high efficiency in the thickness trade study form [63].

The  $AoA$  and  $C_{\mu}$  of the NACA 23112 CFJ airfoil are varied and the corresponding forces, moment and power consumption are displayed in Fig. 7.37. The results are compared with the simulated baseline airfoil with no CFJ. At high  $AoA$ , unsteady simulations are conducted to capture the boundary-layer separation and turbulent mixing. The lift is greatly enhanced by the use of CFJ even though the improvement is not as significant as

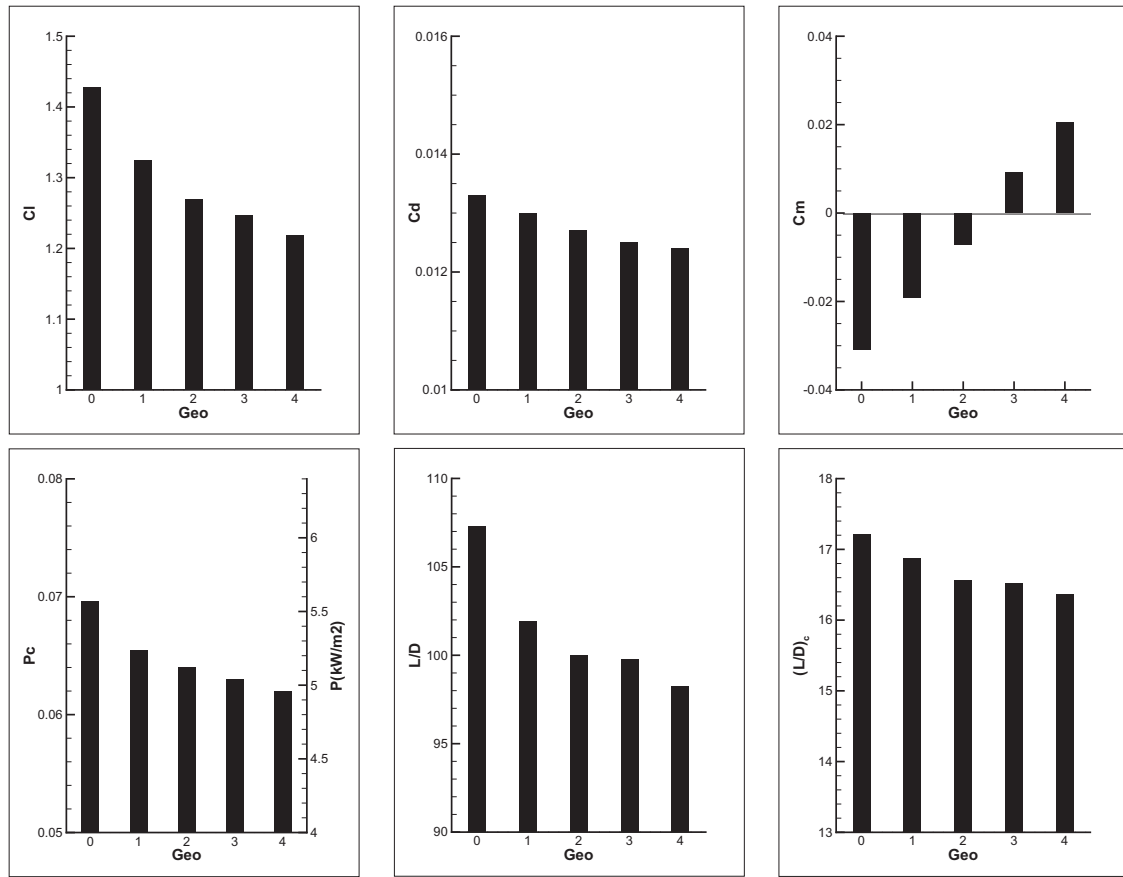


Figure 7.34: Variation of forces, moment and power consumption for the NACA 34121 CFJ airfoils variations at  $AoA = 10^\circ$  and  $C_\mu = 0.16$ .

with the thick NACA 23121 CFJ airfoil [63] because the lower thickness reduces the circulation. The maximum lift coefficient reaches  $C_{Lmax} = 2.40$  for  $C_\mu = 0.16$ , a significant improvement compared with the baseline airfoil that reaches a maximum  $C_{Lmax}$  of 1.50. The CFJ airfoil stall pattern is much sharper than with the NACA 23121 CFJ airfoil ([63]). The CFJ airfoil drag coefficient remains negative until  $AoA \approx 11^\circ$  at  $C_\mu = 0.16$  with a minimum value of  $C_{Dmin} = -0.019$ . The moment coefficient remains fairly flat until  $AoA \approx 15^\circ$  and increases for higher  $AoA$  at  $C_\mu = 0.12$  and  $C_\mu = 0.16$  because of a flow separation developing at the airfoil TE at high  $AoA$ . The stall pattern is different at  $C_\mu = 0.08$ . The weaker jet is unable to overcome the large adverse pressure gradient at the LE and the airfoil stalls with a separation starting at the LE. The power consumption is decreased with the increasing  $AoA$  before the separation occurs. This phenomenon is confirmed by the

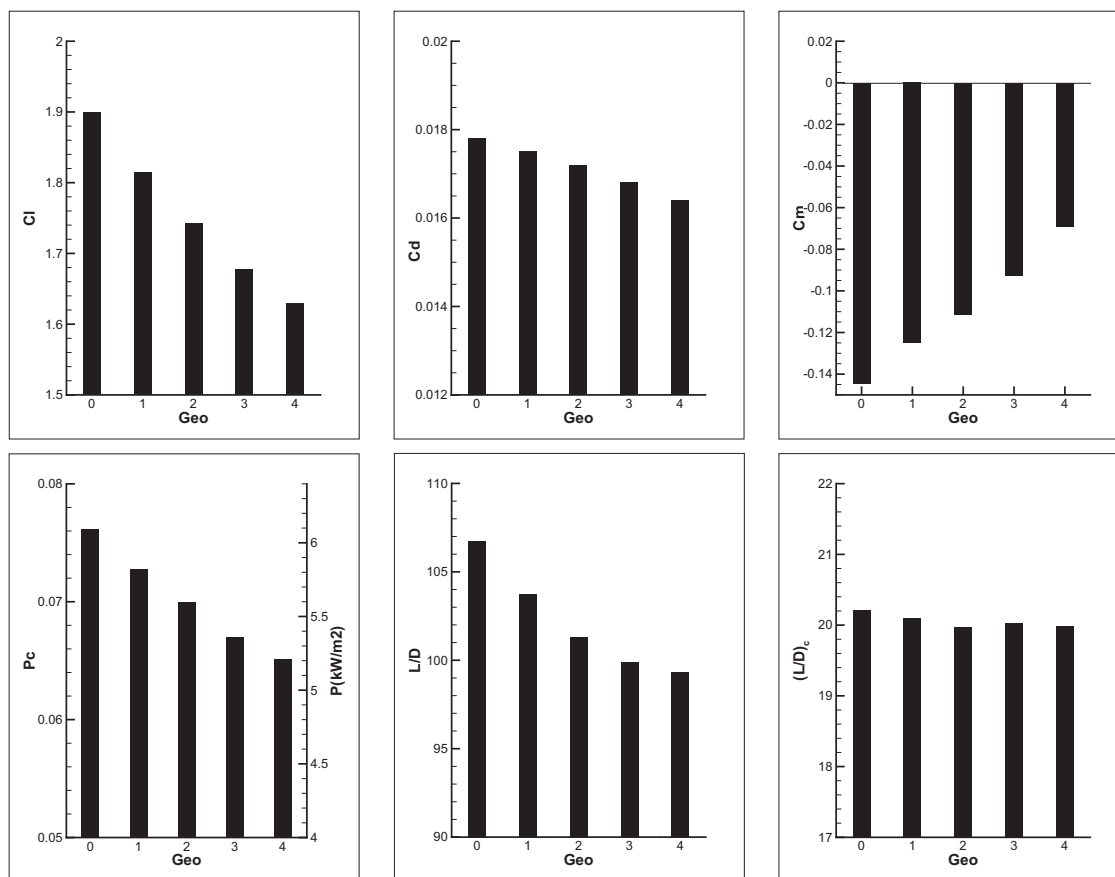


Figure 7.35: Variation of forces, moment and power consumption for the NACA 6321 CFJ airfoils variations at  $AoA = 10^\circ$  and  $C_{\mu} = 0.16$ .

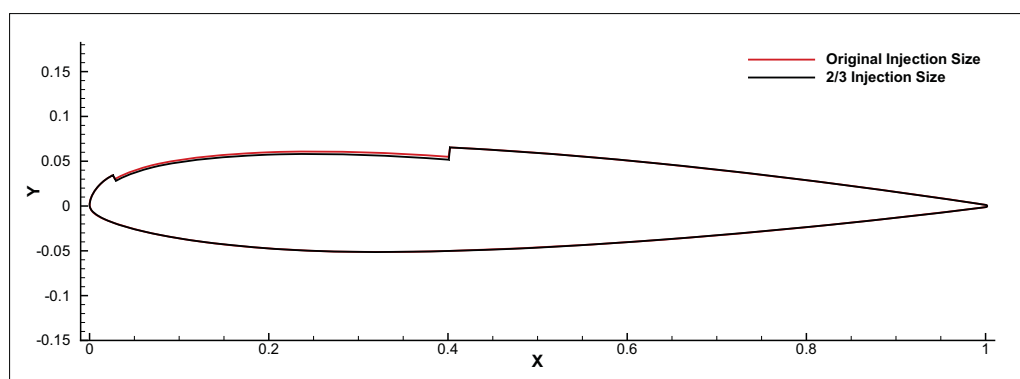


Figure 7.36: Geometry of the NACA 23112 CFJ airfoil with original jet size and the 2/3 jet size.

wind tunnel testing in [96] and the simulations in [61]. The mechanism is that when the  $AoA$  increases, the LE suction is stronger and the pressure of the main flow surrounding the injection slot is lower, hence reducing the pumping power to generate the jet. When the

AoA is too high however, the jet total pressure loss is increased due to the large adverse pressure gradient and flow separation. At  $C_\mu = 0.16$ , the corrected aerodynamic efficiency and power consumption of the CFJ airfoil reach  $(\frac{L}{D})_c = 35.3$  and  $P_c = 0.043$ . Those values are considerably improved for lower  $C_\mu$  and with  $(\frac{L}{D})_c = 64.4$  and  $P_c = 0.011$  at  $C_\mu = 0.08$ . The pure aerodynamic efficiency is tremendously improved for the CFJ airfoil and reaches close to  $L/D = 300$  at  $C_\mu = 0.08$ . At higher  $C_\mu$ , the maximum  $L/D$  reached is infinity when the drag is null.

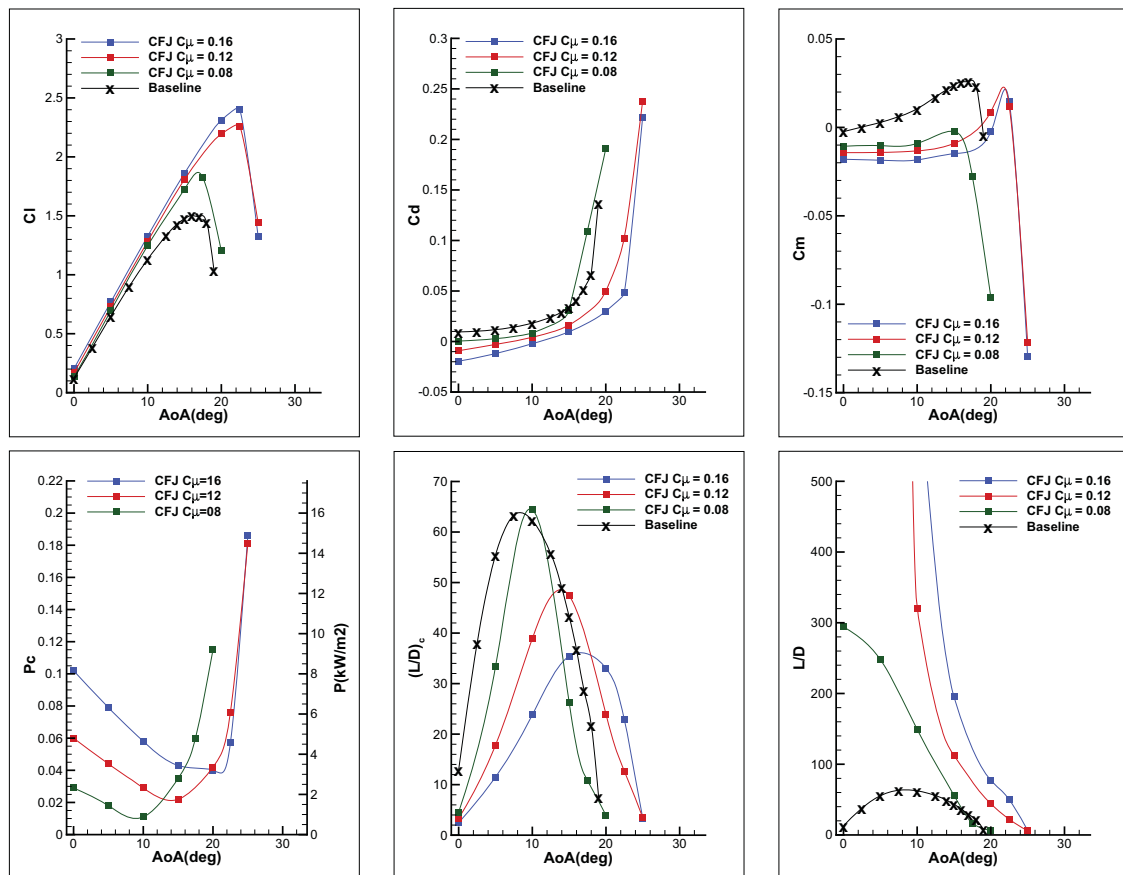


Figure 7.37: Variation of forces, moment and power consumption for the NACA 23112 CFJ airfoils with AoA and  $C_\mu$ .

The NACA 23112 CFJ airfoil injection and suction slot size are reduced by 1/3 and the corresponding forces, moment and power consumption are displayed in Fig. 7.38. The lift and drag are significantly improved for the smaller injection size when compared to the original injection size and reach  $C_{Lmax} = 2.81$  and  $C_{Dmin} = -0.033$  at  $C_\mu = 0.16$ .

The drag is negative until  $AoA \approx 16^\circ$  at  $C_\mu = 0.16$ . The moment is similar to the original injection size for  $C_\mu = 0.12$  and  $C_\mu = 0.16$ . For  $C_\mu = 0.08$  the LE stall pattern observed for the original injection size is not observed here because the smaller injection slot generates a faster jet that enhances the mixing with the main flow, thereby increasing the performance and better prevents the LE flow separation. On the other hand, the smaller and faster jet loses more total pressure by friction, and mixing with the main flow and the pumping power is increased. The drag reduction and lift enhancement are not enough to balance the power increase and the corrected aerodynamic efficiency is decreased to  $(\frac{L}{D})_c = 28.9$  and  $P_c = 0.068$  at  $C_\mu = 0.16$ . Those values are considerably improved for lower  $C_\mu$  with  $(\frac{L}{D})_c = 51.9$  and  $P_c = 0.018$  at  $C_\mu = 0.08$ . The pure aerodynamic efficiency  $L/D$  is tremendously improved for the CFJ airfoil and reaches infinity when the drag is null.

The corrected aerodynamic efficiency versus  $C_D$  plot shown in Fig. 7.39 indicates that the more thrust the airfoil generates, the lower the efficiency. The smaller injection size achieves negative drag more efficiently than the original injection size.

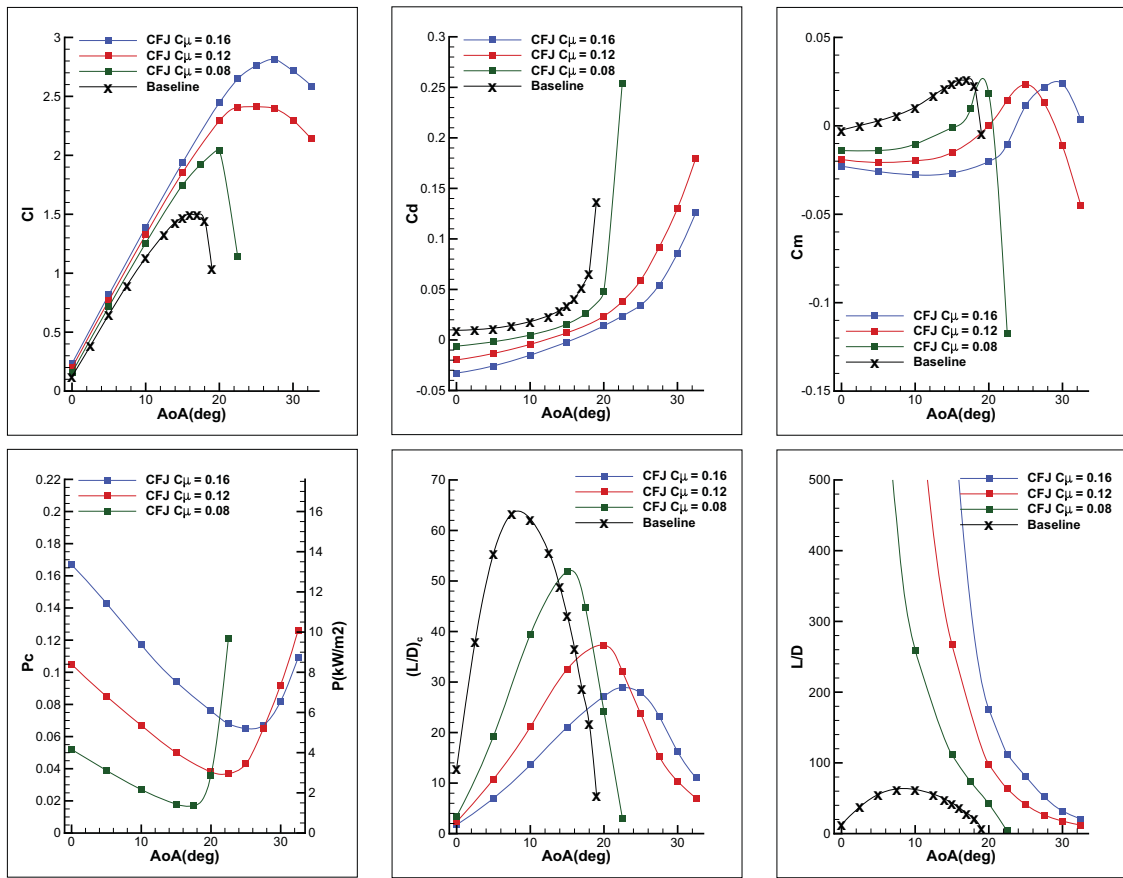


Figure 7.38: Variation of forces, moment and power consumption for the NACA 23112 CFJ airfoils with AoA and  $C_{\mu}$ . The jet size is reduced to 2/3 of the original jet size.

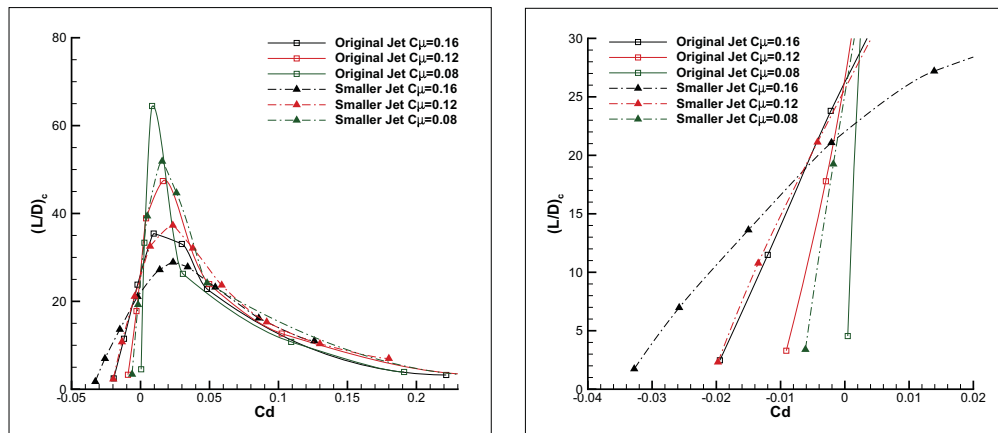


Figure 7.39:  $(\frac{L}{D})_c$  versus  $C_D$  for the NACA 23112 CFJ airfoil with original and reduced injection sizes plotted for various  $C_{\mu}$ . The thrust generation area is zoomed-in on the right plot.

## Chapter 8

# Numerical Investigation of Pitching CFJ Airfoils

This chapter investigates CFJ pitching airfoils energy expenditure and performance enhancement at subsonic and transonic speeds [62, 77].

The first section reports the performance enhancement of an oscillating SC1095 airfoil with CFJ. The free stream Mach number is 0.3, the Reynolds number is  $3.93 \times 10^6$  and the reduced frequency varies from 0.05 to 0.2. The objective is to study the ability of CFJ to remove dynamic stall in the typical pitching airfoil working range. The drastic lift increase, drag reduction, and moment variation mitigation are recoded. This is the first time CFJ has ever been applied to pitching airfoils.

The second section presents the performance enhancement at a free stream Mach number of 0.4, where the flow field is transonic. The reduced frequency is 0.1 and the Reynolds number is  $5.24 \times 10^6$ . The purpose is to investigate the effects of CFJ on pitching airfoil at high Mach number, where strong shock-boundary layer interactions are unavoidable, making flow control a more difficult task.

## 8.1 CFJ Pitching Airfoils at $M_\infty = 0.3$

### 8.1.1 Mesh

The computation mesh is constructed using the O-mesh topology in order to achieve high quality around the airfoil. The CFJ SC1095 airfoil mesh displayed Fig. 8.1 uses a total of 360 points placed around airfoil partitioned into 240 points on suction surface and 120 points on the pressure surface. 180 points are placed in the direction normal to the airfoil with an additional 50 points across the jet. Total mesh size is 77,800 cells, partitioned into 23 blocks for the parallel computation.

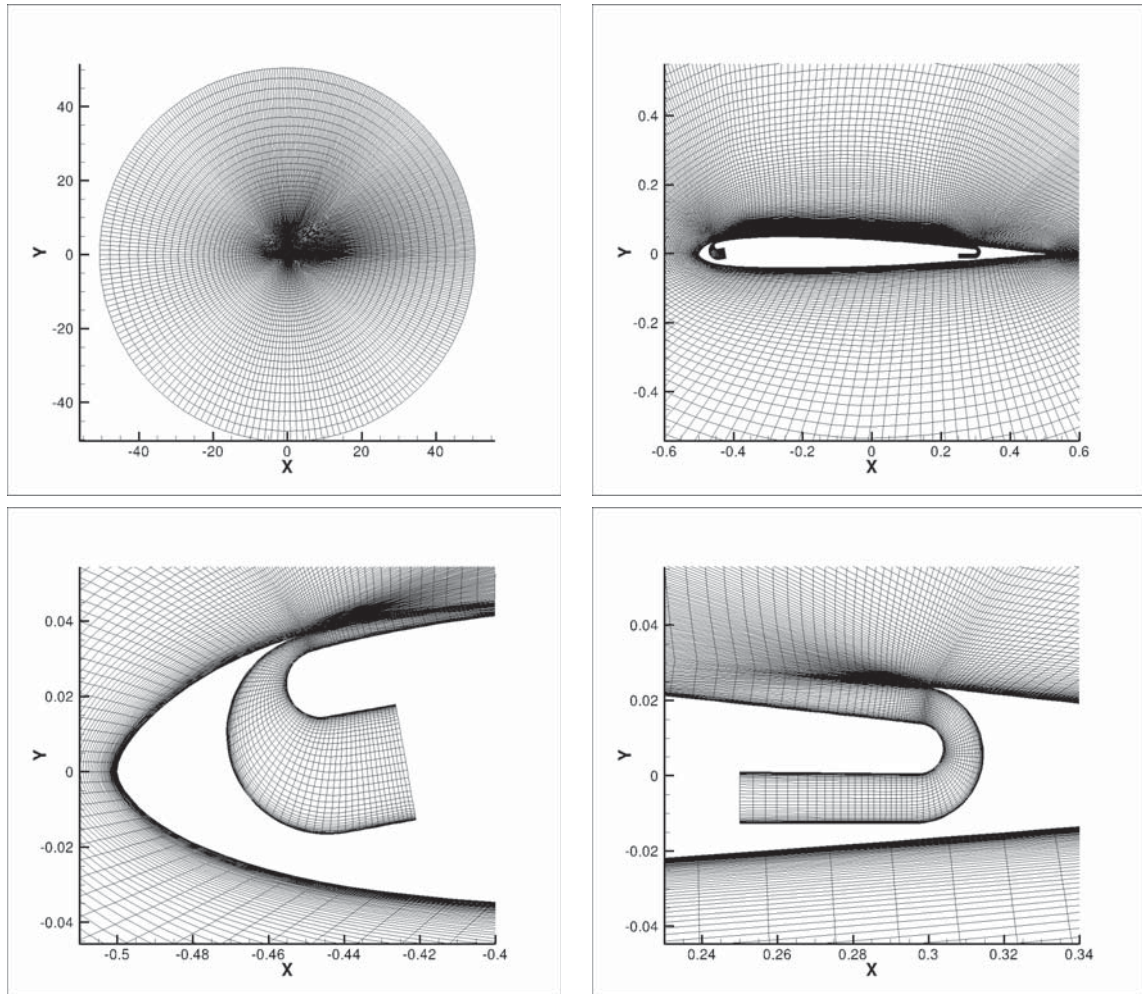


Figure 8.1: SC1095 CFJ pitching airfoil mesh topology.

The farfield boundary is located 50 chords away from the airfoil. To resolve the turbulent boundary layer, the first grid point is placed at  $y^+ \approx 0.5$ . The baseline airfoil mesh is constructed using the same strategy. The total baseline airfoil mesh size is 54,000 cells with 271 points around the airfoil and 181 points normal to the airfoil. The baseline airfoil mesh is split into 9 blocks for the parallel computing. For both baseline airfoil and CFJ airfoil, a refined grid is constructed using 50% more points in every direction and  $y^+ \approx 0.35$ . Block definition for CFJ airfoil can be found in Table 8.1.

Block	$\xi$ -Direction	$\eta$ -Direction	Cell number
1-18	41	91	3600
19	71	51	3500
20-22	41	51	2000
23	71	51	3500
Total mesh size			77800

Table 8.1: Block dimensions for CFJ SC1095 airfoil

### 8.1.2 Geometry and Oscillation Description

The baseline airfoil SC1095 used on the UH-60 Black Hawk US-army helicopter is chosen due to the existence of experimental data from NASA [71]. CFJ is implemented on the SC1095 profile via multiple geometries depicted in Table 8.2. For most cases geometry 1 performs well. However for a high  $C_\mu$ , a bigger jet slot is used in order to keep the jet exit Mach number within acceptable range. A bigger suction slot is also used to suck in the increasing mass flow.

Mach number of 0.3 and Reynolds number of  $3.93 \times 10^6$  at reduced frequency from 0.05 to 0.2 are used to match the experimental data. The CFJ airfoil uses the same conditions with  $C_\mu$  in the range of 0.08-0.24. The oscillation of the baseline and CFJ airfoils is described by

$$AoA = \alpha_0 + \alpha_1 \sin(k \tau)$$

From the no-stall case to the deep-stall case, the maximum AoA is increased from  $14^\circ$  to  $19.68^\circ$ . The parameters of the cases studied are given Table 8.3.

Geometry	Inj. height	Inj. location	Suc. height	Suc. location	Designed from
1	0.50	5.0	0.75	80.0	SC1095
2	0.75	5.0	1.12	70.0	SC1095
3	1.00	5.0	1.50	70.0	SC1095

Table 8.2: Pitching airfoil geometry description, length are given in % of chord.

Case name	$\alpha_0$ ( $^\circ$ )	$\alpha_1$ ( $^\circ$ )	k
no-stall	3.88	10.11	0.15
mild-stall	9.93	4.91	0.05
deep-stall	9.78	9.90	0.10

Table 8.3: Pitching airfoil oscillation description.

### 8.1.3 Baseline and CFJ Airfoils Undergoing No-stall Oscillation

Fig. 8.2 shows the computed baseline results for  $C_l$ ,  $C_d$  and  $C_m$  compared with the experimental data. Good agreement exists between the lift and drag at lower AoA. At high AoA the prediction under-estimates the magnitude of both lift and drag with a 12% difference for the peak  $C_l$  and 20% difference for the peak  $C_d$ . The moment is slightly over-predicted by the computation. Those uncertainty are somewhat higher than the measurement uncertainty [71]. Time refinement study was performed by decreasing the unsteady time step by a factor 2. The results show perfect agreement with the baseline time step size, and indicate that the solution is converged based on time step size. Spatial mesh refinement is performed as indicated in the mesh section. The refined mesh shows overall the same results as the baseline mesh.

Fig. 8.3 shows the CFJ pitching airfoil  $C_l$ ,  $C_d$  and  $C_m$  during the oscillation cycle at  $C\mu = 0.08$ . The maximum  $C_l$  increased from roughly 1.4 for the baseline airfoil to almost

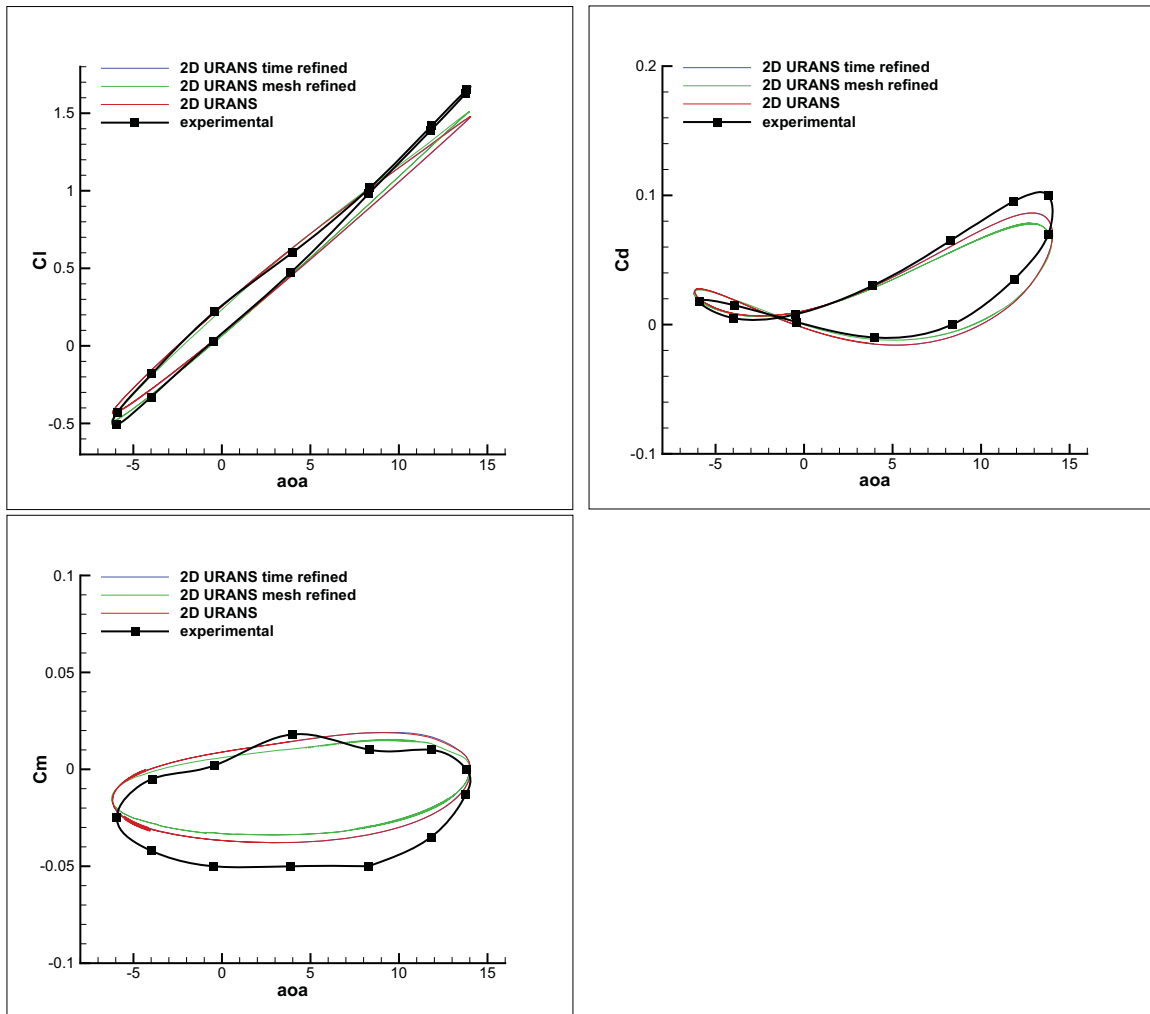


Figure 8.2: Baseline pitching airfoil  $C_l$ ,  $C_d$  and  $C_m$  compared with experimental data for the no-stall case.

1.8 for the CFJ airfoil. The  $C_d$  is decreased and remain negative during part of the plunging motion. The  $C_m$  variation is smooth.

#### 8.1.4 Baseline Airfoil Undergoing Mild-Stall Oscillation

Fig. 8.4 shows the baseline SC1095 pitching profile instantaneous Mach contour with streamlines at different AoA for the mild-stall case. The dynamic stall process is well captured with the flow attached at low AoA and a large separation moving dynamically at high AoA. The stall originates from the TE of the pitching airfoil.

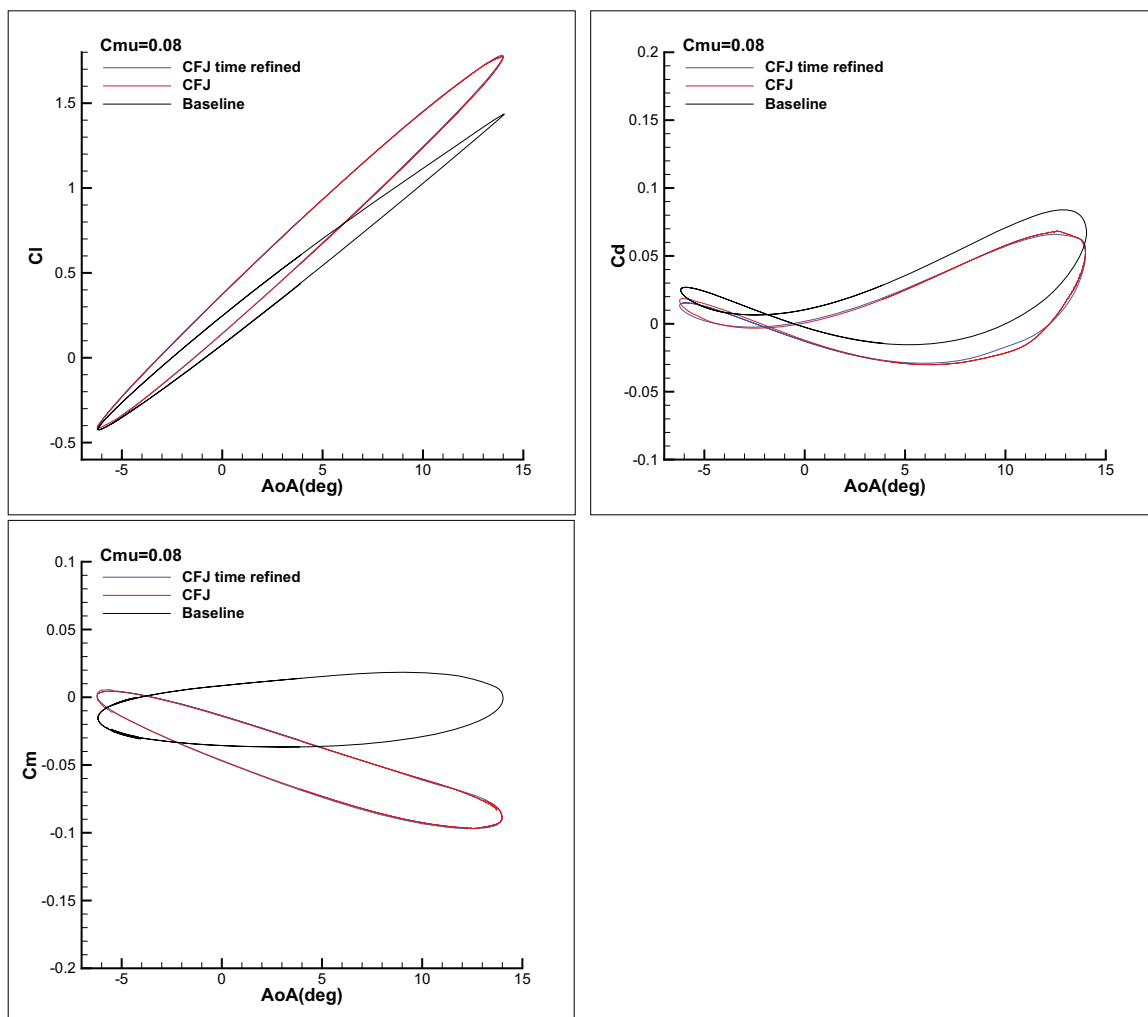


Figure 8.3: CFJ pitching airfoil  $C_l$ ,  $C_d$  and  $C_m$  compared with baseline calculation for the no-stall case.

Fig. 8.5 shows the computed baseline results for  $C_l$ ,  $C_d$  and  $C_m$  compared with the experimental data. Similarly to previous case, good agreement exists between the data at lower AoA. However the lift is once again under-predicted at high AoA with a difference of 5% for the peak value, which is within the measurement uncertainty [71]. Also stall shape prediction varies. It appears that the 2D URANS model does not capture accurately the complicated turbulence during a dynamic stall and predicts a sharper stall. The moment coefficient is in good agreement except for the over-estimated peak value. The drag prediction is in good agreement with a slight under-prediction at low AoA and a peak value that matches the experiments. Time refinement study was performed by decreasing the

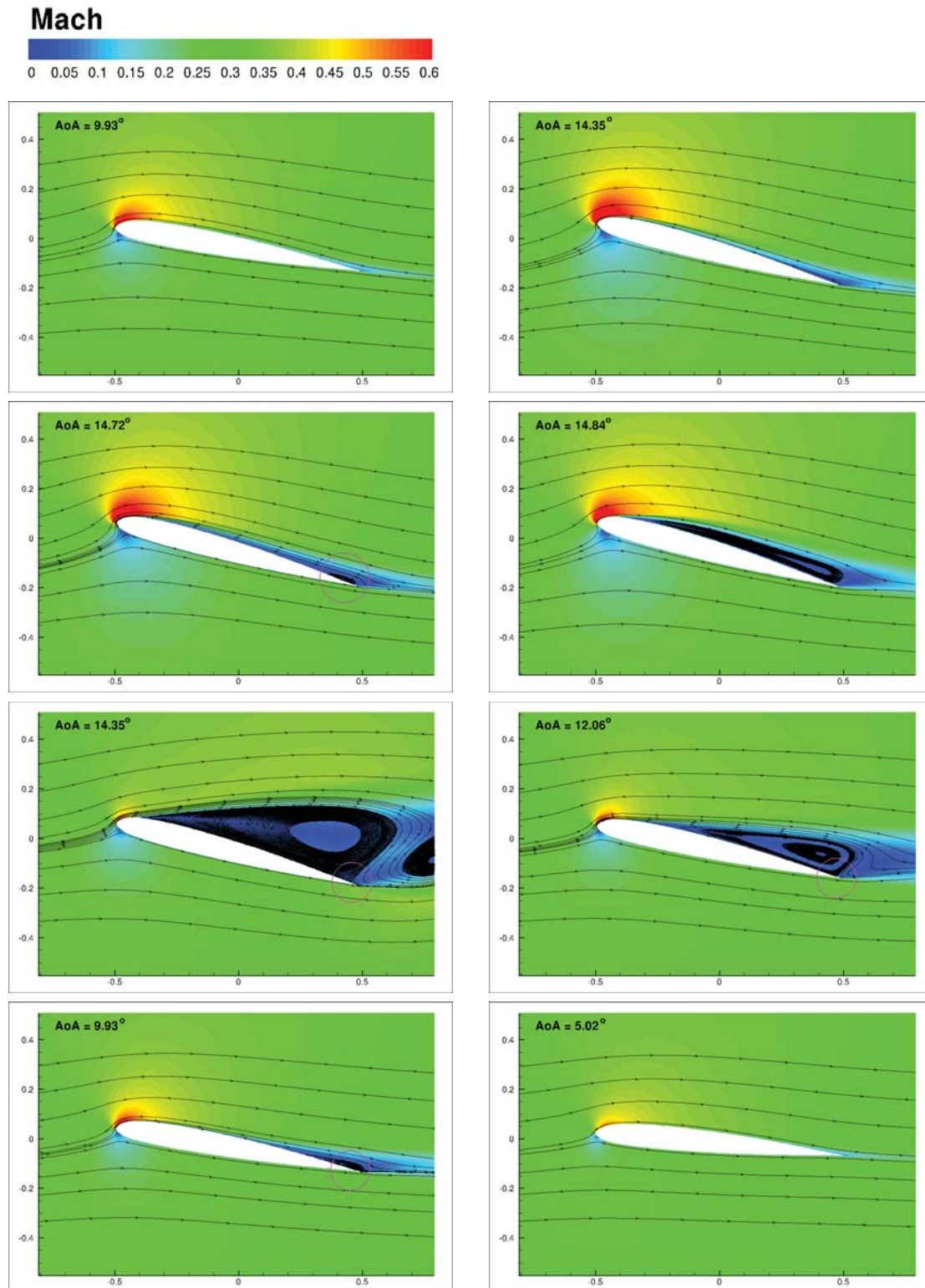


Figure 8.4: Instantaneous Mach contour of the baseline pitching airfoil with streamlines at different AoA for the mild-stall case.

unsteady time step by a factor of 2. The results show an excellent agreement with the baseline time step. The spatial mesh refinement basically gives the same results with a slight improvement.

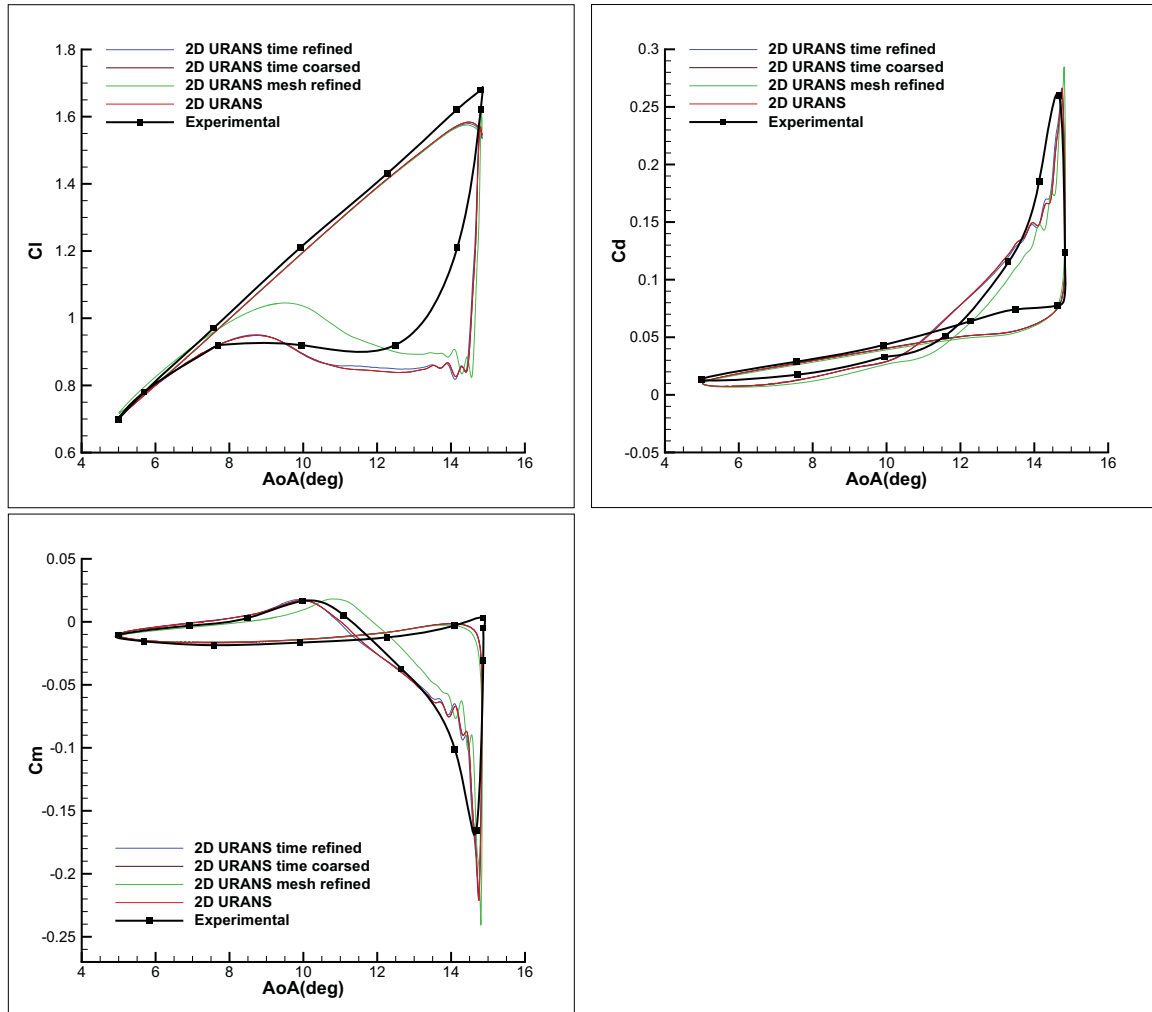


Figure 8.5: Baseline pitching airfoil  $C_l$ ,  $C_d$  and  $C_m$  compared with experimental data for the mild-stall case.

### 8.1.5 CFJ Airfoil Undergoing Mild-Stall Oscillation

Fig. 8.6 shows the CFJ SC1095 pitching airfoil instantaneous Mach contour with streamlines at different AoA for the mild-stall case with  $C_\mu = 0.08$ . A zoomed-in picture of the injection and suction region are added. Those regions use their own scale defined in the

header of the plot. The CFJ completely removes the dynamic stall for the mild-stall case at relatively low  $C_{\mu}$ .

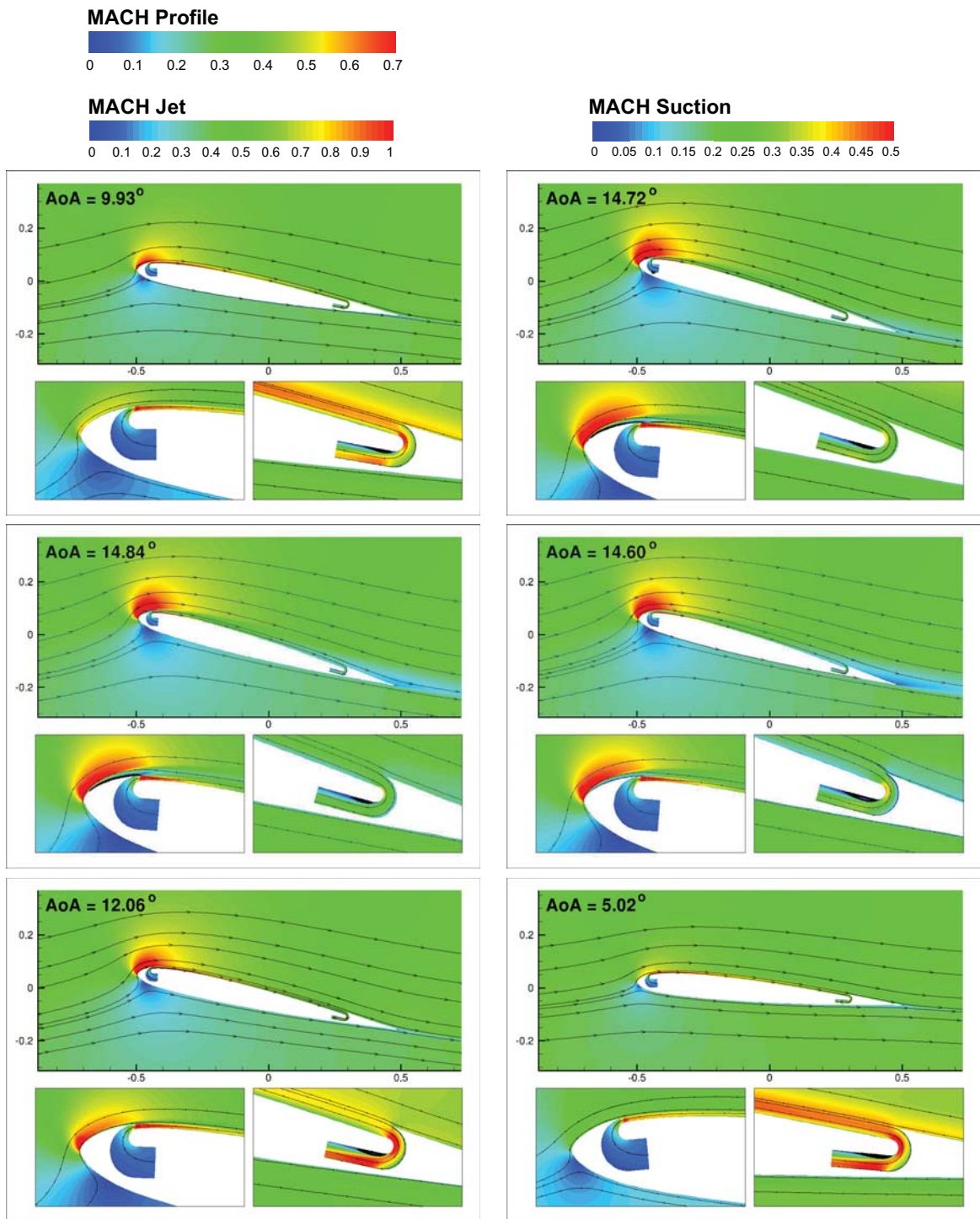


Figure 8.6: Instantaneous Mach contour of the CFJ pitching airfoil at  $C_{\mu} = 0.08$  with streamlines at different AoA for the mild-stall case.

The LE suction surface peak velocity reaches  $M \approx 0.7$ , greater than the baseline peak velocity of  $M \approx 0.6$ . The very strong LE adverse pressure gradient generates a small LE flow recirculation at high AoA which interacts with the jet and dissipate some of its energy. This results in an increased wake and increase in the jet strength or  $C_\mu$  necessary to prevent the dynamic stall.

Fig. 8.7 shows the CFJ pitching airfoil  $C_l$ ,  $C_d$  and  $C_m$  during the oscillation cycle at  $C_\mu = 0.08$ . The CFJ pitching airfoil reaches an increase of lift by up to a factor of 2.2 with an associated drag reduction by a factor of 6.2. The drag is negative during most of the pitching motion and remains very low otherwise.

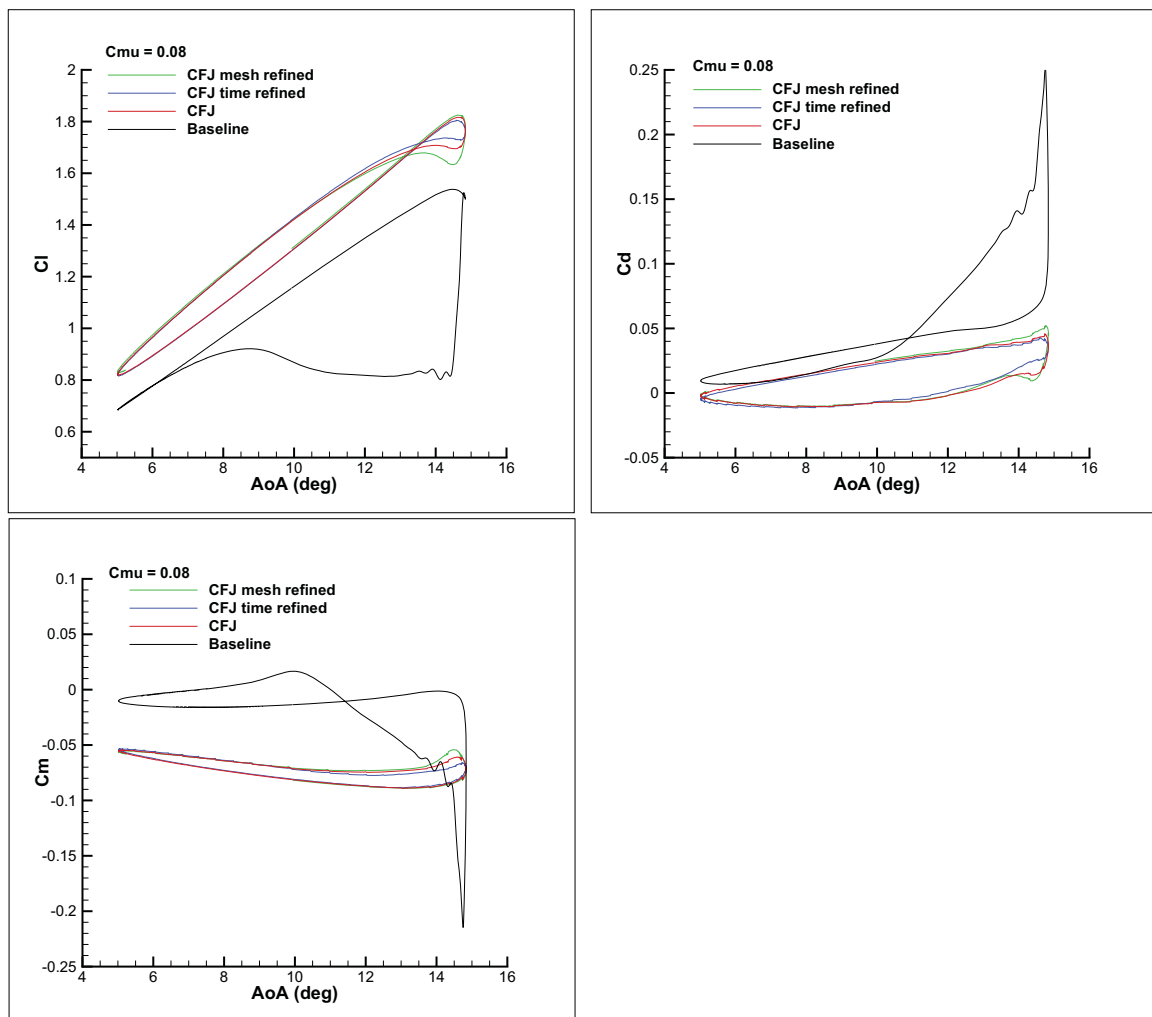


Figure 8.7: CFJ pitching airfoil  $C_l$ ,  $C_d$  and  $C_m$  compared with Baseline calculation for the mild-stall case.

The top of Fig. 8.8 shows the injection and suction mass flow during the oscillation. The mean injection mass flow is  $M_{inj} = 0.0137$  while the mean suction mass flow is  $M_{suc} = 0.0134$  which is a 2.2% difference. Due to the pitching oscillation, the static pressure of the main flow at CFJ injection location also oscillates with the AoA. To maintain a constant injection mass flow rate, the injection total pressure hence needs to be oscillating as shown in the bottom of Fig. 8.8. At high AoA, the suction surface pressure behind the airfoil LE is lower, hence a lower injection total pressure is needed to maintain a constant injection mass flow rate. At low AoA, the suction surface pressure behind LE is higher, a higher injection total pressure is used to achieve the same mass flow rate.

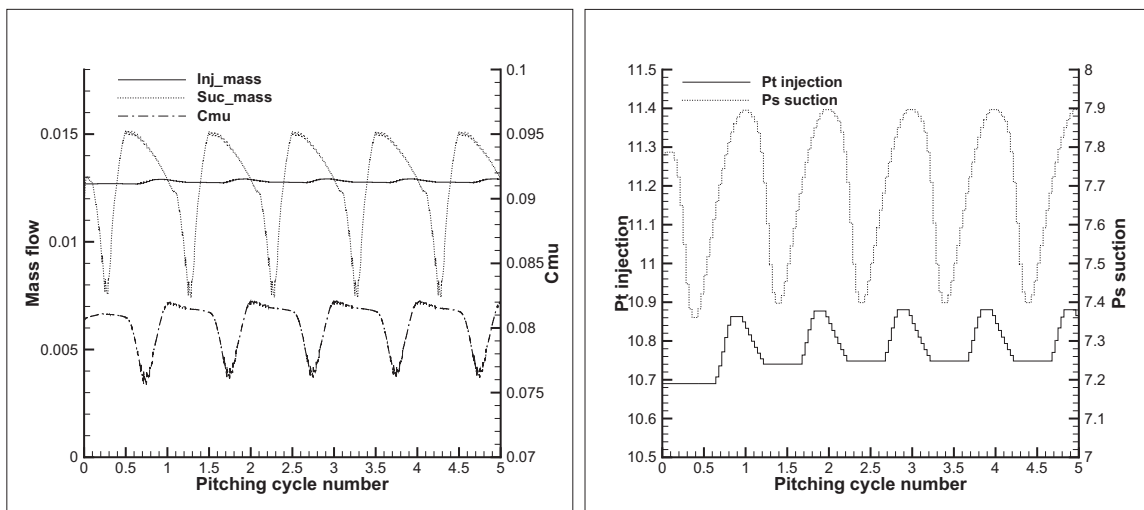


Figure 8.8: Evolution of injection mass flow, suction mass flow and  $C_{\mu}$  (top) and injection and suction pressure (bot) with the oscillation cycle for the mild-stall case.

The bottom of Fig. 8.8 shows the oscillation of the suction cavity static pressure and mass flow. At low AoA, a lower suction pumping power is required due to the high jet momentum at the suction slot. In consequence the suction cavity static pressure remains relatively high. At large AoA, the LE wake size increases and an increasing share of the jet momentum is used to re-energize the wake. The available jet momentum at the suction slot decreases and a lower suction cavity static pressure is used to keep the mass flow steady. At the end of the pitching motion, deprived of the incoming jet momentum, the suction slot fails for a brief instant to suck in the required mass flow.

At high AoA, lowering further the suction cavity pressure had little effect on the suction mass flow. This suggest other solutions have to be implemented to keep the suction mass flow steady. Those solutions include reducing the LE wake by modifying the airfoil profile and/or put the injection slot at more aft position. Using a variable geometry suction slot that would open up the suction slot when more pumping power is required. Finally using of a buffer zone inside the injection or suction cavities to allow the CFJ airfoil to work properly with a brief difference between injection and suction mass flow.

Fig. 8.9 shows the computed  $C_p$  coefficient on the wall for the baseline and the CFJ profile. A jump occurs at the injection and suction slots as the  $C_p$  is measured on discontinuous wall surfaces. The suction surface loading is significantly higher than the baseline airfoil, which gives a higher lift.

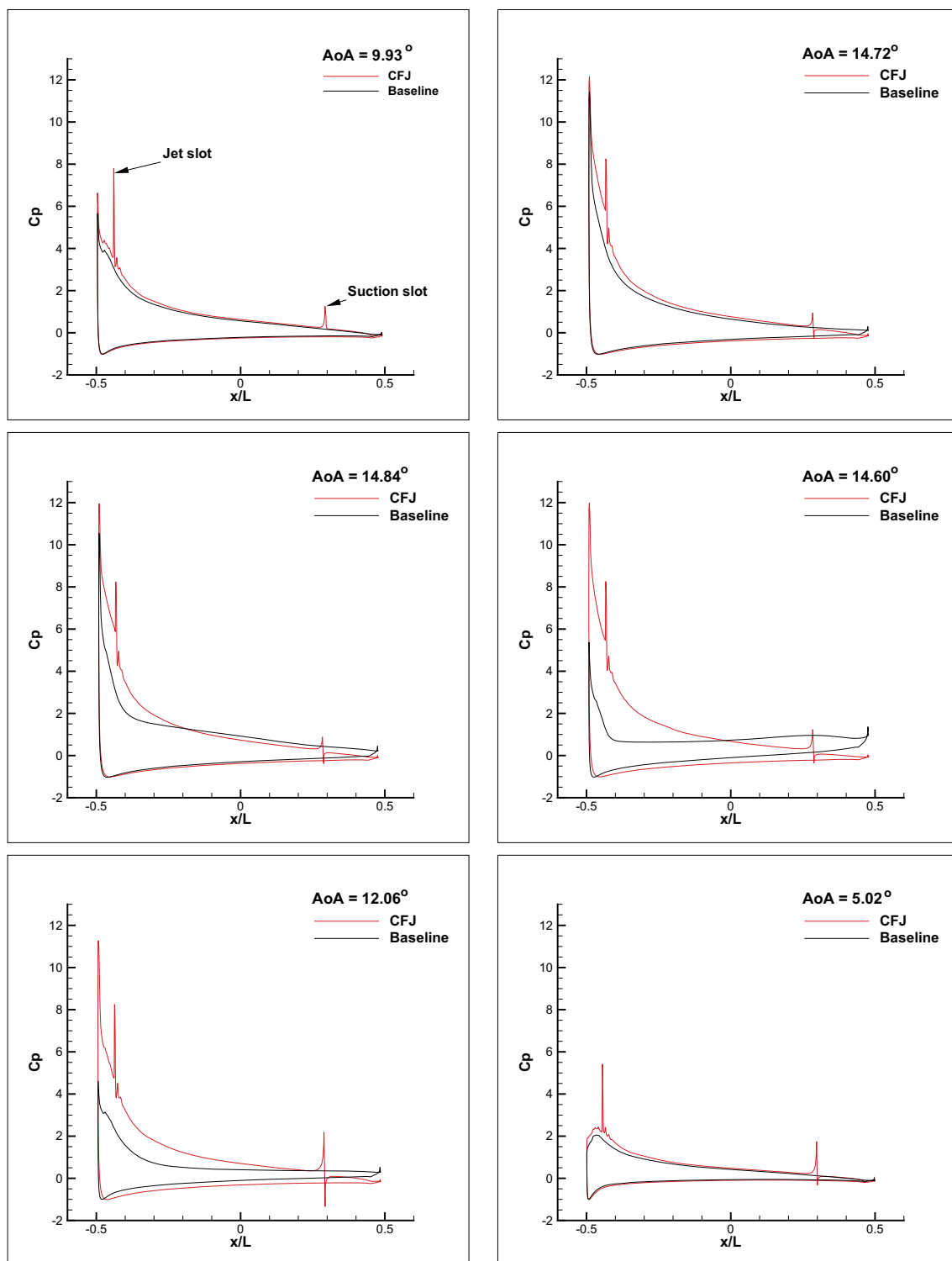


Figure 8.9: Numerically obtained pressure coefficient comparison between CFJ pitching airfoil and baseline pitching airfoil for the mild-stall case.

### 8.1.6 Baseline Airfoil Undergoing Deep-Stall Oscillation

Fig. 8.10 shows the baseline SC1095 pitching airfoil instantaneous Mach contour with streamlines at different AoA for the deep-stall case. It clearly exhibits a massive separation that originates from the LE and moves to the TE. Compared with the mild-stall case, the flow separation inception location differs and the separation region is significantly larger due to the higher maximum AoA.

Fig. 8.11 shows the computed baseline results for  $C_l$ ,  $C_d$  and  $C_m$  compared with the experimental data. Fairly good agreement is obtained between computation and experiment. The numerical simulation tends to stall slightly earlier by about  $1^\circ$  and in a sharper manner than the experiments. The peak lift is slightly under-predicted but remains within the measurement uncertainty [71]. The mesh and time refinement results agree very well with the baseline mesh and time step with some slight difference in the stall region of the oscillation. When compared with 2D calculations from other research laboratories, the results displayed show some improvement on the overall forces predictions [100].

### 8.1.7 CFJ Airfoil Undergoing Deep-Stall Oscillation

To study the CFJ effect on the deep-stall case, 3 CFJ geometries are created as seen in Table 8.2. The  $C_\mu = 0.08$  albeit beneficial for the mild-stall case, fails to remove the deep-stall. For this reason higher  $C_\mu$  are selected depending on the geometry slot size.

Fig. 8.12, 8.13 and 8.14 show the instantaneous Mach contour of the CFJ SC1095 geometry 1, 2 and 3 with streamlines at different AoA and  $C_\mu$  for the deep-stall case. A zoomed-in picture of the injection and suction region are added. Those regions use their own scale defined in the header of the plot.

Geometry 1 strongly mitigate the deep-stall negative effects at  $C_\mu = 0.12$ . Fig. 8.15 shows the dynamic stall that occurs only during a limited range of AoA. At high AoA, the large adverse pressure gradient at the LE creates a localized micro-recirculation. At  $AoA = 18.50^\circ$  the LE micro-recirculation and its associated wake reach their peak size. The

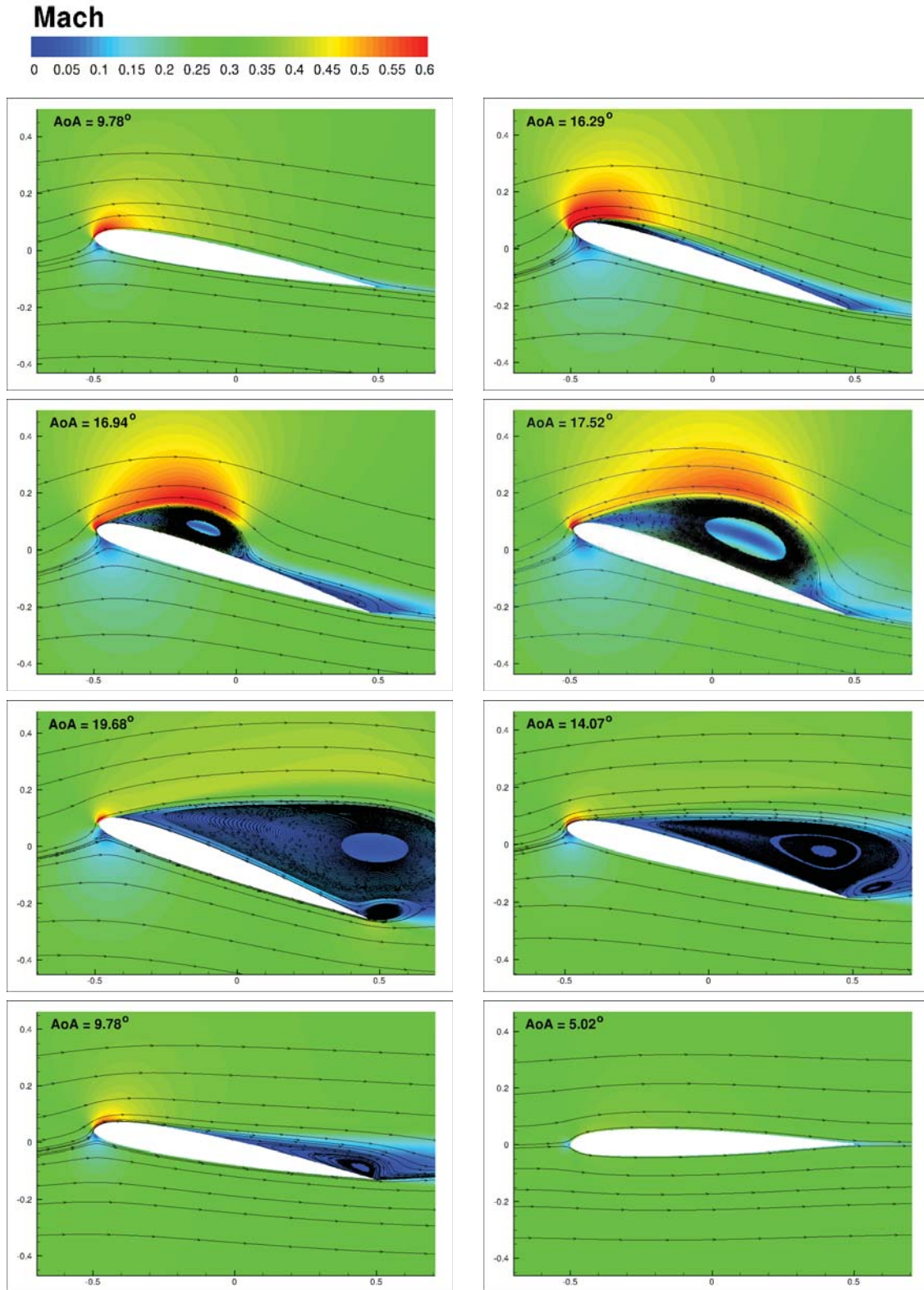


Figure 8.10: Instantaneous Mach contour of the baseline pitching airfoil with streamlines at different AoA for the deep-stall case.

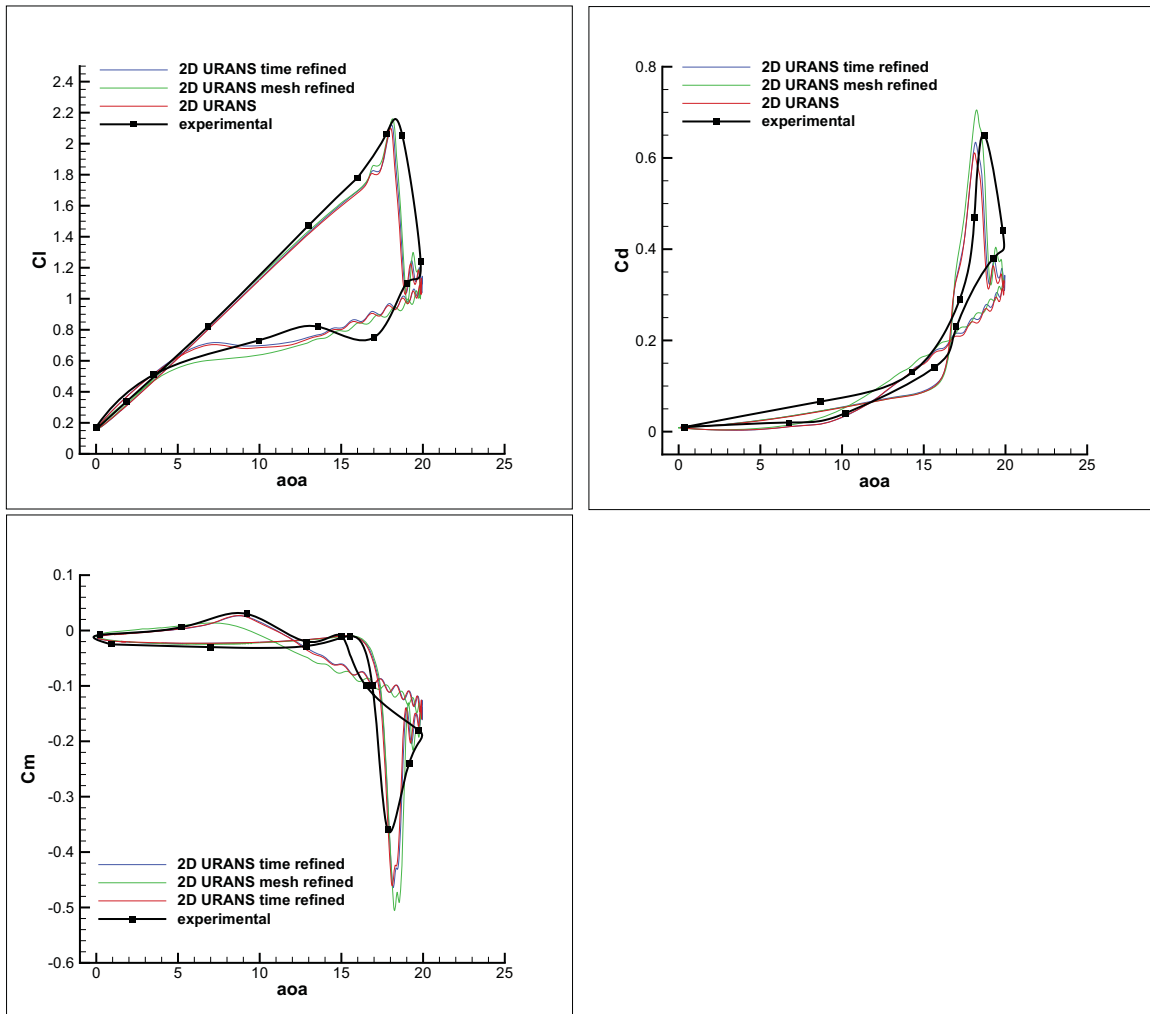


Figure 8.11: Baseline pitching airfoil  $C_l$ ,  $C_d$  and  $C_m$  compared with experimental data for the deep-stall case.

jet is too weak to re-energize the low speed wake flow and a recirculation region develops close to the TE of the wing. At  $AoA = 19.52^\circ$  the TE micro-recirculation recedes and the flow reattaches. The abrupt change of  $C_p$  seen at the bottom of Fig. 8.15 coincides with the growth and burst of the LE micro-recirculation. The LE suction surface peak velocity reaches  $M \approx 0.8$ , greater than the baseline peak velocity of  $M \approx 0.6$ . Interestingly the low ambient pressure above the jet exit slot at large AoA allows the supersonic jet to expand and to reach higher velocity than the jet exit. Low supersonic jets are more costly to produce than subsonic jets, but they carry extra momentum that is beneficial from a performance point of view. However achieving jet velocity above roughly  $M = 2.0$  is expected to trigger

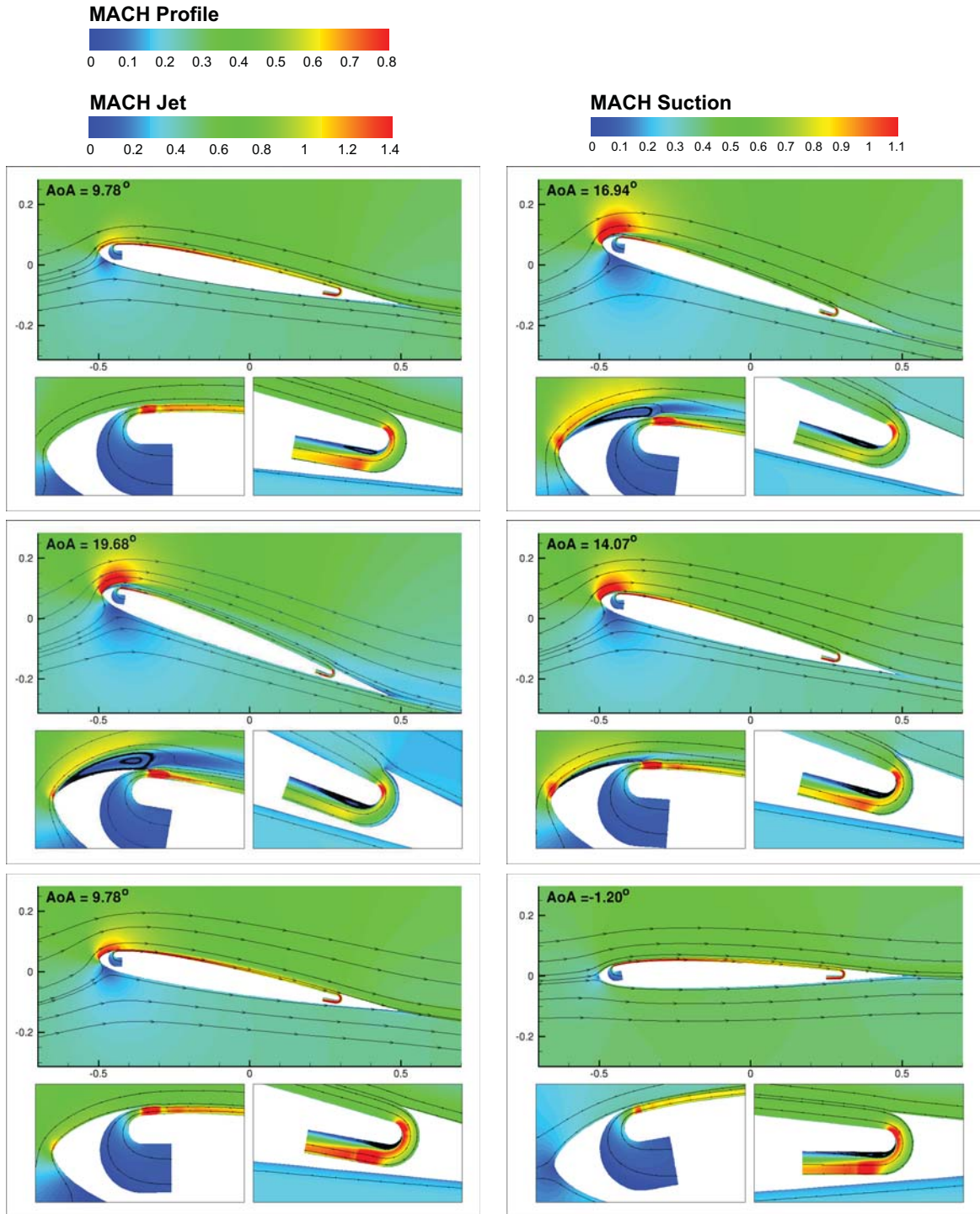


Figure 8.12: Instantaneous Mach contour of the CFJ pitching airfoil geometry 1 at  $C\mu = 0.12$  with streamlines at different AoA for the deep-stall case.

strong lambda shock wave and to create an earlier stall as seen in previous steady airfoil study [61].

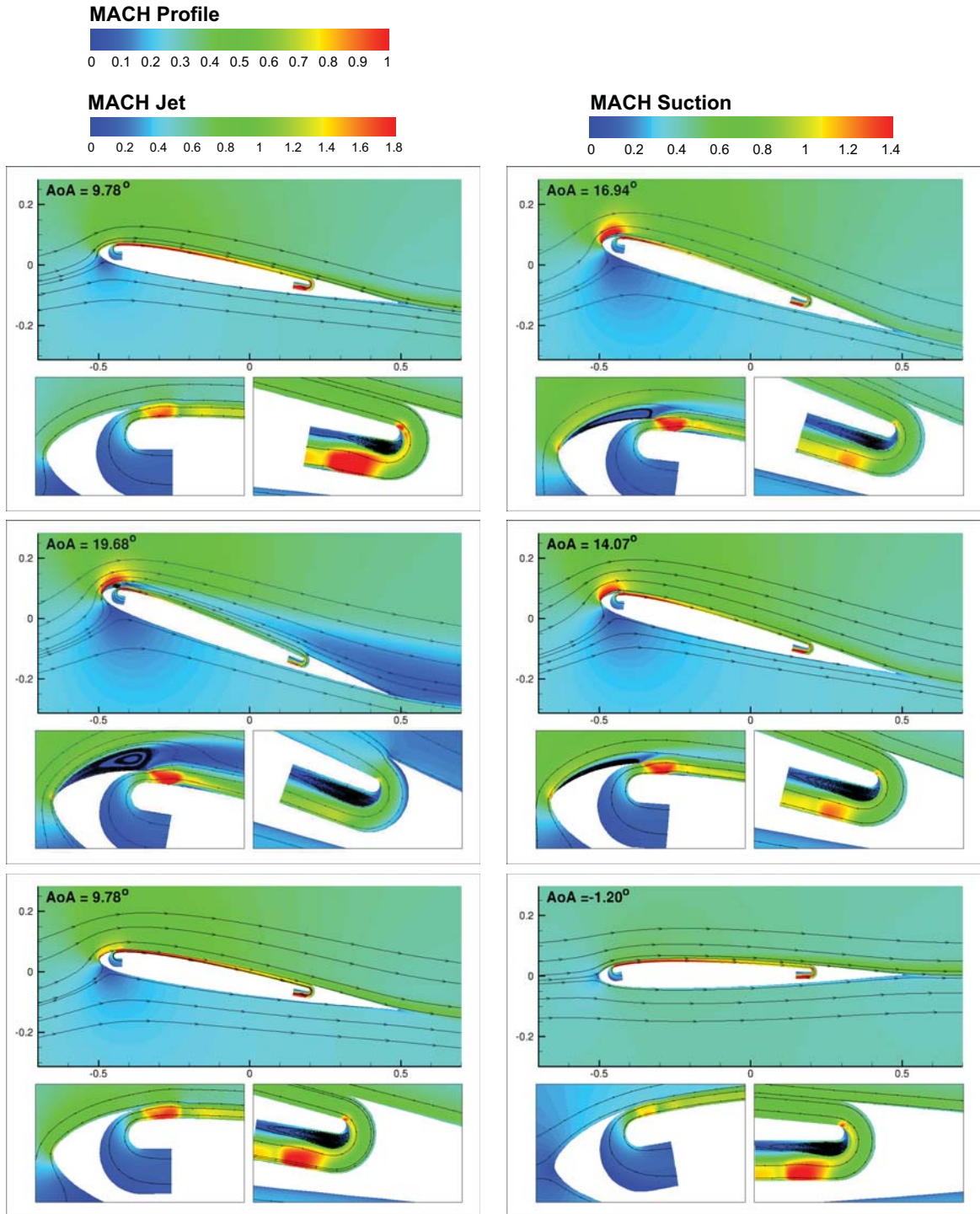


Figure 8.13: Instantaneous Mach contour of the CFJ pitching airfoil geometry 2 at  $C_{\mu} = 0.20$  with streamlines at different AoA for the deep-stall case.

Geometry 2 and geometry 3 completely remove the dynamic stall at  $C_{\mu} = 0.20$  and  $C_{\mu} = 0.24$  respectively. The size of the jet slot shows no influence on the LE micro-

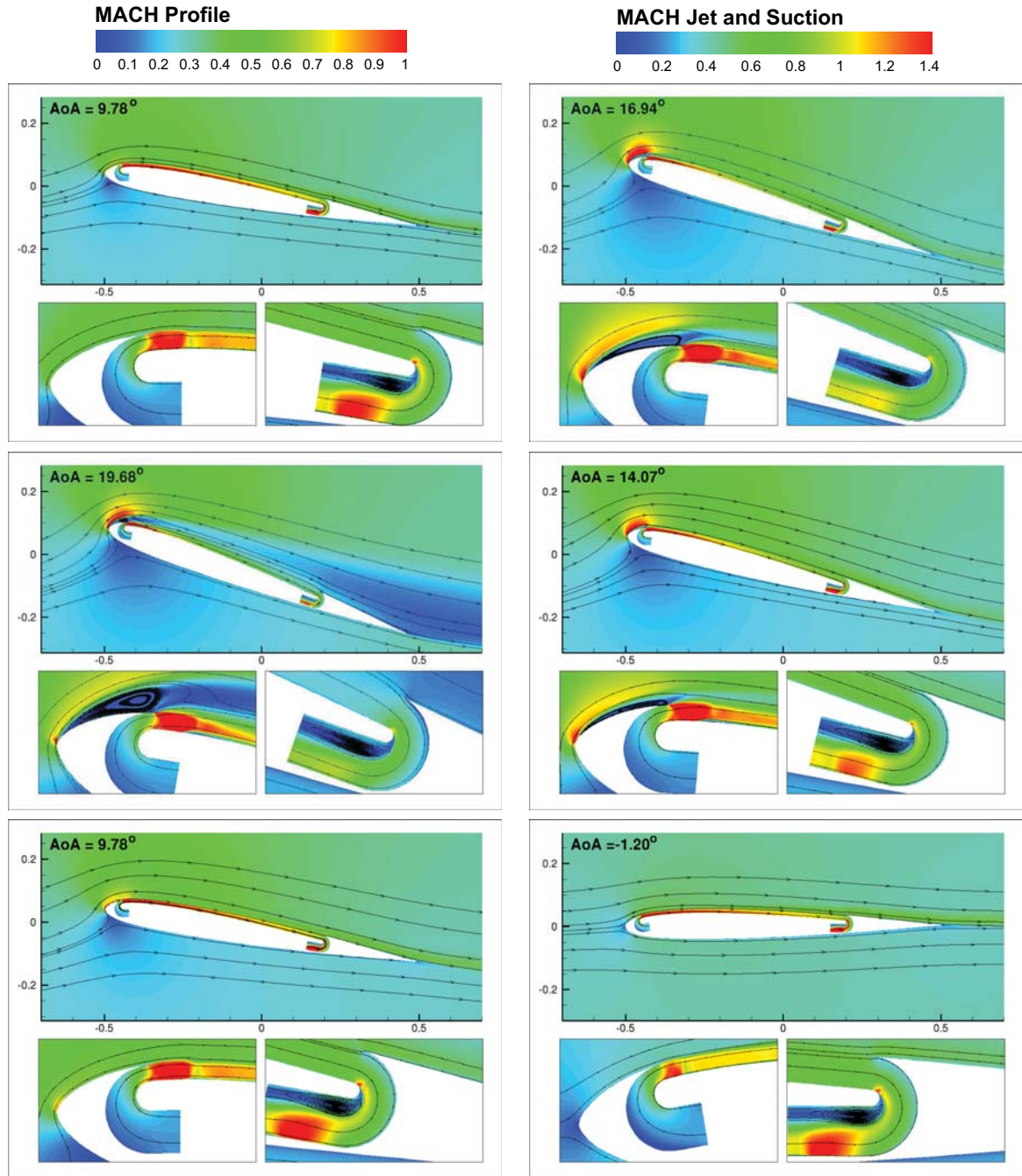


Figure 8.14: Instantaneous Mach contour of the CFJ pitching airfoil geometry 3 at  $C_{\mu} = 0.24$  with streamlines at different AoA for the deep-stall case.

recirculation size. The larger jet slot high of geometry 3 allow to reach higher  $C_{\mu}$  at a relatively low jet velocity. This makes the geometry 3 jet more cost effective at similar  $C_{\mu}$  than geometry 2. The LE suction surface peak velocity reaches  $M \approx 1.0$ .

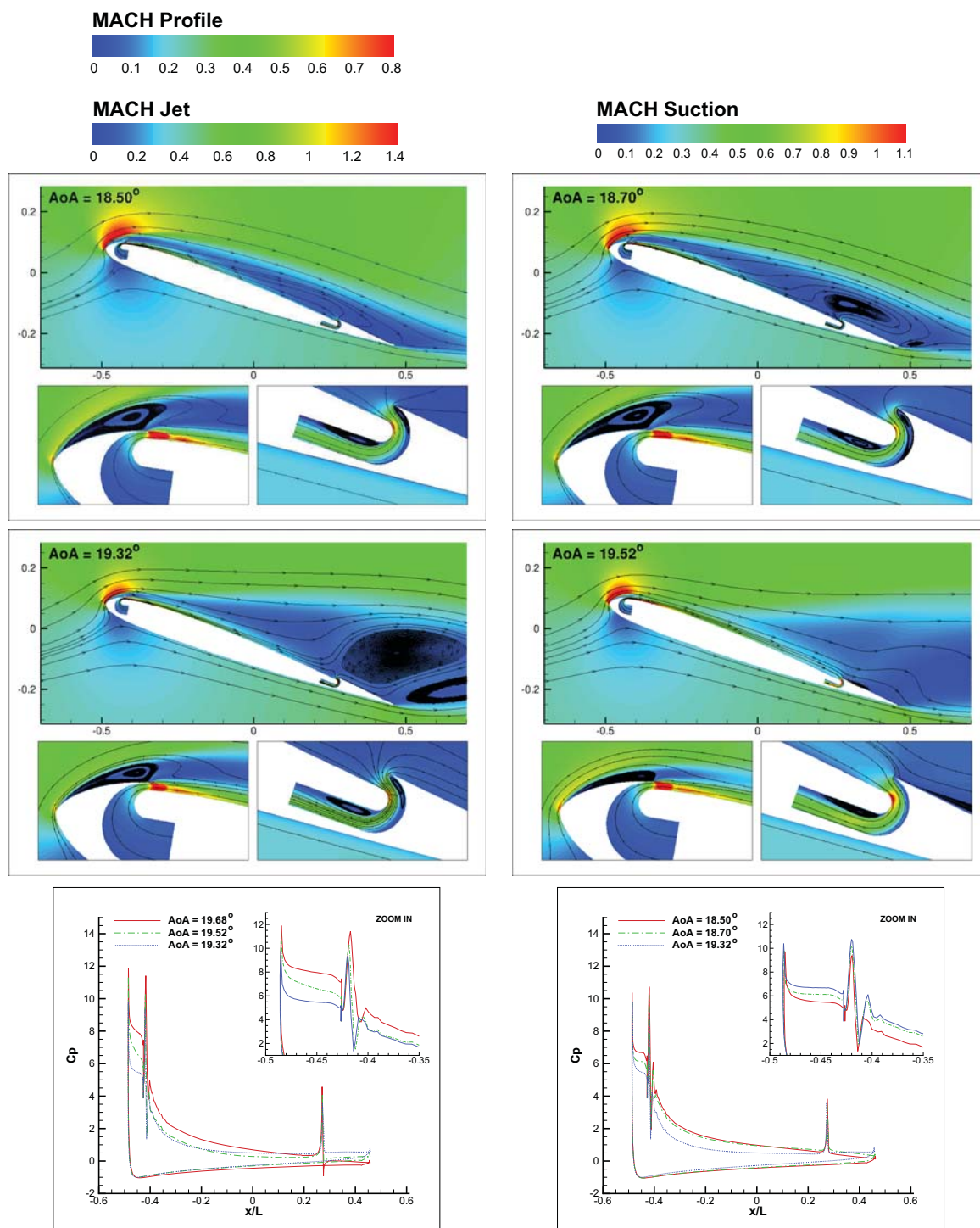


Figure 8.15: Dynamic-stall analysis using the instantaneous Mach contour and pressure coefficient of the CFJ pitching airfoil geometry 1 at  $C\mu = 0.12$ .

Fig. 8.16 shows the CFJ pitching airfoil  $C_l$ ,  $C_d$  and  $C_m$  during the oscillation cycle for geometry 1, 2 and 3. Each geometry uses a different  $C\mu$  depending on the jet exit size.

Geometry 1 mitigates the dynamic stall negative effects and provide higher lift and reduced drag compared to the baseline pitching airfoil. The moment peak associated with the deep-stall remains contained which indicates that this flight regime would be acceptable from a mechanical and maneuverability point of view. Geometry 2 and 3 completely remove the dynamic stall and provide an increase of lift by up to a factor of 2.1 with an associated drag reduction by a factor of 6.0. The drag is negative during most of the pitching and plunging motion. There is no abrupt change of  $C_m$  during the pitching cycle.

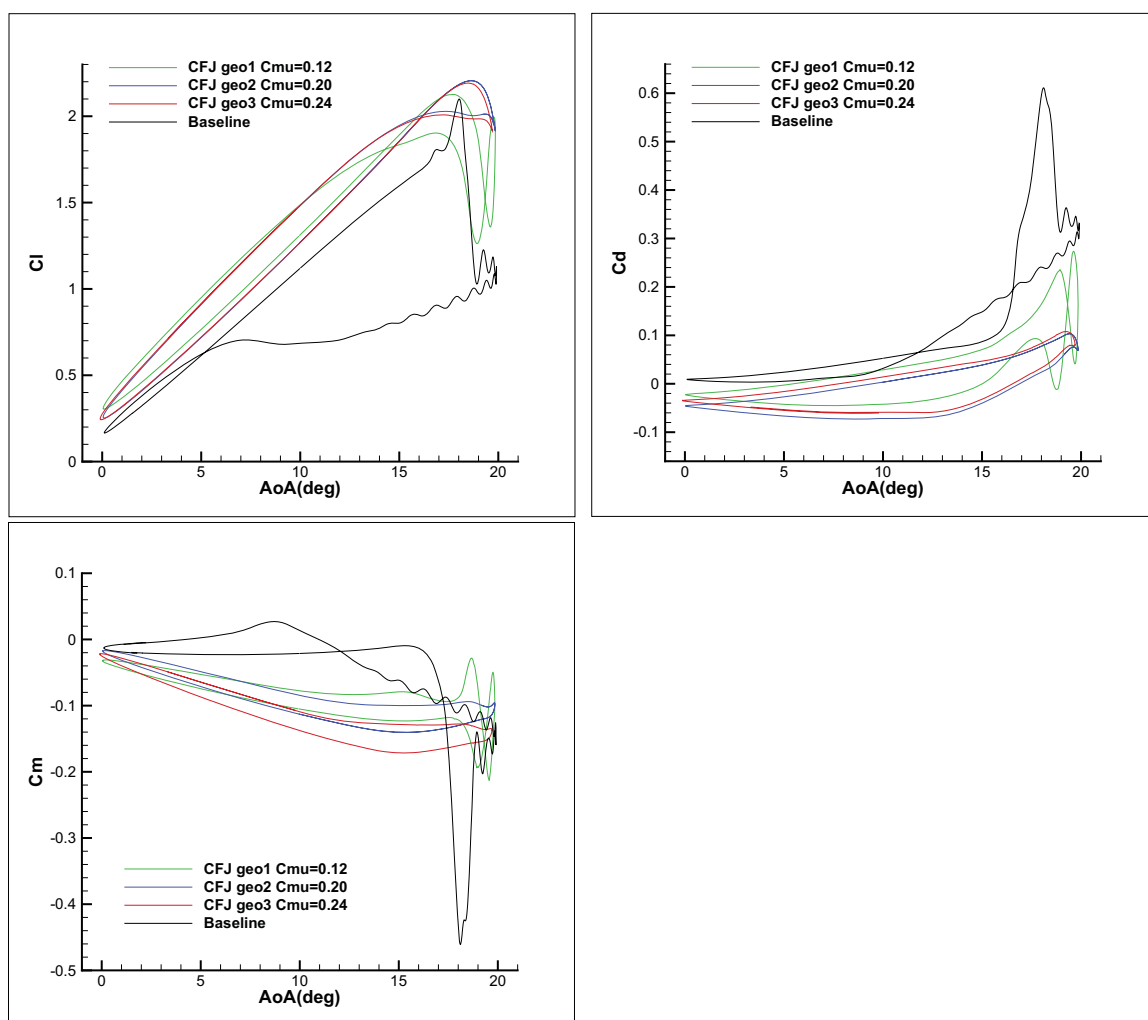


Figure 8.16: CFJ pitching airfoil  $C_l$ ,  $C_d$  and  $C_m$  compared with Baseline calculation for the deep-stall case.

Fig. 8.17 shows the computed  $C_p$  coefficient on the wall for the baseline and the different CFJ geometries. The injection and suction  $C_p$  jumps are more important due to the

higher  $C_{\mu}$ . Geometry 2 which features the highest jet exit pressure show the highest  $C_p$  jump. As the LE micro-recirculation is created,  $C_p$  increases. Once the micro-recirculation further develop  $C_p$  drops abruptly. This explains the  $C_l$  sharp peak just before the deep-stall as seen Fig. 8.11. The suction surface pressure is significantly lower than the baseline airfoil, thereby the lift is increased.

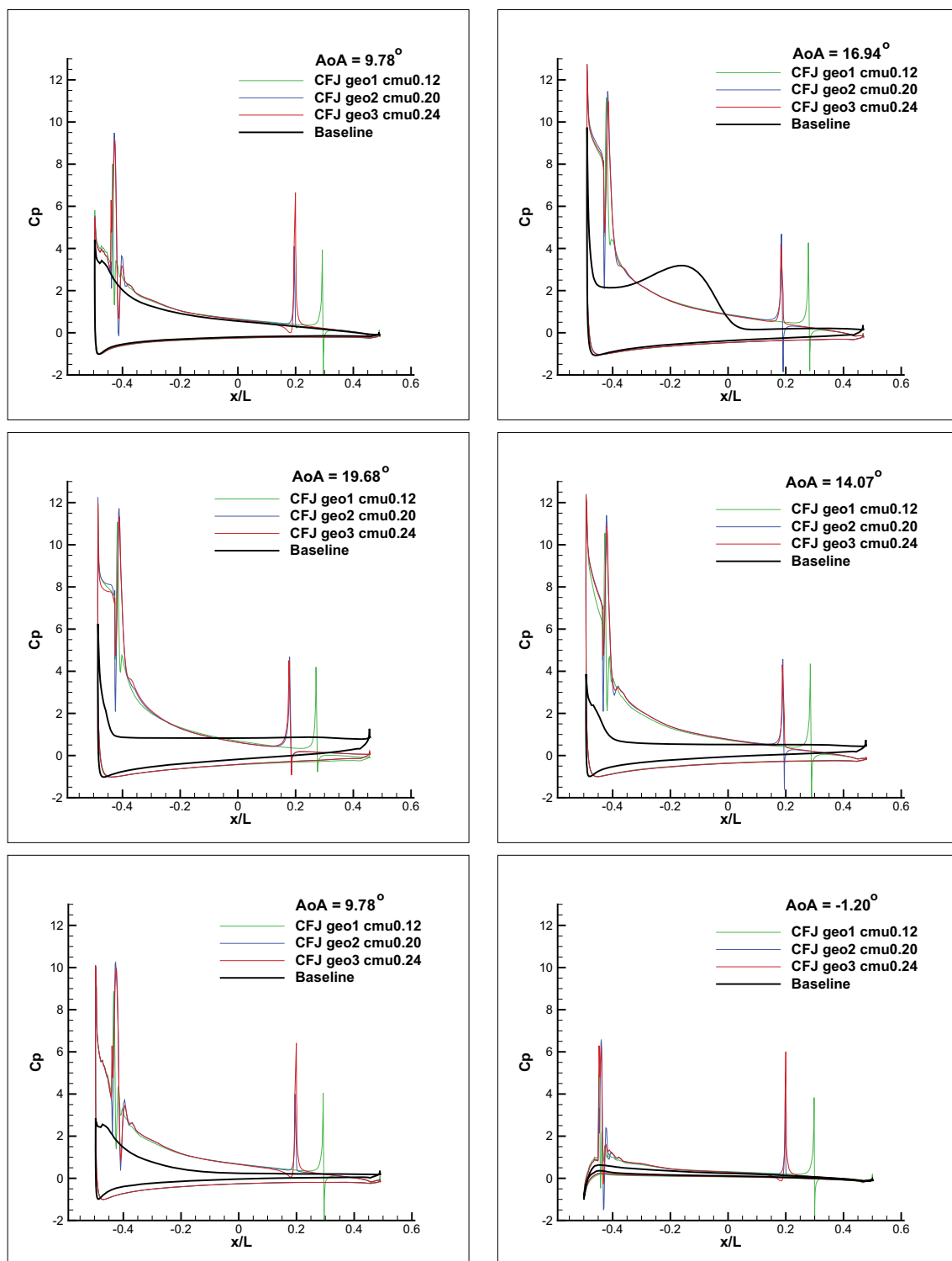


Figure 8.17: Numerically obtained pressure coefficient comparison between 3 CFJ pitching airfoil geometries and baseline pitching airfoil for the deep-stall case.

Case	$C\mu$	$Cl_{ave}$	$Cd_{ave}$	$\Delta Cm$	$(L/D)_{ave}$
No-stall baseline	X	0.51	0.027	0.05	19.2
Mild-stall baseline	X	1.01	0.053	0.23	19.1
Deep-stall baseline	X	0.78	0.114	0.49	6.8
No-stall CFJ geo1	0.08	0.87	0.018	0.10	48.9
Mild-stall CFJ geo1	0.08	1.33	0.011	0.04	118.3
Deep-stall CFJ geo1	0.12	1.23	0.031	0.18	39.9
Deep-stall CFJ geo2	0.20	1.28	-0.008	0.12	-156.0
Deep-stall CFJ geo3	0.24	1.27	7E-4	0.15	1844.4

Table 8.4: Summary of the aerodynamic performance for all the cases studied. The  $(L/D)_{ave}$  consider only the aerodynamic forces applied on the airfoil and not the pumping power.

### 8.1.8 Discussion

The summary of the aerodynamic performance for all the cases studied can be seen in Table 8.4. All the data are time-averaged. The CFJ airfoil increase significantly the aerodynamic performance in all the cases studies. For the deep-stall case using geometry 2 and  $C\mu = 0.20$  the CFJ airfoil thrust overcome the drag, proving the feasibility of a CFJ helicopter blade using its pump as the only source of power. In addition, CFJ airfoils reduce the variation of momentum  $\Delta Cm$  during the pitching cycle, simplifying the rotor design and improving the maneuverability.

## 8.2 CFJ Pitching Airfoils at $M_\infty = 0.4$

### 8.2.1 Mesh

The computation mesh is constructed using the O-mesh topology in order to achieve high quality around the airfoil. The CFJ SC1095 airfoil mesh displayed Fig. 8.18 uses a total of 360 points around the airfoil partitioned into 240 points on suction surface and 120 points on the pressure surface, 180 points in the direction normal to the airfoil with an additional

50 points across the jet. Total mesh size is 77,800 cells, partitioned into 23 blocks for parallel computation.

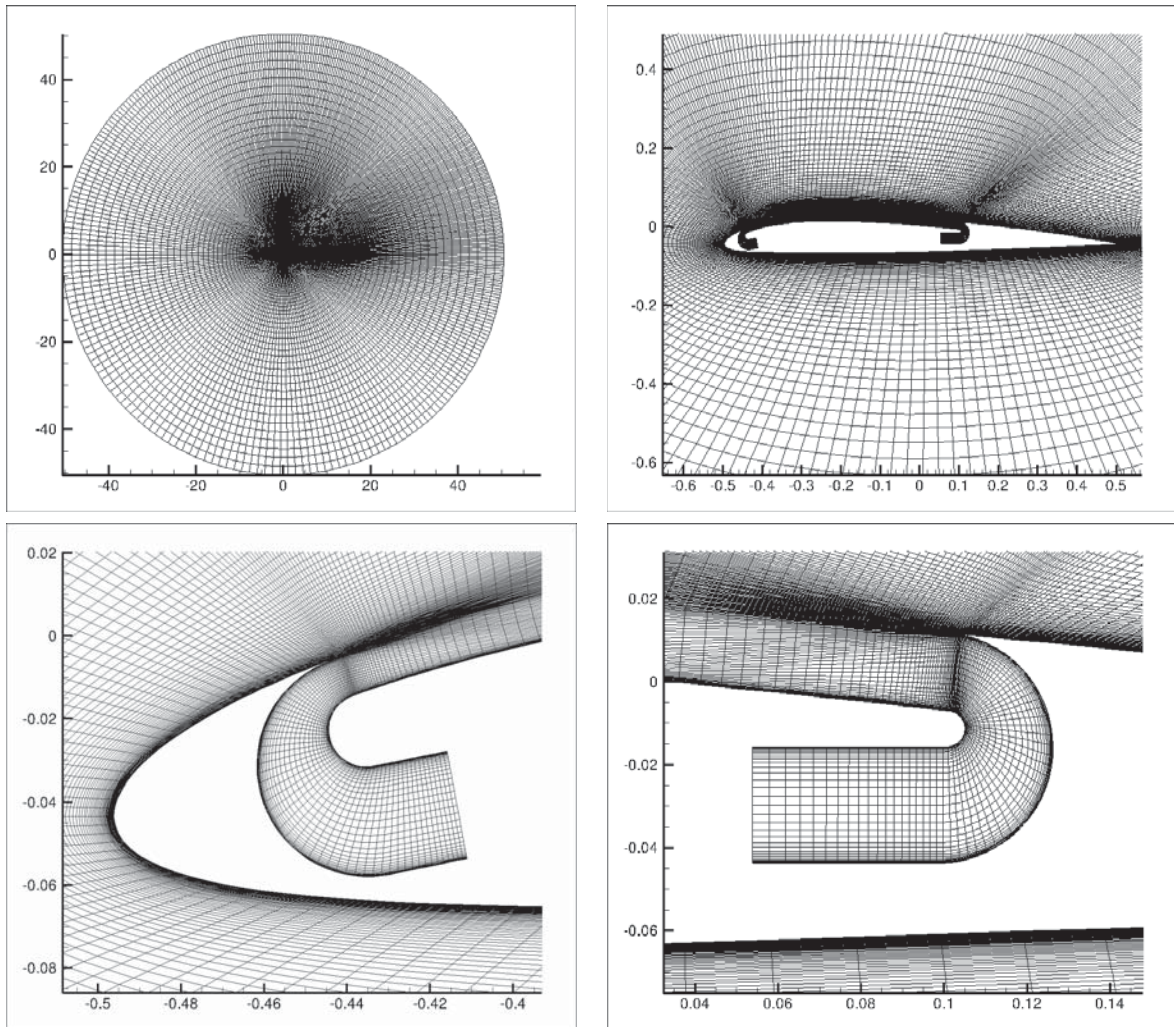


Figure 8.18: Design 3 (CFJ-NACA2209a) airfoil mesh topology. Similar mesh is applied to the other airfoils.

The farfield boundary is located 50 chords away from the airfoil. To resolve the turbulent boundary layer, the first grid point is placed at  $y^+ \approx 0.75$ . The baseline airfoil mesh with no flow control is constructed using the same strategy. The total baseline airfoil mesh size is 54,000 cells with 271 points around the airfoil and 181 points normal to the airfoil. The baseline airfoil mesh is split into 27 blocks for the parallel computing. For both baseline airfoil and CFJ airfoil, a refined grid is constructed using 50% more points in every direction and  $y^+ \approx 0.50$ . Block definition for CFJ airfoil can be found in Table 8.1.

### 8.2.2 Geometry and Oscillation Description

The baseline SC1095 airfoil used on the UH-60 Black Hawk US-army helicopter is chosen due to the existence of experimental data from NASA [71] at  $M=0.3$ . Those experimental data were validated in [62]. SC1095 CFJ pitching airfoil performs well at  $M=0.3$ . However the performance is decreased at  $M=0.4$  due to a prominent LE stall that is difficult to remove with CFJ. This motivates to create a better CFJ airfoil for  $M=0.4$ . For this purpose we generated 4 airfoils with no LE stall tendency. This is done through the use of moderate camber to transfer part of the adverse pressure gradient from the LE to a more aft position where the jet will help the flow to stay attached. Cambered pitching airfoil generally suffer from larger nose-down moment peak compared to their symmetric counterpart which can make their use problematic [101]. However implementing CFJ on cambered airfoils smoothen the moment coefficient. In other words, CFJ can be implemented on high performance cambered airfoil with only limited nose-down moment. To ensure a reasonable injection jet exit velocity and reduce the jet exit shock structures, the injection slot size is doubled compared to previous study [62]. The suction slot size is also doubled. Finally the suction slot is moved upstream to 60% chord in order to increase the mass flow withdrawn at large AoA. The injection location is kept very close to LE to effectively remove dynamic stall. All airfoils have the same thickness of 9.5% chord to be consistent with the SC1095 airfoil.

Four airfoils are created as the iteration process to improve the performance. The first airfoil, namely Design 1, has a thick rounded LE to give space for the injection cavity and a very upstream injection slot location to prevent LE separation. A small camber is used to prevent LE separation at large AoA and increase the aerodynamic performance. The Design 2 and Design 3 (CFJ-NACA1209 and CFJ-NACA2209a) CFJ airfoils are implemented based on a NACA1209 and a NACA2209. Those airfoils feature a moderate camber of 1.6% respectively 2.4%. The Design 4 CFJ airfoil (CFJ-NACA2209b) is identical to the CFJ-NACA2209a airfoil, at the exception of the injection and suction cavity.

that were redesigned to avoid the internal flow separation. The redesigned injection cavity also features a slightly higher and more uniform jet exit pressure. The airfoils and cavities geometries are shown and compared Fig. 8.19 and Table 8.5

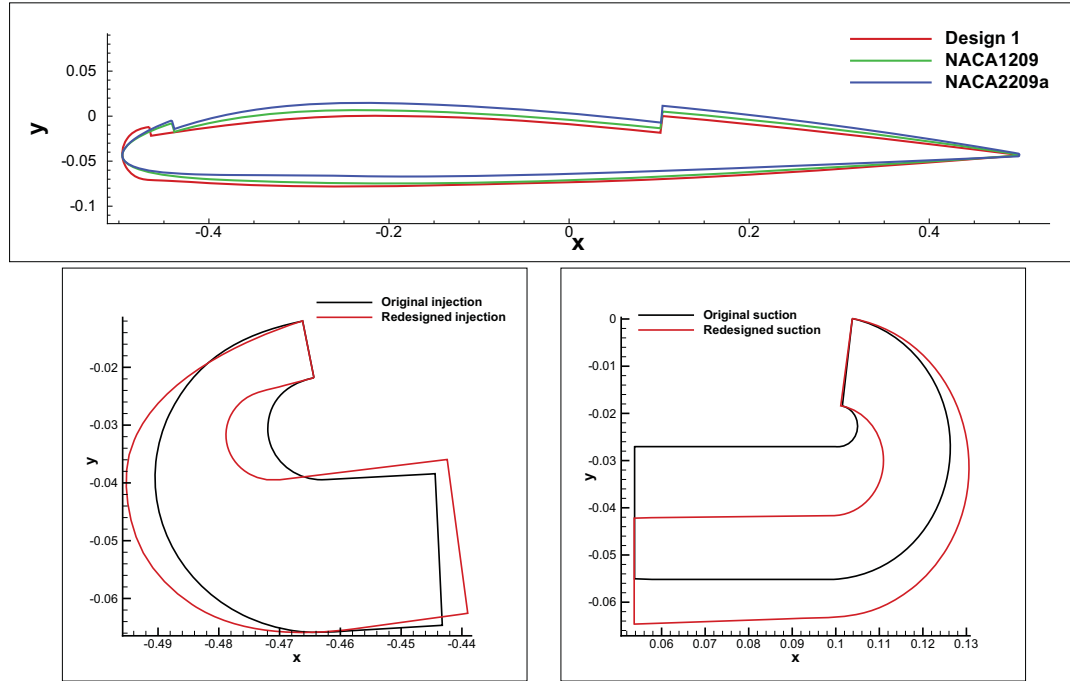


Figure 8.19: Airfoils and cavities geometry comparison.

The Mach number is 0.4 and Reynolds number is  $5.24 \times 10^6$  at reduced frequency 0.10. For the CFJ airfoil, the  $C_{\mu}$  used in this study is in the range of 0.08 – 0.14 for the Design1, Design2 and Design3 airfoils and in the range 0.05 – 0.08 for the low power consumption Design 4 airfoil. The oscillation of the baseline and CFJ airfoils is described by

$$AoA = \alpha_0 + \alpha_1 \sin(k \tau)$$

The parameters of the cases studied are given Table 8.6.

### 8.2.3 Design 1 Airfoil

Due to the absence of experimental data available at  $M=0.4$ , the simulation validation is done at  $M=0.3$  for the SC1095 airfoil. A good agreement is obtained between the computa-

Design	Inj. height	Inj. location	Suc. height	Suc. location	Designed from
1	1.00	5.0	1.50	60.0	Custom
2	1.00	5.0	1.50	60.0	NACA1209
3	1.00	5.0	1.50	60.0	NACA2209
4	1.00	5.0	1.50	60.0	NACA2209

Table 8.5: Pitching airfoil geometry description, length are given in % of chord.

Case name	$\alpha_0$ ( $^\circ$ )	$\alpha_1$ ( $^\circ$ )	k
oscillation 1	10.0	5.0	0.10
oscillation 2	10.0	7.5	0.10
oscillation 3	10.0	10.0	0.10

Table 8.6: Pitching airfoil oscillation description.

tion and the experiment [62]. Also a mesh and time step refinement study are performed for numerous computation cases and very good agreement have been found with the baseline results. All of these validations have laid a good foundation for the numerical simulations below.

The Design 1 baseline and CFJ airfoils flow fields are shown in Figs. 8.20 and 8.21 during oscillation 1. The thick LE generates a strong adverse pressure gradient that triggers an early separation at  $AoA \approx 11.5^\circ$  on the baseline airfoil as seen in Fig. 8.22. The CFJ airfoil increases the LE flow acceleration and the flow becomes choked at upstream of the injection slot. The flow is supersonic downstream of the slot as displayed on Fig. 8.21. The choked injection flow limits the injection energy added to the main flow and the pitching airfoil still has a large separation that is difficult to remove.

When the shock is strong enough, it detaches the BL. Most of the jet energy is lost to the wake of the LE separation. Deprived from the jet momentum, a recirculation region appears at the TE of the airfoil.

This separation is difficult to eradicate with CFJ airfoils. Nevertheless, using a high  $C_\mu$  values, the CFJ airfoil can remove the dynamic stall as seen in Fig. 8.22 for oscillation 1. The oscillation found at  $C_\mu = 0.10$  results from the unsteady shock-BL interaction at

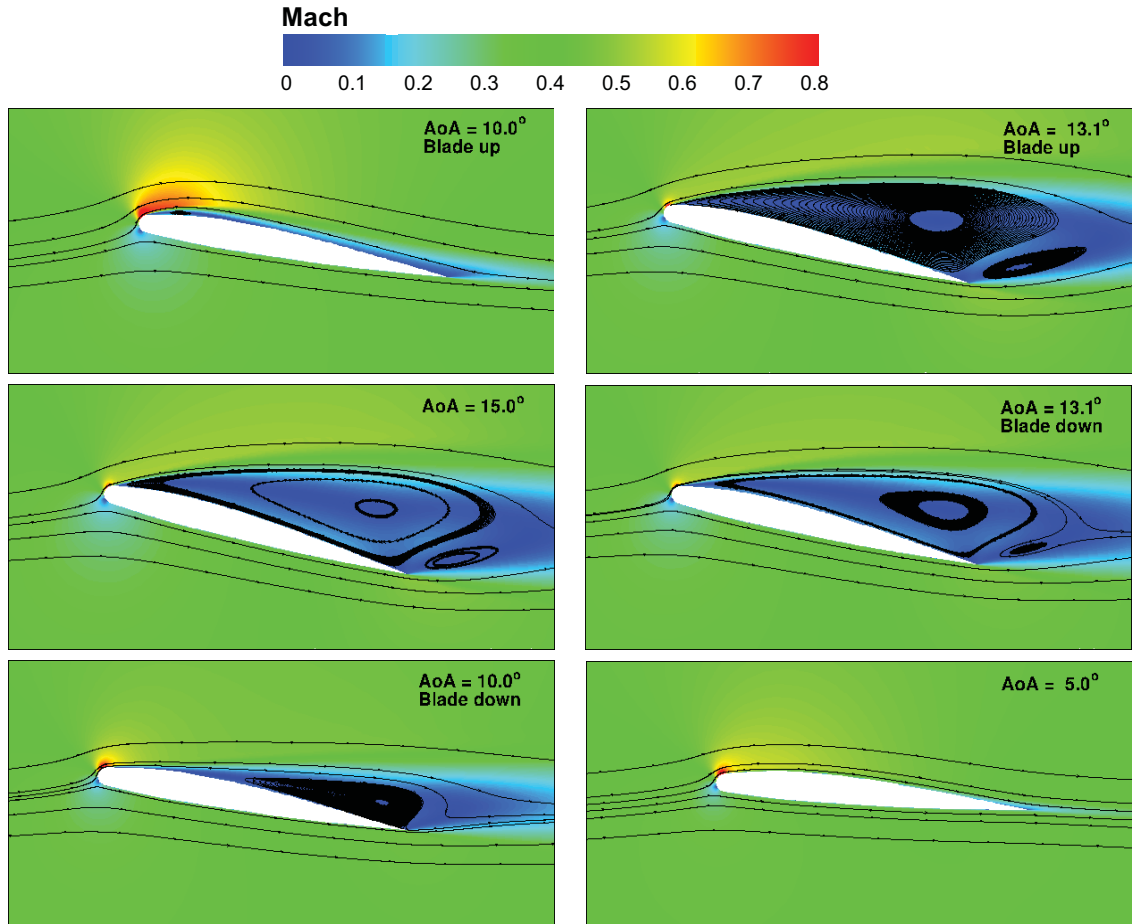


Figure 8.20: Instantaneous Mach contour of the baseline design1 pitching airfoil with streamlines at different AoA during oscillation 1.

the LE of the airfoil. The moment during oscillation 1 is much smoother than the baseline moment for every  $C_{\mu}$  studied. A similar conclusion holds for oscillation 2 and 3, however the unsteady shock-BL interaction becomes severe and offset part of the benefit of CFJ. The time-averaged values for the forces and moment can be seen Fig. 8.23. Those results show an increase of lift and a decrease of drag for all oscillations and  $C_{\mu}$  studied.  $L/D_{ave}$  value reaches 43.3 for oscillation 1 at  $C_{\mu} = 0.14$ . The moment variation amplitude  $\Delta C_m$  is also greatly reduced. The unsteady shock-BL interaction increases the moment amplitude.

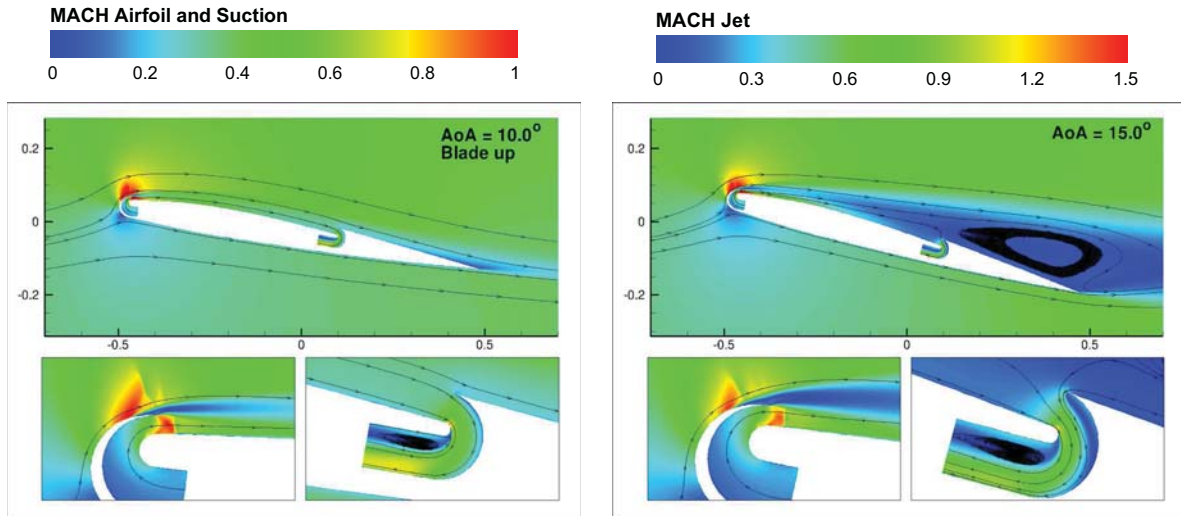


Figure 8.21: Instantaneous Mach contour of the CFJ Design 1 pitching airfoil at  $C_{\mu} = 0.08$  with streamlines at different AoA during oscillation 1.

#### 8.2.4 Design 2 (CFJ-NACA1209) and Design 3(CFJ-NACA2209a) Airfoils

The NACA2209 baseline airfoil flow field is seen in Fig. 8.24 during oscillation 1. The flow field appears to be more attached than the baseline airfoil.

After implementing CFJ, the LE acceleration is contained during oscillation 1 and a weak shock wave appears at the airfoil LE. The shock intensity increases during oscillation 2 and 3. The dynamic stall is either removed or largely mitigated for each  $C_{\mu}$  and oscillation studied as seen on Figs. 8.25 and 8.26.

The Lift, drag and moment amplitude behaviors are significantly improved over the baseline airfoil. The time-averaged forces and moment shown in Fig. 8.27 confirm this trend for the 3 oscillations studied. The  $L/D_{ave}$  value reaches 50.7 for oscillation 1 at  $C_{\mu} = 0.14$  while the moment amplitude is reduced by a factor of 10 under the same conditions. The unsteady shock-BL interaction increases  $\Delta C_m$  during oscillation 3 at high  $C_{\mu}$ .

The Design 2 and Design 3 CFJ airfoils have similar performance although the Design 2 time-averaged lift and L/D are slightly lower due to the lower camber. The moment is similar between the two airfoils suggesting that CFJ can be implemented on highly cam-

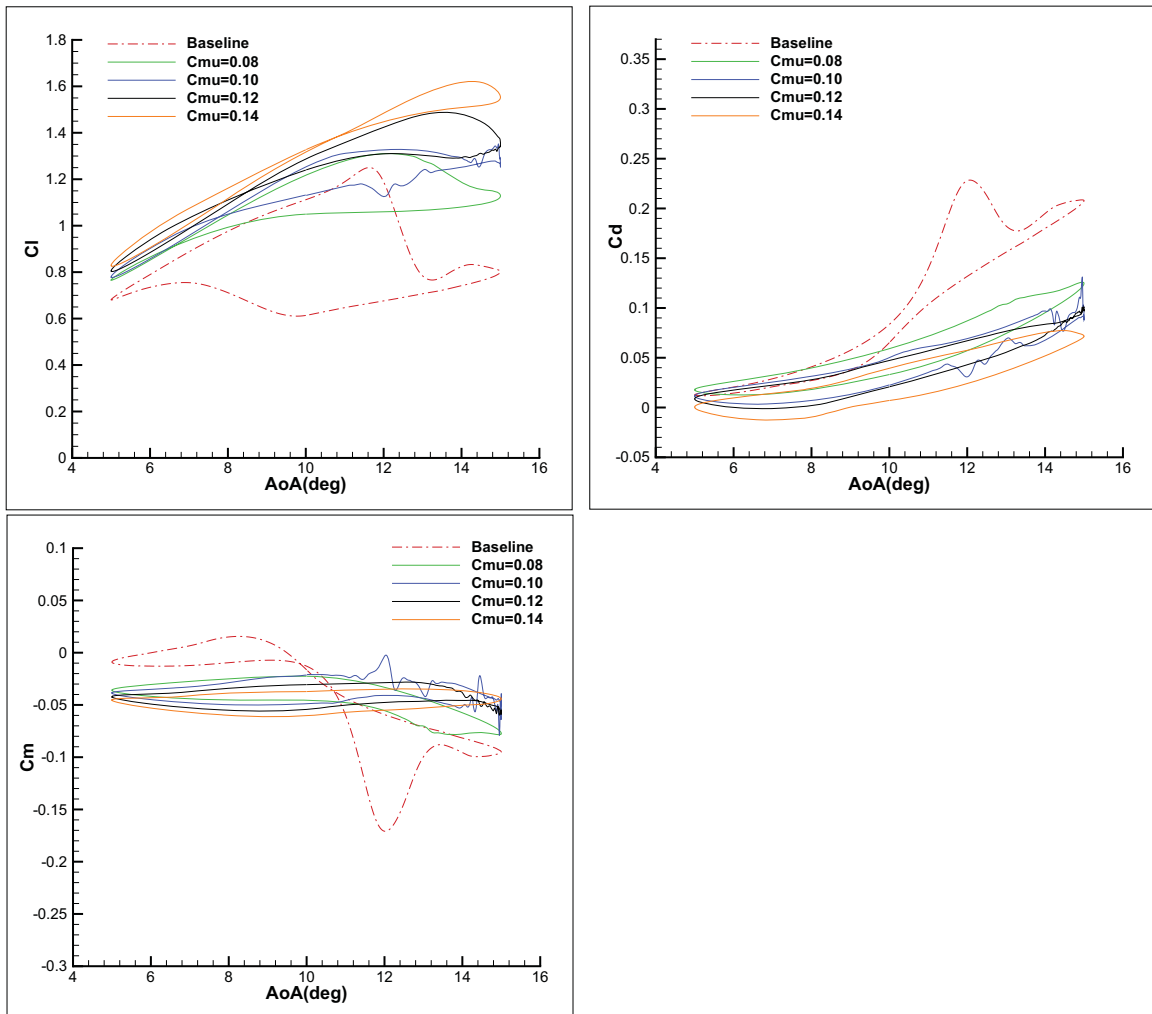


Figure 8.22: Design1 baseline pitching airfoil  $C_l$ ,  $C_d$  and  $C_m$  compared with Design1 CFJ data during oscillation 1.

bered pitching airfoils without suffering from the large nose-down moment peak typically associated with highly cambered pitching airfoils.

### 8.2.5 Design 4(CFJ-NACA2209b) Airfoil

The Design 4 airfoil is generated to lower the power consumption by removing the suction cavity recirculation and injecting a jet with a slightly higher and more uniform pressure. The  $C_\mu$  is lowered to the range 0.05 – 0.08 to further reduce the power consumption.

The Design 4 airfoil flow field is shown Fig .8.28 for oscillation 1 at  $C_\mu = 0.06$ . The flow remains attached during most of the pitching motion. A small recirculation located

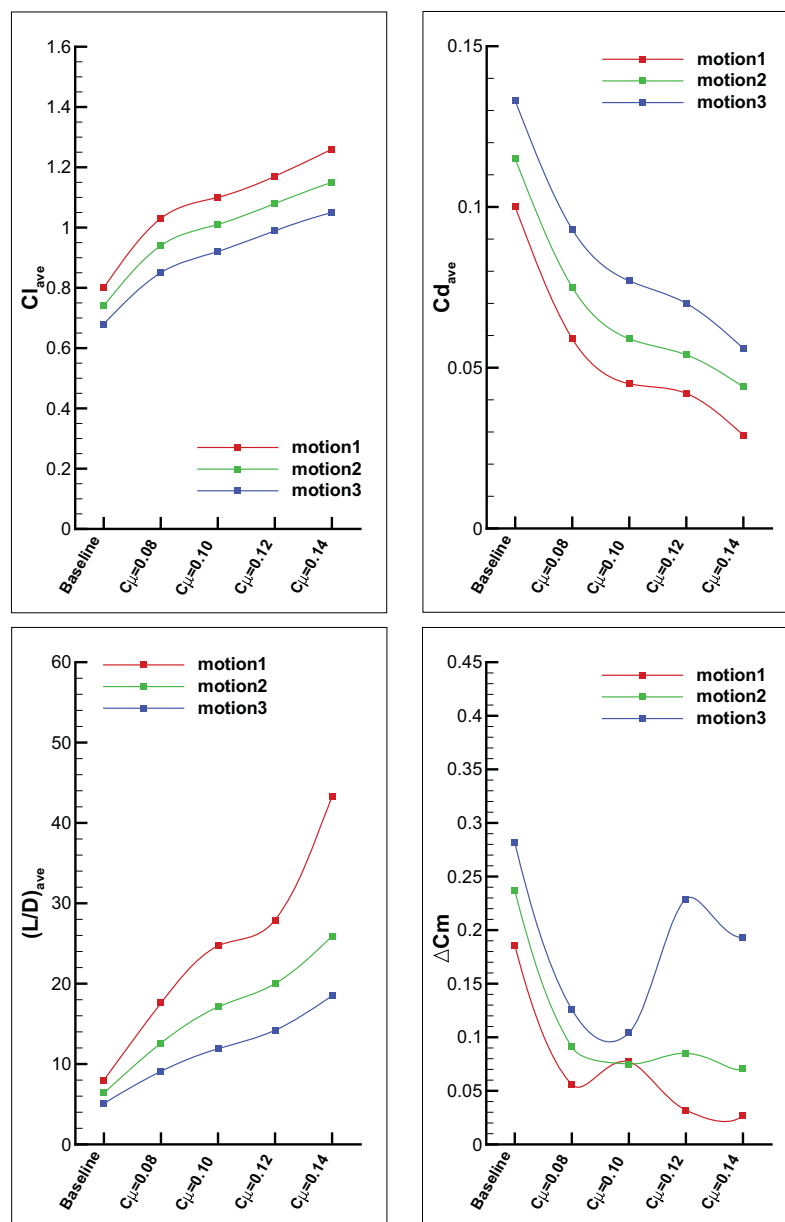


Figure 8.23: Time-averaged performance of the Design 1 baseline and CFJ airfoils.

between the suction slot and the TE of the airfoil appears between  $AoA = 13.9^\circ$  pitching up and  $AoA = 13.9^\circ$  pitching down. Overall losses due to this recirculation are limited as seen Fig. 8.25. At high AoA, a shock wave structure appears just upstream the injection slot. There are virtually no jet-exit shock structures as seen in previous designs. This is due to the redesigned injection cavity as well as to the reduced  $C_{\mu}$ . In addition there is virtually no suction cavity recirculation.

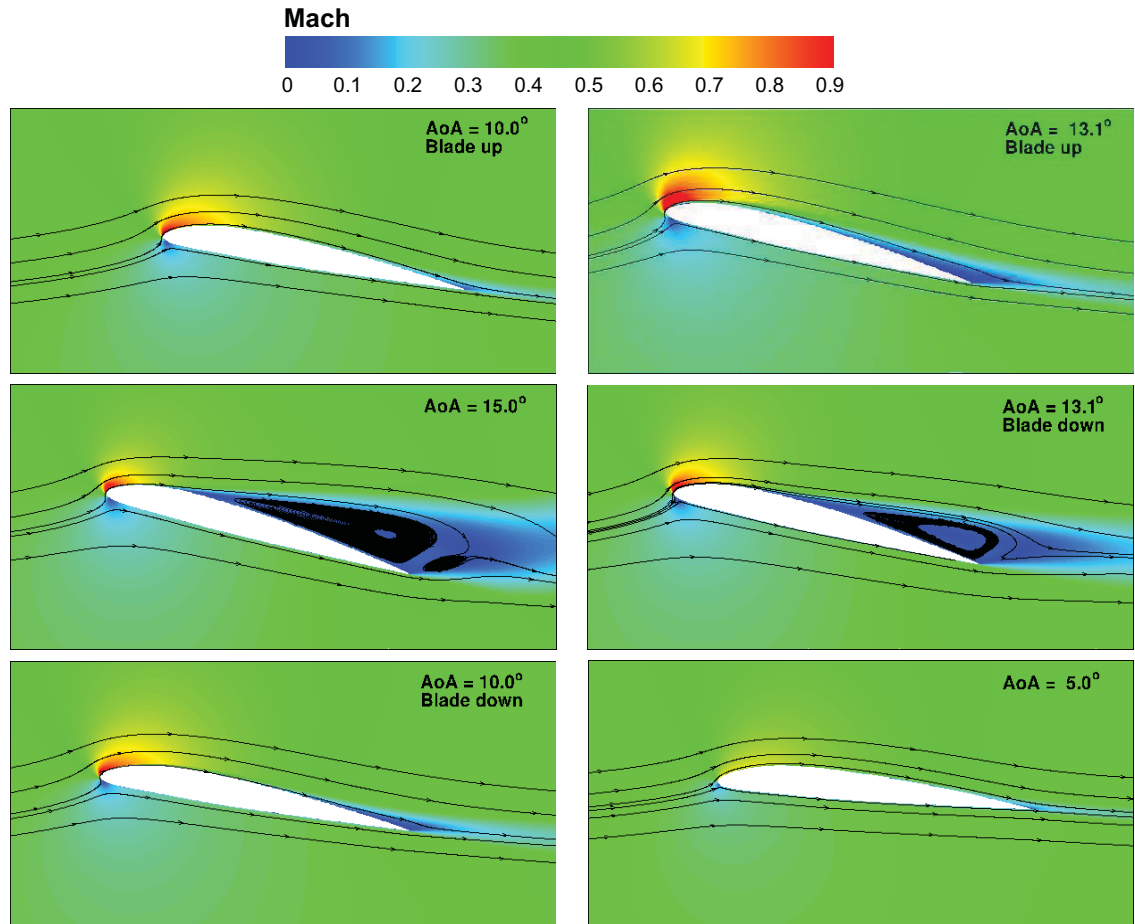


Figure 8.24: Instantaneous Mach contour of the baseline NACA2209 pitching airfoil with streamlines at different AoA during oscillation 1.

Fig. 8.25, and 8.26 show a radical lift, drag and moment improvement for all oscillations at  $C_{\mu} \geq 0.06$ . The  $C_{\mu} = 0.05$  jet is not capable of reattaching the flow downstream the LE shock which leads to lower performance than the baseline profile that exhibits no LE shock. No high frequency oscillation is found which indicate that the redesigned injection cavity and the lower  $C_{\mu}$  used in this study successfully removed the unsteady shock-BL phenomena. The dynamic stall is removed for oscillation 1 and largely mitigated for oscillation 2 and oscillation 3.

The time-averaged forces and moment seen in Fig. 8.31 show a performance improvement for all oscillations and  $C_{\mu}$  studied except for the oscillation 1 at  $C_{\mu} = 0.05$ . The power consumption shown in Fig. 8.32 remains contained. With no unsteady shock-BL interac-

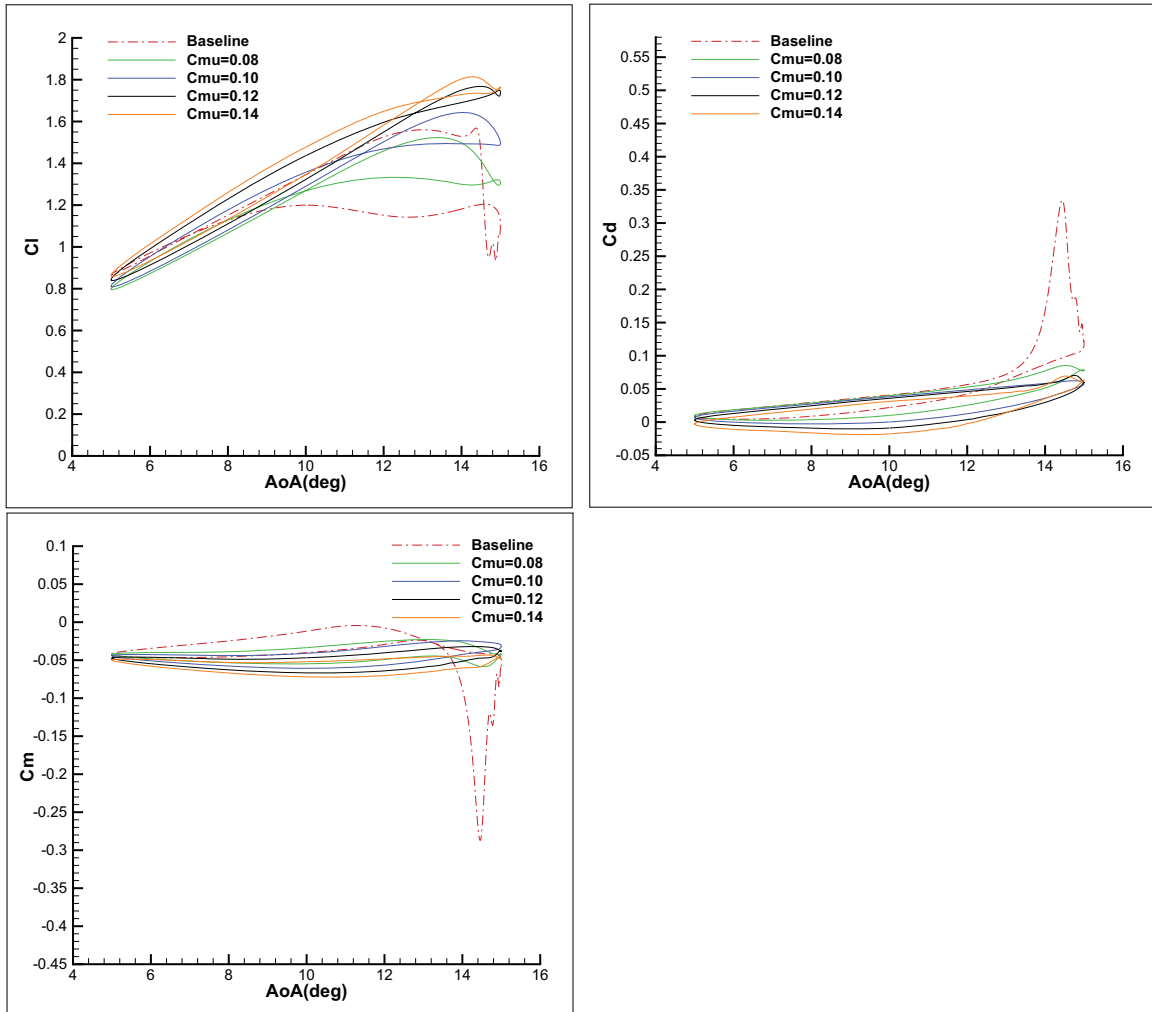


Figure 8.25: NACA2209 baseline pitching airfoil  $C_l$ ,  $C_d$  and  $C_m$  compared with Design 2 data during oscillation 1.

tion, the moment variation is greatly reduced in a monotonic manner. When comparing the Design 4 to the Design 3 airfoil, during oscillation 1 at  $C_\mu = 0.08$ , the time-averaged L/D is increased by 2% and reaches 34.6 while the power consumption is reduced by 29% to 0.74. Those achievements suggest that the injection and suction cavity design are critical for the power consumption of a given CFJ airfoil. The best performance improvement for the energy consumption is achieved at  $C_\mu = 0.06$ . During oscillation 1, a  $C_\mu$  reduction from 0.08 to 0.06 reduces the time-averaged L/D by only 15% and the power consumption by 40%.

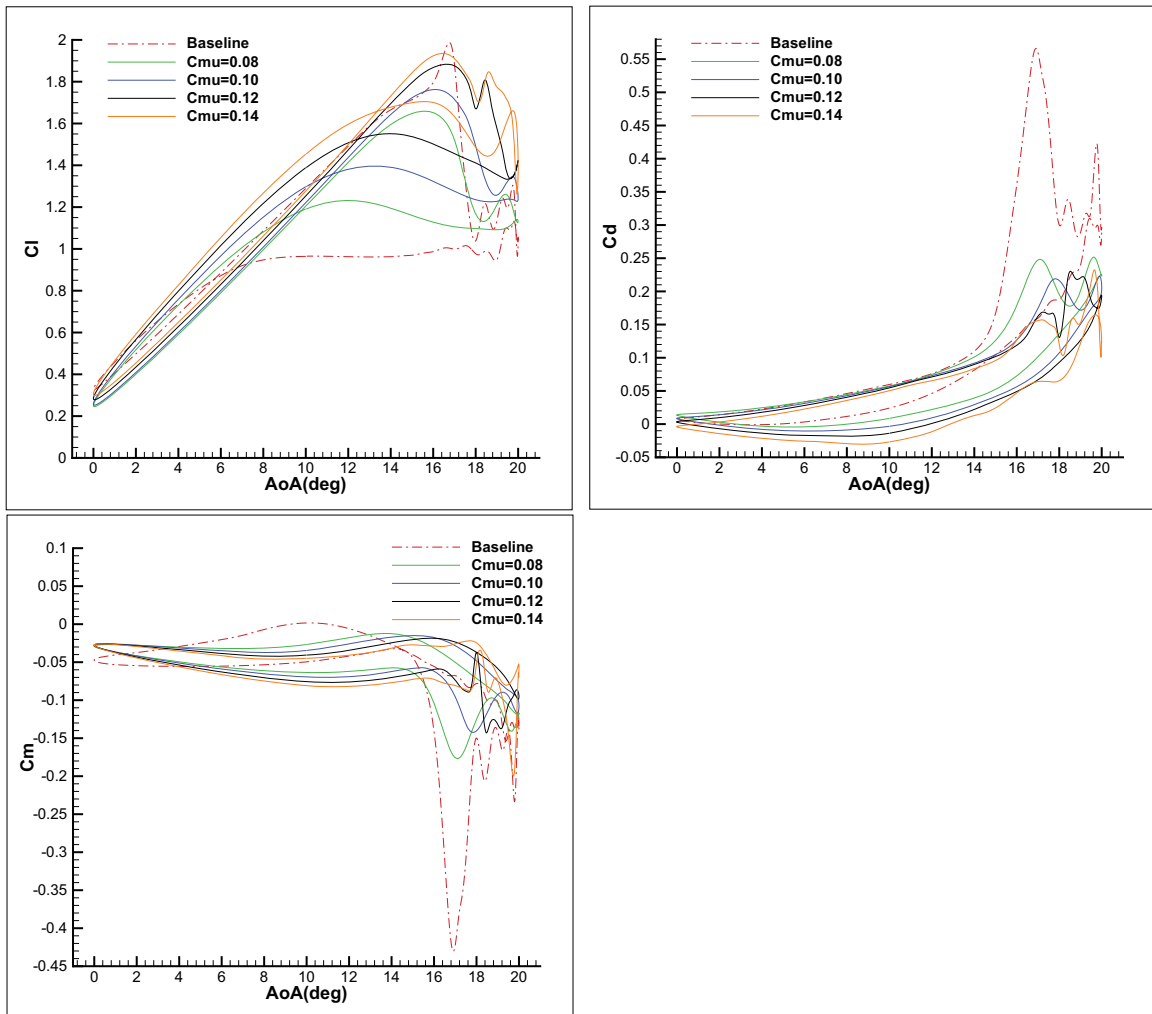


Figure 8.26: NACA2209 baseline pitching airfoil  $C_l$ ,  $C_d$  and  $C_m$  compared with Design 3 data during oscillation 3.

The instantaneous forces and moment values shown in Figs. 8.33, 8.34 and 8.35 show the performance improvement for all oscillations and  $C_{\mu}$  studied. The dynamic stall is completely removed for  $C_{\mu} \geq 0.06$  during oscillation 1 and significantly mitigated for the oscillations 2 and 3. As aforementioned, the lift is increased, especially during the downstroke, the drag is decreased and the moment is smoothed by the use of CFJ at  $C_{\mu} \geq 0.06$ .

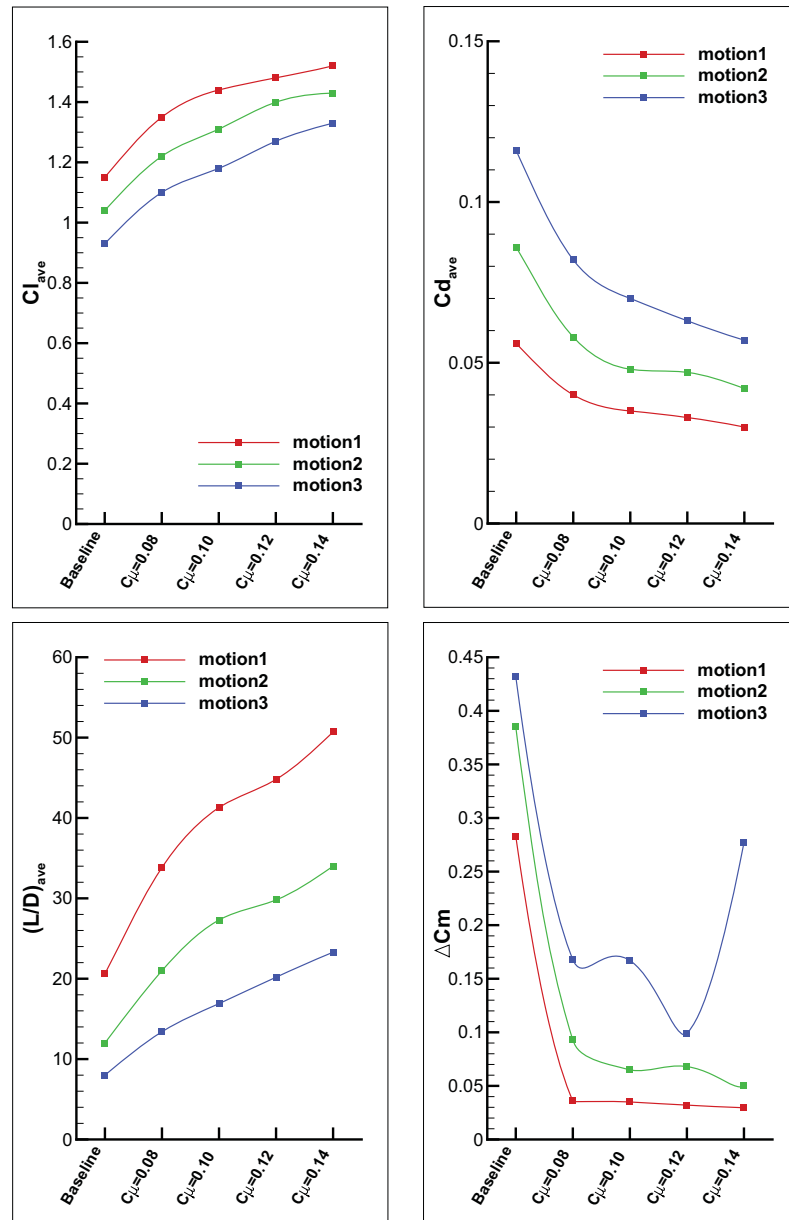


Figure 8.27: Time-averaged performance of the NACA2209 baseline and Design 3 airfoil.

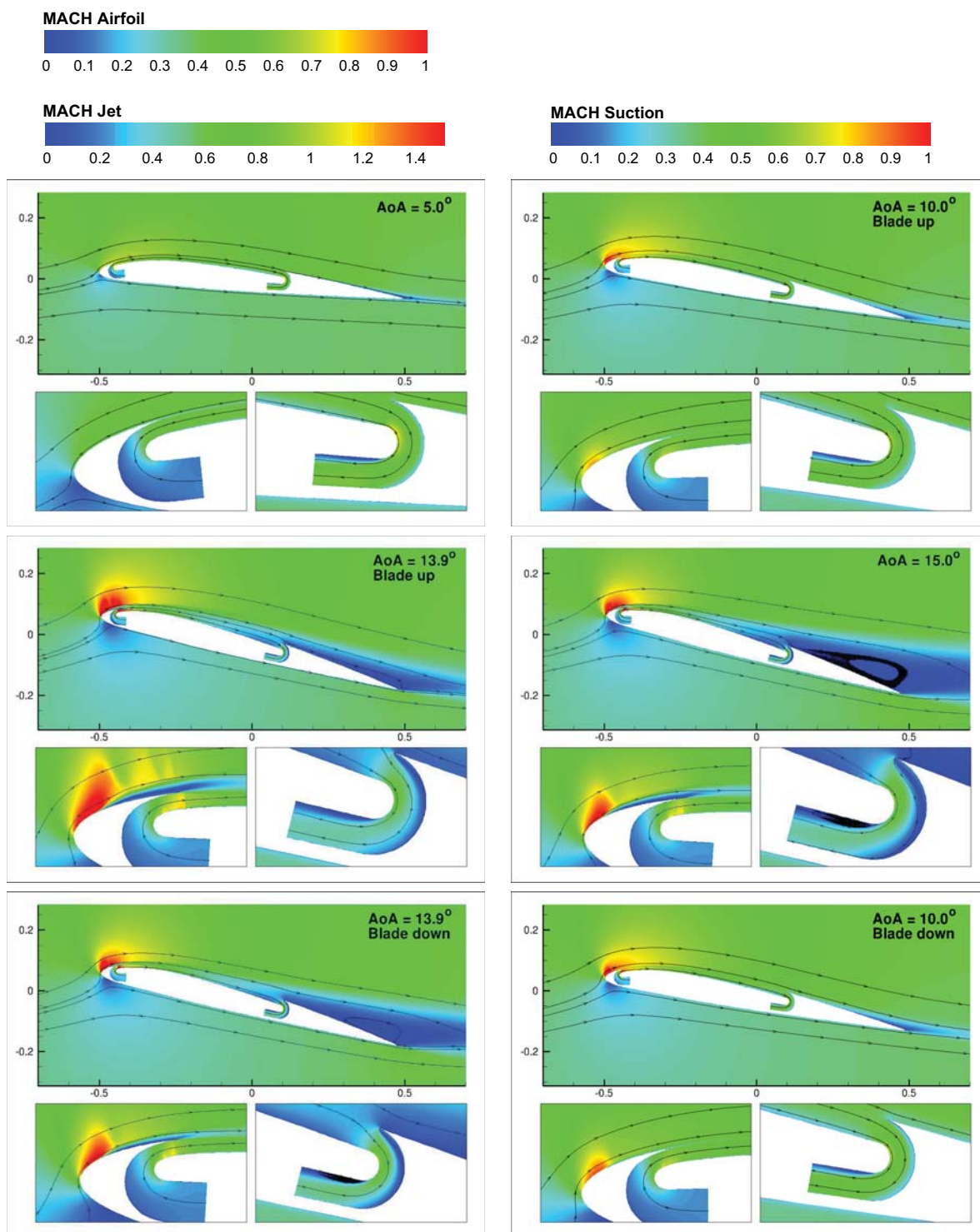


Figure 8.28: Instantaneous Mach contour of the Design 4 pitching airfoil at  $C_{\mu} = 0.06$  with streamlines at different AoA during oscillation 1.

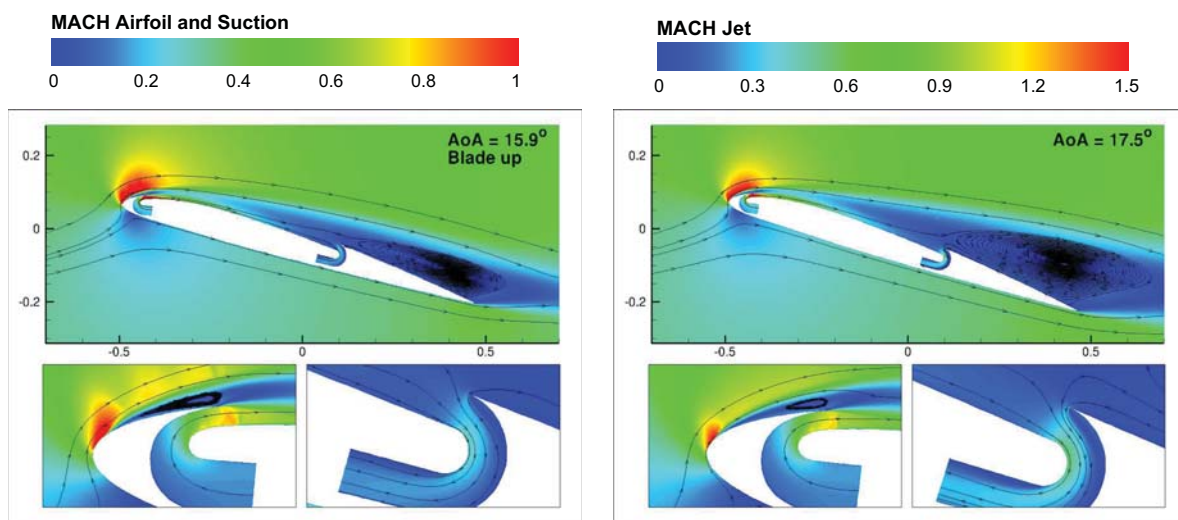


Figure 8.29: Instantaneous Mach contour of the Design 4 pitching airfoil at  $C_{\mu} = 0.08$  with streamlines at different AoA during oscillation 2.

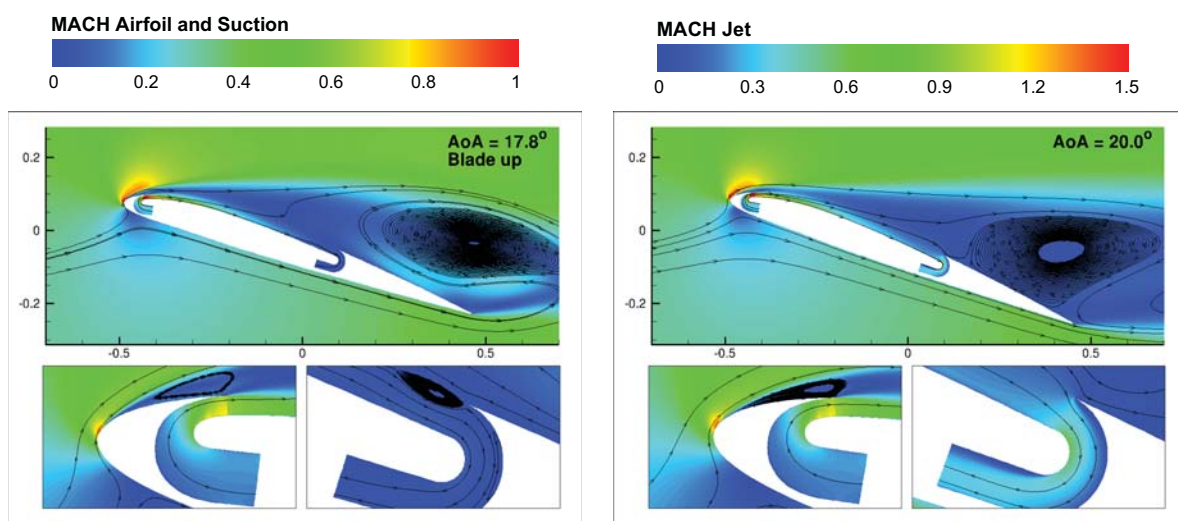


Figure 8.30: Instantaneous Mach contour of the Design 4 pitching airfoil at  $C_{\mu} = 0.08$  with streamlines at different AoA during oscillation 3.

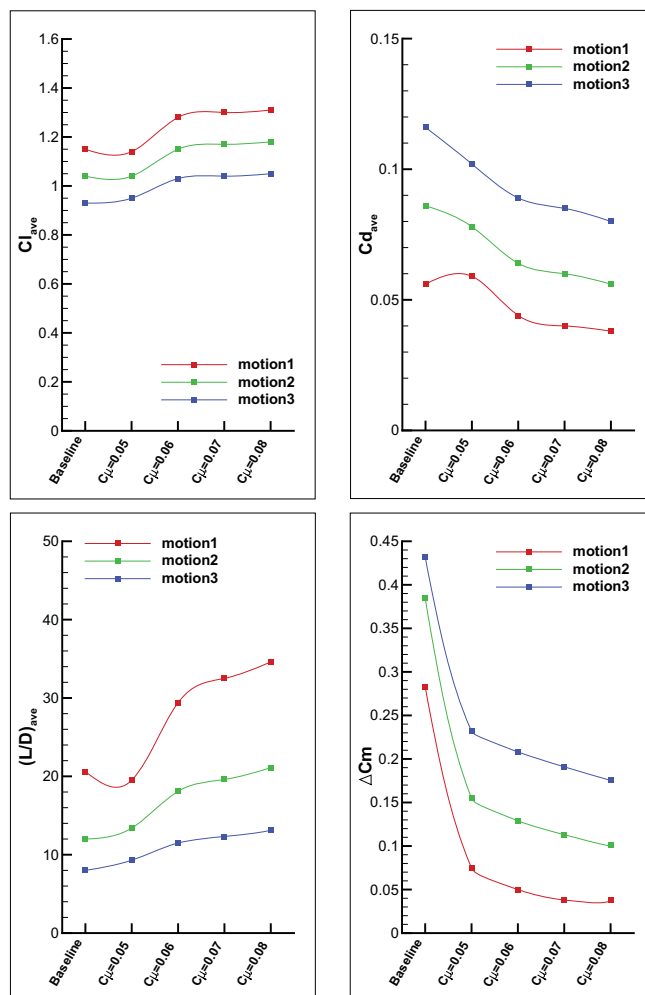


Figure 8.31: Time-averaged performance of the NACA2209 baseline and Design 4 airfoil.

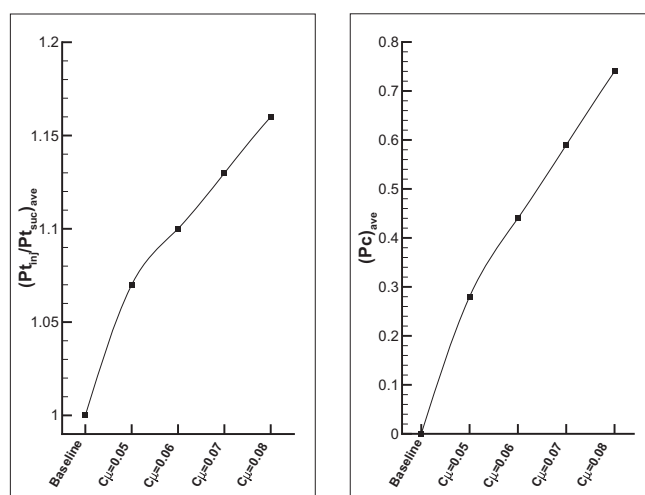


Figure 8.32: Time-averaged total pressure ratio and power coefficient of the Design 4 airfoil during motion 1.

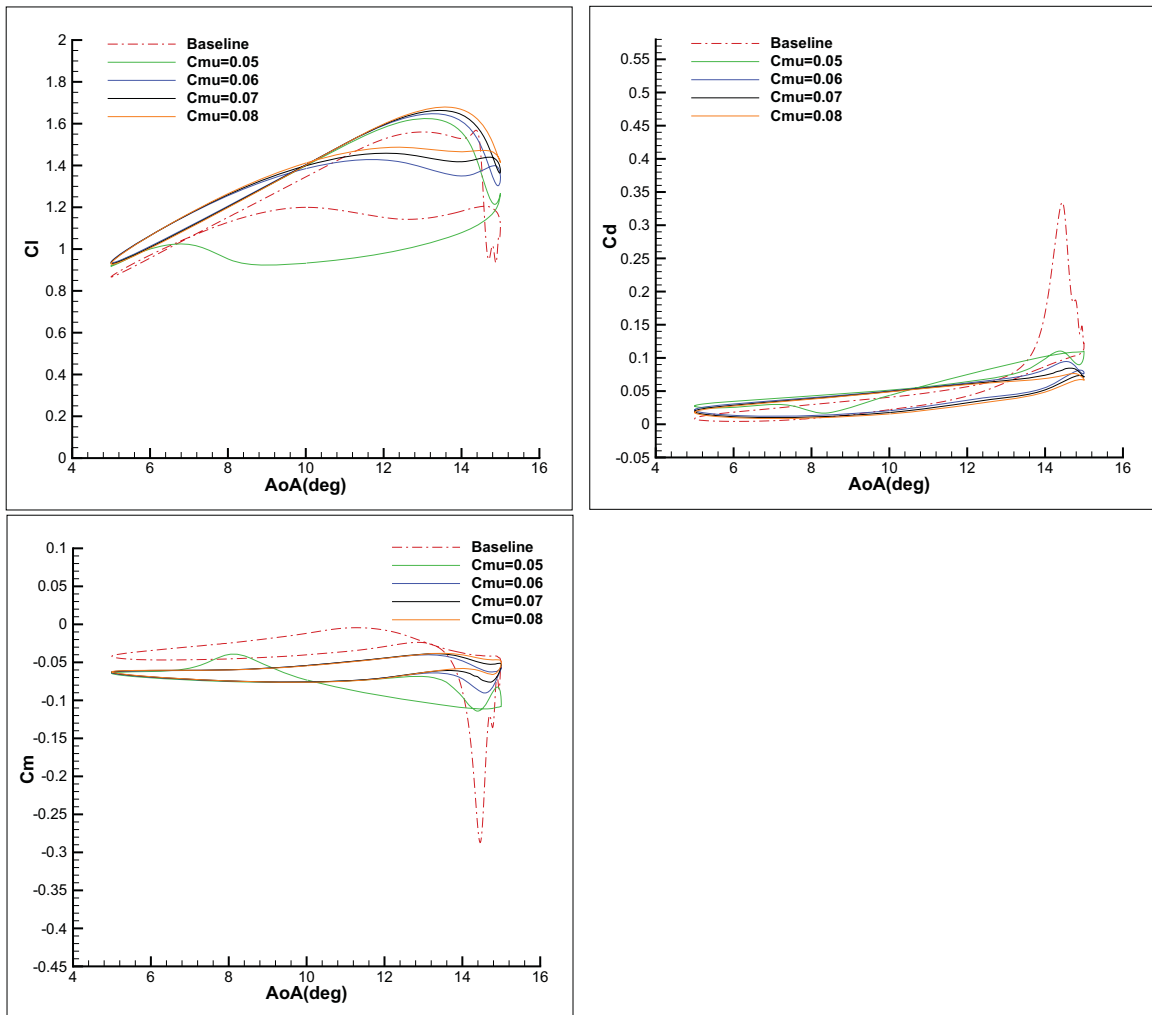


Figure 8.33: NACA2209 baseline pitching airfoil  $C_l$ ,  $C_d$  and  $C_m$  compared with Design 4 data during oscillation 1.

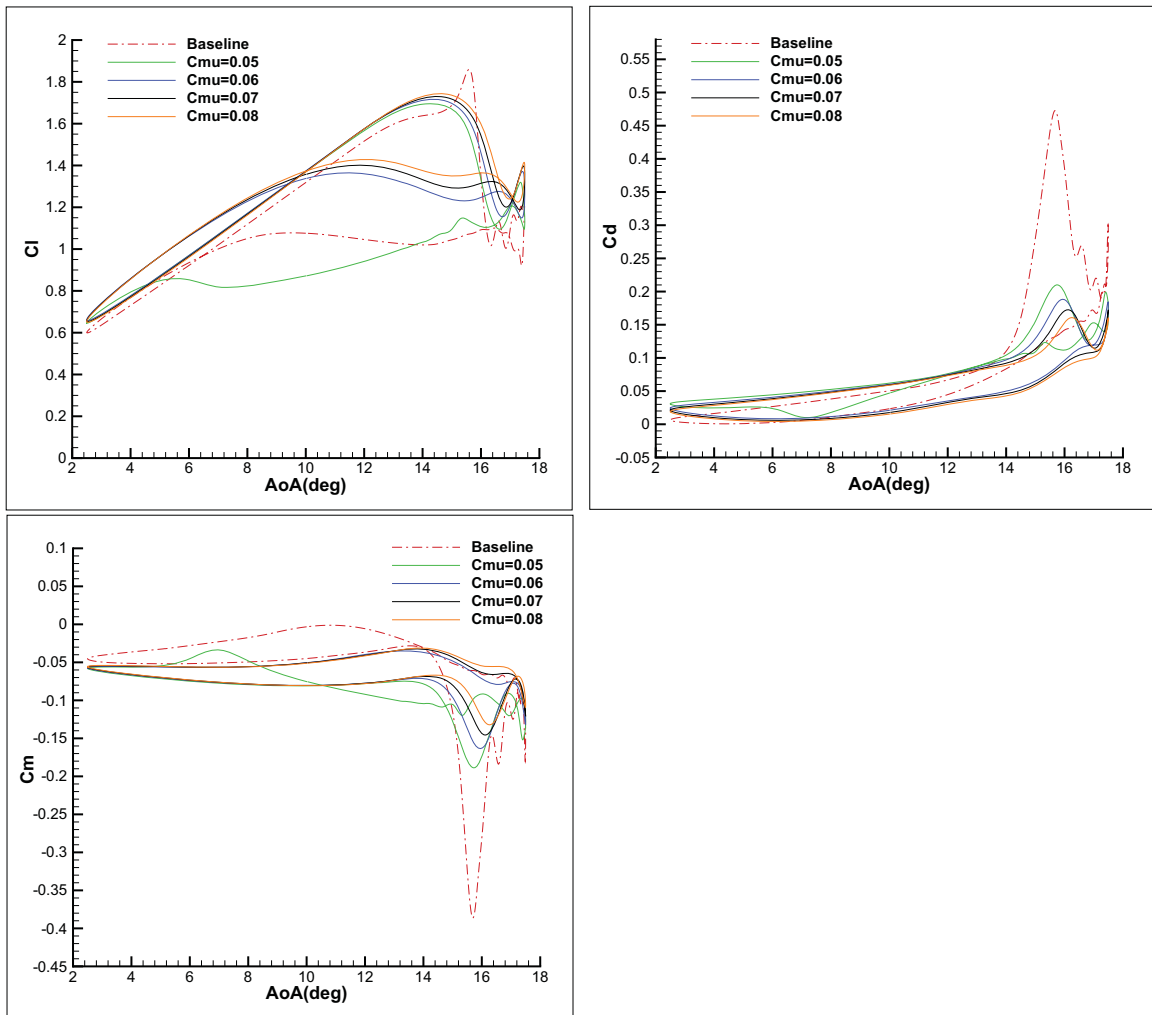


Figure 8.34: NACA2209 baseline pitching airfoil  $C_l$ ,  $C_d$  and  $C_m$  compared with Design 4 data during oscillation 2.

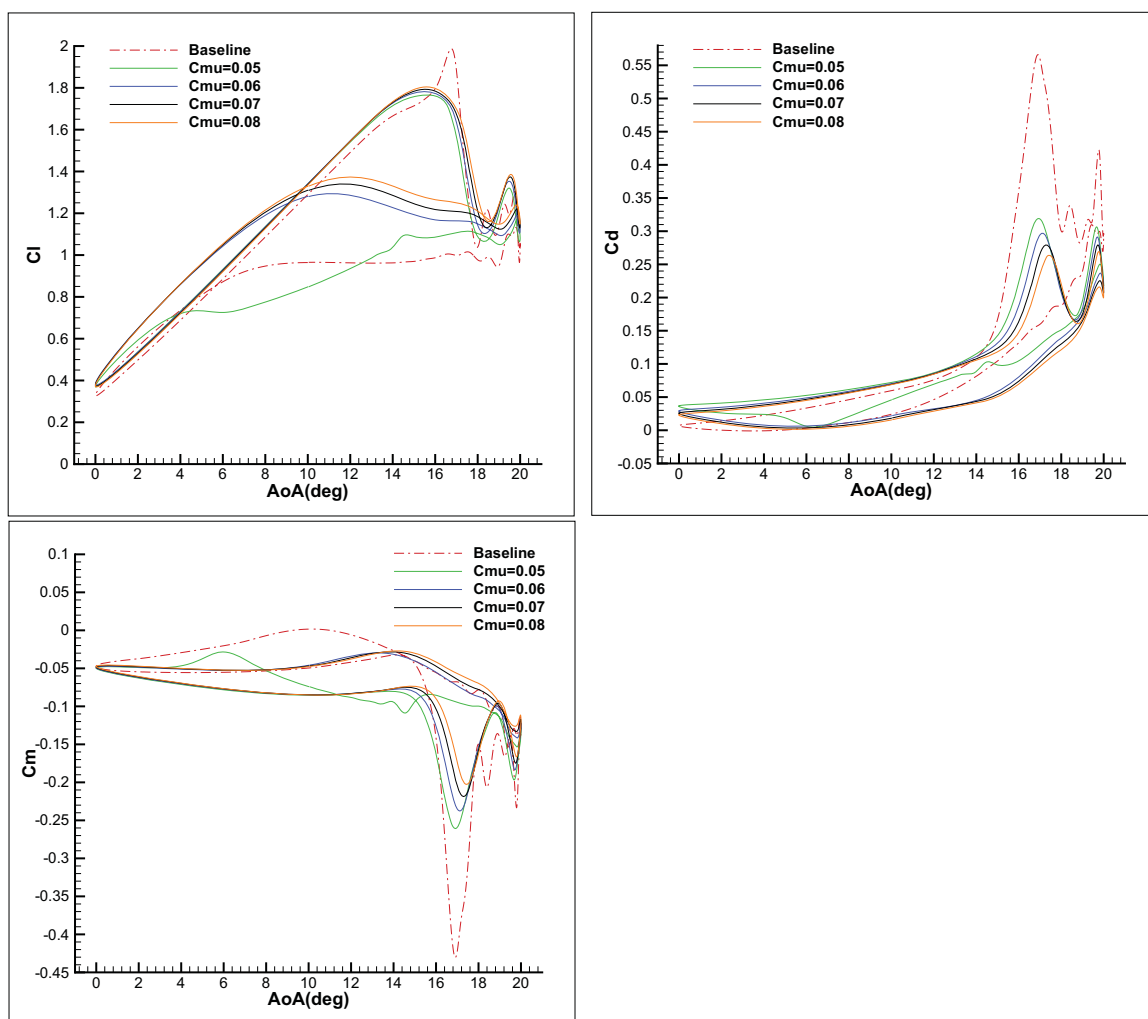


Figure 8.35: NACA2209 baseline pitching airfoil  $C_l$ ,  $C_d$  and  $C_m$  compared with Design 4 data during oscillation 3.

# Chapter 9

## Numerical Investigation of CFJ Wings

The results of the first trade study on 3D CFJ wings are presented in this chapter. The investigations constitute a follow-up of the two parametric studies on 2D CFJ airfoil conducted by Lefebvre and Zha in [63, 64] and presented in the previous chapter. Several geometry parameters are modified, including the CFJ injection and suction locations, cavities configuration, airfoil thickness and aspect ratio. First, a CFJ wing with a NACA 6415 CFJ airfoil is simulated. This case is of particular importance due to the availability of 2D experimental and computational results that can be used for reference and comparison [58, 61, 98, 102]. Then the CFJ location, injection and suction cavities geometry, airfoil thickness and wing aspect ratio are investigated. The ultimate goal is to generate a CFJ wing with high cruise wing loading and aerodynamic efficiency, high maximum lift coefficient, low moment, and low power consumption. This study also lays a foundation for a futuristic CFJ wing aircraft, for which a proof of concept have been studied in [65] and presented in the next chapter.

### 9.1 Mesh

The NACA 6415 baseline wing mesh, shown in Fig. 9.1, is constructed using the O-mesh topology in order to achieve high quality around the wing. 160 points are placed around

the wing partitioned equally between the suction and the pressure side, 80 points in the direction normal to the wing, 60 points in the spanwise direction. An O-mesh topology is also used for the wing tip. The total mesh size is 1.7 million points, split into 34 blocks for the parallel computation. The far field boundary is located 30 chords away from the wing. The first grid point on the wing surface is placed at  $y^+ \approx 1$  except on the wing tip wall where  $y^+ \approx 50$  is used with the wall function boundary condition to reduce the mesh size.

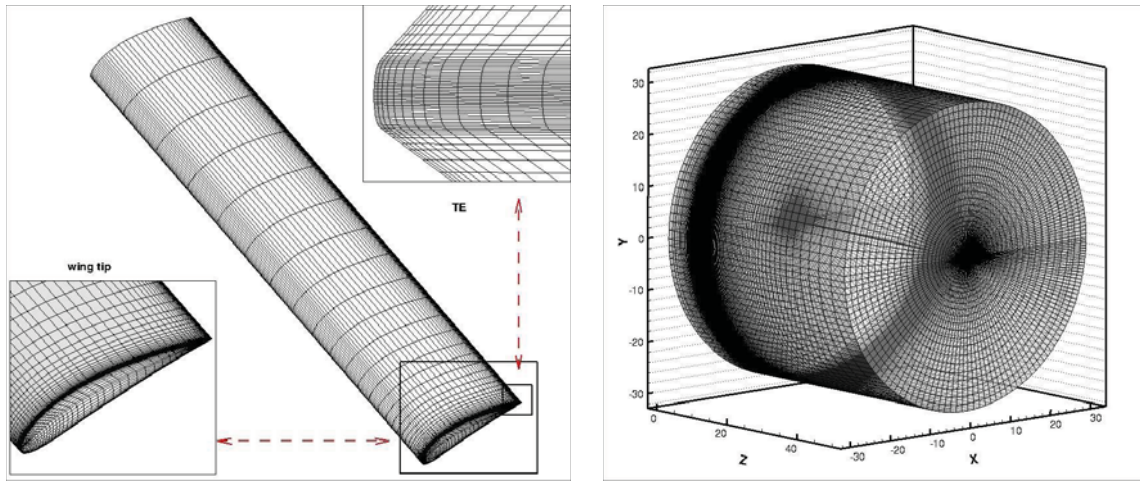


Figure 9.1: NACA 6415 baseline wing mesh topology. The surface mesh is displayed on the left plot and the outer mesh on the right plot.

The typical NACA 6415 CFJ wing mesh, shown in Fig.9.2, uses a similar mesh topology. 280 points are placed around wing partitioned equally between the suction and the pressure side, 80 points in the direction normal to the wing, 40 points across the jet and 80 points in the spanwise direction. An O-mesh topology is also used for the wing tip. The total mesh size is 3.6 million points, split into 111 blocks for the parallel computation. The far field boundary is located 50 chords away from the wing. The first grid point on the wing surface is placed at  $y^+ \approx 1$  except on the wing tip wall where  $y^+ \approx 50$  is used with the wall function boundary condition to reduce the mesh size.

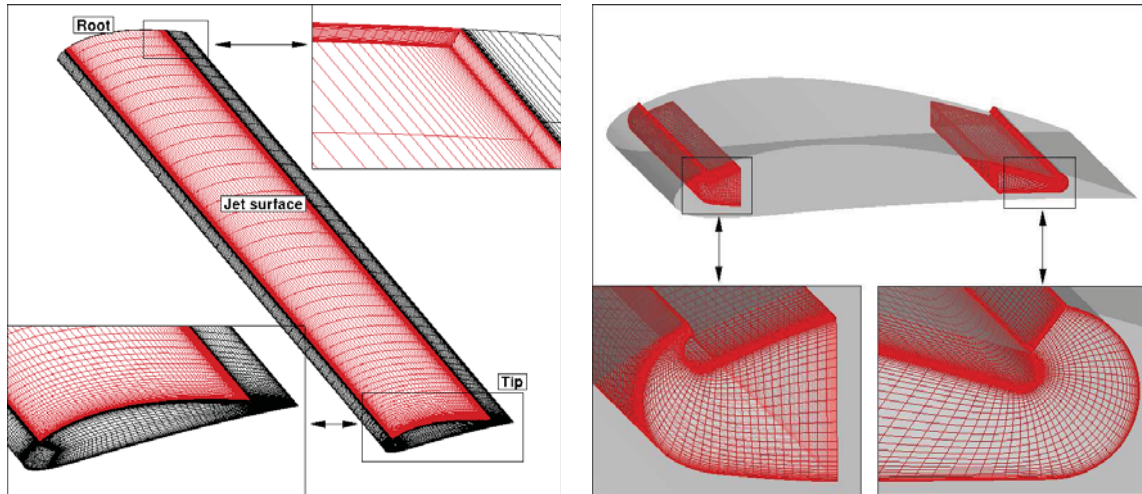


Figure 9.2: NACA 6415 CFJ wing mesh topology. The surface mesh is displayed on the left plot and the injection and suction cavity mesh on the right plot.

## 9.2 Wing Configurations

The geometry characteristics of the five CFJ wings designed in this trade study are summarized in Table 9.1 and the airfoils used in this trade study. Each CFJ wing is constructed from a rectangular planform with no sweep and aspect ratio 20 (Design 1-4) or 10 (Design 5) by stacking the airfoils shown in Fig. 9.3. The top airfoil is the original 15% thickness airfoil utilized in the wind tunnel experiment and previous simulation. The middle airfoil has the injection and suction cavities redesigned. Furthermore, the injection slot is moved to a more forward position. The bottom airfoil is a 21% thickness airfoil that uses the same cavity design and slot position than the middle airfoil. The Design 1-2 use the top airfoil, the Design 3 uses the middle airfoil and the Design 4-5 use the bottom airfoil. Each CFJ airfoil is constructed from the baseline NACA airfoil by lowering the suction surface until and an injection and a suction slots of size 0.65% chord and 1.30% chord respectively appears on the modified suction surface (see Fig. 1.10). For instance, the CFJ airfoil used for the Design 1 and 2 is built from a NACA 6415 airfoil by lowering the suction surface between 7% chord and 83.3% chord until the injection and suction slots are of the proper size. The Design 1 CFJ wing results are compared with the Baseline 1 wing with no CFJ that uses the NACA 6415 airfoil on the same planform. Each one of the Design 2-5 is then created to

show the influence of a specific parameter. For instance the influence of the spanwise area of the CFJ on the wing performance can be seen by comparing Design 1 (CFJ applied to 100% span) and Design 2 (CFJ applied only to 75% span) CFJ wings. The influence of the injection and suction cavity design and location is investigated by comparing the Design 1 (experiment cavities with injection slot located at 7% chord) and Design 3 (redesigned cavities with injection slot located at 2% chord) CFJ wings. The airfoil thickness is varied from 15% for the Design 3 to 21% for the Design 4. Finally the wing aspect ratio is reduced from 20 to 10 between the Design 4 and the Design 5.

Calculations are conducted at Mach number 0.15 with  $0.04 \leq C_{\mu} \leq 0.08$ , a suitable cruise Mach number and  $C_{\mu}$  range for a general aviation airplane equipped with CFJ. The Design 4 CFJ wing is also simulated at Mach number 0.10 with  $0.16 \leq C_{\mu} \leq 0.28$  to simulate the typical takeoff and landing conditions.

	Baseline 1	Baseline 2	Baseline 3	Design 1	Design 2	Design 3	Design 4	Design 5
Planform	Rectangular							
Aspect Ratio	20	20	10	20	20	20	20	10
Baseline airfoil	NACA 6415	NACA 6421	NACA 6421	NACA 6415	NACA 6415	NACA 6415	NACA 6421	NACA 6421
CFJ location (% span)	N/A	N/A	N/A	100	75	100	100	100
Injection slot location (% chord)	N/A	N/A	N/A	7.00	7.00	2.00	2.00	2.00
Suction slot location (% chord)	N/A	N/A	N/A	83.3	83.3	80.0	80.0	80.0
Injection slot size (% chord)	N/A	N/A	N/A	0.65	0.65	0.65	0.65	0.65
Suction slot size (% chord)	N/A	N/A	N/A	1.30	1.30	1.30	1.30	1.30
Cavities geometry	N/A	N/A	N/A	Experiment	Experiment	Redesigned	Redesigned	Redesigned

Table 9.1: CFJ wings geometry.

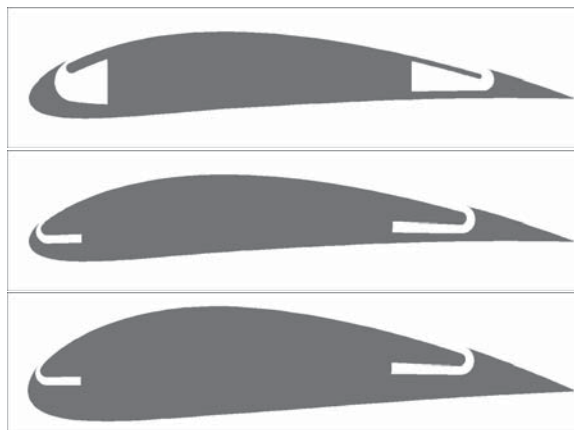


Figure 9.3: CFJ airfoils geometry.

### 9.3 Design 1 CFJ Wing

The Design 1 CFJ wing is used as the first iteration of this trade study. The CFJ wing geometric characteristics are shown in Table 9.1. Fig. 9.4 shows the Design 1 CFJ wing surface pressure contours at AoA  $15.0^\circ$  and  $25.0^\circ$  with  $C_\mu = 0.08$ . At  $AoA = 15.0^\circ$  the main flow and the jet are fully attached. The  $25.0^\circ$  AoA however is just past the stall AoA and a flow separation appears at the wing TE. The flow is attached at the wing tip due to the lower local lift loading.

The Mach contours at 0%, 50%, and 99% span are plotted Fig. 9.5 in the same flow conditions. The higher AoA plots feature a stagnation point located more downstream on the pressure side of the wing with a stronger LE acceleration. The flow separation appears clearly with a recirculation located just upstream of the suction slot. Both AoAs plots show a much lower LE flow acceleration at 99% span hence a lower LE suction effect. This results in a lower jet velocity in the wing tip region even though the injection cavity pressure is constant. The close up view at the injection and suction cavities seen in Fig. 9.6 shows a jet Mach number about 0.4 at mid-span, AoA  $15.0^\circ$  and  $C_\mu = 0.08$ . The flow is separated in the suction cavity due to the large area expansion, which will be corrected in the next suction cavity geometry as shown later.

Fig. 9.7 shows the chordwise distributions of the pressure coefficient and isentropic Mach number for the Baseline 1 wing at different span. The loading, visualized on the  $C_p$  and the isentropic Mach number plots, is similar on the inner 75% span of the wing. On the outer 25% span the loading is gradually decreased due to the wing tip effect. The same behavior is observed for the Design 1 CFJ wing as shown in Fig. 9.8. The spikes on the pressure distribution and isentropic Mach number are due to the injection and suction slots. The CFJ greatly augment the circulation on the suction surface due to the increased flow velocity as seen on the isentropic Mach number plots. Furthermore, the CFJ airfoil has a significantly higher suction peak near the LE than the baseline airfoil as seen on the  $C_p$  plots. The combination of those effects increase the lift and lower the pressure drag of the

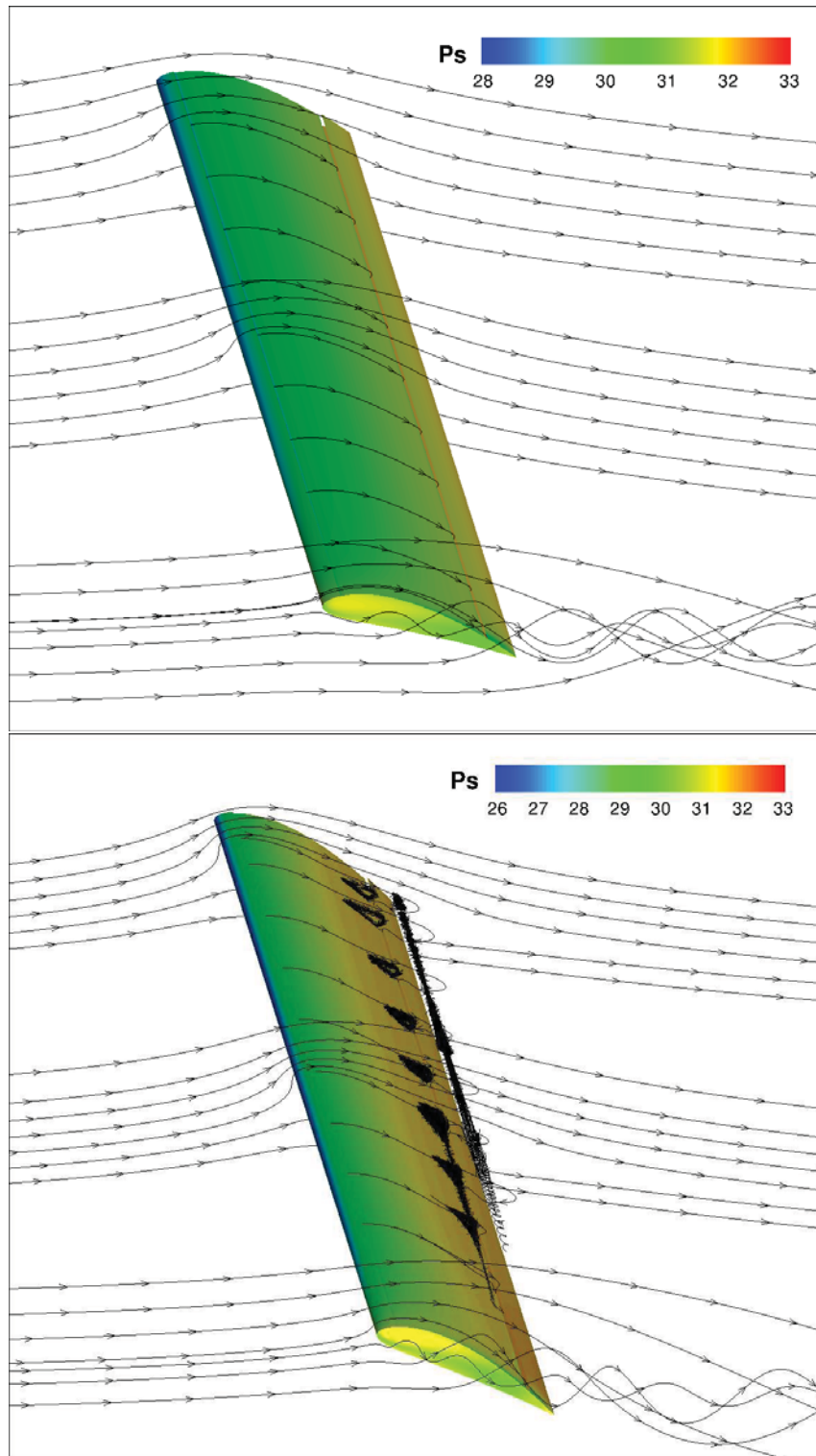


Figure 9.4: Surface pressure contours with streamlines for the Design 1 CFJ wing at  $C_{\mu} = 0.08$ . The AoA is  $15^{\circ}$  on the left and  $25^{\circ}$  on the right.

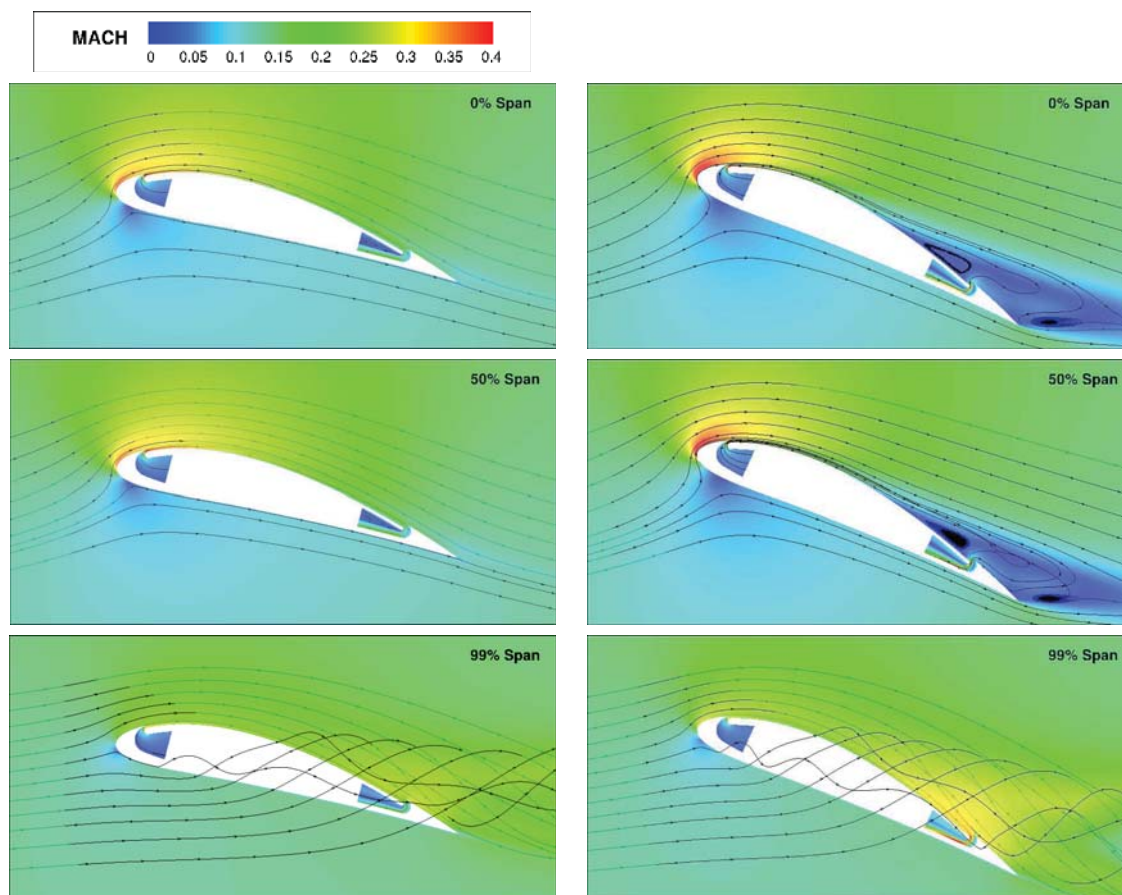


Figure 9.5: Mach contours with streamlines at 0%, 50% and 99% spanwise location for the Design 1 CFJ wing at  $C_{\mu} = 0.08$ . The AoA is  $15^{\circ}$  for the left plots and  $25^{\circ}$  for the right plots.

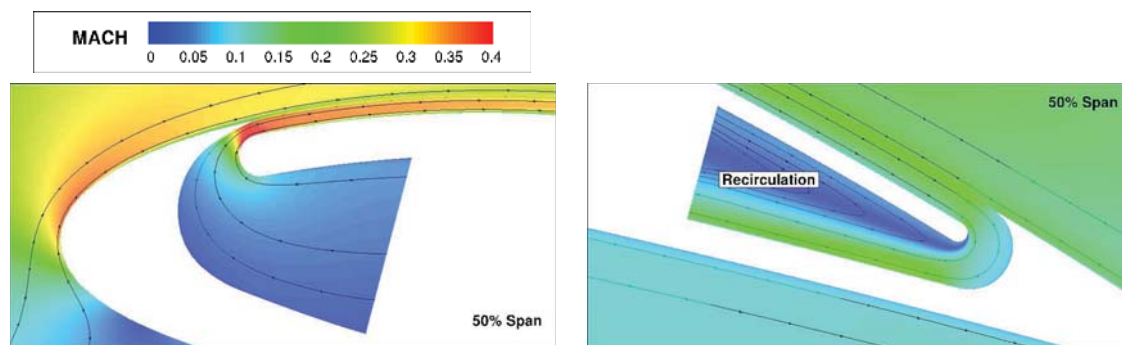


Figure 9.6: Close up view of the experimental injection and suction cavities for the Design 1 CFJ wing. Mach contours at 50% spanwise location,  $C_{\mu} = 0.08$  and  $AoA = 15^{\circ}$ .

airfoil. The maximum  $-C_p$  is 6.2 for the CFJ wing, an increase of roughly 50% over that of the Baseline 1 wing. Similarly the maximum isentropic Mach number of the CFJ wing is 0.41, an increase of roughly 20% over that of the baseline wing.

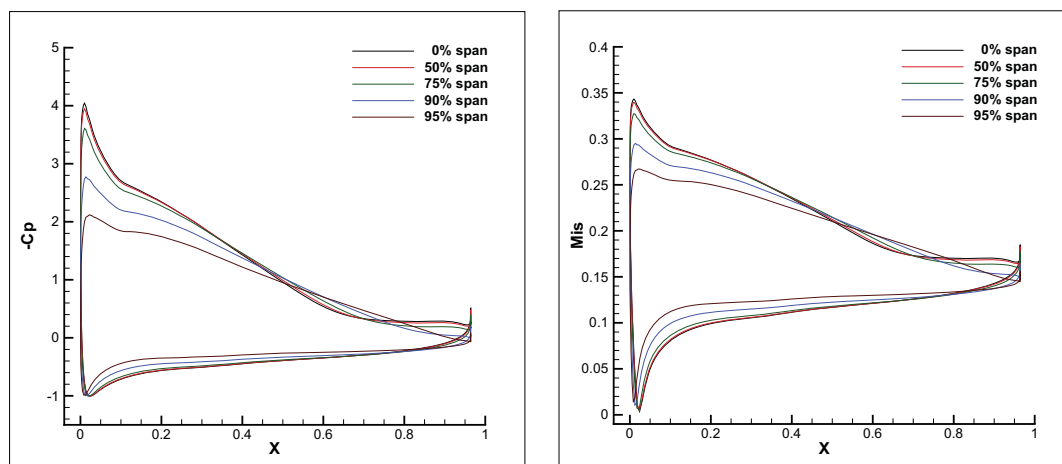


Figure 9.7: Pressure coefficient (left) and isentropic Mach number (right) at various spanwise location for the baseline NACA 6415 wing without CFJ at  $AoA = 15^\circ$ .

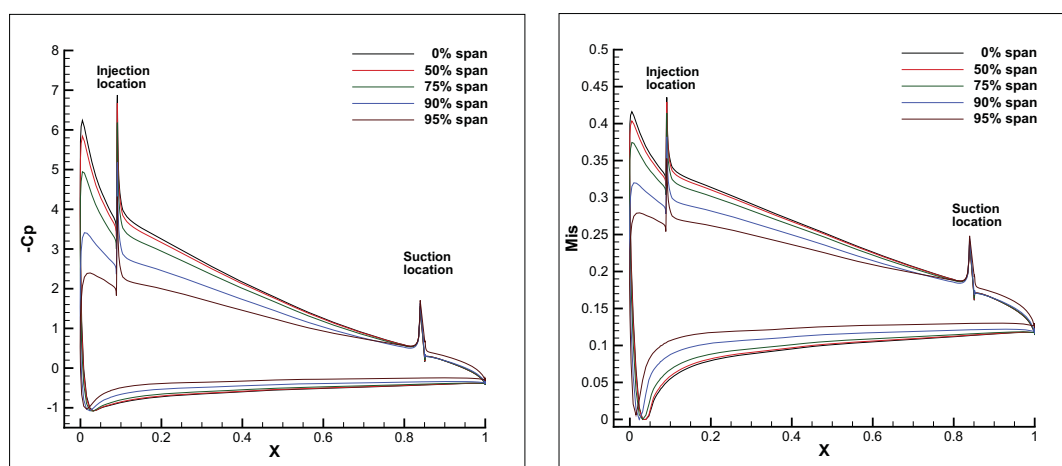


Figure 9.8: Pressure coefficient (left) and isentropic Mach number (right) at various spanwise location for the Design 1 CFJ wing at  $AoA = 15^\circ$  and  $C_\mu = 0.08$ .

The forces, moment and power consumption versus  $AoA$  for the Design 1 CFJ wing are shown in Fig. 9.9. As aforementioned, the CFJ wing lift coefficient is significantly increased and reaches  $C_{LMAX} = 2.3$  at  $AoA = 25.0^\circ$  and  $C_\mu = 0.08$ , an increase of 41% over the Baseline 1 wing. The high lift generated downside is the higher lift-induced drag which is the reason why at same  $AoA$ , the drag coefficient remains high. More precisely, the drag coefficient is higher than the baseline wing in the range  $5 - 15^\circ$  and lower for  $AoA \leq 5^\circ$  and  $AoA \geq 20^\circ$  at  $C_\mu = 0.06 - 0.08$ . However, the drag increase is more than compensated by the higher lift coefficient and the L/D is excellent. The maximum L/D

reaches the value of 62 at  $AoA = 0.0^\circ$  and  $C_\mu = 0.08$ . The CFJ increases the pitch down moment, and the effect increases with the  $C_\mu$ . Unlike the baseline wing, the CFJ wing moment is fairly flat at low AoA and increases close to the stall AoA.

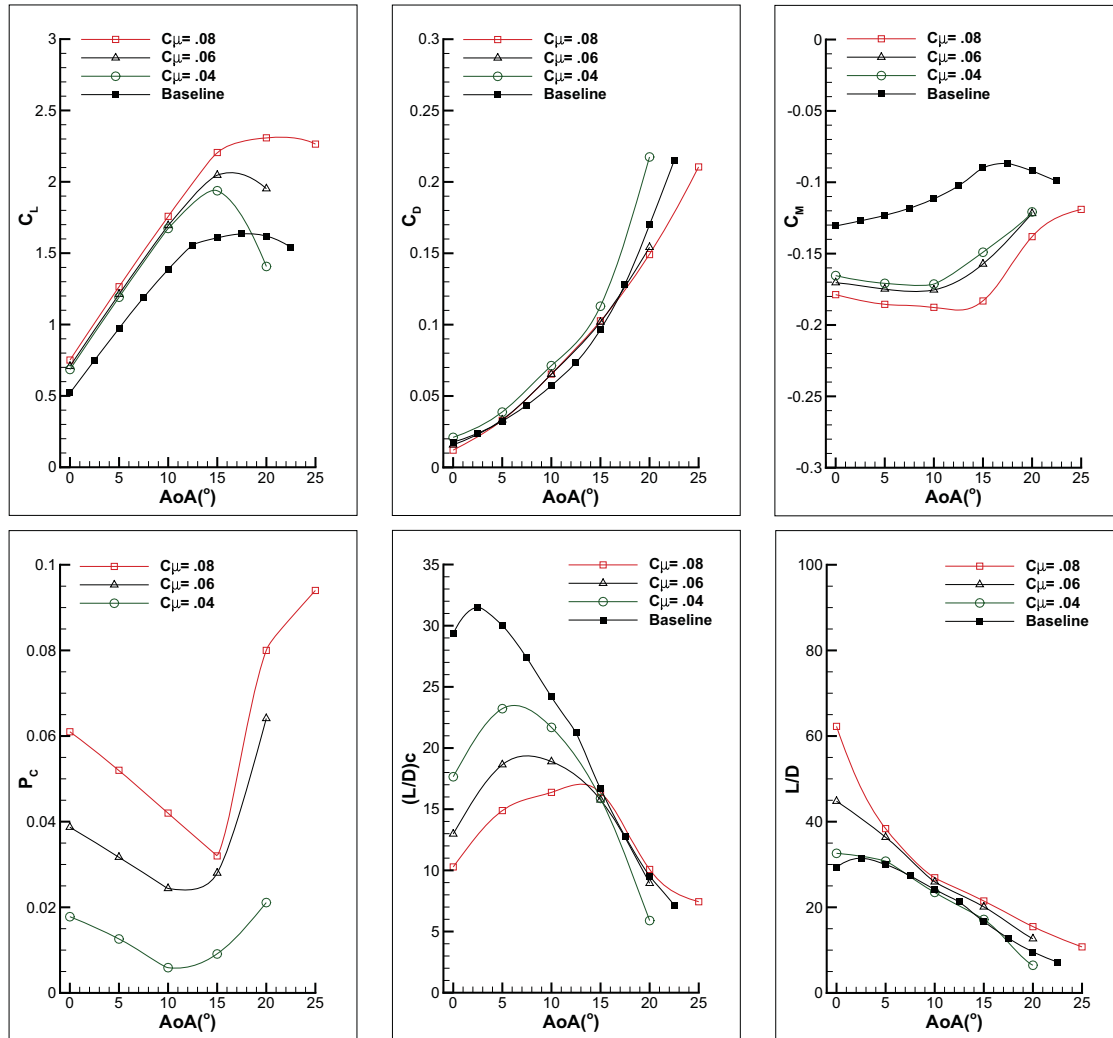


Figure 9.9: Forces, moment and energy expenditure versus AoA for the Design 1 CFJ wing. Simulations performed at  $M=0.15$  and  $0.04 \leq C_\mu \leq 0.08$ .

The power coefficient decreases with the increase of AoA until the near stall. When the flow separation occurs, the power coefficient is significantly increased due to the high total pressure loss as seen on Fig. 9.10. The minimum power coefficient is significantly smaller than  $C_\mu$ . For instance, at  $C_\mu = 0.04$ , the minimum  $P_c$  is 0.006. A higher  $C_\mu$  increases the power coefficient. The corrected aerodynamic efficiency reaches a maximum value of 23.2

at  $AoA = 5.0^\circ$  and  $C_\mu = 0.04$ . This value is lower than the peak  $L/D$  of 33 achieved by the baseline wing, but is achieved for a lift coefficient almost twice higher.

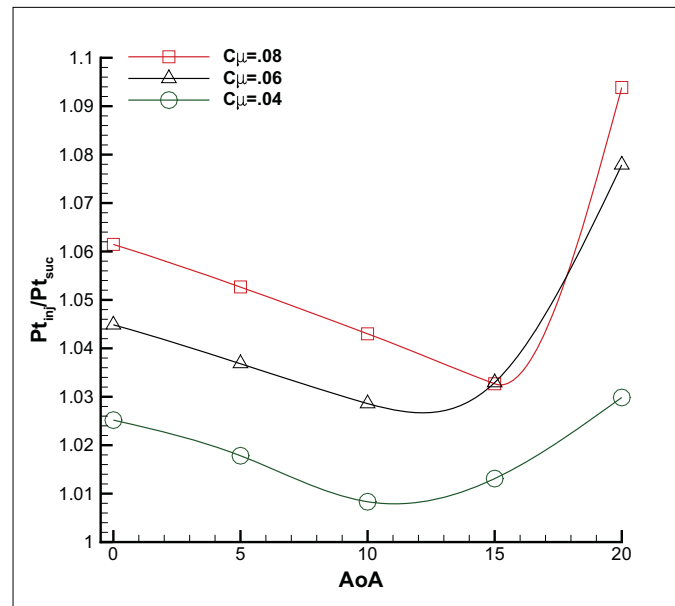


Figure 9.10: Mass-averaged total pressure ratio between the injection and suction cavities for the Design 1 CFJ wing.

For a fixed  $C_\mu$ , the power consumption depends mostly on the mass flow and total pressure ratio between the injection and suction cavities (see Eq. (4.12)). On the range of  $AoA$  studied, the mass flow is mostly constant, thereby, the changes in the pressure ratio are the main driver of the power consumption changes. Consequently, the behavior of the pressure ratio, seen Fig. 9.10, is similar to that of the power coefficient seen Fig. 9.9). The total pressure ratio is only about 1% at  $AoA = 10.0^\circ$  and  $C_\mu = 0.04$ . Fig. 9.11 shows the total pressure ratio between the injection cavity and the free stream. The ratio decreases with an increasing  $AoA$  due to the stronger LE suction. When the  $AoA$  is high enough, the  $C_\mu = 0.04 - 0.06$  where able to achieve a ratio lower than one, which means than the injection cavity total pressure is actually lower than the free stream.

Fig. 9.12 shows a close up view of the static pressure contours in the vicinity of the injection region. The CFJ wing is in cruise condition at  $AoA = 5.0^\circ$  and  $C_\mu = 0.04$ . The injection static pressure is not uniform due to the centrifugal forces that results from the flow turning. The inner portion of the injection can be as low as 95% of the free stream

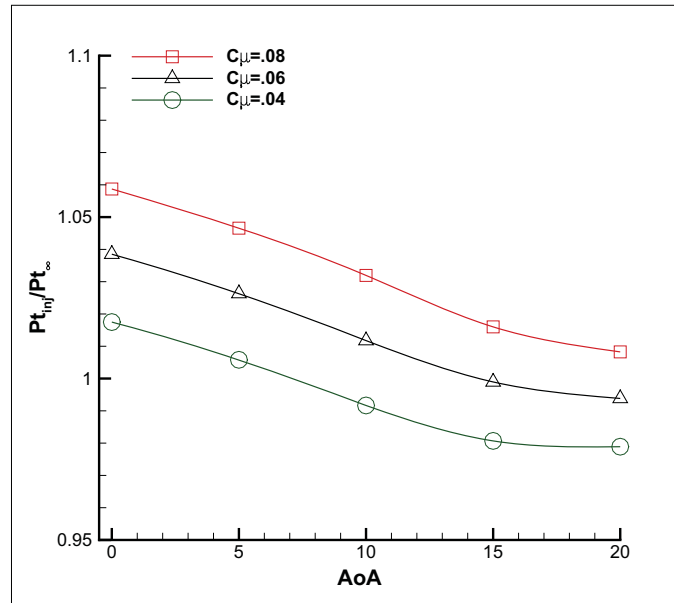


Figure 9.11: Mass-averaged total pressure ratio between the injection cavity and the free stream for the Design 1 CFJ wing .

pressure. The injection cavity pressure away from the injection slot is only about 2% above the free stream pressure and hence the mechanical stress resulting from the pressure force is low.

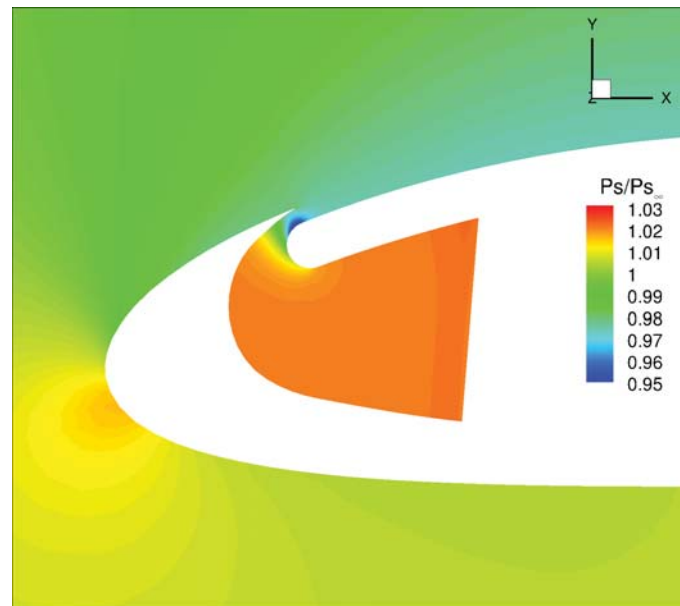


Figure 9.12: Static pressure contours at 50% spanwise location for the Design 1 CFJ wing. The CFJ wing is in cruise condition at  $AoA = 5.0^\circ$  and  $C_{\mu} = 0.04$ . The free stream static pressure is 1.00.

## 9.4 CFJ Spanwise Location

The Design 2 CFJ wing has the CFJ covering the 75% inner span. Everything else remains the same as the previous design. The wing surface pressure contours is shown in Fig. 9.13. Unlike the Design 1 CFJ wing, the flow is mostly attached up to  $AoA = 25.0^\circ$  and  $C_\mu = 0.08$ . This is because the jet is distributed on the inner 75% span only and hence it is actually stronger than for a jet distributed on the full span for a same  $C_\mu$ . The outer 25% span of the wing is also mostly attached due to the lower local loading.

The forces, moment and power consumption versus AoA for the Design 2 CFJ wing are shown in Fig. 9.14. When compared with the Design 1 CFJ wing, the stronger jet of the Design 2 CFJ wing yield a higher stall AoA, a slightly lower drag coefficient and a higher power coefficient. The moment coefficient is similar for both wings. The moment increase near the stall AoA is less pronounced with the Design 2 CFJ wing. Overall, the L/D of the Design 2 is slightly higher than that of the previous design at same AoA and  $C_\mu$ . However the  $(L/D)_c$  is a little lower due to the increase in power consumption. For the cruise condition at  $AoA = 5.0^\circ$  and  $C_\mu = 0.04$ , the L/D and  $(L/D)_c$  reach 34.2 and 22.5 respectively, with a cruise  $C_L$  of 1.16.

## 9.5 CFJ Injection Location & Redesigned Cavities

The Design 3 CFJ wing injection slot is moved upstream to a 2% chord location to maximize the benefits from the LE suction effect on the jet power consumption. Furthermore, the injection and suction cavities are modified to reduces the duct diffusion and avoids the flow separation as shown in Fig. 9.15. Everything else remains the same as the Design 1 CFJ wing.

The resulting wing performance changes are shown in Fig. 9.16. The lift and moment coefficients are virtually unaffected by the design modification at the exception of a slightly lower stall AoA at  $C_\mu = 0.08$ . On the contrary, the drag and power coefficients

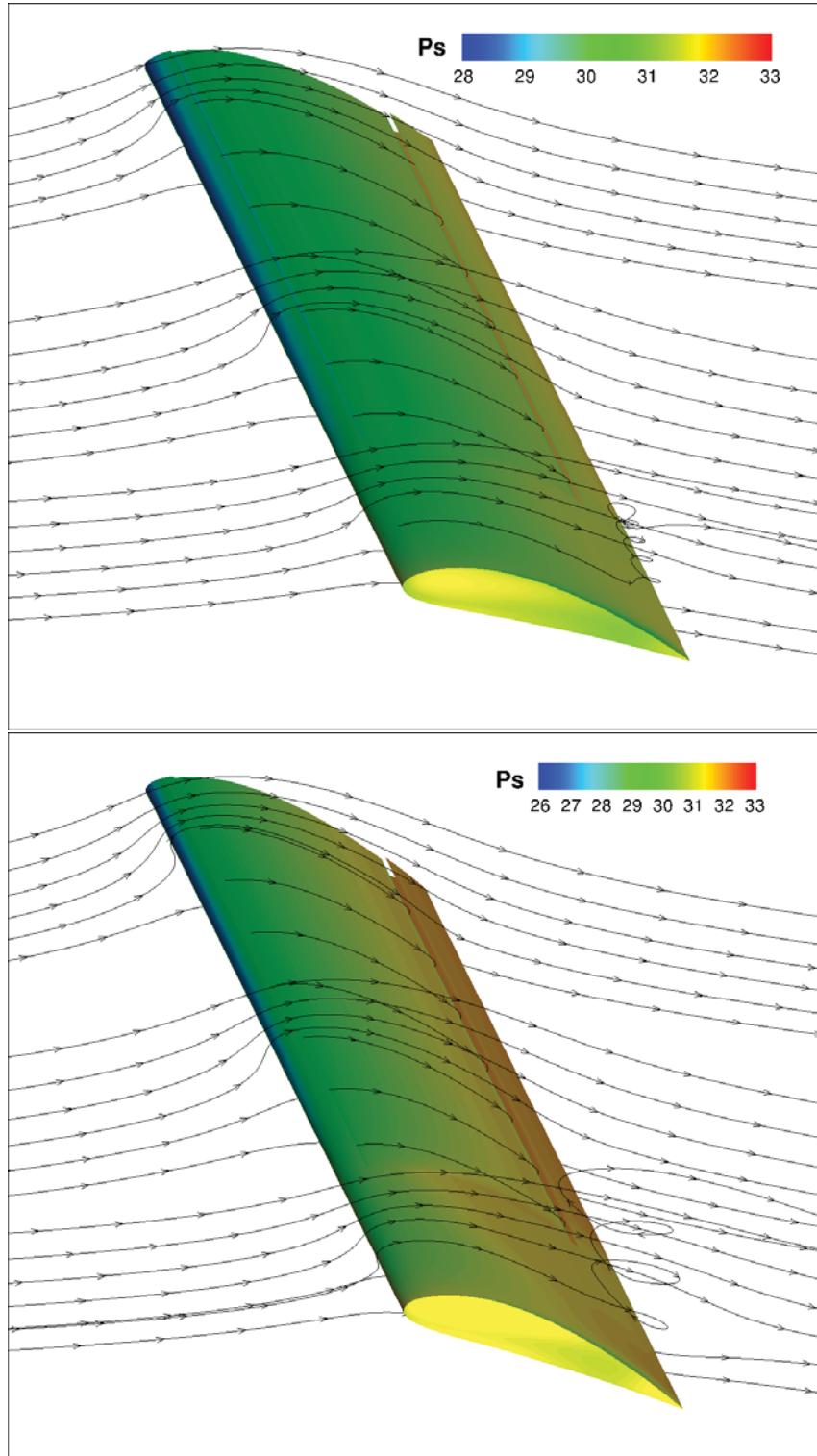


Figure 9.13: Surface pressure contours with streamlines for the Design 2 CFJ wing at  $C_{\mu} = 0.08$ . The top plot is at  $\text{AoA} = 15^{\circ}$  and the bottom plot at  $\text{AoA} = 25^{\circ}$ .

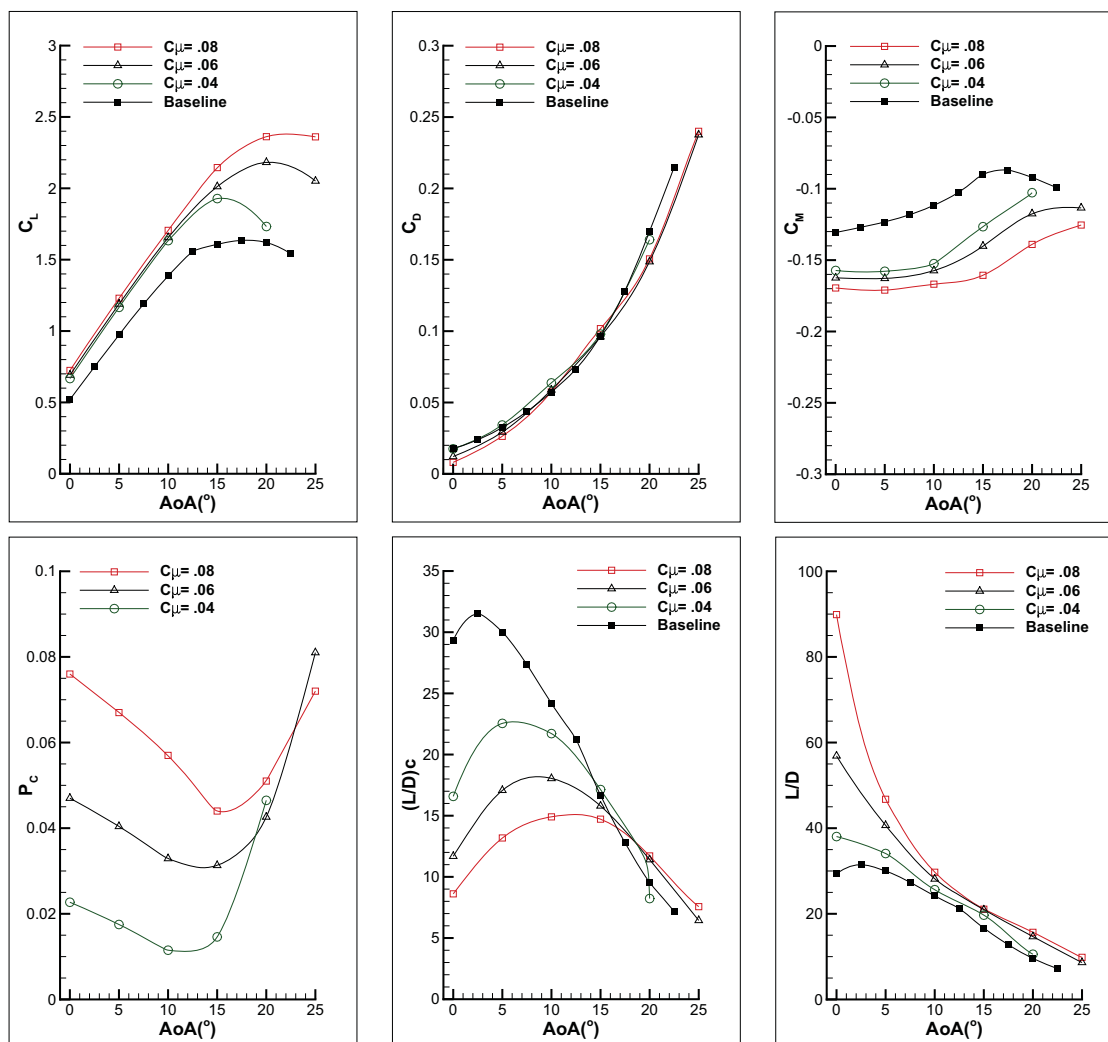


Figure 9.14: Forces, moment and energy expenditure versus AoA for the Design 2 CFJ wing. Simulations performed at  $M=0.15$  and  $0.04 \leq C_{\mu} \leq 0.08$ .

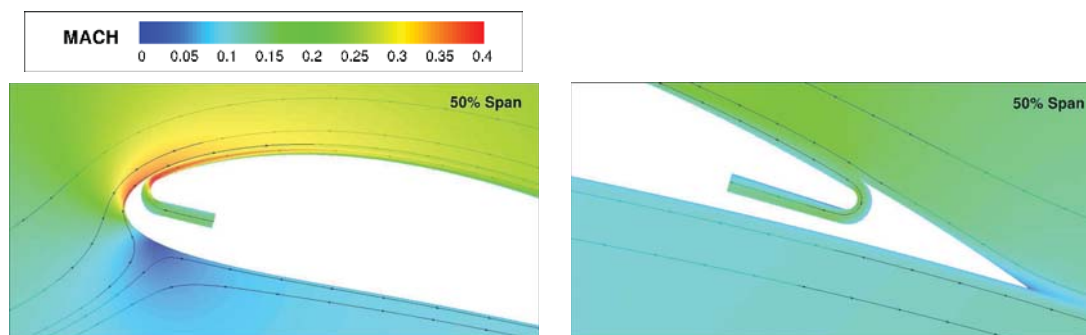


Figure 9.15: Mach contours with streamlines at 50% spanwise location for the Design 3 CFJ wing at  $C_{\mu} = 0.08$  and  $AoA = 15^\circ$ . A close up view of the redesigned injection and suction cavities is provided.

are both lower. A  $P_c$  reduction of about 45% is achieved for  $C_\mu = 0.08$ . However, this power reduction decreases with  $C_\mu$  and at  $C_\mu = 0.04$ , little gains are observed. The lower power coefficient and lower drag yield a significantly higher  $L/D$  and  $(L/D)_c$ . For instance, during cruise at  $AoA = 5.0^\circ$  and  $C_\mu = 0.04$ , the cruise  $L/D$  and  $(L/D)_c$  are 38.5 and 26.8 respectively. The cruise  $C_L$  is virtually unchanged. The stall  $AoA$  is slightly lower with the redesigned cavities. This might be because the jet with the injection slot located at 2% chord has less energy at the TE of the airfoil and hence the airfoil is more prone to TE separation.

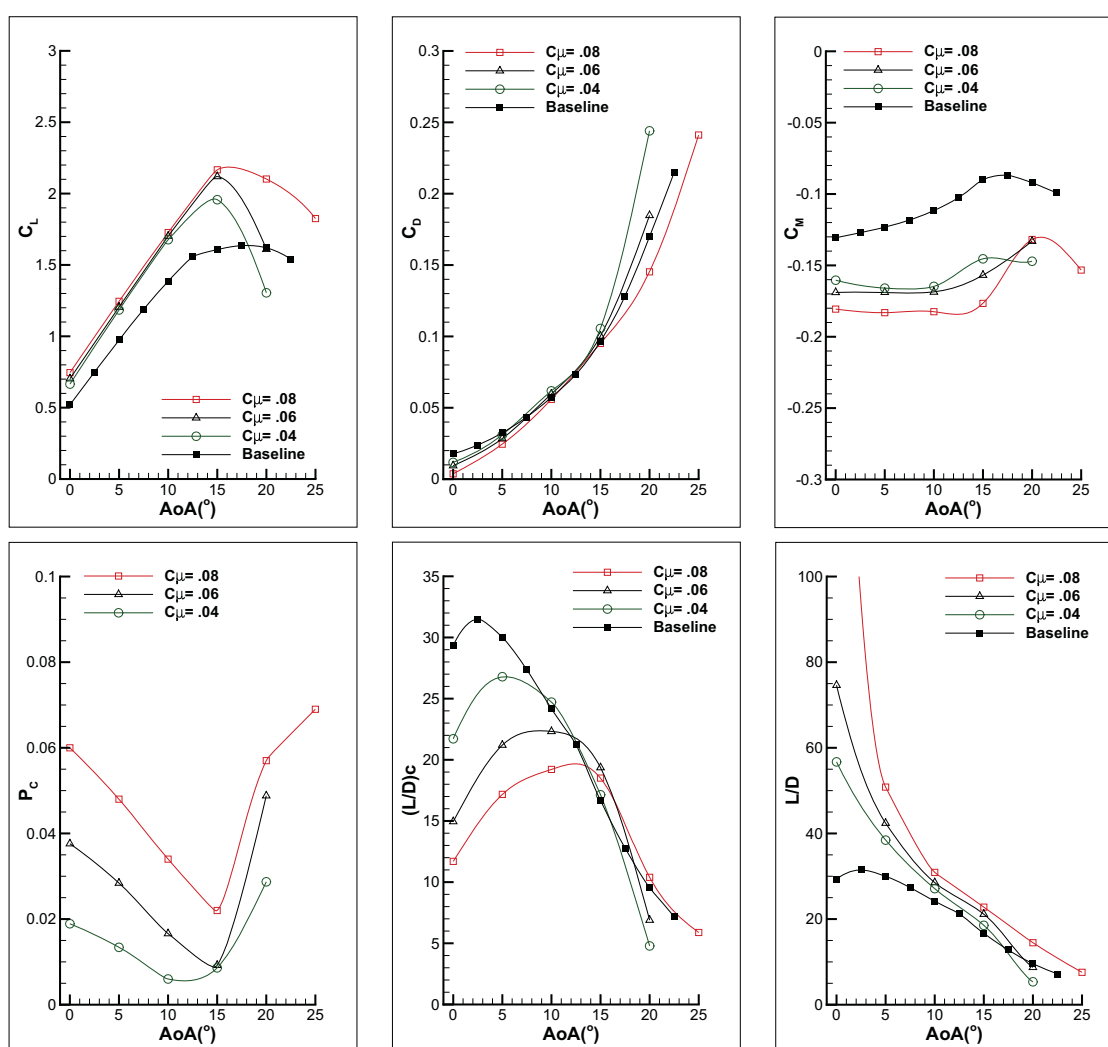


Figure 9.16: Forces, moment and energy expenditure versus AoA for the Design 3 CFJ wing. Simulations performed at  $M=0.15$ ,  $0.04 \leq C_\mu \leq 0.08$ .

## 9.6 Airfoil Thickness

The Design 4 CFJ wing is constructed with the thicker NACA 6421 CFJ airfoil with everything else the same as Design 3, including the injection and suction cavity geometries and the slots locations. The reflected wing performance changes are shown in Fig. 9.17. The lift coefficient is significantly increased at low and medium AoA because a thicker airfoil increases the circulation if the flow is not separated. However, the stall AoA is slightly decreased and hence the CFJ wing maximum  $C_L$  is similar ( $C_\mu = 0.08$ ) or slightly lower ( $C_\mu = 0.04 - 0.06$ ) to that of the previous design. The drag coefficient is similar to that of the thinner CFJ wing. The pitch down moment is slightly increased. The power consumption of the thicker CFJ wing is slightly increased, and the  $(L/D)_c$  is slightly decreased. For the cruise condition at  $AoA = 5.0^\circ$  and  $C_\mu = 0.04$ , the  $L/D$  and  $(L/D)_c$  are 38.8 and 25.3 respectively. The cruise  $C_L$  is increased by 5% and reaches 1.22. Fig. 9.17 also indicates that the Baseline 2 wing with no CFJ suffers a significant  $L/D$  loss due to the increased drag coefficient, whereas the thick CFJ airfoil only has the  $(L/D)_c$  slightly reduced. Thereby, a CFJ wing can be designed to be very thick with little aerodynamic and energetic penalties. Such a wing would benefit from important structural advantages in term of weight, strength and inner volume.

## 9.7 Wing Aspect Ratio

To study the effect of the aspect ratio, the Design 5 CFJ wing aspect ratio is decreased from 20 to 10. Everything else remains the same than the Design 4 CFJ wing. The reflected wing performance changes are shown in Fig. 9.18. The lower aspect ratio CFJ wing is more affected by the wing tip downwash, which reduces the lift at same AoA and  $C_\mu$ . In addition, the total drag is significantly increased due to the higher lift induced drag. Consequently the  $L/D$  ratio is significantly reduced when compared to the aspect ratio 20 wing. However, it remains much higher than that of the Baseline 3 wing which also

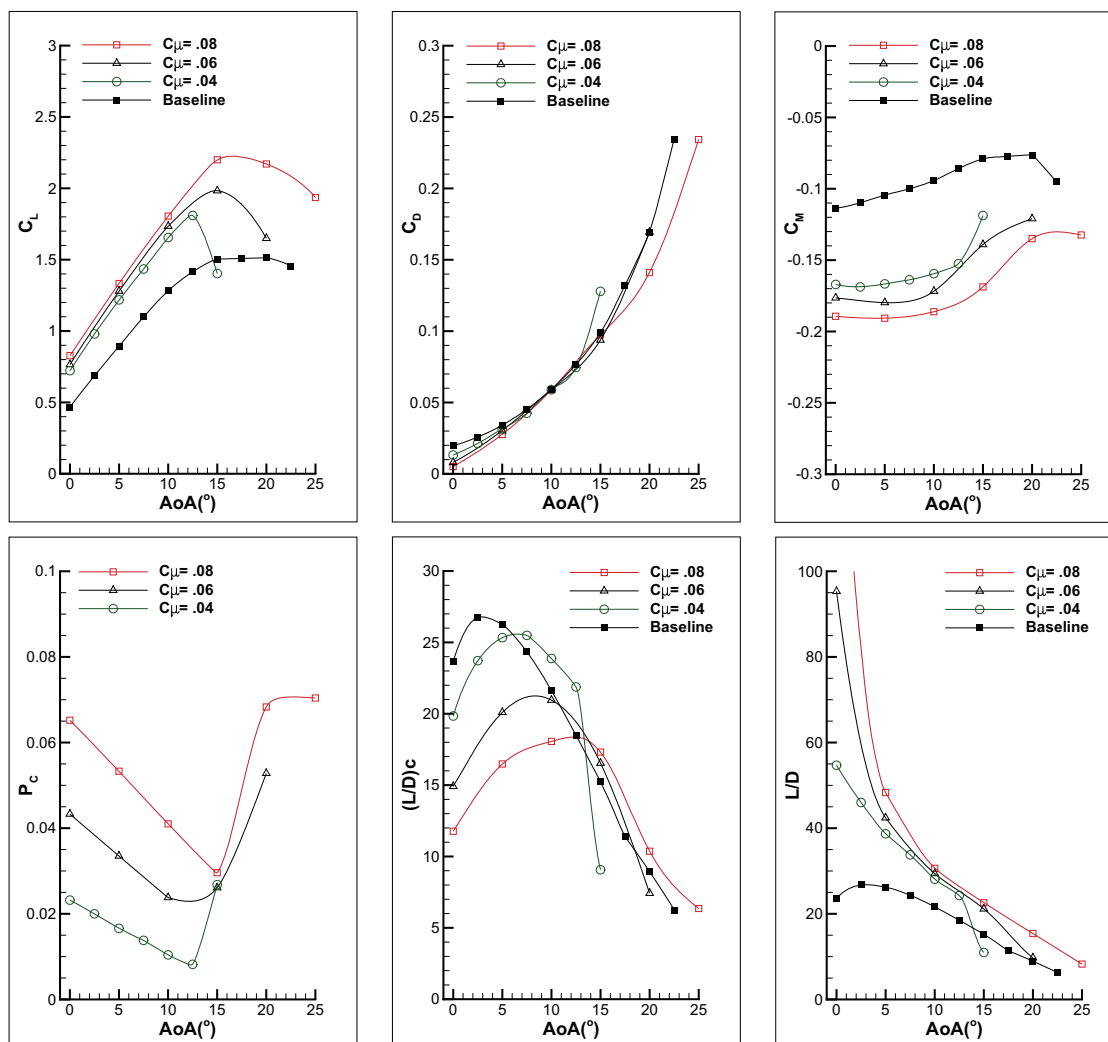


Figure 9.17: Forces, moment and energy expenditure versus AoA for the Design 4 CFJ wing. Simulations performed at  $M=0.15$ ,  $0.04 \leq C_{\mu} \leq 0.08$ .

feature an aspect ratio 10 but no CFJ (see Table 9.1). The stall AoA is increased due to the lower wing loading and overall, the maximum lift coefficient is similar for  $C_{\mu} = 0.04$  and  $C_{\mu} = 0.06$  and even slightly increased for  $C_{\mu} = 0.08$ . The moment and power coefficients are virtually unaffected by the aspect ratio. For the cruise condition at  $AoA = 5.0^\circ$  and  $C_{\mu} = 0.04$ , the  $L/D$  and  $(L/D)_c$  are 23.7 and 17.2 respectively, a significant reduction when compared with the aspect ratio 20 of the Design 4 CFJ wing.

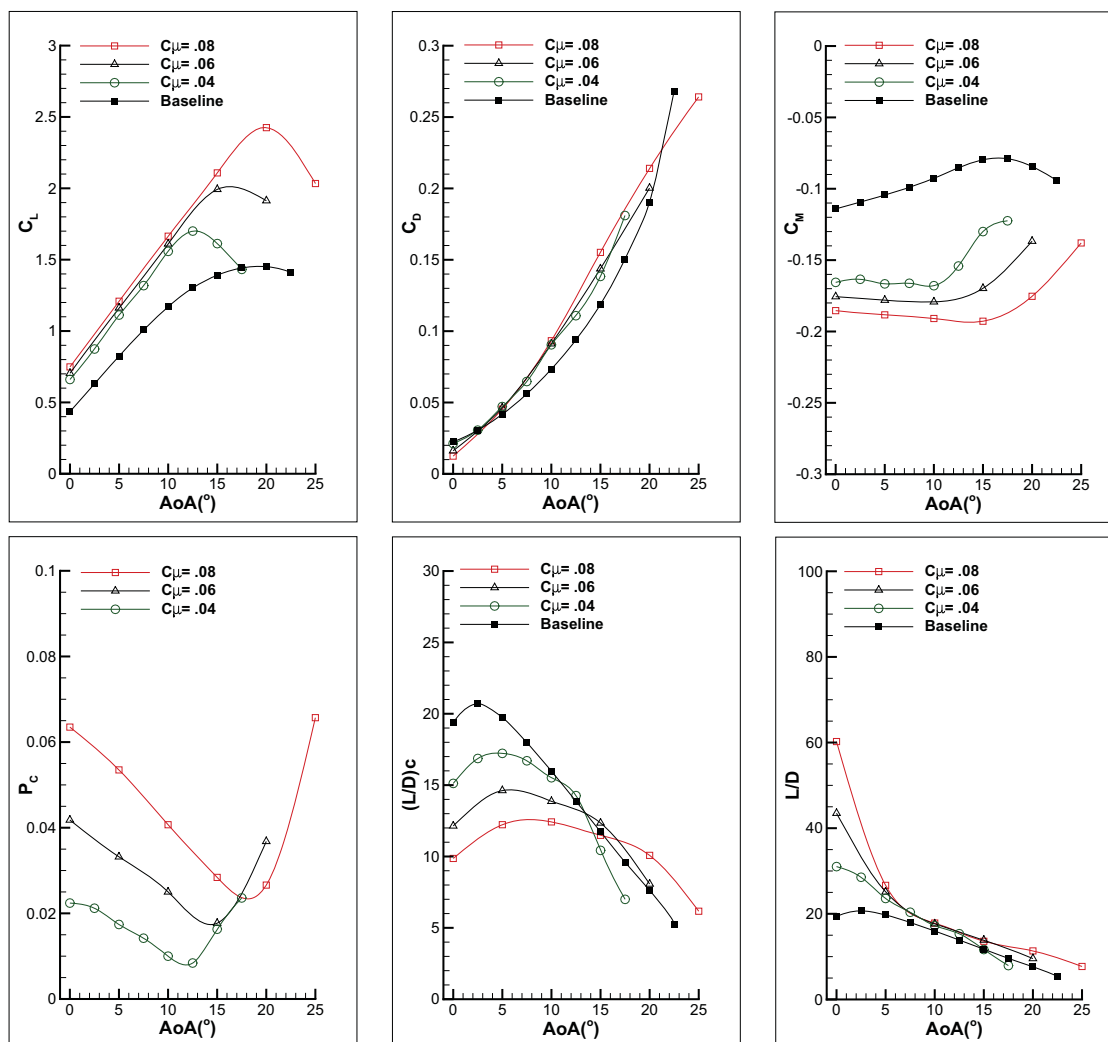


Figure 9.18: Forces, moment and energy expenditure versus AoA for the Design 5 CFJ wing. Simulations performed at  $M=0.15$ ,  $0.04 \leq C_\mu \leq 0.08$ .

## 9.8 Recapitulation of the CFJ Wings Performance at Cruise

The corrected aerodynamic efficiency versus  $C_L$  is plotted Fig. 9.19 to summarize the CFJ wings performance at cruise and provide a clear comparison of the various designs. For all designs, the baseline airfoil is efficient at low  $C_L$  but is surpassed by the CFJ airfoil at  $C_L$  typically above 1.2 for  $C_\mu = 0.04$  (and at a higher  $C_L$  for larger  $C_\mu$ ). The design 1 and 2 performance are similar, therefore, having CFJ implemented on all the wing span or only the inner 75% span doesn't affect much the overall performance in the range of AoA and  $C_\mu$  studied. However the design 3 performance is much improved over design 1 and 2,

proving that the cavity design is crucial to maximize the CFJ wing performance. When the wing thickness is increased to 21%, the baseline airfoil performance is much lower, which is expected from such a thick airfoil. However, when CFJ is applied to the thick airfoil, the performance is very similar to that of the 15% thickness CFJ wing. Hence it is possible to design a much thicker CFJ wing than what is possible with a conventional wing without reducing the efficiency significantly. When the wing aspect ratio is reduced to 10, the conclusion for aspect ratio 20 wing, that the CFJ wing outperforms the baseline wing in term of maximum  $C_L$  and efficiency at high  $C_L$ , is still valid. Indeed the disparity between the maximum  $C_L$  of the baseline and the CFJ wing is even greater for an aspect ratio 10 wing.

## 9.9 CFJ Wing Maximum Lift Coefficient in Takeoff or Landing Condition

The Design 4 CFJ wing is simulated at high AoA and high  $C_\mu$  at a lower Mach number of 0.1 to simulate the takeoff/landing conditions. The resulting surface isentropic Mach number contours are shown Fig. 9.20. Large flow accelerations are located at the airfoil LE and suction surface, which responsible for the very high lift and low pressure drag. The flow is fully attached for this case at  $AoA = 20.0^\circ$ .

The wing performance is shown on Fig. 9.21. At  $C_\mu = 0.28$  the flow is attached up to  $AoA = 40.0^\circ$  and the  $C_L$  reaches an outstanding value of 4.7. The drag at  $AoA = 20.0^\circ$  and  $AoA = 25.0^\circ$  is similar for all the momentum coefficients. However at higher AoA, a higher  $C_\mu$  yield a higher drag coefficient mostly because of the greater lift induced drag. The moment coefficient remains contained between -0.2 and -0.3. The power coefficient is significantly increased because of the high  $C_\mu$ . However the actual power consumption increase, which depends on the cube of the free stream velocity as indicated by Eqs. 4.12 and 4.13, is much lower. Even with a very high  $C_L$ , the CFJ wing achieves a good L/D and (L/D)<sub>c</sub>. For example, during a typical takeoff/landing at  $AoA = 25.0^\circ$  and  $C_\mu = 0.20$ , the

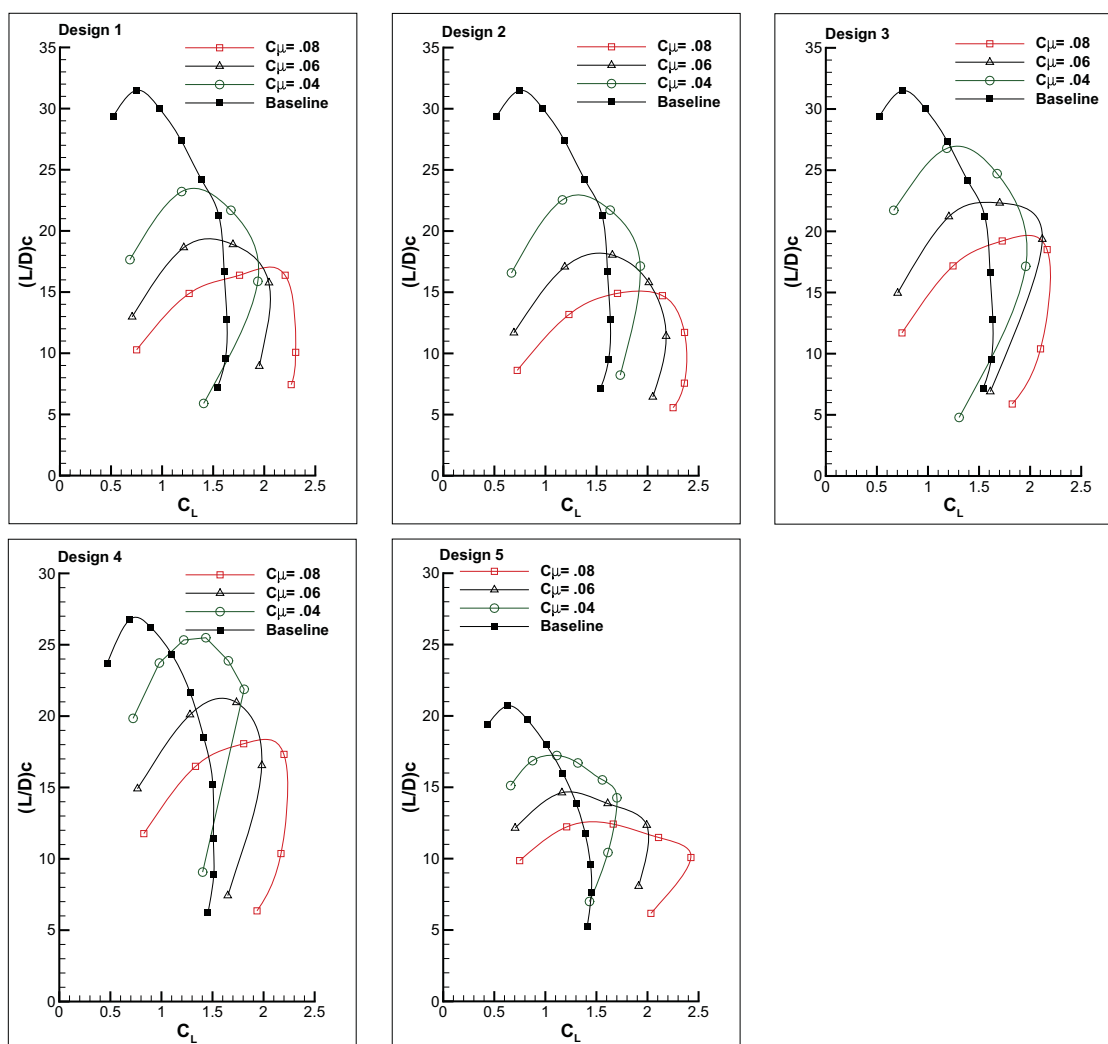


Figure 9.19: Corrected aerodynamic efficiency versus  $C_L$  for the Design 1-5 CFJ wings. Simulations performed at  $M=0.15$  and  $0.04 \leq C_\mu \leq 0.08$  to simulate typical cruise conditions.

lift coefficient is a 3.5 with a corresponding  $L/D$  and  $(L/D)c$  of 16.3 and 10.4 respectively. In this conditions, the wing still has a wide stall margin of about  $10.0^\circ$ .

The corrected aerodynamic efficiency versus  $C_L$  is plotted Fig. 7.30. From this plots, it is possible to interpolate the CFJ wing peak efficiency change with  $C_\mu$ , as indicated by the CFJ peak efficiency line. For instance, if the CFJ wing produces a  $C_L$  of 3.1, then a  $C_\mu$  of 0.16 will generate the best efficiency of 11.7. This is useful to achieve the most efficient combination of  $C_L$ - $C_\mu$ .

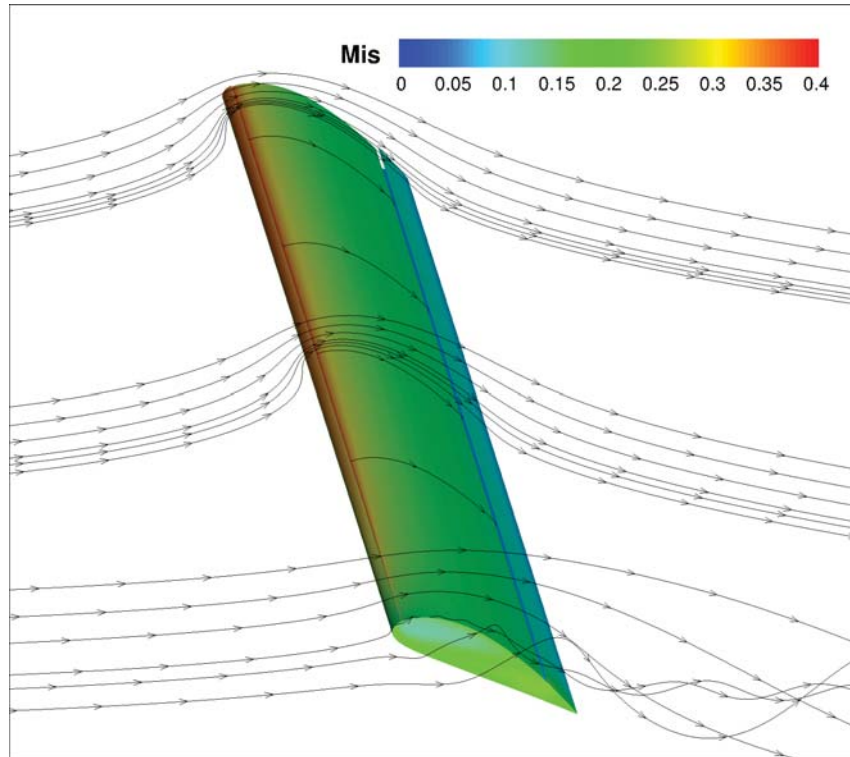


Figure 9.20: Surface isentropic Mach number contours with streamlines for the Design 4 CFJ wing at  $AoA = 25^\circ$  and  $C_\mu = 0.20$ . Simulations performed at  $M=0.1$ , to simulate the takeoff and landing conditions.

Even for the very large AoA studied here, the power coefficient still decreases with the increase of AoA until the near stall. When the flow separation occurs, the power coefficient is significantly increased due to the high total pressure loss as seen on Fig. 9.23. This behavior is similar to what we have seen on Fig. 9.10 for the cruise condition, albeit with higher value of AoA and  $C_\mu$ . The total pressure ratio is increased when compared to cruise, but remains contained to less than 1.04 for a typical takeoff or landing.

Fig. 9.24 shows a close up view of the static pressure contours in the vicinity of the injection region. The CFJ wing is in takeoff/landing condition at  $AoA = 25.0^\circ$  and  $C_\mu = 0.20$ . Similarly to the cruise condition seen Fig. 9.12, the injection cavity pressure away from the injection slot is only about 2% above the free stream pressure and hence the mechanical stress resulting from the pressure force is low.

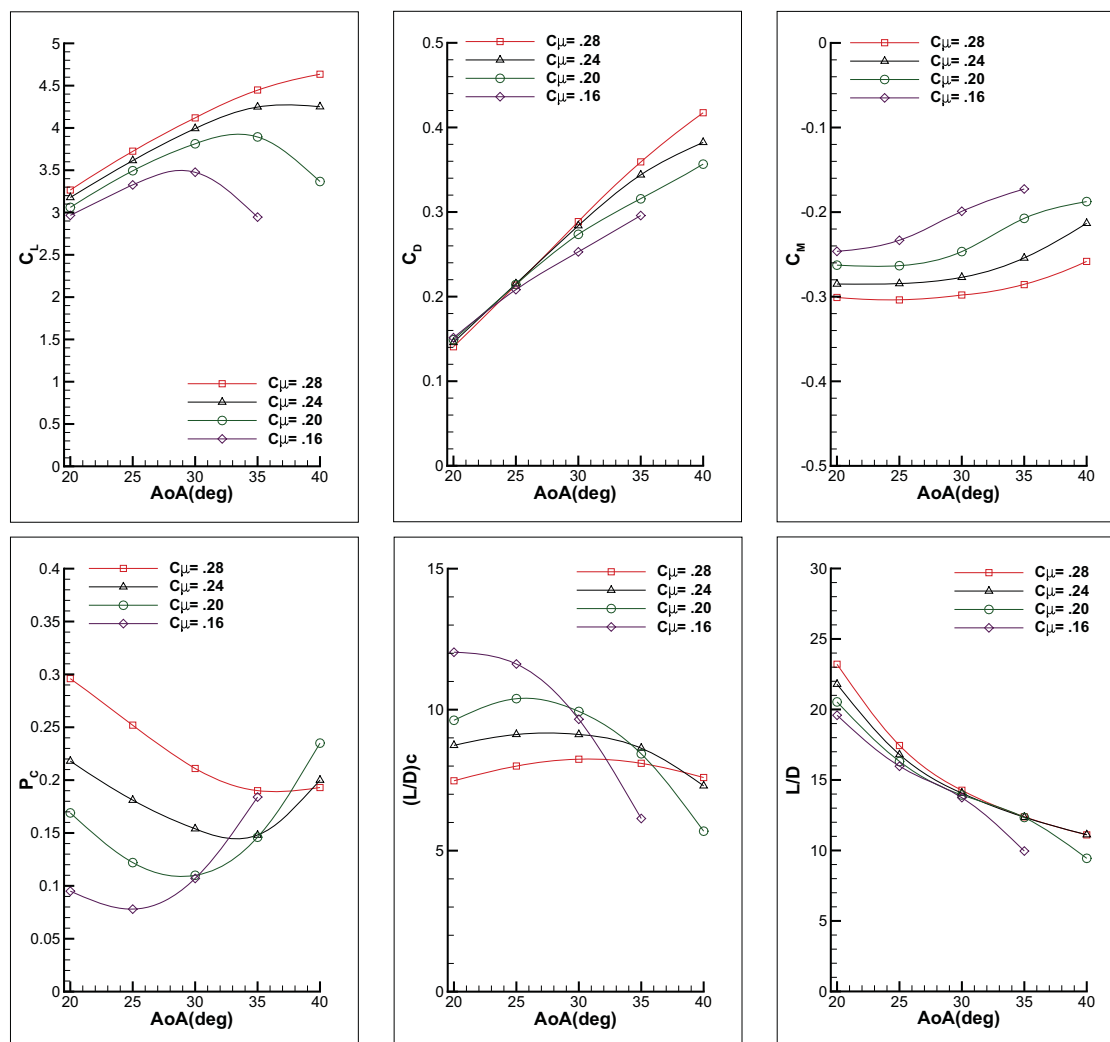


Figure 9.21: Forces, moment and energy expenditure versus AoA for the Design 4 CFJ wing. Simulations performed at  $M=0.1$  and  $0.16 \leq C_{\mu} \leq 0.28$  to simulate the takeoff and landing conditions.

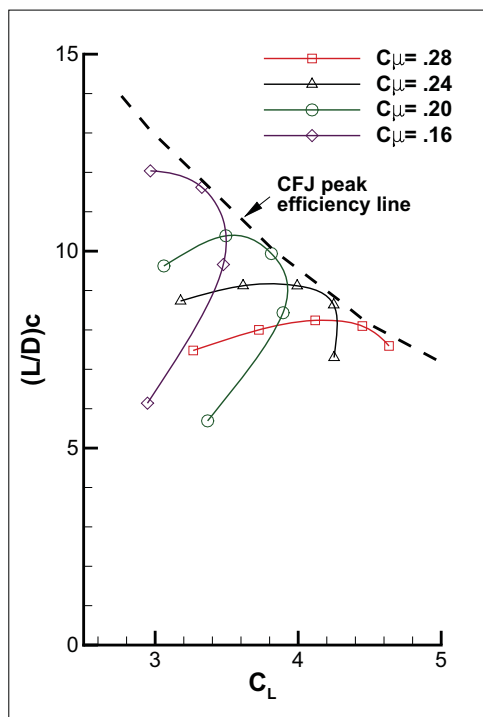


Figure 9.22: Corrected aerodynamic efficiency versus AoA for the Design 4 CFJ wing. Simulations performed at  $M=0.1$  and  $0.16 \leq C_{\mu} \leq 0.28$  to simulate the takeoff and landing conditions.

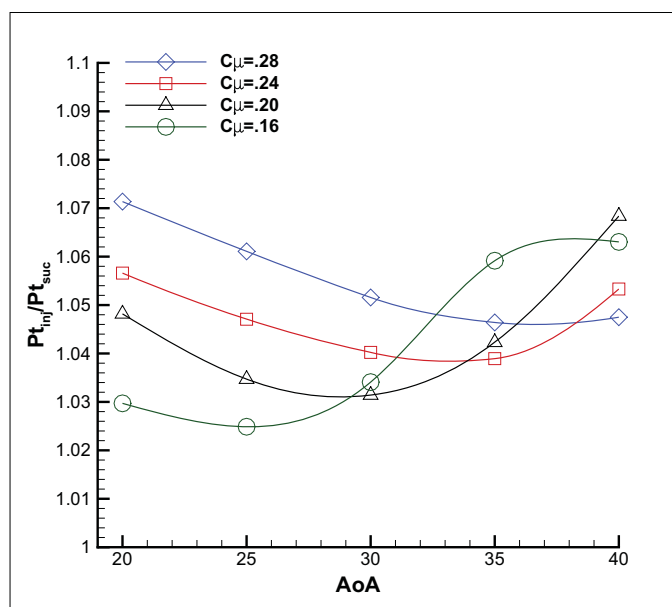


Figure 9.23: Mass-averaged total pressure ratio between the injection and suction cavities for the Design 4 CFJ wing for a typical takeoff or landing.

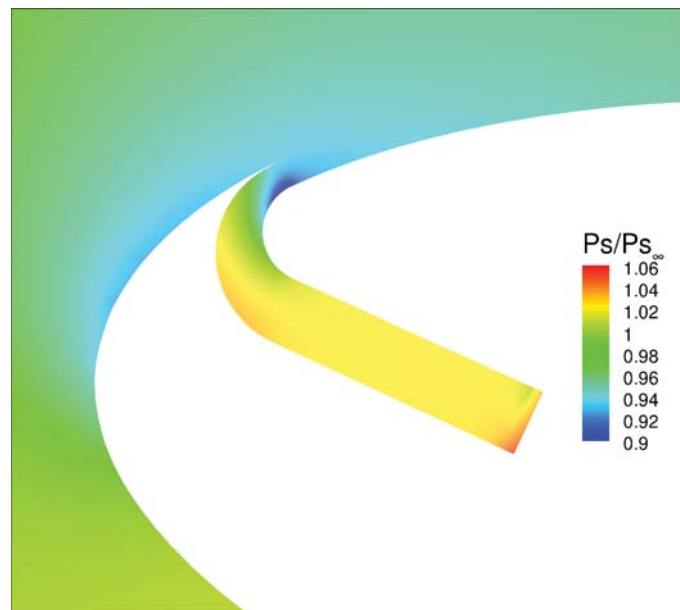


Figure 9.24: Static pressure contours at 50% spanwise location for the Design 4 CFJ wing. The CFJ wing is in takeoff/landing condition at  $AoA = 25.0^\circ$  and  $C_\mu = 0.20$ . The free stream static pressure is 1.00.

# Chapter 10

## Conceptual Design of a CFJ Electric

### Aircraft

Two conceptual electric airplane (EA) designs utilizing Co-Flow Jet (CFJ) flow control are presented in this chapter. The first design is a flying wing (FW) CFJ-EA which maximizes the lifting area and the volume inside the airplane. The second airplane is a glider-like design, whose high aspect ratio (HAR) CFJ wing is based on the study in 9. The HAR wing is specially designed to reduce the lift induced drag, and improve the cruise efficiency [65]. The mission of those CFJ Electric Aircraft is to carry 4 passengers at a cruise Mach number of 0.15 over the longest range possible. The designs are trimmed in cruise condition and the static stability margin is modest for the FW design, and large for the HAR design.

The motivation for designing an electric airplane is driven by the necessity for mankind to lower its environmental footprint and to prepare for the rarefaction of liquid fuels. While the electric plane performance is not expected, in the short term, to reach those of internal combustion airplanes, continuous improvements in electric storage coupled with the price increase of kerosene could make the electric private plane market grow considerably in the next decade.

## 10.1 The CFJ Flying Wing Design

### 10.1.1 Mesh

The baseline FW EA mesh, shown in Fig. 10.1, is constructed with 140 points around airfoil partitioned equally between the suction and the pressure surfaces, 120 points in the direction normal to the wall and 80 points in the spanwise direction. The total mesh size is 2.4 million cells, split into 104 blocks for parallel computation. The far field boundary is located 50 chords away from the airfoil. The first grid point is placed at  $y^+ \approx 1$  except on the wing tip wall where  $y^+ \approx 50$  is used in combination with the wall function to reduce the mesh size.

The CFJ CFJ-EA Design 1, Design 2 and Design 3 meshes, shown in Fig. 10.2, are constructed using an O-mesh topology displayed in black and an H-mesh topology displayed in red. A typical mesh uses a total of 280 points around the airfoil partitioned equally between the suction and the pressure surfaces, 120 points in the direction normal to the airfoil, 60 points across the jet and 120 points in the spanwise direction. The total mesh size is 6.2 million cells, split into 265 blocks for parallel computation. The far field boundary is located 50 chords away from the airfoil. The first grid point is placed at  $y^+ \approx 1$  to resolve the turbulent boundary layer except for the wing tip wall where  $y^+ \approx 50$  is used with the wall function boundary condition to reduce the mesh size.

A refined grid is constructed for both the baseline EA and the CFJ-EA using 50% more points in every direction with  $y^+ \approx 0.7$  at the walls except at the wing tip wall where  $y^+ \approx 35$ . The refined mesh results agree very well with the original mesh.

### 10.1.2 Aircraft Configuration

The FW EA geometry is the result of a trade study on the planform shape, the airfoil design and the wing twist. The planform shape features a 6m long central section for maneuverability with long and tapered wing for the aerodynamic performance. The wing

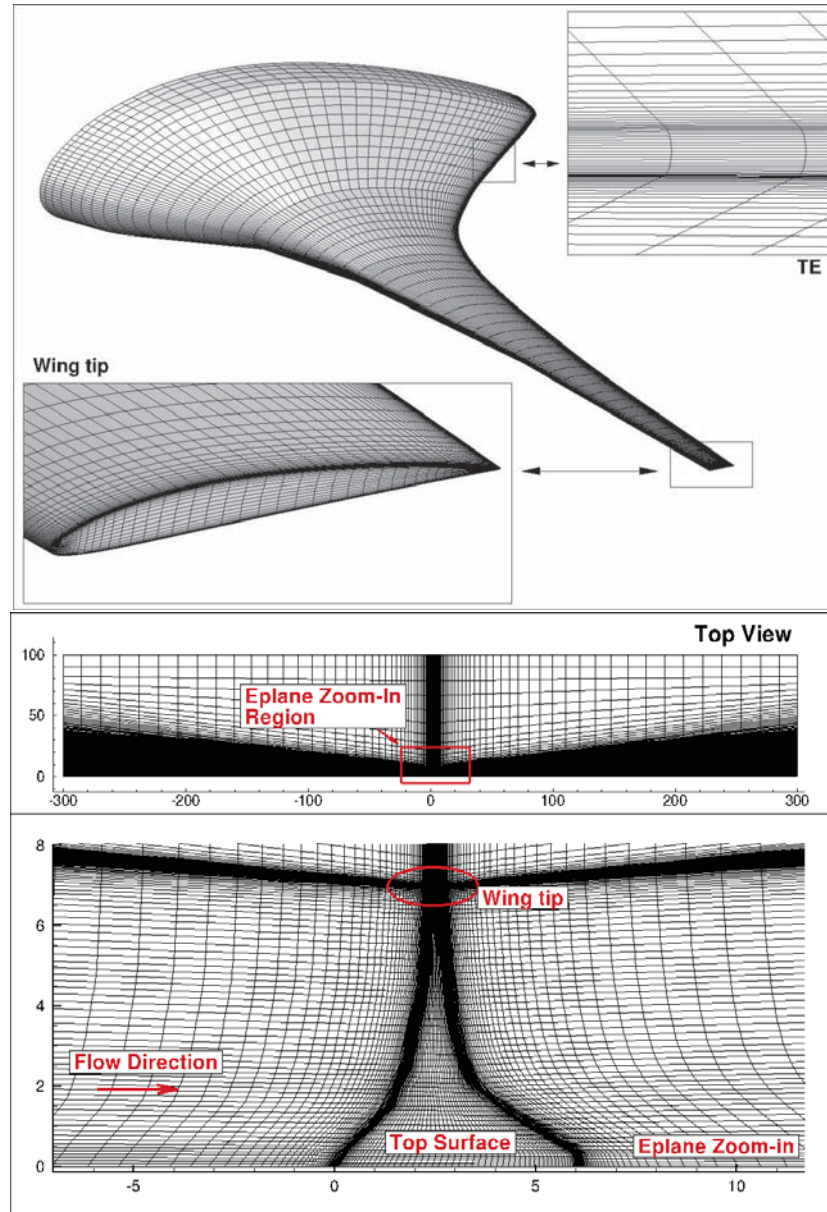


Figure 10.1: Geometry and mesh overview for the baseline Eplane.

placement has a strong influence on the aircraft center of aerodynamic forces. However to achieve the longitudinal static stability, an airfoil with a neutral or slightly positive moment is desirable. For this reason, the baseline and CFJ airfoils designs are based on a NACA 5 digits series to which we applied some reverse camber at the rear as seen in Fig. 10.3. The CFJ airfoils utilize a little more reverse camber at the TE to compensate for the nose-down moment generated by the jet. More details about the CFJ airfoil design can be found in [63,64].

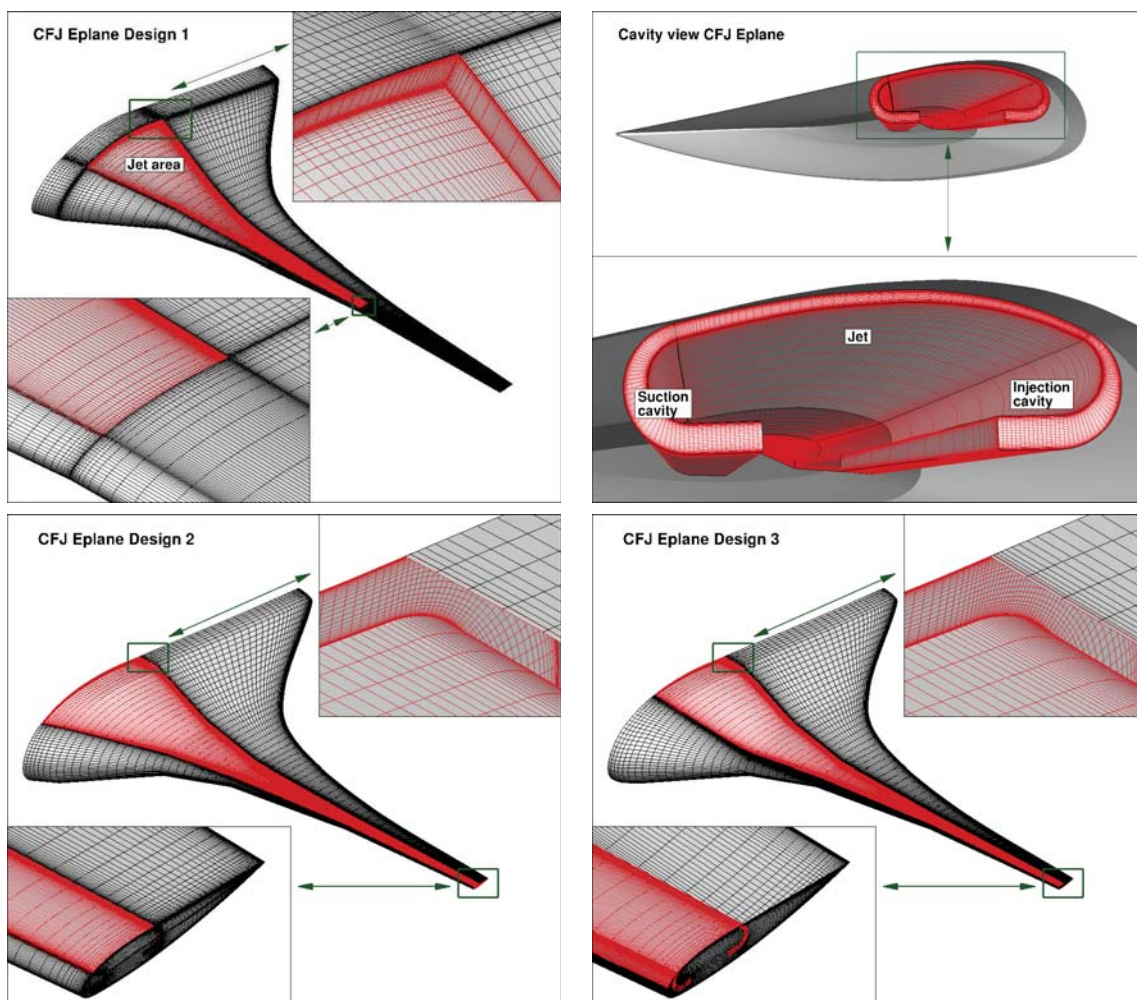


Figure 10.2: Geometry and mesh overview for the CFJ-EA Design 1, Design 2 and Design 3.

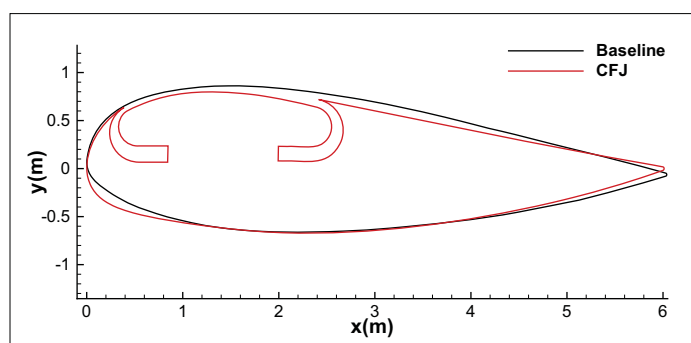


Figure 10.3: Slightly off-center profile comparison between the baseline and CFJ-EA.

The center sections airfoils use a moderate reflex camber, with a TE deflection of  $4^\circ$ . This is found to bring the best compromise between performance and moment for this design. Wing twist is applied to the center section and to the wing tip section to increase

the aerodynamic efficiency. The sections between 15% span and 75% span are not twisted and are utilized as reference for the AoA. The center section is twisted by  $-2^\circ$  and the wing tip is twisted by  $-3^\circ$  (a positive twist angle is defined by convention as a twist that would increase the AoA of the section). A wing dihedral angle of  $3^\circ$  is applied to increase the aircraft lateral stability and the clearance between the wing tip and the runway. The EA airfoil thickness varies from 25% in the center section to 12% at the wing tip section. The 6m length central section combined with the thickness of the center airfoils provide a spacious cabin to fit 4 passengers with luggage and has extra space for battery. The planform area of  $24.2m^2$  and the wing span of 14m give the EA an aspect ratio of 8.1. The main geometric parameters are listed in Table 10.1.

Geometry Parameters								
Length	Span	Area	AR	Airfoil thickness	Wing twist	Wing dihedral	CFJ slot size	CFJ slot location
(m)	(m)	(m <sup>2</sup> )		(% chord)	(deg)	(deg)	(% chord)	(% chord)
				center, mid-span, tip	center, mid-span, tip	center, mid-span, tip	injection, suction	injection, suction
6.0	14.0	24.2	8.1	25%, 15%, 12%	-2, 0, -3	3, 3, 3	0.75%, 1.5%	5%, variable

Table 10.1: EA geometry parameters.

The CFJ-EA Design 1 is covered by CFJ from 5% span to 65 % span. The sections without CFJ are identical to the baseline EA. The CFJ-EA Design 2 is modified from the Design 1 to utilize CFJ from wing tip to wing tip. The CFJ-EA Design 3 is modified from Design 2 to have an injection direction more parallel to the main flow. The last design, the hybrid CFJ-EA, has a baseline EA geometry for cruise and the CFJ-EA geometry during the TO, climbing and landing phases when the high lift is desirable. The geometry change is done by translating the surface between the injection and suction slots upward or downward, to close or open, the injection and suction slots. No simulation is done for this design because we assume that it will have either the baseline EA flight characteristic during cruise and the CFJ-EA Design 3 ones during the TO, climbing and landing phases.

### 10.1.3 Qualitative Analysis

This section presents the flow visualization of the baseline and CFJ EA plotted at cruise AoA with  $C_{\mu} = 0.08$  for the CFJ-EA.

The baseline EA surface pressure contours with streamlines is plotted Fig. 10.4 cruise AoA of  $5^{\circ}$ . A color code is applied to help visualize the streamlines. The red streamlines originate from the pressure surface and the blue streamlines originate from the suction surface of the aircraft. The stagnation point appears clearly below the nose of the aircraft. From there the flow goes around the central section with a strong spanwise flow component. This strongly reduces the circulation over the central sections which is visualized by the very light blue color at their TE. Off-center sections generate a much lower pressure hence the deeper blue color at their TE. The top view shows the flow deviation between the suction and pressure surface of the wing. The 3D flow structures are further observed on the front view.

The CFJ-EA Design 1 surface pressure contours with streamlines is shown Fig. 10.5. At the outer span, the jet exits parallel to the main flow and remain attached until it get sucked in the suction slot, in a similar manner to 2D CFJ flow [61–64]. At the inner section of the wing, the high sweep angle of the injection makes the jet flow towards the central section of the plane instead of parallel to the free stream. Upon colliding with the side wall, the jet detaches. The jet detachments have two main negative effects. First, it reduces the aerodynamic efficiency because of the drag increase. Second, because of the jet spanwise velocity and the jet separation, less jet momentum reaches the suction slot, which increases the pumping energy consumption.

In order to reduce the jet detachment, the CFJ-EA Design 2 is generated with CFJ from wing tip to wing tip which removes the side wall. Fig. 10.6 shows that the separation still occurs in the center part of the aircraft mainly due to the high jet sweep angle in the central section region. The separation is however much milder as indicated by the increase of peak efficiency from approximately 11.2 for Design 1 to 13.3 for Design 2 at  $C_{\mu} = 0.08$

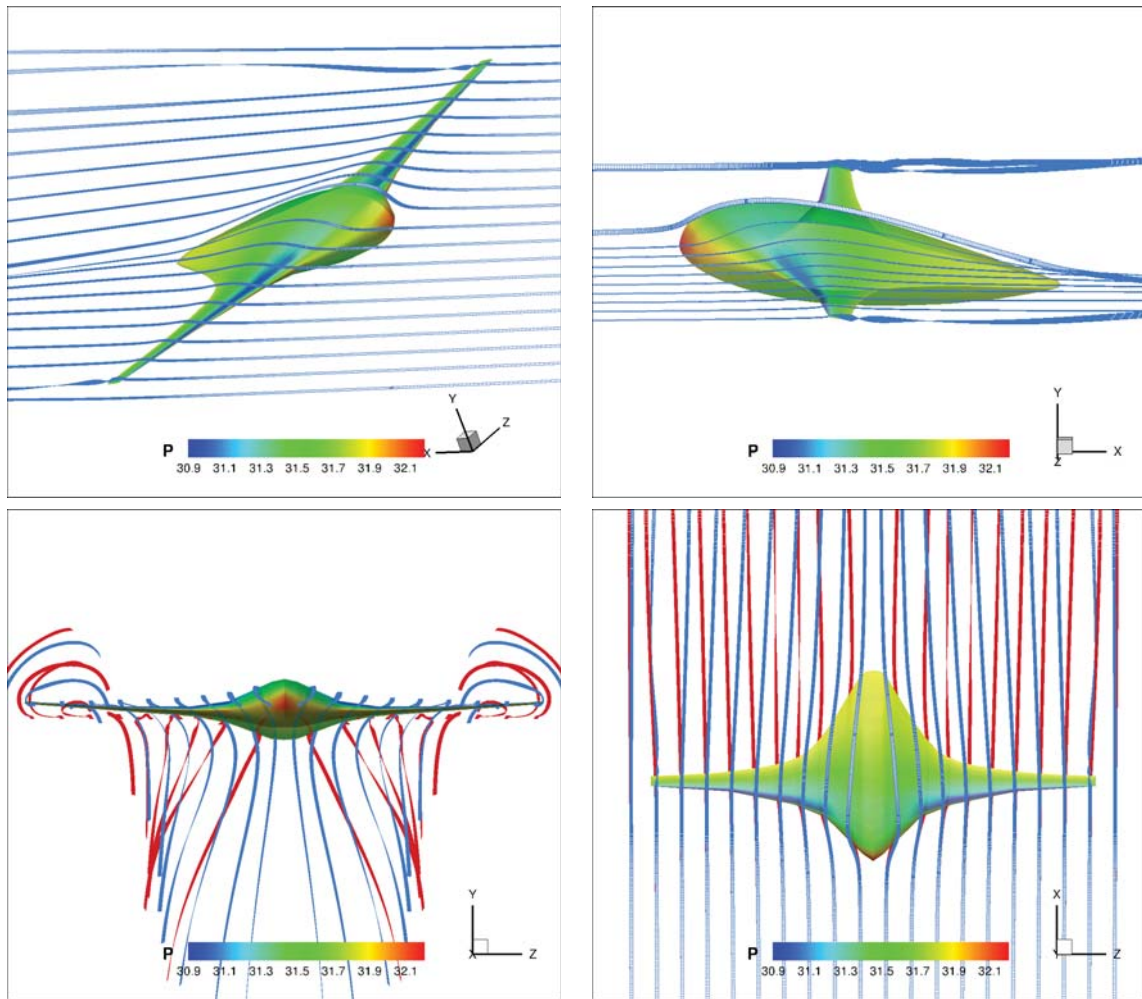


Figure 10.4: Surface pressure contours with streamlines for the baseline EA at  $AoA = 5^\circ$ . The red, respectively blue, streamlines originate from the pressure side, respectively the suction side, of the aircraft.

The CFJ-EA Design 3 is designed with a jet exit slot more perpendicular to the main flow to reduce the jet spanwise component. The jet detachment shown Fig. 10.7 is mild and localized which is confirmed by the peak efficiency that reaches approximately 14.9 at  $C_\mu = 0.08$ .

Fig. 10.9 gives further details about the flow field around the CFJ-EA Design 3. The jet remains attached on most of the aircraft. However, for the central section, the jet detaches almost right after the jet exit. Once detached, the jet goes horizontally, significantly increasing the wake of the aircraft. In addition to the jet spanwise component, the elevated suction cavity pressure in the center section, shown Fig. 10.8, is found to play a key role

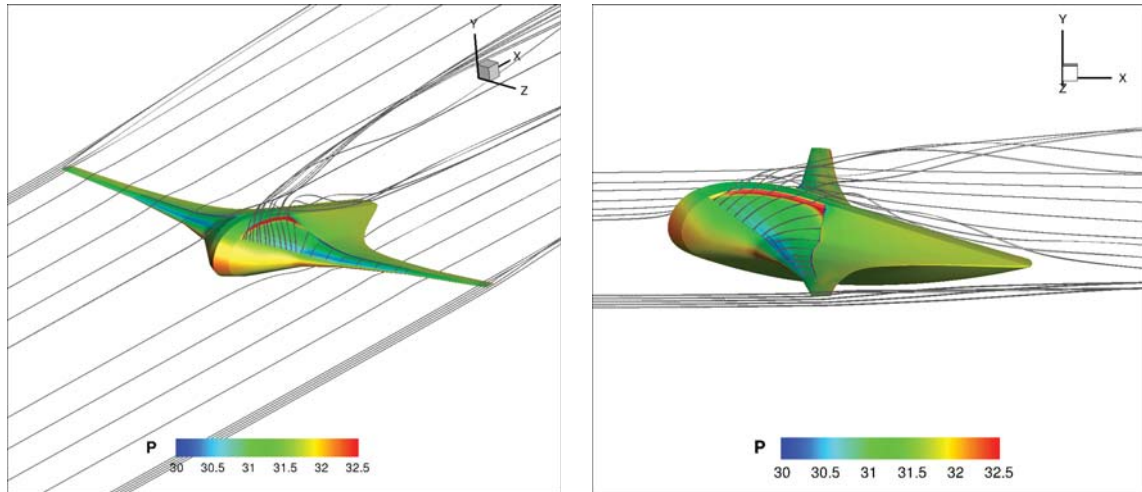


Figure 10.5: Surface pressure contours with streamlines for the CFJ-EA Design 1 at  $C_{\mu} = 0.08$  and  $AoA = 5^{\circ}$ .

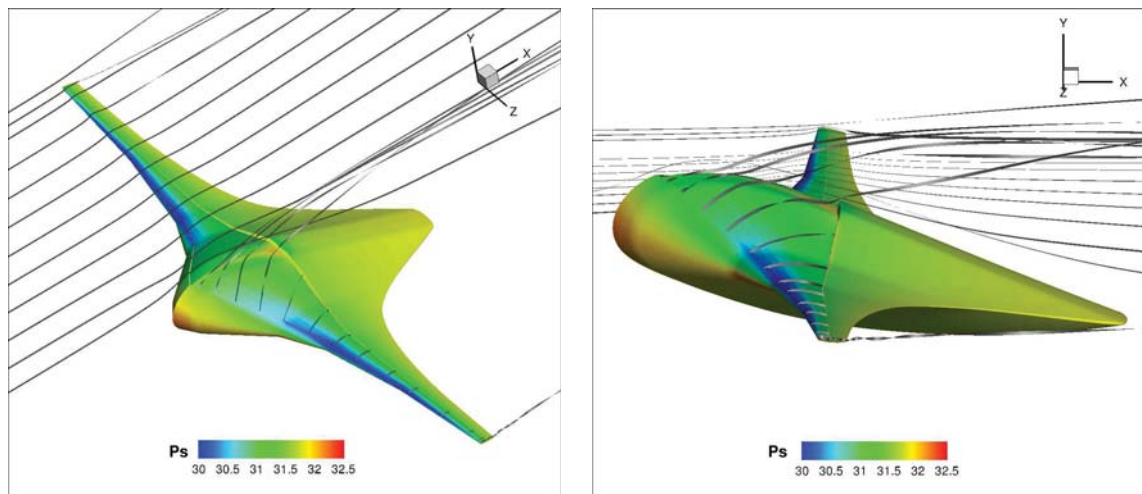


Figure 10.6: Surface pressure contours with streamlines for the CFJ-EA Design 2 at  $C_{\mu} = 0.08$  and  $AoA = 10^{\circ}$ .

for the jet detachment. The suction cavity pressure is set iteratively during the calculation to equalize the injection and suction mass flows. Typically the suction pressure is almost equal to the free stream pressure because the jet momentum and the suction slot thickness can easily capture the required mass flow. The relatively high suction pressure does not trigger jet separation for the outer span because the high jet momentum forces the jet into the suction slot. However for the inner part of the wing, the lower jet momentum and the stronger spanwise component prevent the jet from overcoming the slight adverse pressure gradient at the suction slot entrance and the jet detaches. In the future, stronger suction will

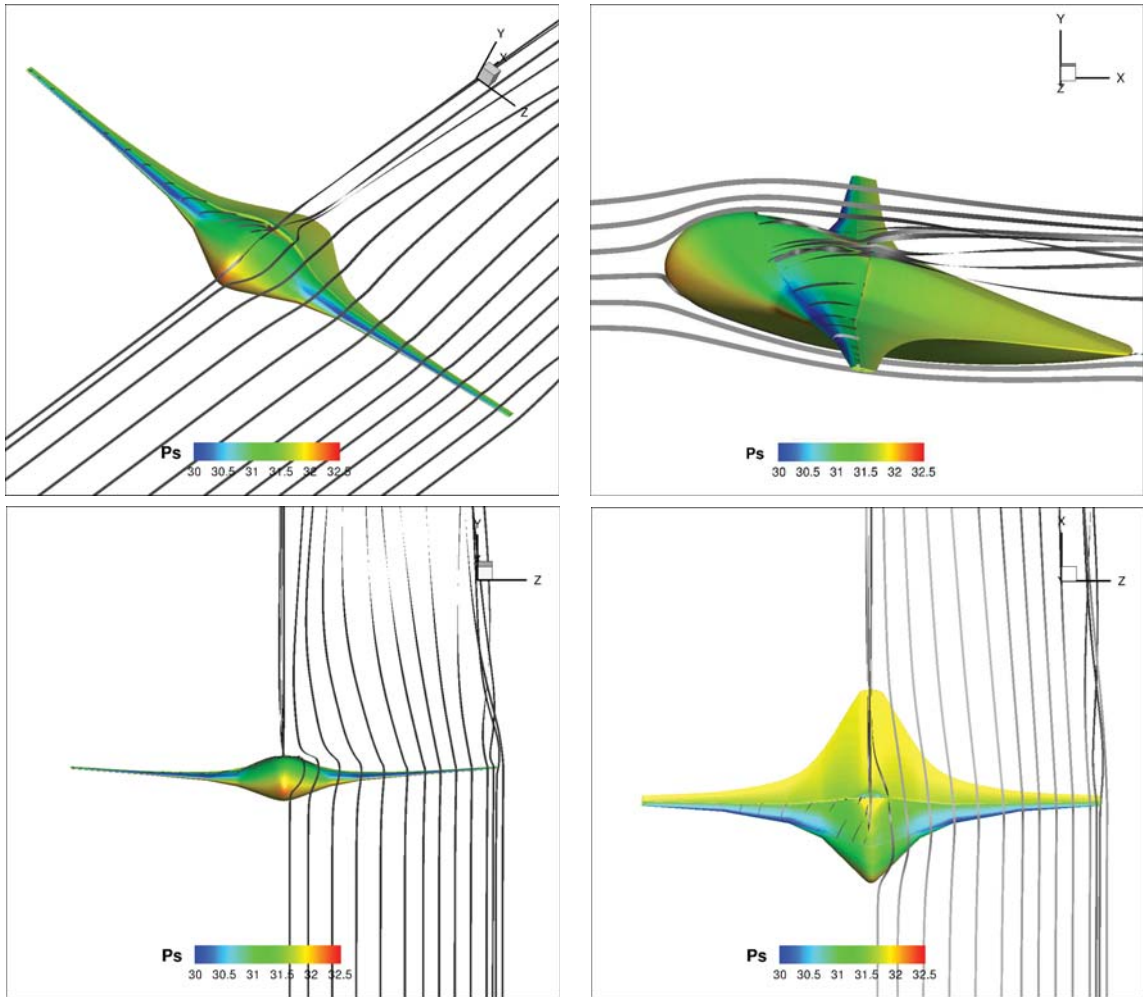


Figure 10.7: Surface pressure contours with streamlines for the CFJ-EA Design 3 at  $C_{\mu} = 0.08$  and  $AoA = 10^{\circ}$ .

be applied in the center of the aircraft to prevent the jet detachment while still equalizing the injection and suction mass flow.

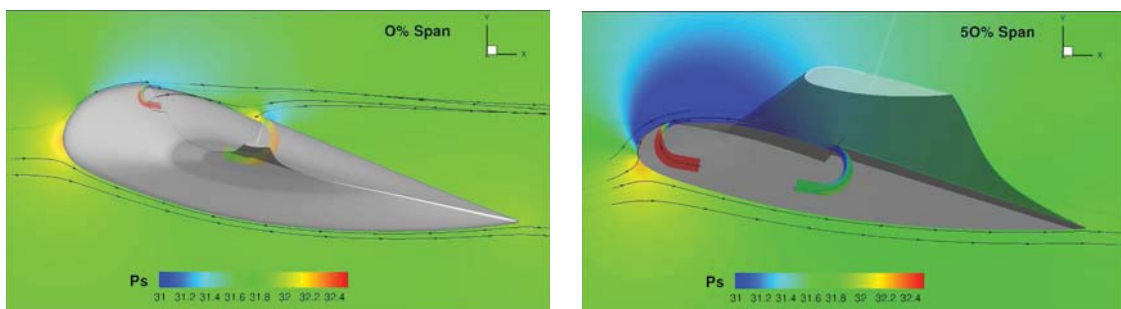


Figure 10.8: Surface pressure contours with streamlines at 0% span and 50% span for the CFJ-EA Design 3 at  $C_{\mu} = 0.08$  and  $AoA = 10^{\circ}$ .

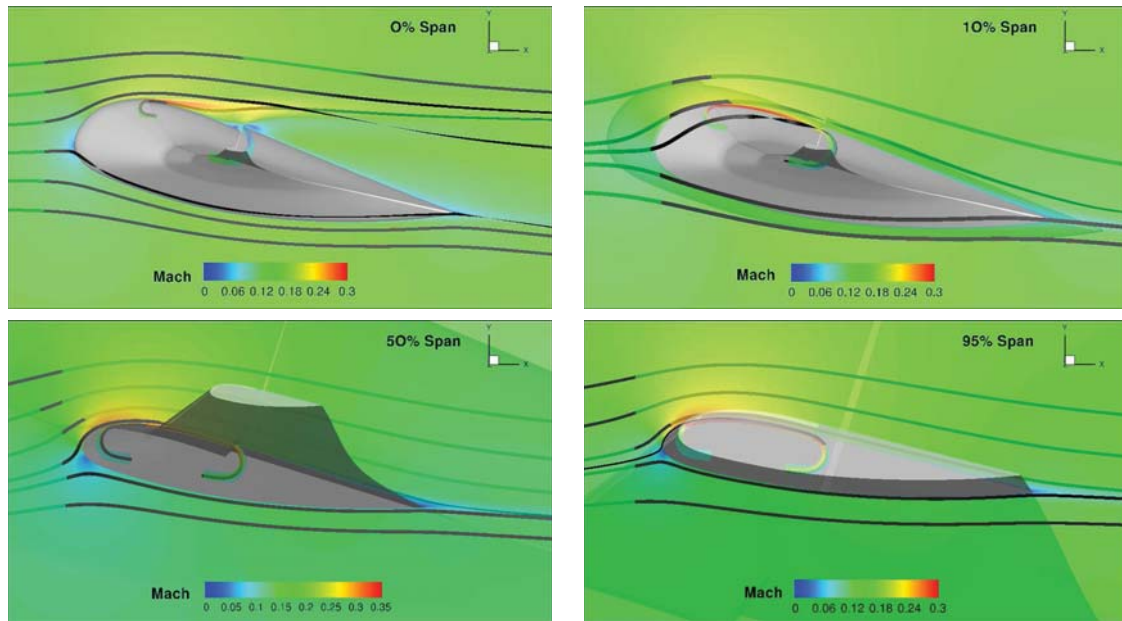


Figure 10.9: Mach contours with streamlines at various span for the CFJ EA Design 3 at  $C_{\mu} = 0.08$  and  $AoA = 10^{\circ}$ .

Fig. 10.10 shows the CFJ-EA Design 3 pressure contours at maximum  $C_l$   $AoA$  of  $25^{\circ}$ . The LE suction is much lowered than at  $AoA = 10^{\circ}$ . The flow appears fully attached with only minor jet separation in the center section. This is because of the lower suction cavity pressure. The 3D flow structures are more pronounced at high  $AoA$  with strong spanwise inward, respectively outward, component of the flow on the suction side, respectively pressure side. The wing tip vortices are also more pronounced.

#### 10.1.4 Quantitative Analysis

Fig. 10.11 shows the lift, drag and moment coefficients for the Baseline EA and the CFJ-EA Design 3. CFJ significantly delays the stall angle such that at  $C_{\mu} = 0.12$ , the flow is still attached at  $AoA = 35^{\circ}$ , and the maximum lift coefficient reaches approximately 2.0. This is an increase beyond  $15^{\circ}$  for the stall angle, and beyond 100% for the maximum  $C_l$  when compared to the Baseline EA. At low  $AoA$  however, the CFJ-EA lift is slightly lower than for the Baseline EA. This is believed to be due to the jet detachment discussed in previous section that decreases the circulation in the center sections. The CFJ-EA drag coefficient

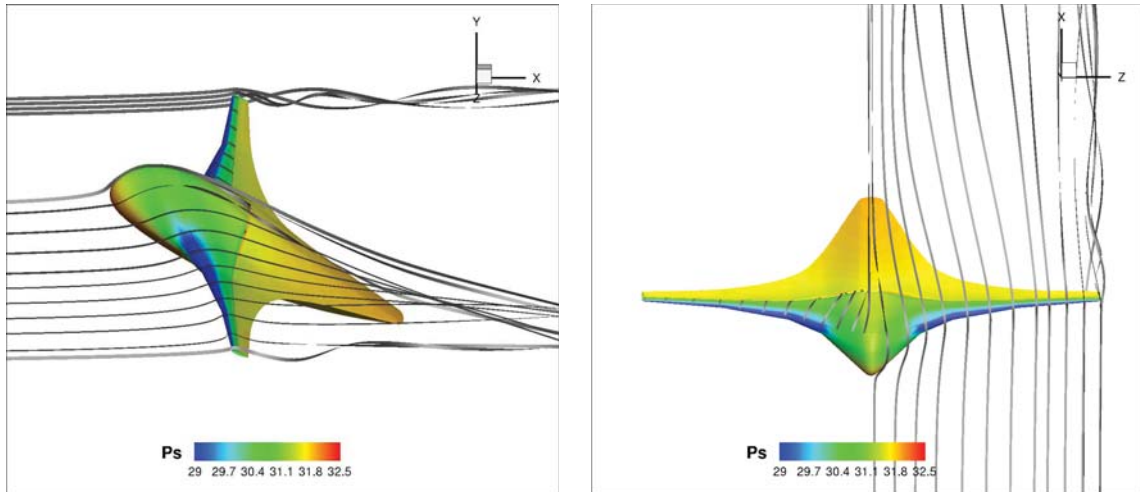


Figure 10.10: Surface pressure contours with streamlines for the CFJ-EA Design 3 at  $C_{\mu} = 0.08$  and  $AoA = 25^{\circ}$ .

is reduced over the baseline EA drag to such extent that at  $C_{\mu} = 0.12$ , the drag is negative (thrust generation) for  $AoA$  as high as  $8^{\circ}$ . The aircraft SSM is calculated with the following formulation :

$$SSM = -\frac{\delta C_m}{\delta C_l} \quad (10.1)$$

It can be inferred from the above formulation that positive SSM requires  $C_m$  to decrease when  $C_l$  increase. According to this definition, the baseline EA is stable during normal flight condition, but unstable when approaching the stall angle of  $20^{\circ}$ . On the contrary, the CFJ-EA is stable for all  $C_{\mu}$  and  $AoA$  studied. Both the baseline EA and CFJ-EA are trimmed in cruise condition which is at  $AoA = 5^{\circ}$  for the baseline EA and at  $AoA = 10^{\circ}$  with  $C_{\mu} = 0.06$  for the CFJ-EA. The SSM in cruise condition ranges from 4% to 5% depending on the case. The large nose-down moment beyond the stall point facilitates the stall recovery.

The power consumption and efficiencies of the EA are shown Fig. 10.12. The baseline configuration reaches a peak  $L/D$  of 20.6 during cruise condition. The CFJ configuration reaches a peak  $L/D$  in excess of 30 at  $C_{\mu} = 0.06$ . For higher  $C_{\mu}$ , the behavior of the  $L/D$  plots is asymptotic because when drag approaches 0, the aerodynamic efficiency approaches infinity. On the left of the asymptotes, the drag is negative. The power co-

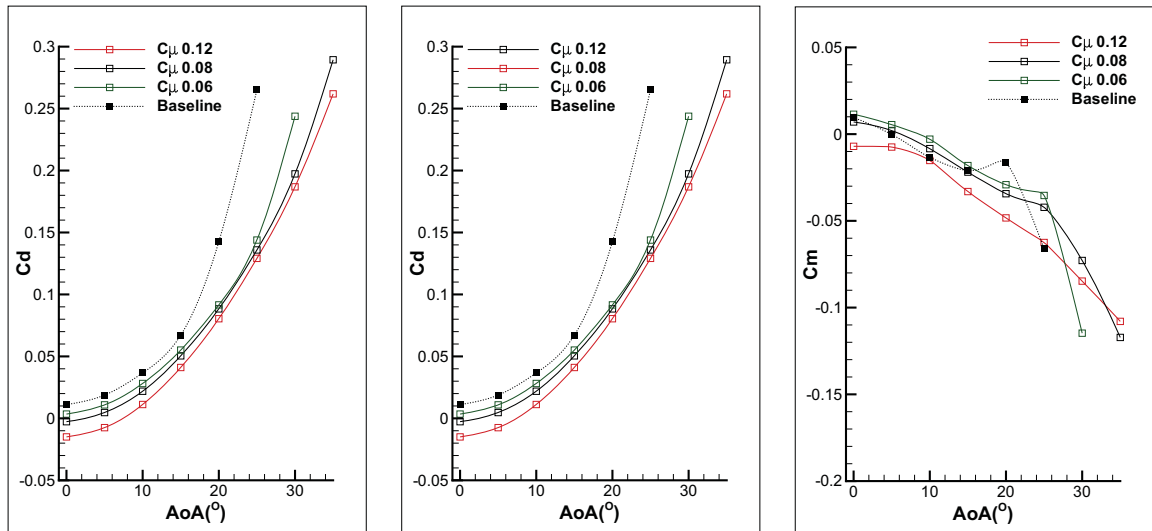


Figure 10.11: Lift, drag and moment coefficients versus AoA for the CFJ-EA Design 3 and the baseline EA.

efficient is very low for  $C_{\mu} = 0.06$  but increase dramatically with  $C_{\mu}$ . The lowest power consumption AoA is increased with the  $C_{\mu}$ . In order to generate a fair comparison between the baseline case and the CFJ case, we incorporated the power consumption term into the aerodynamic efficiency term as seen in Eq. (4.15). The power consumption is previously scaled up due to the pumping efficiency of 85%. The corrected efficiency plot shows a higher peak efficiency for the baseline but a better efficiency for the CFJ-EA at high AoA. Also the peak efficiency of the CFJ-EA is shifted toward higher AoA when  $C_{\mu}$  is increased.

The corrected aerodynamic efficiency versus  $C_L$  plotted Fig. 10.13 shows that the baseline airplane is efficient at low  $C_L$ . It is however surpassed by the CFJ aircraft both in term of maximum  $C_L$  and efficiency at high  $C_L$ . The baseline airfoil achieves its maximum efficiency at  $C_L = 0.4$ , whereas the CFJ airfoil reaches it at  $0.6 < C_L < 1.3$  depending on the  $C_{\mu}$  value.

### 10.1.5 Mission Analysis

The mission analysis is performed using the formulations found in chapter 5. Three configurations are studied, the baseline EA, the CFJ-EA Design 3, and the hybrid CFJ-EA. The results are compared with the data for the kerosene burning Cessna 172 and the elec-

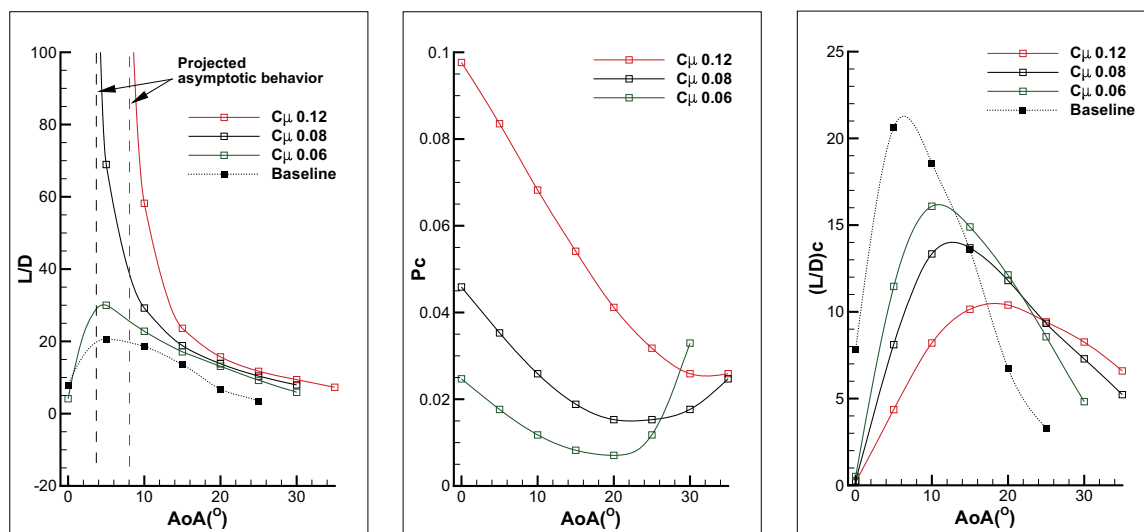


Figure 10.12: Aerodynamic efficiency, power coefficient, and corrected efficiency versus AoA for the CFJ-EA Design 3 and the baseline EA.

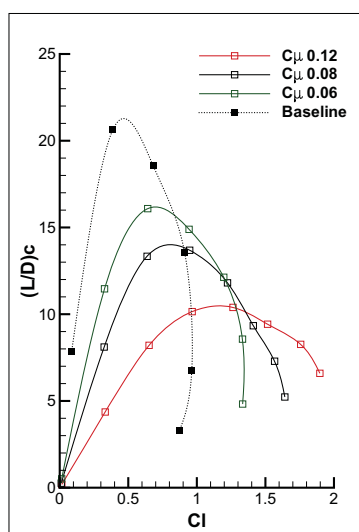


Figure 10.13: Corrected efficiency versus lift coefficient for the CFJ-EA Design 3 and the baseline EA.

tric aircraft Antares 20. All mission analysis are performed for a payload of 320 kg (706 lbs) composed of both passengers and luggage. The structural weight is 40% of the gross weight for all the configurations. The batteries account for the rest of the weight of the aircraft. The batteries have a specific energy density  $E^*$  of 180 Wh/kg (397 Wh/lbs) which corresponds to the current mainstream Li-ion battery technology. The range of the EA is also calculated with  $E^* = 1750$  Wh/kg that is expected in the next 20 years, as an exam-

ple of what will be possible to achieve with electric aircraft in two decades. The overall propulsive efficiency is fixed at 73% to account for the efficiency of the propeller, controller, electric motor and gearbox. In addition, a pumping efficiency of 85% is considered. Finally, 20% of the energy storage is reserved for the start-up, take-off, acceleration to cruise velocity and altitude and landing. More information about the mission analysis can be found in 5. The mission analysis is performed for a TO at sea level, climb to cruise altitude of 5000 ft, cruise at  $M=0.15$ , descent to sea level and landing.

The baseline EA has the smallest range of 46nm because it is limited by the battery weight it can carry. It also has the poorest TO performance because of the fairly poor  $C_L(TO)$  of 0.8. Increasing the battery weight would increase the range at the expense of the TO performance. The CFJ-EA range is 2.5 times greater with 116nm, mostly due to the increased battery weight carried. The Hybrid CFJ-EA combine the increased maximum lift offered by CFJ during the TO, climb and landing phases and the high aerodynamic efficiency of the baseline EA during the cruise. It offers the best range with 129nm. If we use  $E^* = 250$  Wh/Kg, which is achievable with current Li-ion battery technology, then the range is increased to 180nm.

For both the CFJ and Hybrid EA, TO and landing performance are good due to the high  $C_L(TO)$  of 1.6 made possible with the use CFJ at  $C_{\mu} = 0.12$ . All three configurations have a SSM of about 4%. The range of the EA is also calculated with  $E^* = 1750$  Wh/kg, which is used as the projection for the next 20 years [78]. This projection increases the range could be increased by about 7 times to 900nm. This is a significant range, even when compared to today's general aviation standards like the Cessna 172.

Aircraft	Cesna 172	Antares 20E	Baseline	CFJ Eplane FW	CFJ Eplane FW Hybrid
<b>Geometry</b>					
Wing span (m)	11.00	20.00	14.00	14.00	14.00
Wing area (m <sup>2</sup> )	16.20	12.60	24.20	24.20	24.20
AR	7.3	31.7	8.1	8.1	8.1
Length (m)	8.28	7.40	6.00	6.00	6.00
<b>Cruise data</b>					
CL	0.32	0.38	0.39	0.64	0.68
CD	0.046	0.01	0.045	0.038	0.037
Pc	N/A	N/A	N/A	0.016	0.016
Velocity (m/s)	63	51	51	51	51
Altitude (ft)	5000	5000	5000	5000	5000
<b>Weight</b>					
Gross weight (kg)	1,111	660	1,314	2,156	2,291
Structure ratio	0.69	0.70	0.50	0.40	0.40
Structure weight (kg)	767.0	460.0	656.9	862.4	916.3
Passenger + payload (kg)	250.0	140.0	320.0	320.0	320.0
Battery weight (kg)	N/A	60.0	336.9	973.5	1,054.4
<b>Propulsion / Battery</b>					
Propulsive eff (%)	39	73	73	73	73
Pump efficiency (%)	N/A	N/A	N/A	85	85
Battery specific E (Wh/Kg)	N/A	136	250	180	180
Energy available (kWh)	N/A	8.2	84.2	175.2	189.8
Propeller power cruise (kW)	251.6	15.2	103.9	87.4	84.4
CFJ power cruise (kW)	N/A	N/A	N/A	32.66	32.66
Total power drawn cruise (kW)	251.6	15.2	103.9	120.1	117.1
<b>Performance</b>					
Estimated Range (nm)	700	43	64	116	129
MPG*Passengers	58	237	145	125	128
Cruise time (h)	5.7	0.4	0.6	1.2	1.3
Range with 20 year tech. (nm)	700	298	450	810	900
Wing loading (kg/m <sup>2</sup> )	68.6	52.9	54.3	89.1	94.7
TO distance (ft)	1700	1900	1800	1450	1500
Cruise static margin (%)	N/A	N/A	4.4%	4.2%	4.4%

Table 10.2: Mission analysis for the baseline EA, CFJ-EA Design 3 and the hybrid EA. A comparison is made with the kerosene burning Cessna 172 and the electric aircraft Antares 20. Some of the data are only estimates.

## 10.2 The High Aspect Ratio Wing Design

### 10.2.1 Mesh

The CFJ-EA mesh, shown in Fig. 10.14, is constructed using a cylindrical mesh topology, around the plane fuselage. The cylindrical topology is interrupted by the main wing which

is enclosed in a O-mesh topology with 240 points around the airfoil, 40 points in the direction normal to the wall completed by an additional 40 points in the jet region, and 80 points in the spanwise direction. In a similar manner the horizontal tail is also enclosed in an O-mesh with 120 points around the airfoil, 40 points in the direction normal to the wall and 60 points in the spanwise direction. The total mesh size is 10.4 million points, split into 225 blocks for parallel computation. The far field boundary is located 30 fuselage length away from the plane. The first grid point is placed at  $y^+ \approx 1$  except on the wing and tail tip walls where  $y^+ \approx 50$  is used with the wall function boundary condition to reduce the mesh size. The baseline EA without CFJ is constructed using the same mesh topology. The main wing O-mesh has a smaller mesh size due to the absence of jet and is constructed with 160 points around the airfoil, 40 points in the direction normal to the wall and 80 points in the spanwise direction. The total mesh size is 8.2 million points, split into 166 blocks for parallel computation. A similar mesh topology is used on the DLR-F6 wing/body drag prediction to benchmark our code. The coefficient of lift, drag, and moment are in good agreement with the experiment.

### 10.2.2 Aircraft Configuration

The present CFJ-EA geometry with dimensions is shown on the isometric views in Fig. 10.15. The center of gravity, around which the moments are calculated, is located 2.43 meters from the aircraft nose, slightly below the fuselage longitudinal axis as indicated by the pin on the side view.

The present EA wing geometry is based on the result of a trade study conducted in [103]. A simple rectangular wing planform with a thick CFJ airfoil (21% thickness/chord) is chosen as a compromise between wing performance, manufacturing simplicity and structural weight of the wing. The CFJ airfoil, seen in Fig. 10.14 is based on the NACA 6421 airfoil, with an injection and slot located at 2% chord and 80% chord respectively. The injection and suction size are 0.65% chord and 1.30% chord respectively. The CFJ wing

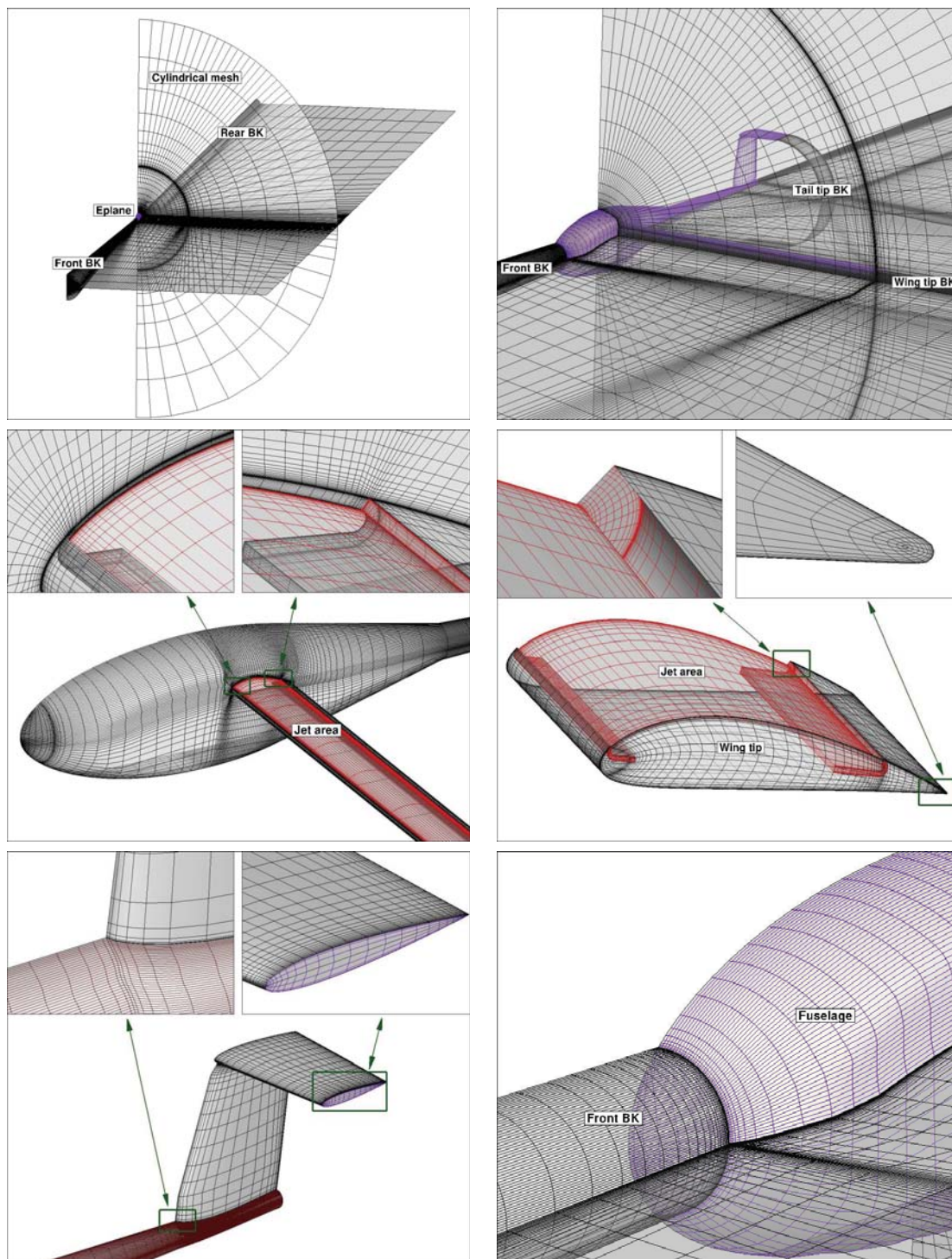


Figure 10.14: Mesh overview for the CFJ-EA. Only one mesh point out of two is displayed for clarity.

performance and energy consumption is studied in detailed in [103]. It combines very high wing loading with a high aerodynamic efficiency and the energy expenditure is low.

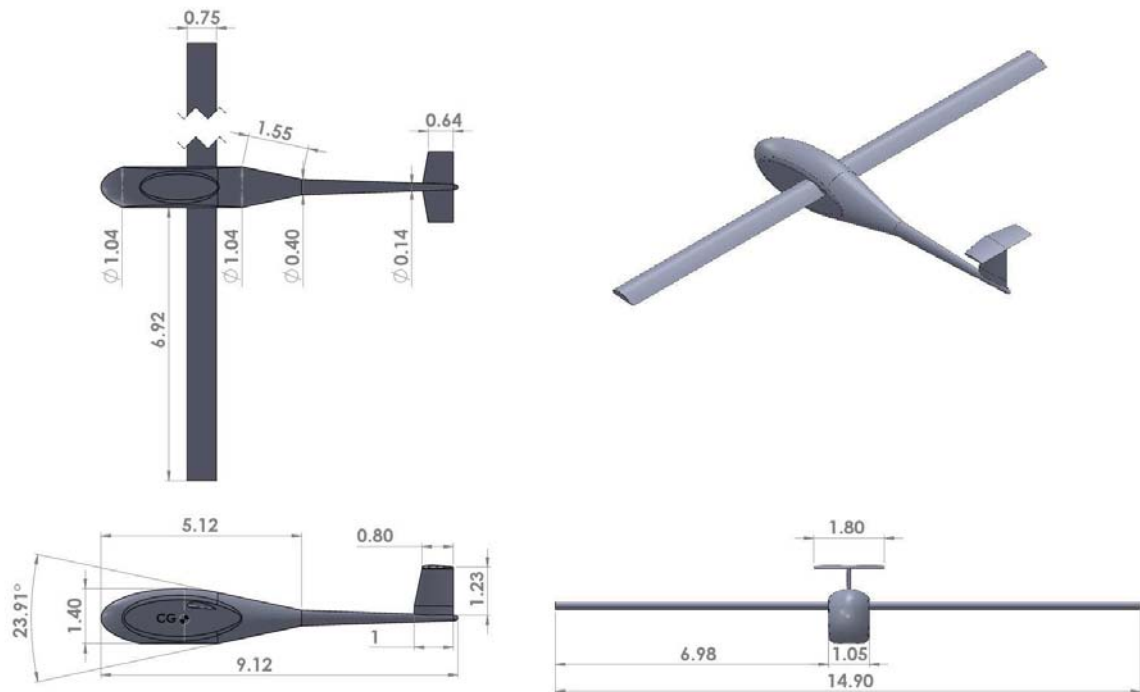


Figure 10.15: CFJ-EA isometric view (unit: meters).

At cruise, the CFJ-EA fuselage is horizontal and the wing AoA is  $5^\circ$ . At TOL, the wing AoA is  $25^\circ$ . To reach such a high AoA without rotating the fuselage excessively, the wing rotates by  $15^\circ$  around its spar axis. The remaining  $5^\circ$  are achieved by rotation of the fuselage. The moderate fuselage AoA ensures a good visibility for the pilot during the TOL phases. The wing placement on a high position directly behind the passengers is chosen to allow the wing spar to go through the fuselage without affecting the passenger headroom and leaves the space below for battery storage. The side surface of the fuselage is flat so that the wing can be rotated around the wing spar axis.

The tail is sized to achieve stability in pitch and sufficient control authority. Both the horizontal and vertical tail uses a NACA 0012 airfoil. The horizontal and vertical tail sizes are  $1.3m^2$  and  $1.0m^2$  respectively. The wing area is  $10.44m^2$  and the wing span is 14.90m, thereby the wing aspect ratio is 21.3. The fuselage length is 9.12m. The cabin size is constructed from an ellipsoid body with a major axis of 4m, a minor axis of 1.5m and

a vertical axis of 1.5m to which we flattened the bottom and the side surfaces. Its final dimensions are 4.0m x 1.4m x 1.05m (Length x Height x Width) and the internal volume is 4.3m<sup>3</sup>. Less than 1m<sup>3</sup> is expected to be used for battery and related power equipment. The rest of the volume is used to accommodate the 4 passengers with luggage and the wing rotation system.

### 10.2.3 Cruise Condition with Low $C_{\mu}$

The CFJ-EA surface pressure contours with streamlines are plotted in Fig. 10.16 for the cruise condition, which is  $AoA = 5^{\circ}$  and  $C_{\mu} = 0.04$ . The stagnation region is centered on the aircraft nose. From there, the flow curves around the cabin with a small upward component, which increases the local incidence of the wing. The local lift loading is maximum in the inner section of the wing as shown by the low pressure in deeper blue color. The wing tip is affected by the downwash generated by the wing tip vortices, which reduces the tip loading, as shown by the lighter blue color. The wing suction surface streamlines in Fig. 10.16 indicates that the jet is well aligned with the main flow. This is very desirable to make CFJ effective and reduce the energy expenditure.

The horizontal tail role is to generate enough downforce for the aircraft to be stable during cruise but not so much as to decrease the overall aircraft performance. The present CFJ-EA design horizontal tail  $AoA$  is 0, but its incidence is slightly negative due to the wing and fuselage downwash as visualized on Fig. 10.16 by the slightly downward streamlines direction. Hence the horizontal tail generates a slight downforce during cruise.

The local lift loading can be further seen on the pressure coefficient ( $C_p$ ) and isentropic Mach number plots shown in Figs. 10.17 and 10.18. The spikes at 3% and 80% chord correspond to the injection and suction location respectively, where the surface of the airfoil is discontinuous. Both plots show that the lift loading is fairly uniform in the inner 85% span, while the outer 15% span loading is decreased due to tip vortex. The CFJ airfoil has a high suction peak near the LE, this contributes to the lift increase and the pressure

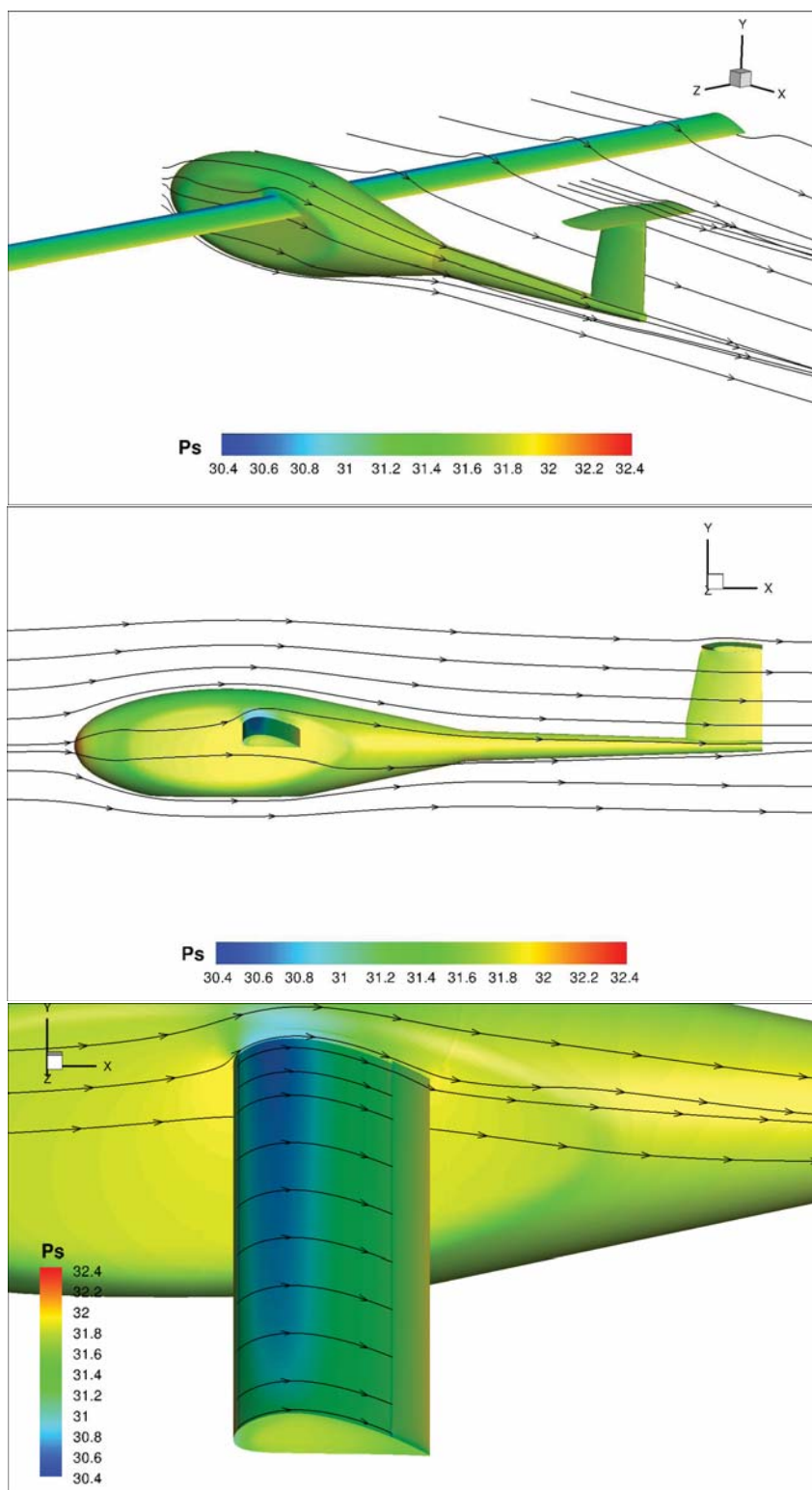


Figure 10.16: Surface pressure contours, cruise conditions,  $C_{\mu} = 0.04$  and  $AoA = 5^{\circ}$ .

drag decrease. The lowest  $C_p$  and isentropic Mach number achieved are -2.1 and 0.26 respectively.

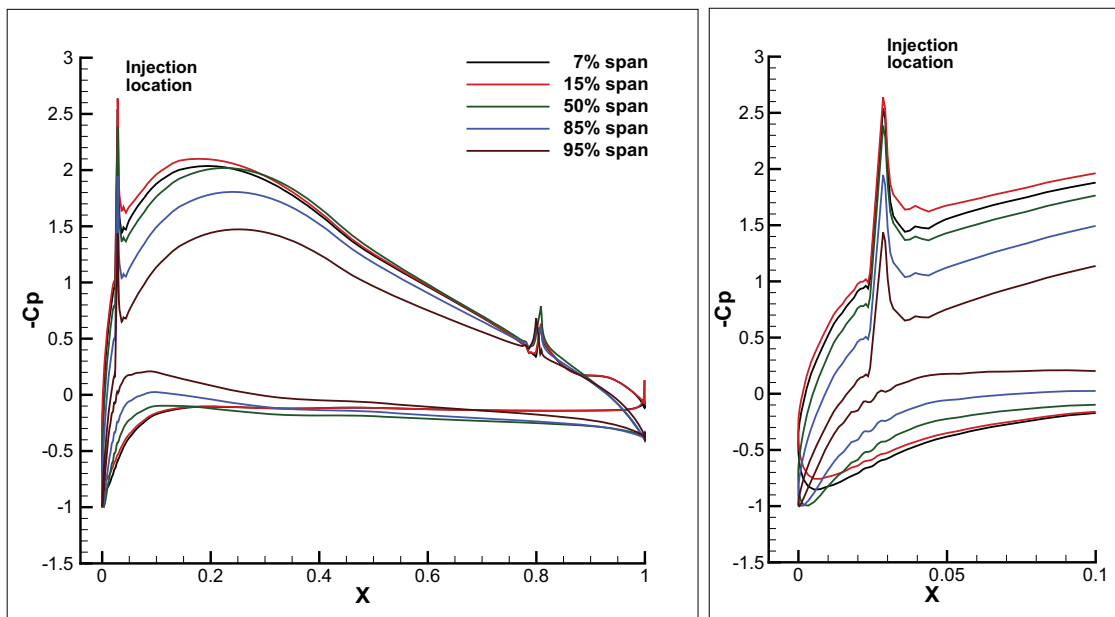


Figure 10.17:  $C_p$  at different spanwise locations, cruise conditions,  $C_{\mu} = 0.04$  and  $AoA = 5^\circ$ . The 7% spanwise location corresponds to the wing root.

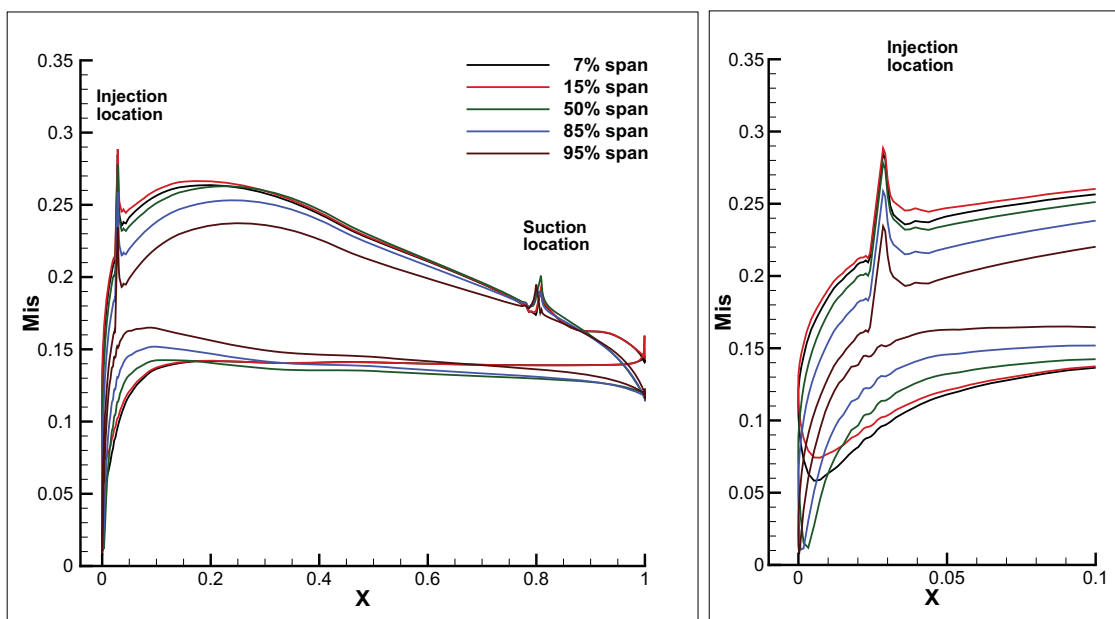


Figure 10.18: Isentropic Mach number at different spanwise locations, cruise conditions,  $C_{\mu} = 0.04$  and  $AoA = 5^\circ$ . The 7% spanwise location corresponds to the wing root.

The CFJ-EA Mach contours with streamlines are plotted for the cruise condition at different spanwise locations in Fig. 10.19. Note that the color map range for the three fuselage sections is a little different from the three wing sections to best highlight their

flow feature. As can be seen in Fig. 10.19, the fuselage generates some lift due to the convex shape of the fuselage upper surface, which also makes the air flow upward. This upward flow increases the local incidence of the wing in the vicinity of the fuselage. As mentioned earlier, the tail generates a small negative lift due to the downwash. The T-tail configuration reduces the interaction of the horizontal tail with the aircraft wake and downwash. It also suppresses the tip vortex of the vertical tail and increases the vertical tail control effectiveness. The CFJ wing wake is energized by the jet and remains very small. The 99% span flow field shows the influence of the wing tip vortex, which reduces the tip lift loading.

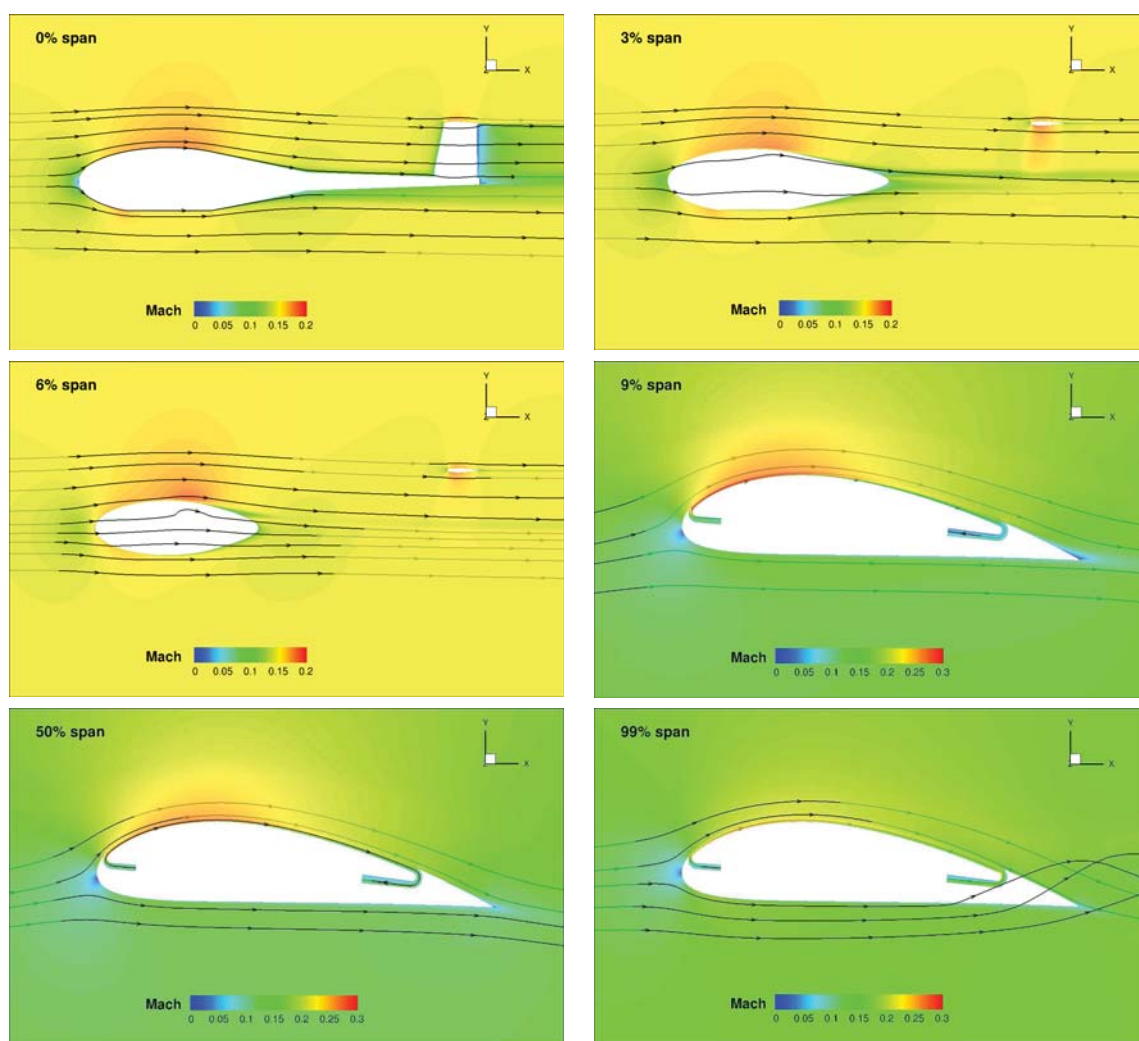


Figure 10.19: Eplane Mach contours at various spanwise locations, cruise conditions,  $C_{\mu} = 0.04$  and  $AoA = 5^{\circ}$ .

Fig. 10.20 and 10.21 show the CFJ-EA at  $AoA=15^\circ$  and  $C_\mu = 0.04$ . The wing-fuselage interaction causes a separation region at the inner span that cannot be overcome by the CFJ at such low  $C_\mu$  value. The outer span flow remains attached. Even though the horizontal tail's  $AoA$  is  $15^\circ$ , its actual incidence is much lower due to the fuselage and wing downwash. All these features ensure the horizontal tail flow remains attached beyond the stall  $AoA$  of the main wing. When the  $C_\mu$  is increased to 0.08, the wing root separation is removed as shown in 10.22.

The lift, drag and moment coefficients for the EA at cruise Mach number are shown in Fig. 10.23. As a comparison, the baseline airplane, which uses the original NACA 6415 airfoil with no CFJ for the wing, is also simulated. At constant  $AoA$ , the CFJ-EA  $C_L$  is significantly higher than the baseline EA. Higher  $C_\mu$  yields a higher lift coefficient. In addition, the use of CFJ delays the stall  $AoA$  from  $10^\circ$  for the baseline EA to  $20^\circ$  for the CFJ-EA at  $C_\mu = 0.08$ . The maximum  $C_L$  is increased from 1.5 for the baseline EA to 2.6 for the CFJ-EA at  $C_\mu = 0.08$ . For all  $C_\mu$ , the drag of the CFJ-EA is significantly lower than the baseline EA until the stall  $AoA$  is reached.

The CFJ-EA is trimmed in cruise condition, which is at  $M=0.15$ ,  $AoA = 5^\circ$  and  $C_\mu = 0.04$ . If we calculate the aircraft Static Stability Margin (SSM) with the following formulation :

$$SSM = -\frac{dC_m/d\alpha}{dC_l/d\alpha} = -\frac{dC_m}{dC_l} \quad (10.2)$$

both the baseline and CFJ-EA are statically stable in pitch with a cruise SSM of 0.36 and 0.29 respectively. The use of CFJ decreased the cruise SSM by about 0.07, but the remaining SSM is more than enough to maintain the aircraft stability.

The aerodynamic efficiency and energy consumption for the EA at cruise Mach number are shown in Fig. 10.24. The power coefficient is calculated assuming an efficiency of 85% for the pump based on equations 4.12 and 4.13. The minimum  $P_c$  is 0.012 for  $C_\mu = 0.04$  at  $AoA = 10^\circ$ . When the  $C_\mu$  is increased, the power consumption is dramatically increased. The minimum power consumption  $AoA$  is increased with the  $C_\mu$ . The baseline

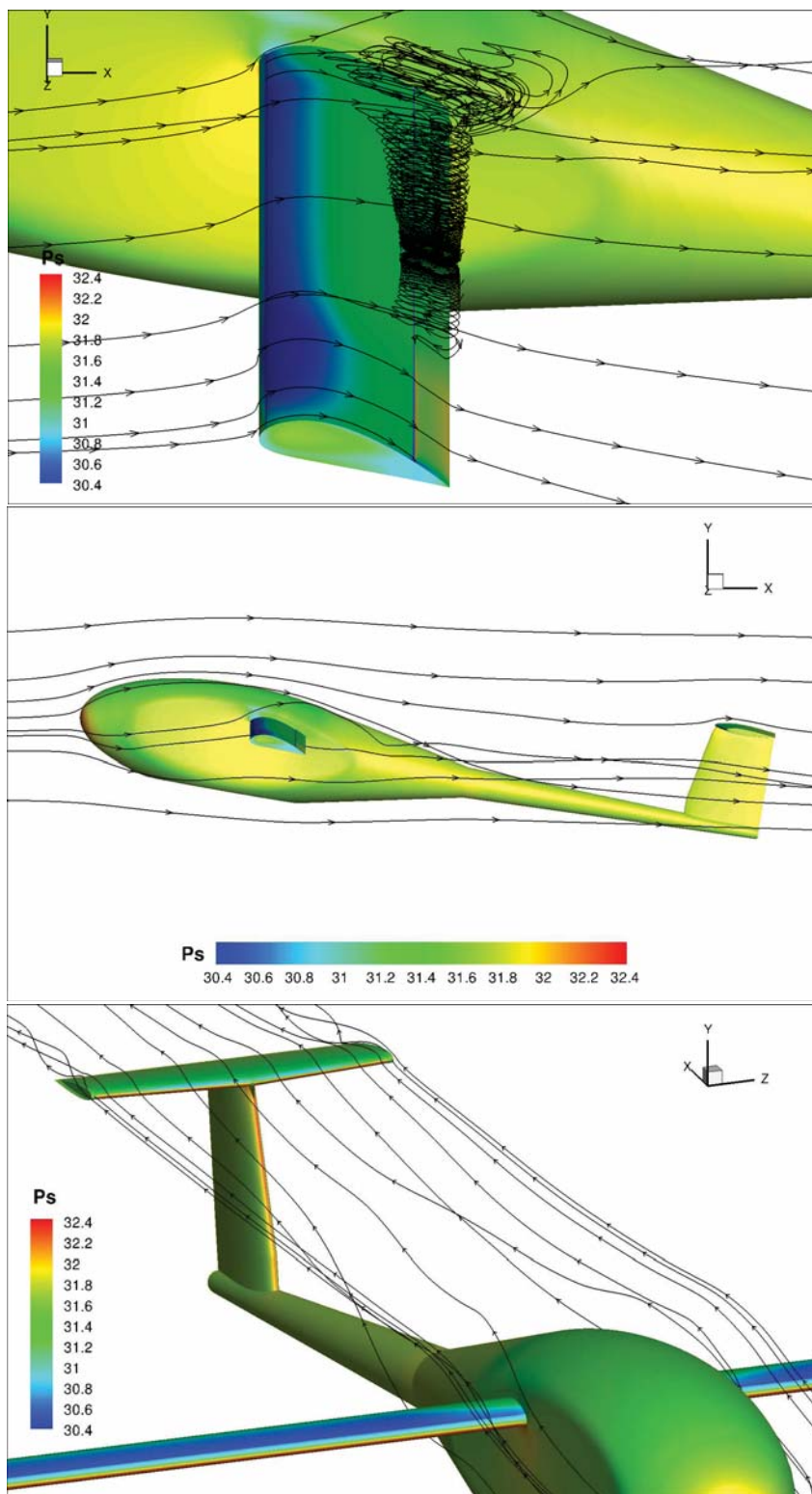


Figure 10.20: Eplane surface pressure contours, maneuvering,  $C_{\mu} = 0.04$  and  $AoA = 15^{\circ}$ .

configuration reaches a peak aerodynamic  $L/D$  of 22.5 during cruise condition. The CFJ-EA reaches a peak  $L/D$  of 36.3 at  $C_{\mu} = 0.04$  and up to 64.6 at  $C_{\mu} = 0.08$ . The peak  $(L/D)_c$

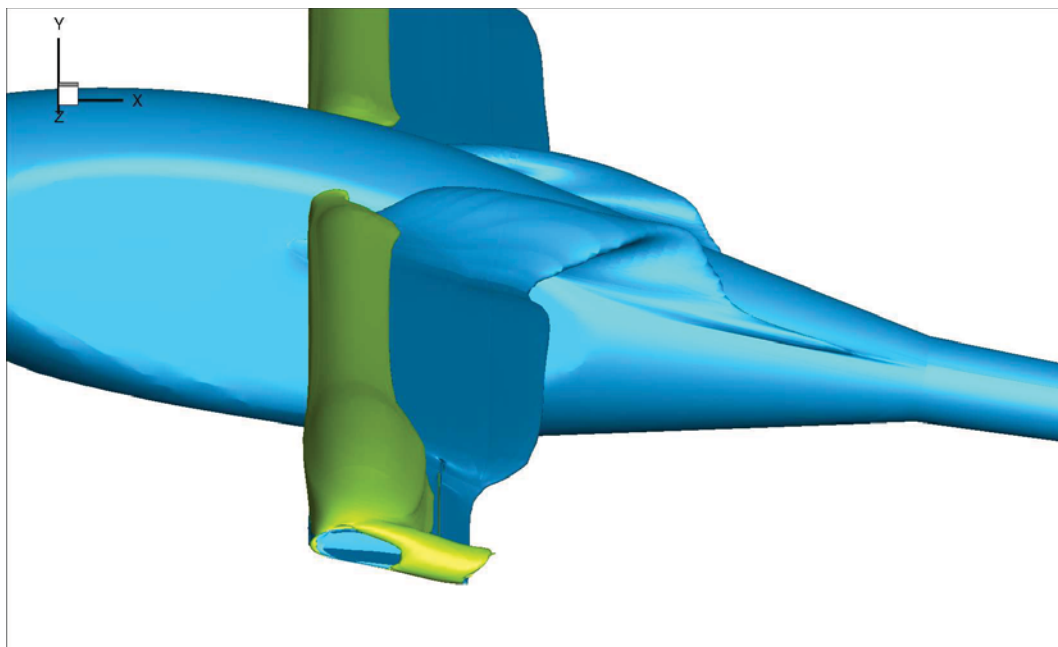


Figure 10.21: Iso-surfaces at Mach 0.05 (blue) and Mach 0.20 (green) for the CFJ EA at  $C_{\mu} = 0.04$  and  $AoA = 15^{\circ}$ .

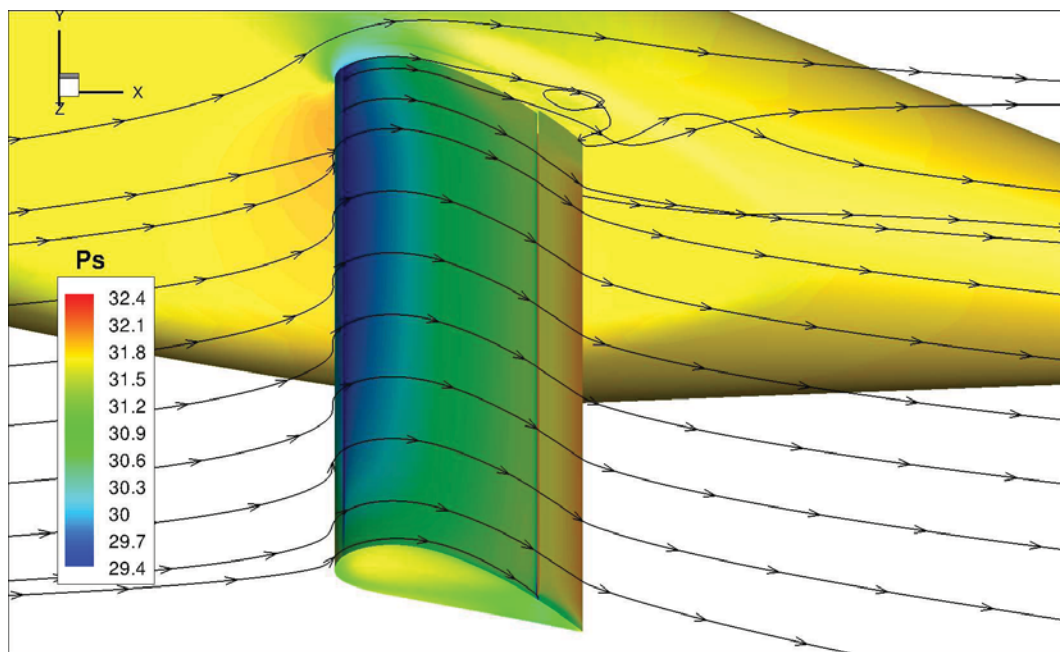


Figure 10.22: Surface pressure contours, maneuvering,  $C_{\mu} = 0.08$  and  $AoA = 15^{\circ}$ .

for the CFJ-EA at  $C_{\mu} = 0.04$  is higher than the baseline aircraft  $L/D$  peak, suggesting that the overall energy efficiency of the aircraft is improved with the use of CFJ. This is also the reason that the  $C_{\mu} = 0.04$  is chosen for cruise. When the  $C_{\mu}$  is increased, the

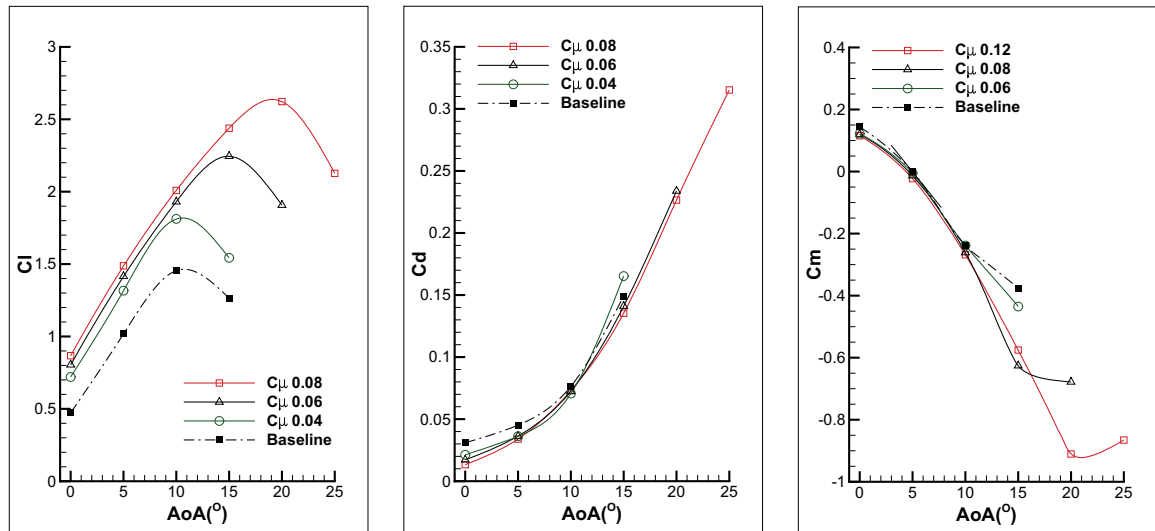


Figure 10.23: Forces and moment versus AoA, simulations performed at  $M=0.15$ ,  $0.04 \leq C_{\mu} \leq 0.08$ .

aerodynamic  $L/D$  continue to increase. However the  $(L/D)_c$  is decreased because of the increased power consumption. Similarly to the  $P_c$  behavior, the peak  $(L/D)_c$  of the CFJ-EA is shifted toward higher AoA when the  $C_{\mu}$  is increased.

The CFJ-EA cruises at a very high  $C_L$  of 1.3, which produces a wing loading of  $182.3 \text{ kg/m}^2$ , about 3 times higher than that of a conventional general aviation airplane. The excellent cruise  $(L/D)_c$  of 24 combined with the high cruise wing loading give the CFJ-EA an exceptionally compact size airplane, with high payload and long range.

The corrected aerodynamic efficiency versus  $C_L$  plotted Fig. 10.25 shows that the aircraft using CFJ has a higher peak efficiency (at  $C_{\mu} = 0.04$ ) than the baseline airplane without CFJ. In addition, this peak efficiency is obtained for a high  $C_L$  of about 1.3 which makes the design very efficient while flying with a high wing loading. In conclusion, for this design, there are compelling arguments to use the CFJ during cruise, due to both the enhanced cruise  $C_L$  made possible by the CFJ and the enhanced cruise efficiency.

For a fixed  $C_{\mu}$ , the power consumption depends mostly on the mass flow and total pressure ratio between the injection and suction cavities (see Eq. (4.12)). On the range of AoA studied, the mass flow is mostly constant, thereby, the changes in the pressure ratio are the main driver of the power consumption changes. Consequently, the behavior

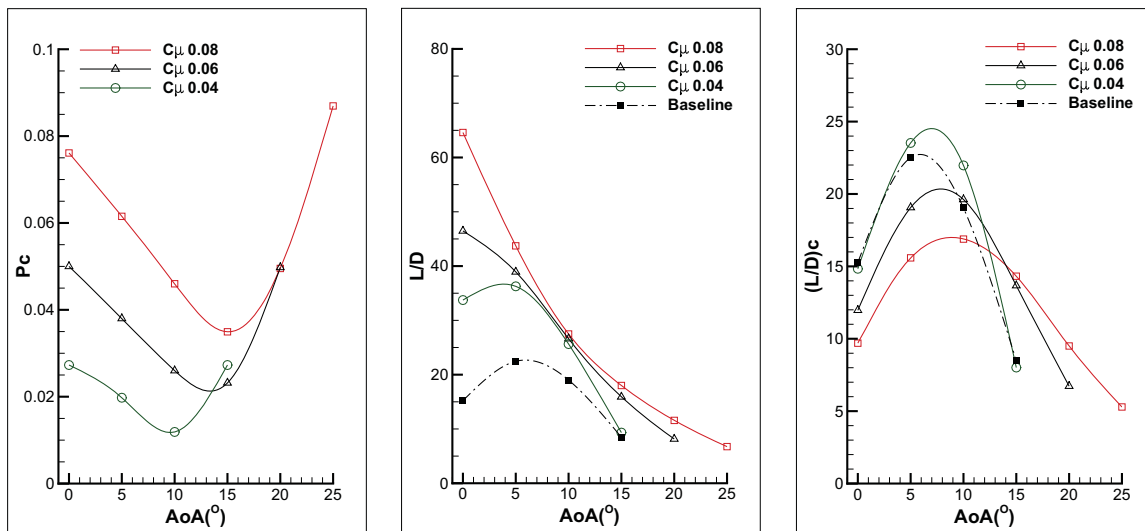


Figure 10.24: Energy expenditure and aerodynamic efficiency versus AoA, simulations performed at  $M=0.15$ ,  $0.04 \leq C_{\mu} \leq 0.08$ . The pumping efficiency is 85%.

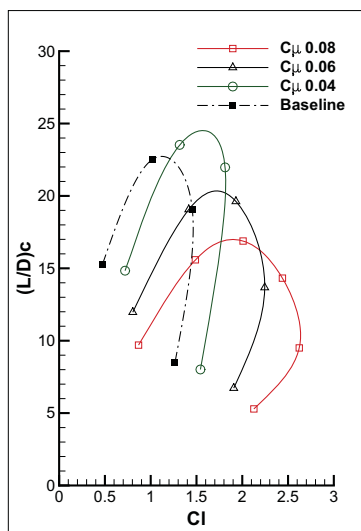


Figure 10.25: Corrected aerodynamic efficiency versus  $C_L$ , simulations performed at  $M=0.15$ ,  $0.04 \leq C_{\mu} \leq 0.08$ . The pumping efficiency is 85%.

of the pressure ratio, seen Fig. 10.26, is similar to that of the power coefficient seen Fig. 10.24). In cruise condition, the mass-averaged injection total pressure is 2.5% higher than the suction total pressure, the mass-averaged jet velocity magnitude is 1.76 times that of the free stream velocity and the jet mass flow is 6.91 kg/s. This results in a cruise  $P_c$  of 0.020, which corresponds to a power consumption of 14.3 kW (see Eq. (4.13)), including the pumping efficiency of 85%.

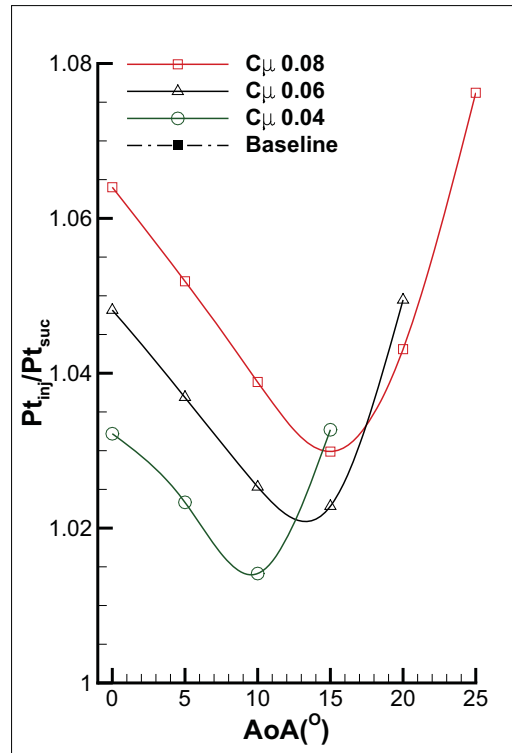


Figure 10.26: Mass-averaged total pressure ratio between the injection and suction cavities, simulations performed at  $M=0.15$ ,  $0.04 \leq C_{\mu} \leq 0.08$ .

Fig. 10.27 shows a close up view of the static pressure contours in the vicinity of the injection region. The injection static pressure is not uniform due to the centrifugal forces that results from the flow turning. The inner portion of the injection can be as low as 96% of the free stream pressure. The injection cavity pressure away from the injection slot is only about 2.1% above the free stream pressure and hence the mechanical stress resulting from the pressure force is low.

#### 10.2.4 Takeoff/Landing Condition with High $C_{\mu}$

In order to evaluate the TOL performance, we simulate the behavior of the CFJ-EA at high AoA and high  $C_{\mu}$ . The calculations are performed at  $M=0.1$  to simulate the typical TOL velocity of a general aviation airplane.

The CFJ-EA surface isentropic Mach contours with streamlines are plotted in Fig. 10.28 for the TOL condition, which is  $AoA = 25^{\circ}$  and  $C_{\mu} = 0.24$ . The fuselage lift is

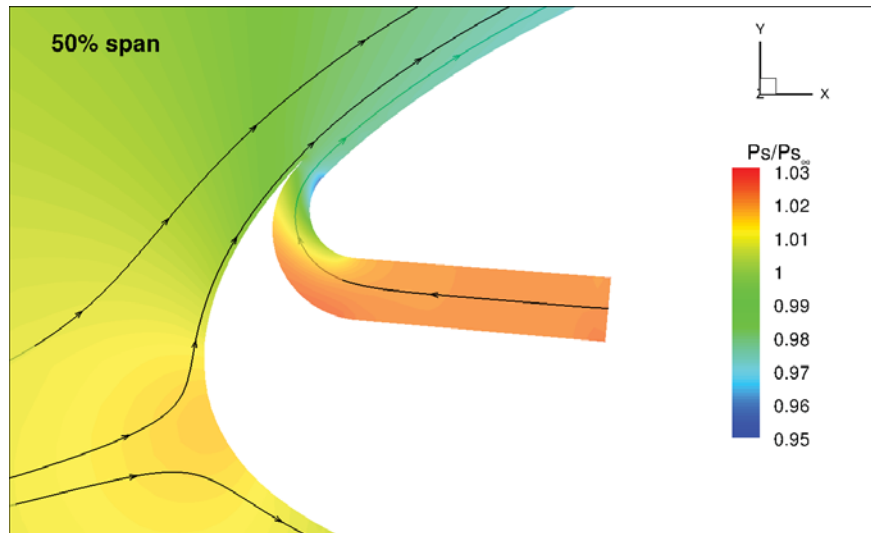


Figure 10.27: Static pressure contours at 50% spanwise location. The aircraft is in cruise condition. The free stream static pressure is 1.00.

enhanced by the lower stagnation region location, just under the aircraft nose, and the relatively large flow acceleration on the top surface of the cabin. The wing is significantly loaded, as indicated by the very high isentropic Mach number at the wing LE and the stagnation point located at a more downstream position on the pressure surface. The LE flow acceleration is much smaller in the wing tip region. Even though the horizontal tail AoA is  $25^\circ$ , the flow remains fully attached. This is because its incidence is much lower due to the fuselage and wing downwash.

The lift, drag and moment coefficients for the CFJ-EA in TOL condition are shown Fig. 10.29. A higher  $C_\mu$  yield a higher lift coefficient. However, due to the strong lift-induced drag, there is a significant drag penalty for the higher  $C_\mu$  cases. The maximum  $C_L$  achieved is 4.8 at  $C_\mu = 0.28$ . However, to lower the power consumption and conserve a comfortable stall margin of  $10^\circ$ , the TOL is performed at  $AoA = 25^\circ$  with a  $C_\mu$  of 0.24. In these conditions, the  $C_{LTO}$  is 3.9. With  $C_{Lmax}=4.8$ , the stall velocity is 24.55m/s(55mile/h). A reasonable TOL velocity would hence be taken as 1.2 times this value with an approximate Mach number of 0.085. We use Mach number of 0.01 as the takeoff Mach number to be conservative. The flow is also insensitive to the Mach number in this incompressible range. The case is simulated without the horizontal tail flap deflected. It is hence not trimmed

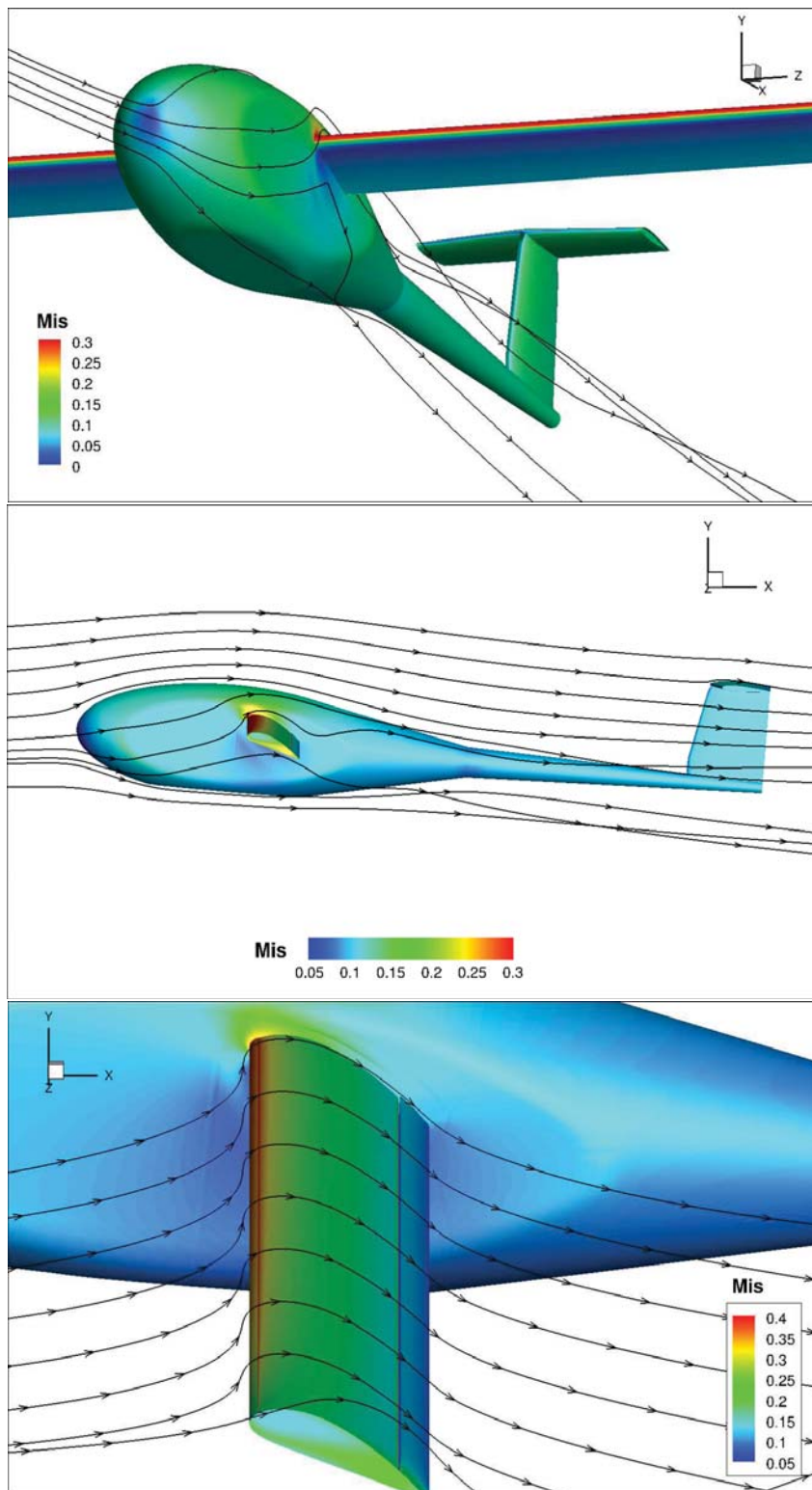


Figure 10.28: Eplane isentropic Mach contours, takeoff/landing condition, maneuvering, simulations performed at  $AoA = 15^\circ$ ,  $M=0.10$  and  $C_\mu = 0.24$ .

at  $AoA = 25^\circ$ . However, the pitching moment is small and would be very controllable by deflecting the flap.

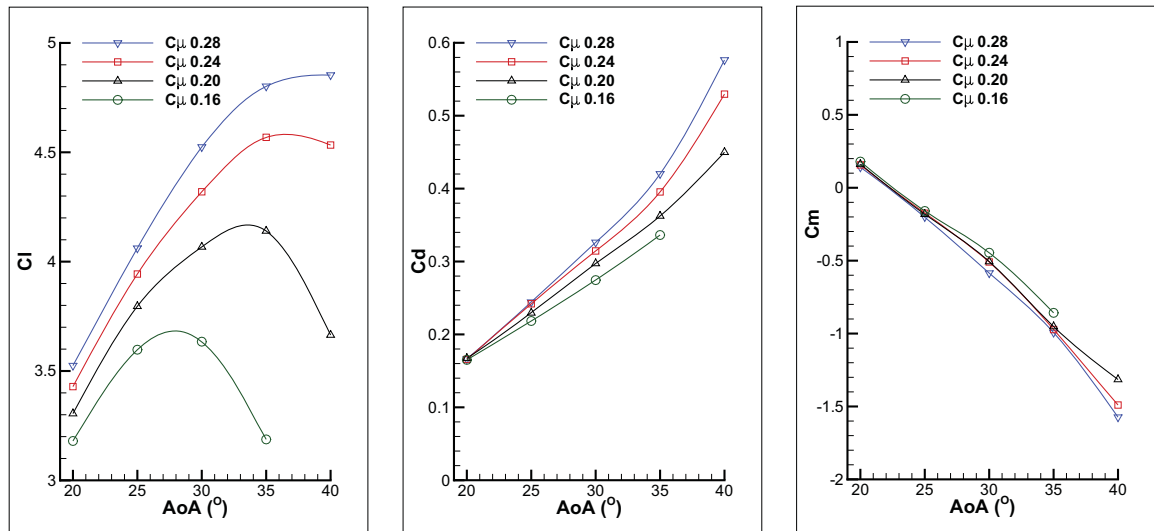


Figure 10.29: Energy expenditure and aerodynamic efficiency versus AoA, simulations performed at  $M=0.10$ ,  $0.16 \leq C_\mu \leq 0.28$

The aerodynamic efficiency and energy consumption for the CFJ-EA at TOL Mach number are shown in Fig. 10.30. As expected, the power coefficient at  $C_\mu = 0.24$  is much higher than at  $C_\mu = 0.04$ . However, since the power consumption is proportional to  $V^3$  (see Eq. 4.13), the actual power consumption increase is only about 3 times higher than at cruise due to the lower TOL speed. For a typical TOL at  $AoA = 25^\circ$  and  $C_\mu = 0.24$ , the aerodynamic  $L/D$  is 16.5. Such a high  $L/D$  at takeoff is made possible by the strong jet that reduces the pressure drag. In the range of AoA studied, the  $L/D$  is similar for all the different  $C_\mu$ .

CFJ at high  $C_\mu$  outperforms the conventional lift enhancement devices such as slats and flaps with a very high maximum lift while keeping the drag and moment low [19,20,63,64]. This is because the use of CFJ generates lift and thrust at the same time, which makes it more efficient than conventional high lift systems. Thus, unlike conventional high lift systems that are used exclusively during takeoff and landing, the CFJ is used for all the flight envelope, with a high  $C_\mu$  for demanding conditions like TOL or high G maneuvers, and a low  $C_\mu$  during cruise.

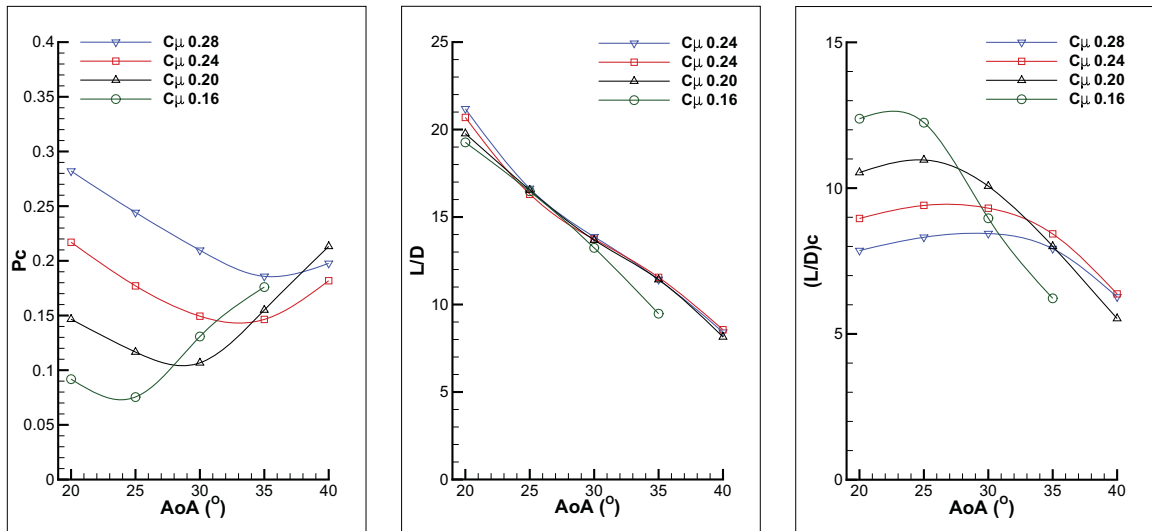


Figure 10.30: Energy expenditure and aerodynamic efficiency versus AoA, simulations performed at  $M=0.10$ ,  $0.16 \leq C_\mu \leq 0.28$ . The pumping efficiency is 85%.

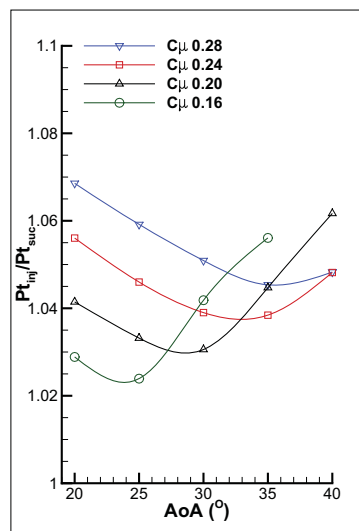


Figure 10.31: Mass-averaged total pressure ratio between the injection and suction cavities, simulations performed at  $M=0.10$ ,  $0.16 \leq C_\mu \leq 0.28$ .

## 10.2.5 Mission Analysis

The cruise condition is taken as  $M=0.15$ ,  $AoA = 5^\circ$  and  $C_\mu = 0.04$  which correspond to the aircraft near maximum  $(L/D)c$ . The TOL condition is taken as  $M=0.1$ ,  $AoA = 25^\circ$  and  $C_\mu = 0.24$  which provides a  $C_L$  value of 3.9 while still conserving a sufficient stall margin AoA of  $10^\circ$ . The CFJ-EA performance is compared with a reciprocating engine powered airplane and three electric airplanes in Table 10.3. The Cessna 172 is chosen for comparison

to represent the current mainstream general aviation reciprocating engine airplane. The electric airplanes selected for comparison are the Antares 20, a motor-glider and the two state-of-the-art E-Genius, and Taurus G4. The mission analysis is performed for a payload of 364 kg for passengers and luggage. The structure factor of the CFJ-EA is taken as 45%, which means that the empty weight of the aircraft is 45% of the gross takeoff weight. The structure factor is 6% higher than that of the Taurus G4 [104] to be conservative. It is reasonable to believe that a low structure factor is achievable with modern construction materials. The batteries account for the rest of the weight of the aircraft. The battery specific energy density  $E^*$  is 180 Wh/kg to have a fair comparison with the current state-of-the-art electric airplane. However,  $E^* = 250$  Wh/Kg is achievable with current Li-ion battery technology. The range of the EA is also calculated with  $E^* = 1750$  Wh/kg, which is used as the projection for the next 20 years [78]. The overall propulsive efficiency of the CFJ-EA is set at 73% to account for the efficiency of the propeller, controller, electric motor and gearbox. The pumping efficiency is set to 85%. Finally, 20% of the energy storage is reserved for the start-up, takeoff, acceleration to cruise velocity and altitude and landing. The mission analysis is performed for a takeoff at sea level, climb to cruise altitude of 5000 ft, cruise at  $M=0.15$ , descent to sea level and landing. More information about the mission analysis can be found in 5.

The CFJ-EA cruises at a  $(L/D)_c$  of 23.5 (see Table 10.3) which is slightly lower than the aerodynamic  $L/D$  the other EAs. Compared with the Taurus G4 that also carries 4 passengers, the wing area of the present CFJ-EA is 50% smaller and the lift coefficient is 2.6 times greater. As a result, its wing loading reach an outstanding  $182.3\text{kg}/\text{m}^2$ . This allows the CFJ-EA to carry the more battery, even though its wing size is smaller. The large amount of battery and excellent cruise  $(L/D)_c$  allow the CFJ-EA to achieve a range of about 200nm. This range is comparable with the 250nm range of the Taurus G4, or the 216nm of the E-Genius, but the airplane size is much lower. This is achieved for a conservative structure factor  $s$  (the ratio of the empty weight to the gross weight) of 0.45. In addition, TOL performance is good due to the very high  $C_{LTO}$  of 3.9. If, in the near

future, the projected power and energy density of the battery increase about 10 fold, as anticipated in [78] the range of the present CFJ-EA could reach 1300+nm. This is a very significant range, even compared with today's general aviation standards like the Cessna 172 and its 700nm range.

Table 10.4 presents the performance variation of the CFJ-EA with the structure factor and the battery specific energy density. The range is increased proportionally to the battery specific energy (an increase of  $E^*$  by 39% yield a 39% range increase) and about inversely proportional to the structure factor (a decrease of  $s$  by 15% yield a 17% range increase). It is worth mentioning that the MPG\*passenger is independent of both the structure factor and the battery. This is because the aircraft gross weight is constant during the study. Had we kept the battery weight constant during the study (as opposed to the aircraft gross weight constant), the range gains would have been more modest but the MPG\*passengers would have increased. The range achieved for  $E^* = 250 \text{ Wh/Kg}$  and  $s = 0.39$  is in excess of 300nm rendering the CFJ-EA a viable alternative for the general aviation.

Aircraft	Cesna 172	Antares 20E	E-Genius	Taurus G4	CFJ Eplane
<b>Geometry</b>					
Wing span (m)	11.00	20.00	16.90	21.36	14.90
Wing area (m2)	16.20	12.60	14.56	20.30	10.44
AR	7.3	31.7	19.6	22.5	21.3
Length (m)	8.28	7.40	8.10	7.40	9.12
<b>Cruise data</b>					
Nb of passengers	4	1	2	4	4
CL	0.32	0.38	0.57	0.50	1.31
CD	0.046	0.013	0.020	0.018	0.036
Pc	N/A	N/A	N/A	N/A	0.020
L/D	7	30	26	28	36.4
L/Dc	7	30	26	28	23.5
Velocity (m/s)	63	51	45	51	51
<b>Weight</b>					
Max TO weight (kg)	1,111	660	950	1,496	1,896
Structure ratio	0.69	0.70	0.47	0.39	0.45
Structure weight (kg)	767.0	460.0	760.0	632.0	853.0
Passenger + payload (kg)	250.0	140.0	182.0	364.0	364.0
Battery weight (kg)	N/A	60.0	310.0	500.0	678.5
<b>Propulsion / Battery</b>					
Propulsive eff (%)	39	73	73	73	73
Pump efficiency (%)	N/A	N/A	N/A	N/A	85
Battery specific E (Wh/Kg)	N/A	136	180	180	180
Energy available (kWh)	2,212.0	8.2	56.0	90.0	122.1
Propeller power cruise (kW)	251.6	15.2	17.6	32.0	35.7
CFJ power cruise (kW)	N/A	N/A	N/A	N/A	14.3
Total power drawn cruise (kW)	251.6	15.2	17.6	32.0	46.0
Propeller power TOL (kW)	N/A	N/A	N/A	N/A	77.9
CFJ power TOL (kW)	N/A	N/A	N/A	N/A	31.9
Total power drawn TOL (kW)	N/A	N/A	N/A	N/A	109.8
<b>Performance</b>					
Range (nm)	700	43	216	250	194
Miles*Passengers/S	172.8	3.4	29.7	49.3	74.5
MPG*Passengers	57.5	236.8	350.7	505.1	288.2
Crusie time (h)	5.7	0.4	2.5	2.5	2.0
Projected range in 20 year (n)	700	298	1512	1750	1355
Wing loading (kg/m2)	68.6	52.9	61.8	69.6	182.3
TO CL	2.0	1.6	1.8	1.8	3.5
TO distance (ft)	1700	1900	1700+	2000	2000

Table 10.3: Mission analysis comparison between the CFJ-EA, Cessna 172 reciprocating engine airplane and three state of the art electric airplanes. Some of the data are only estimates.

Aircraft	CFJ Eplane B250 s0.45	CFJ Eplane B180 s0.45	CFJ Eplane B250 s0.39	CFJ Eplane B180 s0.39
<b>Weight</b>				
Max TO weight (kg)	1,896	"	"	"
Structure ratio	0.45	0.45	0.39	0.39
Structure weight (kg)	853.0	853.0	739.2	739.2
Passenger + payload (kg)	364.0	"	"	"
Battery weight (kg)	678.5	678.5	792.3	792.3
<b>Propulsion / Battery</b>				
Propulsive eff (%)	73	"	"	"
Pump efficiency (%)	85	"	"	"
Battery specific E (Wh/Kg)	250	180	250	180
Uninstalled power (kWh)	169.6	122.1	198.1	142.6
Propeller power cruise (kW)	35.7	"	"	"
CFJ power cruise (kW)	14.33	"	"	"
Total power drawn cruise (kW)	50.0	"	"	"
Propeller power TOL (kW)	77.9	"	"	"
CFJ power TOL (kW)	31.9	"	"	"
Total power drawn TOL (kW)	109.8	"	"	"
<b>Performance</b>				
Range (nm)	269	194	314	226
Miles*Passengers/S	103.5	74.5	120.8	87.0
MPG*Passengers	288.2	"	"	"
Crusie time (h)	2.7	2.0	3.2	2.3
Projected range in 20 year (nm)	1882	1355	2198	1582
Wing loading (kg/m2)	182.3	"	"	"
TO CL	3.5	"	"	"
TO distance (ft)	2000	"	"	"

Table 10.4: Performance change with the battery specific energy and the structure factor. Identical data are represented with " for clarity.

# Chapter 11

## Conclusions

The performance of co-flow jet flow control and its applications are investigated using experimental testing and computational fluid dynamics simulations. These yield a detailed study of energy expenditure, lift enhancement, drag reduction, stall margin increase, dynamic stall removal, and performance variation with Mach number. The experimental testing is performed on a NACA 6415 wing which has been modified to accommodate the CFJ flow control. The experimental data are closely matched by the numerical simulations using an in-house FORTRAN CFD code. Further numerical investigations are conducted for a variety of stationary airfoils, pitching airfoils and high aspect ratio wings. Lastly, the CFJ is applied to design two high efficiency general aviation electric airplanes.

The initial CFJ airfoil study is performed at Mach 0.03 on the modified NACA 6415 CFJ airfoil. The CFJ is found to increase the lift and reduce the drag when compared to the baseline airfoil at the same AoA. At  $C_{\mu} = 0.28$ , the CFJ airfoil achieves a maximum lift coefficient close to 5.0 with negative drag up to  $10^{\circ}$ . In addition, the moment change due to CFJ airfoil is small. The dependency of power coefficient on jet momentum coefficient and AoA is also studied. A low  $C_{\mu}$  of 0.04 yields a very small Pc in the range 0.01 - 0.02 while a higher  $C_{\mu}$  rapidly increases the Pc. A higher AoA yields a lower Pc until the flow separation occurs, roughly  $2 - 3^{\circ}$  before the stall AoA. Let the corrected aerodynamic efficiency

$(L/D)_c$  be defined as  $(L/D)_c = L/(D + P/V_\infty)$ , where the L and D are the aerodynamic lift and drag, P is the CFJ pumping power and  $V_\infty$  is the free stream velocity.

When the Mach number is increased from 0.03 to 0.3, the suction pressure behind the airfoil leading edge is lowered due to the compressibility effect. This increases the CFJ airfoil maximum lift coefficient and decreases the power coefficient because of the lower required jet injection pressure. The drag coefficient remains fairly stable within this range of Mach numbers. At Mach 0.4, as the AoA increases, the flow on the suction surface becomes transonic. Consequently, a strong  $\lambda$  shock wave interrupts the jet and triggers a boundary-layer separation. The shock wave boundary-layer interaction and wave drag increase the total drag and the power coefficient significantly due to a large increase in entropy. Overall, the CFJ airfoil is found to be very effective to enhance lift, reduce drag, and increase stall margin with a Mach number up to 0.4. Energy expenditure is low for a Mach number up to 0.3 but is significantly increased at Mach 0.4.

A trade study on stationary CFJ airfoils is performed to investigate the effect of the airfoil geometry on the performance. The jet location and AoA are influential parameters for the energy consumption and efficiency. To improve the  $(L/D)_c$ , the jet injection location should be located within the 2%-5% chord range where the leading edge (LE) suction effect is the strongest. This is because a low jet exit pressure reduces the pumping power. The pitch-down moment and energy consumption are reduced when the suction is located more upstream. Alternately, the lift is increased and the drag is decreased when the suction slot is located more downstream. The use of reflex camber further reduces the nose-down moment induced by the CFJ airfoil with little loss in  $(L/D)_c$ .

The effect of CFJ on pitching airfoil is investigated at Mach number 0.3 and 0.4. The CFJ pitching airfoil is found to increase the airfoil performance for every flow studied. The CFJ is able to remove the dynamic stall using relatively low energy jets at  $C_\mu = 0.08$ . The time-averaged lift is increased by 32% and the time-averaged drag is decrease by 80%. A strong dynamic stall is also successfully removed using a  $C_\mu$  in the range 0.12 - 0.20. Due to the removal of the dynamic stall, the CFJ airfoil is able to prevent the sharp moment drop

at high AoA, therefore reducing the blade material fatigue and maneuverability constraints. When the Mach number is increased to 0.4, however, the dynamic stall is found to be very difficult to remove due to the appearance of strong shock waves in the flow.

With the stationary and pitching airfoils thoroughly investigated, the focus of the study turns to 3D CFJ wings performance. All the CFJ wings studied feature open injection and suction slots along the span with a rectangular planform. The CFJ wing with an aspect ratio of 20 achieves a maximum  $(L/D)_c$  of 26.8 at a remarkably high cruise  $C_L$  of 1.20 with an AoA of  $5.0^\circ$  and a low  $C_\mu$  of 0.04. The takeoff/landing performance is also excellent with a maximum  $C_L$  of 4.7 achieved at  $C_\mu$  of 0.28 and AoA of  $40.0^\circ$ . When the wing thickness is increased from 15% to 21%, the aerodynamic performance is similar with a 5% increase in  $C_L$  (for the same AoA) and a 5.5% drop in aerodynamic efficiency. However, the efficiency drop is traded with the gain of increased wing inner volume and greater structural strength. When compared to conventional general aviation designs, CFJ wings achieve about three times higher cruise wing loading with a comparable cruise efficiency. Hence CFJ is particularly suitable to design a compact wing with high wing loading.

In a final attempt to investigate the CFJ flow control performance and its applications, 2 high efficiency general aviation EAs are designed. These 4 passenger airplanes make use of the CFJ technology to increase their wing loading and hence their battery load. The cruise Mach number is 0.15 at an altitude of 5000ft. Each CFJ-EA is compared to its baseline EA counter-part, which is the same airplane without CFJ implementation. The first EA designed, the CFJ flying wing (FW) EA, can carry up to 760 kg (1675 lbs) of batteries. This large battery load is made possible thanks to the highly loaded CFJ wing that cruises at  $C_L = 0.64$ . In addition, the use of the CFJ increases the maximum  $C_L$  to about 2.0 at  $C_\mu = 0.12$ , an increase of more than 100% over the baseline FW EA maximum  $C_L$ . As a result, the CFJ FW EA takeoff and landing distances are shorter and the maximum payload is significantly increased. The FW CFJ-EA peak  $(L/D)_c$  is lower than the baseline aircraft peak  $L/D$  (20.6 vs 16.9). However the FW CFJ-EA peak efficiency occurs at higher AoA which allows for high cruise wing loading with a reasonable efficiencies. This yields a

range of up to 180nm based on current battery technology. The drawback of the CFJ FW is that it is difficult to maintain the jet in streamwise direction due to the highly swept fore-body of the aircraft, which reduces the CFJ effectiveness and efficiency.

The second CFJ-EA design adopts a conventional wing-tube configuration to remove the negative wing sweep effect on the CFJ. The design features a sailplane-like high aspect ratio wing and a slender fuselage shape. The CFJ HAR EA combines ultra-high cruise wing loading ( 2-3 times higher than a typical general aviation), a 792kg battery payload and a high  $(L/D)_c$  of 23.5. This yields to an excellent range of 315nm with a battery specific energy density of 250Wh/kg and a structure ratio of 0.39. The maximum  $C_L$  of the CFJ HAR EA is 4.8, which results in a takeoff and landing distance of 2000ft with a TO power usage 2.2 times of the power at cruise. During takeoff and landing, the wing pivots around its 1/4 chord axis so that it can achieve an AoA of  $25.0^\circ$  with the fuselage rotated by only  $5.0^\circ$ . Compared with the state-of-the-art EAs, the wing planform area of the CFJ-EA is 28% smaller than that of the E-Genius and 49% smaller than that of the Taurus G4.

As a result of the work performed in the thesis, a new CFJ-EA concept is developed which may open the door to a new class of general aviation EA design. The same CFJ airfoil flow control technology is suitable for airplanes using conventional propulsion systems to improve the range, reduce the wing size and/or reduce the takeoff and landing distances. The CFJ airfoil outperforms the slats and flaps configuration of conventional airplane with a much higher maximum lift coefficient while keeping the drag low. This is because the CFJ airfoil generates both lift increase and drag reduction at the same time, which makes it more efficient than conventional systems. This thesis indicates that CFJ airfoil not only has the potential to replace conventional high lift systems for improved takeoff and landing performance, but also can be used efficiently during all the flight envelope, including cruise, as long as the Mach number is lower than 0.4. Therefore, the CFJ airfoil is very suitable for general aviation aircraft and high altitude platforms. For the later, a CFJ wing will have a reduced size with a high cruise lift coefficient to compensate for the low air

density. The CFJ airfoil is also applicable to aircraft for which short takeoff and landing performance are needed, and to rotorcraft to remove the dynamic stall.

# References

- [1] O. Chanute, *Progress in Flying Machines*. American Engineer and Railroad Journal, New York, 1894.
- [2] G. G. Stokes, “On the Effect of the Internal Friction of Fluids on the Motion of Pendulums.” Transactions of the Cambridge Philosophical Society 9: 8-106., 1851.
- [3] O. Reynolds, “An Experimental Investigation of the Circumstances which Determine Whether the Motion of Water Shall be Direct or Sinuous, and of the Law of Resistance in Parallel Channels .” Philosophical Transactions of the Royal Society 174(0): 935-982, 1883.
- [4] E.H. Hirschel, H. Prem and G. Madelung, *Aeronautical Research in Germany - From Lilienthal Until Today*. Springer, 2004.
- [5] L. Prandtl, “Königliche Gesellschaft der Wissenschaften zu Göttingen.” ed. Tragflügeltheorie, 1918.
- [6] B. M. Jones, “Flight Experiments on the Boundary Layer.” JAS, Vol. 5, No.3, pp. 81-94, January 1938.
- [7] “With a View to Practical Solutions.” <http://history.nasa.gov/SP-4305/ch4.htm>.
- [8] “The High-Speed Airfoil Program.” <http://history.nasa.gov/SP-445/ch2-4.htm>.
- [9] L. Prandtl, “In Early Developments of Modern Aerodynamics.” J. A. K. Ackroyd, B. P. Axcell, A. I. Ruban, eds., Butterworth-Heinemann, Oxford, UK (2001), p. 77.
- [10] “Human Flight.” <https://fugahumana.wordpress.com/2012/03/31/bio-mimetic-drag-reduction-part-2-aero-and-hydrodynamics/>, March 31, 2012.
- [11] H. Schlichting, K. Gersten, *Boundary-Layer Theory*. Springer, 8th Edition, 2003.
- [12] A. Smith, “High-Lift Aerodynamics,” *Journal of Aircraft*, vol. 12, pp. 501–530, 1975.
- [13] V. Ciobaca , J. Wild, “An Overview of Recent DLR Contributions on Active Flow-Separation Control Studies for High-Lift Configurations.” *Aerospace Lab Journal* AL06-12, June 2013.

- [14] N. M. McFadden, G. A. Rathert Jr. and R. S. Bray, , “The Effectiveness of Wing Vortex Generators in Improving Maneuvering Characteristics of a Swept Wing Airplane at Transonic Speeds.” NACA TN 3523, 1955.
- [15] B. L. Storms and C. S. Jang, “Lift Enhancement of an Airfoil Using a Gurney Flap and Vortex Generators,” *Journal of Aircraft*, Vol. 31, No. 3, pp. 542-547, 1994.
- [16] H. A. Cole Jr., and E. C. Holleman, “Measured and Predicted Dynamic Response Characteristics of a Flexible Airplane to Elevator Control over a Frequency Range Including Three Structural Modes.” NACA TN4147, 1958.
- [17] R. Barrett and S. Farokhi, “On the Aerodynamics and Performance of Active Vortex Generators,” *AIAA 93-3447, 11th Applied Aerodynamics Conference*, August 1993.
- [18] “Nacelle Vortex Generator.” <http://www.aerospaceweb.org/question/aerodynamics/q0255.shtml>.
- [19] T. A. Harris and R. S. Swanson, “Wind-Tunnel Tests of an NACA 23021 Airfoil Equipped with a Slotted Extensible and Plain Extensible Flap .” Technical Note No. 782, NACA, November 1940.
- [20] T. A. Harris and I. G. Recant, “Wind-Tunnel Investigation of NACA 23012, 23021 and 23030 Airfoils Equipped with 40 Percent Chord Double Slotted Flaps.” Report No. 723, NACA, 1941.
- [21] “High-Lift Systems.” <http://history.nasa.gov/SP-468/ch10-5.htm>.
- [22] J. A. Axelson, G. L. Stevens, “Investigation of a Slat in Several Different Positions on an NACA 64A010 Airfoil for a Wide Range of Subsonic Mach Numbers,” *naca-tn-3129*, March 1954.
- [23] R. H. Liebeck and D. N. Smyth, “Study of Slat-Airfoil Combinations Using Computer Graphics.” *Journal of Aircraft* , Vol. 10, pp. 254-256., April 1973.
- [24] H. L. Morgan, Jr., “Low-Speed Aerodynamic Performance of an Aspect-Ratio-10 Supercritical-Wing Transport Model Equipped with a Full-Span Slat and Part-Span and Full-Span Double-Slotted Flaps,” *NASA-TP-1805, L-13825, NAS 1.60:1805*, 1981.
- [25] O. Schrenk, “Experiments With Wbsaugefliigel.” *Aviation Research*, Vol 12, 1027, 1935.
- [26] E.D. Poppleton, “Boundary Layer Control for High Lift by Suction at the Leading Edge of a 40 Degree Seepback Wing.” *ARC-RM 2897 p294,309*, 1955.
- [27] “Introduction to the Aerodynamics of Flight.” <http://history.nasa.gov/SP-367/chapt4.htm#f67>.
- [28] W. Schwier, “Lift Increase by Blowing Out Air, Tests on Airfoil of 12 Percent Thickness, Using Various Types of Flap.” NACA Technical Memorandum No. 1148, June 1947.

- [29] H. F. Muller-Vahl and D. Greenblatt, "Simulation of Active Flow Control on the Flap of a 2D High-Lift Configuration," *AIAA Journal*, Vol. 53, No. 2, pp. 277-295, February 2015.
- [30] R. Petz and W. Nitsche, "Active Separation Control on the Flap of a Two-Dimensional Generic High-Lift Configuration," *Journal of Aircraft*, Vol. 44, No. 3, pp. 865-874, 2007.
- [31] V. Ciobaca, "Simulation of Active Flow Control on the Flap of a 2D High-Lift Configuration." DLR, Lilienthalplatz 7, 38108, Braunschweig, Germany, 2010.
- [32] V. Ciobaca, "Parameter Study for a Slatless 2D High-Lift Airfoil with Active Separation Control Using a URANS Approach." New Results in Numerical and Experimental Fluid Mechanics VIII. Springer Berlin Heidelberg. pp 135-142, 2013.
- [33] E. Phillips, R. Woszidlo, and J. Wygnanski, "The Dynamics of Separation Control on a Rapidly Actuated Flap," *AIAA 2010-4246, 5th Flow Control Conference*, June-July 2010.
- [34] E. Graff, R. Seele, J. Lin and I. Wygnanski, "Sweeping Jet Actuators - a New Design Tool for High Lift Generation." Conference Paper, 2013.
- [35] P. K. Chang, "Drag Reduction of an Airfoil by Injection of Sound Energy." *Journal Aeronautical Science*, Vol. 28, No. 9, pp. 742-743, September 1961.
- [36] F. G. Collins and J. Zelenevitz, "Influence of Sound upon Separated Flow over Wings." *AIAA Journal*, Vol. 13, No.3, pp. 408-411, 1975.
- [37] L. S. Huang, L. Maestrello and T. D. Bryant, "Separation Control over an Airfoil at High Angles of Attack by Sound Emanating from the Surface ." 19th AIAA, Fluid Dynamics, Plasma Dynamics, and Lasers Conference, 1987.
- [38] F.B. Hsiao, C.F. Liu, and J.Y. Shyu, "Control of Wall-Separated Flow by Internal Acoustic Excitation." *AIAA Journal*, Vol. 28, No.8, pp. 1440-1446, August 1990.
- [39] Y. Ishibashi and K. Miyaji, "Detached-Eddy Simulations of Synthetic Jets for High-Angles-of-Attack Airfoils," *Journal of Aircraft*, Vol. 52, No. 1, pp. 168-175, January-February 2015.
- [40] "PIV Analysis of Plasma Actuators." <http://www.sppl.umd.edu/projects/13-piv-analysis.html>.
- [41] M. L. Post and T. C. Corke, "Separation Control on High Angle of Attack Airfoil Using Plasma Actuators." *AIAA Journal*, Vol. 42, No. 11, pp. 2177-2184, November 2004.
- [42] M. L. Post and T. C. Corke, "Separation Control Using Plasma Actuators: Dynamic Stall Vortex Control on Oscillating Airfoil." *AIAA Journal*, Vol. 44, No. 12, pp. 3125-3135, December 2006.

- [43] T. Corke, B. Mertz, and M. Patel, "Plasma Flow Control Optimized Airfoil," *AIAA 2006-1208, 44th AIAA Aerospace Sciences Meeting and Exhibit*, January 2006.
- [44] J. Little, M. Nishihara, I. Adamovich and M. Samimy, "High-Lift Airfoil Trailing Edge Separation Control Using a Single Dielectric Barrier Discharge Plasma Actuator," *Experiments in Fluids*, 48(3), pp. 521-537, March 2009.
- [45] J. Little, K. Takashima, M. Nishihara, I. Adamovich and M. Samimy, "High Lift Airfoil Leading Edge Separation Control with Nanosecond Pulse Driven DBD Plasma Actuators," *AIAA 2010-4256, 5th Flow Control Conference*, June-July 2010.
- [46] R. Englar and R. M. Williams, "Test Techniques for High Lift, Two Dimensional Airfoils with Boundary Layer and Circulation Control for Application to Rotary Wing Aircraft," *Canadian Aeronautics and Space Journal*, vol. 19, pp. 93-108, 1973.
- [47] R. J. Englar, "Circulation Control for High Lift and Drag Generation on STOL Aircraft," *Journal of Aircraft*, vol. 12, pp. 457-463, 1975.
- [48] R. J. Englar, L. A. Trobaugh, and R. Hemmersly, "STOL Potential of the Circulation Control Wing for High-Performance Aircraft," *Journal of Aircraft*, vol. 14, pp. 175-181, 1978.
- [49] R. J. Englar, "Circulation Control Pneumatic Aerodynamics: Blown Force and Moment Augmentation and Modifications; Past, Present and Future." AIAA 2000-2541, June 2000.
- [50] Y. Liu, L. N. Sankar, R. J. Englar, K. K. Ahuja, and R. Gaeta, "Computational Evaluation of the Steady and Pulsed Jet Effects on the Performance of a Circulation Control Wing Section." AIAA Paper 2004-0056, 42nd AIAA Aerospace Sciences Meeting and Exhibit, Reno, Nevada 5 - 8 Jan 2004.
- [51] G.-C. Zha, W. Gao, and C. Paxton, "Jet Effects on Co-Flow Jet Airfoil Performance," *AIAA Journal*, No. 6., vol. 45, pp. 1222-1231, 2007.
- [52] G. S. Jones, "Pneumatic Flap Performance for a 2D Circulation Control Airfoil, Steady & Pulsed." *Applications of Circulation Control Technologies*, Chapter 7, p. 191-244, Vol. 214, Progress in Astronautics and Aeronautics, AIAA Book Series, Editors: Joslin, R. D. and Jones, G. S., 2006.
- [53] P. F. Zhang, B. Yan, A. B. Liu, and J. J. Wang, "Numerical Simulation on Plasma Circulation Control Airfoil." *AIAA Journal*, Vol. 48, No. 10, pp. 2213-2226, October 2010.
- [54] L. W. Traub and M. Biegner, "Experimental Evaluation of a Self-Contained Circulation-Control Wing," *Journal of Aircraft*, Vol. 50, No. 3, May-June 2013.
- [55] G.-C. Zha and D. C. Paxton, "A Novel Flow Control Method for Airfoil Performance Enhancement Using Co-Flow Jet." *Applications of Circulation Control Technologies*, Chapter 10, p. 293-314, Vol. 214, Progress in Astronautics and Aeronautics, AIAA Book Series, Editors: Joslin, R. D. and Jones, G.S., 2006.

- [56] G.-C. Zha, C. Paxton, A. Conley, A. Wells, and B. Carroll, "Effect of Injection Slot Size on High Performance Co-Flow Jet Airfoil," *AIAA Journal of Aircraft*, vol. 43, 2006.
- [57] G.-C. Zha, B. Carroll, C. Paxton, A. Conley, and A. Wells, "High Performance Airfoil with Co-Flow Jet Flow Control," *AIAA Journal*, vol. 45, 2007.
- [58] Wang, B.-Y. and Haddoukessouni, B. and Levy, J. and Zha, G.-C., "Numerical Investigations of Injection Slot Size Effect on the Performance of Co-Flow Jet Airfoil," *Journal of Aircraft*, vol. 45, No. 6, pp. 2084–2091, 2008,.
- [59] B. P. E. Dano, D. Kirk, and G.-C. Zha, "Experimental Investigation of Jet Mixing Mechanism of Co- Flow Jet Airfoil." AIAA-2010-4421, 5th AIAA Flow Control Conference, Chicago, IL, 28 Jun - 1 Jul 2010.
- [60] B. P. E. Dano, G.-C. Zha, and M. Castillo, "Experimental Study of Co-Flow Jet Airfoil Performance Enhancement Using Micro Discreet Jets." AIAA Paper 2011-0941, 49th AIAA Aerospace Sciences Meeting, Orlando, FL, 4-7 January 2011.
- [61] A. Lefebvre, B. Dano, M. D. Fronzo, W. B. Bartow, and G-C. Zha, "Performance of a Co-Flow Jet Airfoil with Variation of Mach Number," *AIAA paper 2013-490*, Jan 2013.
- [62] A. Lefebvre, G-C. Zha, "Numerical Simulation of Pitching Airfoil Performance Enhancement Using Co-Flow Jet Flow Control," *AIAA paper 2013-2517*, June 2013.
- [63] A. Lefebvre, G-C. Zha, "Cow-Flow Jet Airfoil Trade Study Part I : Energy Consumption and Aerodynamic Performance," *AIAA paper 2014-2682*, June 2014.
- [64] A. Lefebvre, G-C. Zha, "Cow-Flow Jet Airfoil Trade Study Part II : Moment and Drag," *AIAA paper 2014-2683*, June 2014.
- [65] A. Lefebvre and G-C. Zha, "Conceptual Design of an Electric Airplane Utilizing Co-Flow Jet Flow Control," *Proceedings of the AIAA Applied Aerodynamics Conference*, Jan 2015.
- [66] "Rotary-Wing Aerodynamics." <http://aviastar.org/theory/bell-407/index.html>.
- [67] William G. Bousman, "Airfoil Dynamic Stall and Rotorcraft Maneuverability." NASA/TM 2000-209601, AFDD/TR 00-A-008, 2000.
- [68] W.J. McCroskey, L.W. Carr, and K.W. McAlister, "Dynamic Stall Experiments on Oscillating Airfoils." U.S. Army Air Mobility RnD Laboratory, Moffett Field, Calif., 1975.
- [69] Prouty, R. W., "The Whys and Whats of Pitch-Link Loads." *Rotor and Wing International*, vol.22, no.10, 1988, pp 17-19.
- [70] W.J. McCroskey, "Unsteady Airfoils." *Fluid Mechanics*, vol.14, 1982, pp 285-311.

- [71] K. W. McAlister, S. L. Pucci, W. J. McCroskey and L. W. Carr, "An Experimental Study of Dynamic Stall on Advanced Airfoil Sections Volume 1. Summary of the Experiment." NASA TM 84245, 1982.
- [72] K. W. McAlister and C. Tung, "Suppression of Dynamic Stall with a Leading-Edge Slat on a VR-7 Airfoil." NASA Technical Paper 3357, 1993.
- [73] Asitav Mishra, "A Coupled CFD/CSD Investigation of the Effects of Leading Edge Slat on Rotor Performance." University of Maryland, Ph.D. thesis, 2012.
- [74] Kwanjung Yee, Wandon Joo, and Dong-Ho Lee, "Aerodynamic Performance Analysis of a Gurney Flap for Rotorcraft Application." *Journal of Aircraft*, May, Vol. 44, No. 3 : pp. 1003-1014, 2007.
- [75] D. Thakkar, R. Ganguli, "Single-Crystal Piezoceramic Actuation for Dynamic Stall Suppression." *Sensors and Actuators*, Volume 128, Issue 1, 2006.
- [76] M. Sun, S. R. Sheikh, "Dynamic Stall Suppression on an Oscillating Airfoil by Steady and Unsteady Tangential Blowing." *Aerospace Science and Technology*, Volume 3, Issue 6, 1999.
- [77] A. Lefebvre, G-C. Zha, "Pitching Airfoil Performance Enhancement Using Co-Flow Jet Flow Control at High Mach Number," *AIAA Paper 2014-0195*, January 2014.
- [78] M. Hepperle, "Electric Flight - Potential and Limitations," *NATO STO-MP-AVT-209*, 2012.
- [79] Mohamed ElBaradei, "Tackling the Global Energy Crisis." IAEA Bulletin 50-1, September 2008.
- [80] D. Knight, G. Zhou, N. Okong'o, and V. Shukla, "Compressible Large Eddy Simulation Using Unstructured Grids." *AIAA Paper 98-0535*, 1998.
- [81] Z. Hu, "Parallel Computation of Fluid-Structure Interaction Using High Resolution Upwind Schemes." Ph.D. Thesis, University of Miami, May 2005.
- [82] P. Spalart and S. Allmaras, "A One-equation Turbulence Model for Aerodynamic Flows." *AIAA-92-0439*, 1992.
- [83] G.-C. Zha, Y. Shen, and B. Wang, "An Improved Low Diffusion E-CUSP Upwind Scheme," *Journal of Computer & Fluids*, vol. 48, pp. 214–220, 2011.
- [84] Y.Q. Shen, and G.C. Zha, "Improvement of the WENO Scheme Smoothness Estimator," *International Journal for Numerical Methods in Fluids*, vol. 64,, pp. 653–675, DOI:10.1002/fld.2186, 2009.
- [85] Y.Q. Shen, G.C. Zha, and B.Y. Wang, "Improvement of Stability and Accuracy of Implicit WENO Scheme," *AIAA Journal*, vol. 47, pp. 331–334, DOI:10.2514/1.37697, 2009.

- [86] Shen, Y.-Q. and Zha, G.-C., “ Improved Seventh-Order WENO Scheme .” AIAA Paper 2010-1451, 48th AIAA Aerospace Sciences Meeting, Orlando, FL, Jan. 4-6, 2010.
- [87] Y.Q. Shen, G.C. Zha, and X. Chen, “High Order Conservative Differencing for Viscous Terms and the Application to Vortex-Induced Vibration Flows,” *Journal of Computational Physics*, vol. 228(2), pp. 8283–8300, doi:10.1016/j.jcp.2009.08.004, 2009.
- [88] A. Jameson, “Time Dependent Calculations Using Multigrid with Application to Unsteady Flows past Airfoils and Wings.” AIAA Paper 91-1596, 1991.
- [89] J. Alonso, L. Martinelli, and A. Jameson, “Multigrid Unsteady Navier-Stokes Calculations with Aeroelastic Applications.” AIAA Paper 95-0048, 1995.
- [90] Y.-Q. Shen, B.-Y. Wang, and G.-C. Zha, “Implicit WENO Scheme and High Order Viscous Formulas for Compressible Flows .” AIAA Paper 2007-4431, 2007.
- [91] H.-S. IM, “High Fidelity Simulation of Non-Synchronous Vibration for Aircraft Engine Fan/Compressor.” Ph.D. Thesis, University of Miami, May 2012.
- [92] B. Wang, “Detached-eddy Simulation of Flow Non-Linearity of Fluid-Structural Interactions Using High Order Schemes and Parallel Computation.” Ph.D. Thesis, University of Miami, May 2009.
- [93] B.-Y. Wang and G.-C. Zha, “A General Sub-Domain Boundary Mapping Procedure For Structured Grid CFD Parallel Computation,” *AIAA Journal of Aerospace Computing, Information, and Communication*, vol. 5, No.11, pp. 2084–2091, 2008.
- [94] T. C. Corke, *Design of Aircraft*. Prentice Hall, 2003.
- [95] Espinal, D. and Im, H. and Lee, B. and Sposato, H. and Kinard, D. and Dominguez, J. and Zha, G.-C., “ Supersonic Bi-Directional Flying Wing, Part II: Conceptual Design of A High Speed Civil Transport .” AIAA Paper 2010-1393, 48th AIAA Aerospace Sciences Meeting, Orlando, FL, Jan.4-6, 2010.
- [96] B. Dano, A. Lefebvre and G-C. Zha, “Flow Mixing Mechanism of a Discrete Co-Flow Jet Airfoil,” *AIAA paper 3097-113*, 2011.
- [97] Wang, B. Y and Zha, G.-C., “Detached-Eddy Simulation of Transonic Limit Cycle Oscillations Using High Order Schemes,” *To appear in Journal of Computer & Fluids*, 2011.
- [98] Im, H. , Zha, G.-C., and Dano, B. P. E., “Large Eddy Simulation of Coflow Jet Airfoil at High Angle of Attack.” *Journal of Fluids Engineering*, Vol. 136 / 021101-1, Feb. 2014.
- [99] Ira H. Abbott, A. E. von Doenhoff, *Theory of Wing Sections*. Courier Dover Publications, 2012.

- [100] Seongim Choi, Juan J. Alonso, Edwin v.d. Weide , “Validation Study of Aerodynamic Analysis Tools for Design Optimization of Helicopter Rotors.” 25th AIAA Applied Aerodynamics Conference, 2007.
- [101] John Watkinson, *The art of the helicopter*. Burlington MA: Elsevier Butterworth-Heinemann, 2004.
- [102] Wang, B. Y and Zha, G.-C. , “Detached-Eddy Simulation of a Co-Flow Jet Airfoil at High Angle of Attack.” AIAA Journal of Aircraft, Vol. 48, No. 5, 2011.
- [103] A. Lefebvre, “Investigation of Co-Flow Jet Flow Control Airfoil and its Applications.” Ph.D. Thesis, University of Miami, May 2015.
- [104] Jack W. Langelaan, Anjan Chakrabarty, Aijun Deng and Kirk Miles, “Green Flight Challenge: Aircraft Design and Flight Planning for Extreme Fuel Efficiency,” *Journal of aircraft*, vol. Vol. 50, No. 3, pp. 832–846, May-June 2013.